

**SEISMIC FRAGILITY ASSESSMENT FOR REINFORCED CONCRETE
HIGH-RISE BUILDINGS**

BY

JUN JI

AMR S. ELNASHAI

DANIEL A. KUCHMA

Report 07-14
September 2007



Mid-America Earthquake Center

Headquarter: University of Illinois at Urbana-Champaign

Abstract

In contrast to the worldwide rapid growth of high-rise buildings, no probabilistic assessment procedures have been proposed or developed for seismic risk evaluation of this special building group. The new purpose of this report is to provide the earthquake engineering community with an integrated probabilistic seismic fragility assessment framework and a reference application for this special building population.

A complete methodology is presented for the seismic fragility assessment of reinforced concrete high-rise buildings. The key steps of the methodology are illustrated through an example of the fragility assessment of an existing 54-storey building with a dual core wall system. The set of rigorously derived probabilistic fragilities are the first published for high-rise RC buildings, thus they fill an important void in regional earthquake impact assessment in Metropolitan communities. The inelastic dynamic analyses for the fragility assessments are undertaken using a simplified lumped-parameter model that was derived from highly detailed FE models using genetic algorithms. New definitions for performance limit states are based on the results of detailed pushover analyses of a multi-resolution distributed finite element model that includes shear-flexure-axial interaction effects. To develop the fragility relationships, more than two thousand dynamic response history analyses were conducted. This study considered uncertainty in structural material values as well as in seismic demand. Thirty natural and twenty artificial strong motion records were selected for the analyses that would produce an appropriate range in structural response parameters due to variation in magnitude, distance and site condition. The overall approach is generic and can be applied to develop computationally efficient and probabilistically based seismic fragility relationships for RC high-rise buildings of different configurations.

Acknowledgements

This study is a product of project EE-1 'Vulnerability Functions' of the Mid-America Earthquake Center. The MAE Center is an Engineering Research Center funded by the National Science Foundation under cooperative agreement reference EEC 97-01785.

Table of Contents

List of Tables	ix
List of Figures.....	xi
1. Introduction.....	1
1.1 Significance.....	1
1.2 Objectives	5
1.3 Organization of the Report.....	5
2. Seismic Fragility Assessment of RC High-rise Buildings.....	8
2.1 RC High-rise Building Configuration and Design.....	8
2.1.1 High-rise Building Definition	9
2.1.2 Structural Types	9
2.2 Seismic Design and Performance of RC High-rise Systems	13
2.3 Requirements for Fragility Assessment.....	16
3. Analytical Structural Modeling.....	19
3.1 Literature Survey	19
3.1.1 Material Properties.....	19
3.1.2 Structural Components	21
3.1.3 Seismic Analysis Approaches.....	24
3.2 Material Constitutive Relationship	26
3.2.1 Concrete	26
3.2.2 Reinforcement Steel	35
3.3 Beam-Column Members and Wall Panel	36
3.3.1 Beam-Column Members.....	36
3.3.1.1 Beam Model with Fibered Sectional Approach.....	36

3.3.1.2 ZEUS-NL Application	38
3.3.2 Structural Wall Panels.....	39
3.3.2.1 Macroscopic Model	40
3.3.2.2 Microscopic Model	42
3.3.2.3 VecTor2 Application	45
3.3.2.4 Necessity of Lumped-Parameter-Based Modeling	46
3.3.3 Wall-Frame Interaction.....	47
3.3.4 Verifications of Frame and Wall FEM Analysis Software.....	49
3.3.4.1 ZEUS-NL for Frame Analysis.....	49
3.3.4.2 VecTor2 for Wall Analysis.....	50
3.4 Lumped-Parameter-Based Model Derivation.....	57
3.4.1 Methodology.....	59
3.4.2 Reference Building Selection	63
3.4.3 Mass Simulation.....	64
3.4.4 Simplification Stage I Using Genetic Algorithm.....	65
3.4.4.1 ZEUS-NL Pushover Analysis of Full Model.....	65
3.4.4.2 Construct Equivalent Wall Boundary Supports.....	68
3.4.4.3 Parametric Study with Genetic Algorithm.....	69
3.4.5 Simplification Stage II Using Genetic Algorithm	76
3.4.5.1 VecTor2 Analysis Using Continuum FEM Model	76
3.4.5.2 Investigated Wall Lumped Modelling	78
3.4.5.3 Parametric Study with Genetic Algorithm.....	78
3.4.6 Lumped Model Evaluation	82
4. Limit States Definition.....	84

4.1 Literature Survey	84
4.1.1 Overview	84
4.1.2 Consideration of Non-structural Damages.....	90
4.2 Proposed Definitions.....	92
4.2.1 Global Pushover Analysis with Whole Frame Model	93
4.2.2 Structural Wall Pushover Analysis	95
4.2.3 Multi-Resolution Distributed FEM Analysis of Whole Building.....	98
4.2.3.1 Overview.....	98
4.2.3.2 Detailed Algorithm	99
4.2.3.3 Application for Reference Building.....	102
4.2.4 New Damage Measure and Limit States.....	119
5. Uncertainty Modeling.....	123
5.1 Literature Survey	123
5.1.1 Overview.....	123
5.1.2 Probabilistic Seismic Demand	125
5.1.3 Probabilistic System Capacity	126
5.2 Ground Motion Uncertainty.....	127
5.2.1 Three Categories of Natural Record Selection	127
5.2.2 Natural Ground Motions Applicability Evaluation.....	130
5.2.3 Artificial Strong Motion Record Application	142
5.3 Material Uncertainty	148
5.3.1 Concrete Strength.....	148
5.3.2 Steel Strength.....	150
5.3.3 Material Uncertainty Random Effects	152

5.4 Geometric Uncertainty.....	159
5.5 Uncertainty Consideration in Simulation.....	159
6. Fragility Curve Assessment	161
6.1 Literature Survey	161
6.1.1 Existing Fragility Curves.....	161
6.1.2 Limitations of Existing Fragility Curves	162
6.2 Proposed Analytical Fragility Assessment Framework	163
6.2.1 Existing Analytical Fragility Assessment.....	163
6.2.2 Proposed Framework	166
6.3 Numerical Simulation to Assess Fragility Relationships.....	167
6.3.1 Selection and Scaling of Intensity Measures	167
6.3.2 Effective Duration.....	174
6.3.3 Dynamic Response History Analyses	180
6.3.4 Fragility Derivation and Log-Normal Regression Function.....	180
6.3.5 Fragility Comparisons and Discussions.....	185
7. Conclusions and Future Work.....	192
7.1 Conclusions.....	192
7.2 Future Work	196
References	198

List of Tables

Table 2.1 Efficiency of RC High-rise Systems for Seismic Applications (after Laogan and Elnashai (1999)).....	14
Table 2.2 Key Features of Fragility Assessment	18
Table 3.1 Main Types of Floor Systems (after Taranath (2005)).....	24
Table 3.2 Seismic Analysis Approaches (after Elnashai).....	25
Table 3.3 Existing Experimental Results Used for Verification	51
Table 3.4 Basics of FEM Analysis in VecTor2	52
Table 3.5 FEA Results by VecTor2 and Comparisons with Test Data	56
Table 3.6 Comparisons between Standard Algorithm and Genetic Algorithm (after Goldberg (1989)).....	60
Table 3.7 Main Features of Reference Building.....	64
Table 3.8 Modal Periods and Mass Participation Factors (MPF).....	67
Table 3.9 Basic Features of Parametric Studies with GA at Stage I.....	71
Table 3.10 Modal Analyses Comparisons between Original and Simplified Models	73
Table 3.11 Designed Capacities and Applied Load Information.....	78
Table 3.12 Basic Features of Parametric Studies with GA at Stage II	80
Table 3.13 Variation from Original Model to Final Lumped Model.....	83
Table 4.1 Performance Levels at Limit States by FEMA 273 (1997).....	85
Table 4.2 Limit States and Typical Damages Based on HRC-Scale (after Rossetto and Elnashai (2003)).....	86
Table 4.3 General Definitions of Limit States (after Rossetto (2004)).....	89
Table 4.4 Correspondence of Limit States (after Rossetto (2004)).....	89
Table 4.5 Definitions of Limit States with ISD for Structural Wall Systems (after Ghobarah	

(2004))	90
Table 4.6 Definitions of Limit States	93
Table 4.7 Regression Relationship Constants for Limit State Displacements versus Axial Loads	98
Table 4.8 MDFEA Model Size and Control DOFs	112
Table 4.9 Selected Ground Motion Records for MDFEA Evaluation	116
Table 4.10 Limit State Criteria for Reference Building Structure	122
Table 5.1 Selected Natural Ground Motion Records	129
Table 5.2 Filtering Period Ranges of Selected Ground Motion Records.....	132
Table 5.3 Earthquakes and Corresponding Ground Motion Records for Comparison III	136
Table 5.4 Artificial Strong Motion Record Details	146
Table 5.5 Coefficient of Variation for Concrete Compressive Strength (after Hueste, et al. (2004))	149
Table 5.6 Coefficient of Variation for Concrete Tensile Strength (after Hueste, et al. (2004))	149
Table 5.7 Statistics and Beta Distribution for A615 Grade 60 Rebar	152
Table 5.8 Average C.O.V. and Bounds of Demands due to Material Uncertainties	156
Table 5.9 C.O.V. of Capacities at Limit States due to Material Uncertainties.....	159
Table 6.1 Evaluation of Natural Accelerograms Reduced by Effective Duration Concept.....	178
Table 6.2 Evaluation of Artificial Accelerograms Reduced by Effective Duration Concept	179
Table 6.3 Simulated Log-Normal Distribution Function Parameters for Fragilities (Natural GMs)	184
Table 6.4 Simulated Log-Normal Distribution Function Parameters for Fragilities (Artificial GMs)	185

List of Figures

Figure 1.1 Distribution of High-rise Buildings in the World (© http://www.emporis.com , 2006)	2
Figure 2.1 Height Limit of High-rise Building	9
Figure 2.2 Concrete Systems Suitable for Buildings with Different Number of Stories (after Ali (2001))	11
Figure 2.3 General Fragility Assessment Framework	17
Figure 3.1 Typical Structural Wall Cross Sections	22
Figure 3.2 Typical FEM Seismic Analysis Algorithm	26
Figure 3.3 Concrete Responses to Compression Load (Mehta and Monteiro (1993))	27
Figure 3.4 Typical Stress Strain Curves of Different f'_c Levels (from Mendis (2003))	28
Figure 3.5 Enhancement Effects by Confining Pressures (from Candappa et al. (1999))	28
Figure 3.6 Variations of Strength as a Function of Strain-rate: Crushing Strength for Concrete (left) and Yield Strength for Steel (Right) (from Bruneau et al. (1998))	29
Figure 3.7 Compressive Constitutive Models Suitable for NSC: Popovics (1973) (Upper) and Hognestad Parabola (Lower)	30
Figure 3.8 Modified Popovics Constitutive Model Suitable for HSC (Collins and Porasz (1989))	30
Figure 3.9 Vecchio and Collins-Mitchell Tension Stiffening Response Models	31
Figure 3.10 Mohr-Coulomb and Drucker-Prager Failure Criteria	33
Figure 3.11 Multi-surface Plasticity Models for Concrete	34
Figure 3.12 Stress-strain Relationship of Reinforcing Steel	35
Figure 3.13 Configuration of Beam Using Timoshenko Beam Theory	37
Figure 3.14 Construction of a Fiber Element (after Spacone et al. (1996))	37
Figure 3.15 Structural Wall Failure Modes (Top) and Cyclic Response (Bottom): Flexural (Left) and Shear (Right) Modes (Paulay and Priestley, 1992)	39

Figure 3.16 Macroscopic Structural Wall Models (after Vulcano (1992))	40
Figure 3.17 Macroscopic Structural Wall Models (after Ghobarah and Youseff (1999)).....	42
Figure 3.18 Smearred Concrete Element Model.....	43
Figure 3.19 Mohr’s Circle of Average Strains	44
Figure 3.20 Hysteretic Models for Concrete (after Palermo and Vecchio (2003)).....	53
Figure 3.21 LSW1 Test Structure and Data vs. FEM Model and Analysis Results.....	56
Figure 3.22 MSW1 Test Structure and Data vs. FEM Model and Analysis Results	57
Figure 3.23 Equivalent Nonlinear Springs at Wall Joint	59
Figure 3.24 Structure of Genetic Algorithm	61
Figure 3.25 Global Stick (Lumped) Model Derivation Using Genetic Algorithm.....	62
Figure 3.26 Reference Building SAP2000 Model (Left), Half Plane View (Middle) and ZEUS- NL Model (Right)	63
Figure 3.27 Lumped Mass Model in Selected Structure.....	65
Figure 3.28 Structural Model in ZEUS-NL (a) and Typical Component Cross Sections (b ~ d)	66
Figure 3.29 First Five Natural Modal Shapes.....	67
Figure 3.30 Distributed Lateral Loads Following Mixed Modal Shape.....	68
Figure 3.31 Main Features in Simplified Model Stage I	69
Figure 3.32 Pushover Response Comparisons between Original and Lumped Models.....	74
Figure 3.33 Pushover Deformed Shape Comparisons at X Direction	74
Figure 3.34 Dynamic Response History Comparisons between Original and Lumped Models ...	76
Figure 3.35 Discrete FEM model of Core Wall Panel.....	77
Figure 3.36 Investigated Lumped Wall Models	78
Figure 3.37 Pushover Comparisons for SVLEM and MVLEM with VecTor2 Model	81
Figure 4.1 Limit States Corresponding to Structural Behavior (after Ghobarah (2004)).....	90

Figure 4.2 Typical Non-structural Components in Building (from WJE (1994)).....	91
Figure 4.3 Global Pushover Responses and Equivalent Simulations	94
Figure 4.4 One-storey Wall Panel Pushover Analysis with N-V Combinations.....	96
Figure 4.5 Processed and Simulated Pushover Curves (Upper) and Limit State Displacements for Different Axial Load Levels (Lower)	97
Figure 4.6 Architecture of UI-SIMCOR Framework (Spencer et al. (2006)).....	102
Figure 4.7 Frame Beam Element and Wall Continuum Element Interface (Left) and Model DOFs (Right).....	104
Figure 4.8 Upper Wall Beam and Lower Wall Continuum Element Interface Models: (a). Interface Model with One Control Point per Floor (Left); (b). Interface Model with Three Control Points per Floor (Right).....	107
Figure 4.9 Wall Interface Interpolation Approaches and DOFs: (a). One-control-point Approach (Upper). (b). Three-control-point Approach (Lower)	108
Figure 4.10 Multi-resolution Distributed Simulation for Reference Building Combining ZEUS- NL and VecTor2 within UI-SIMCOR	111
Figure 4.11 UI-SIMCOR Main Control Window	112
Figure 4.12 Static Loading Histories in MDFEA	113
Figure 4.13 Pushover Comparisons between Results from MDFEA and Complete ZEUS-NL Approaches	114
Figure 4.14 Crack Map and Vertical Strain Distribution of the Wall at Load Step 50	115
Figure 4.15 Spectral Acceleration Diagrams of Selected GMs for MDFEA.....	116
Figure 4.16 Deformed Shapes of Three Modules from DRHA Using the MDFEA Framework	117
Figure 4.17 Sample Displacement Histories and Comparisons between MDFEA and ZEUS-NL Approaches	118
Figure 4.18 Quantitative Definitions for Limit States 1 and 2 Using MDFEA Results	120
Figure 4.19 Wall Shear versus Inter-storey Drift (ISD) and Drift Components Evaluation	121

Figure 4.20 Inter-storey Member Deformation Geometry	121
Figure 5.1 Uncertainty Sources for System Demand and Capacity.....	124
Figure 5.2 Significant Uncertainty Sources for System Demand and Capacity.....	125
Figure 5.3 Selected GM Spectral Accelerations at First Four Modes of Reference Structure	134
Figure 5.4 Modal Significance Factor (MSF) of Ground Motions.....	135
Figure 5.5 Effects of Ground Motion Features on Maximum Seismic Demands	137
Figure 5.6 ISD_{max} Result, Mean, and C.O.V. Values for Selected GM Categories (Continuous Lines in ISD_{max} vs. PGA Plots Are Mean Values, Dashed Lines Are Individual GMs)	139
Figure 5.7 $ISPT_{max}$ Result, Mean, and C.O.V. Values for Selected GM Categories (Continuous Lines in $ISPT_{max}$ vs. PGA Plots Are Mean Values, Dashed Lines Are Individual GMs)	140
Figure 5.8 Fourier and Power Spectra of Category I.....	141
Figure 5.9 Fourier and Power Spectra of Category II.....	141
Figure 5.10 Fourier and Power Spectra of Category III	141
Figure 5.11 Three Artificial Accelerograms Samples from BEQ Series	144
Figure 5.12 Three Artificial Accelerograms Samples from SEQ Series.....	145
Figure 5.13 Fourier and Power Spectra of BEQ Series	147
Figure 5.14 Fourier and Power Spectra of SEQ Series.....	147
Figure 5.15 Histogram with Probability Density Function for Yield Strength of All A615 Grade 60 Bars (by Bournonville et al. (2004)).....	151
Figure 5.16 ISD_{max} and $ISPT_{max}$ Variation for Each Natural Ground Motion Record with Three Levels of Material Strengths f'_c and f_y : 5%, 95%, Mean	154
Figure 5.17 Variation of Maximum Demand Values due to Material Uncertainties.....	155
Figure 5.18 C.O.V. of ISD_{max} and $ISPT_{max}$ for Each Natural Ground Motion Record due to Material Strength Uncertainties	156
Figure 5.19 MDFEA Pushover Comparisons for Different Material Strengths.....	157

Figure 5.20 Quantitative Definitions for Limit States 1 and 2 Using MDFEA Results with Material Uncertainty–induced Variation	157
Figure 5.21 ISD_{max} and $ISPT_{max}$ Capacity Variations due to Material Uncertainties along Pushover Loading History	158
Figure 6.1 Proposed Analytical Fragility Assessment Framework.....	167
Figure 6.2 Average Spectral Intensities for All Ground Motion Records.....	172
Figure 6.3 PGA and SA (T=0.2s, 1.0s) for All Ground Motion Records.....	173
Figure 6.4 Sample Derivation of Effective Duration for Selected Ground Motions	176
Figure 6.5 Spectral Acceleration Plots for Original and Effective Natural Accelerograms	177
Figure 6.6 Spectral Acceleration Plots for Original and Effective Artificial Accelerograms	179
Figure 6.7 ISD_{max} and $ISPT_{max}$ along Height within Time History.....	180
Figure 6.8 Derived Fragility Relationships for All Intensity Measures (from Natural GMs)	183
Figure 6.9 Derived Fragility Relationships for Intensity Measure Using PGA from Artificial GMs: BEQ Series (Left Plot); SEQ Series (Right Plot)	184
Figure 6.10 Fragility Comparisons for Close and Small Earthquake Categories (Derived from Natural (Left) and Artificial (Right) Records)	186
Figure 6.11 Fragility Comparisons for Distant and Large Earthquake Categories (Derived from Natural (Left) and Artificial (Right) Records)	186
Figure 6.12 Fragility Comparisons for Close to Source Earthquake Categories with Different Magnitude Levels	188
Figure 6.13 Fragility Comparisons for Large Magnitude Earthquake Categories with Different Distances to Source	189
Figure 6.14 Fragility Comparisons for Selected Ground Motion Sets from Same Earthquakes but with Different Site Soil Conditions	190

1. Introduction

1.1 Significance

□ **Urbanization and Growth of Cities**

The process of urbanization has been a common feature throughout the past decades, as communities generally intended to settle in favorable locations and to focus their commercial, political and cultural activities around central points. United Nation sources predict that between 1990 and 2020 the urban population of developing countries will increase by 160%, a total increase of 2.2 billion people. More and more large cities or even ‘mega-cities’ (defined by the United Nations (UN) as a city with a population of over eight million) will be created.

□ **Growth of High-rise Building**

From their emergence in the middle of the last century till the present day, high-rise buildings have always been dominant landmarks in the landscape. High-rise buildings are increasing in number and spreading in distribution around the world. Figure 1.1 shows the distribution of high-rise buildings worldwide. The proliferation of high-rise buildings in urban area is spurred by several considerations amongst which:

- Pressure on land in urban areas and increasing demand for office and residential space needs.
- Desire for aesthetics in urban areas and city skyline.
- Innovation in Structural Systems.
- Development of construction technology.

- Cultural inspiration and human desire for higher building.
- Economic growth.

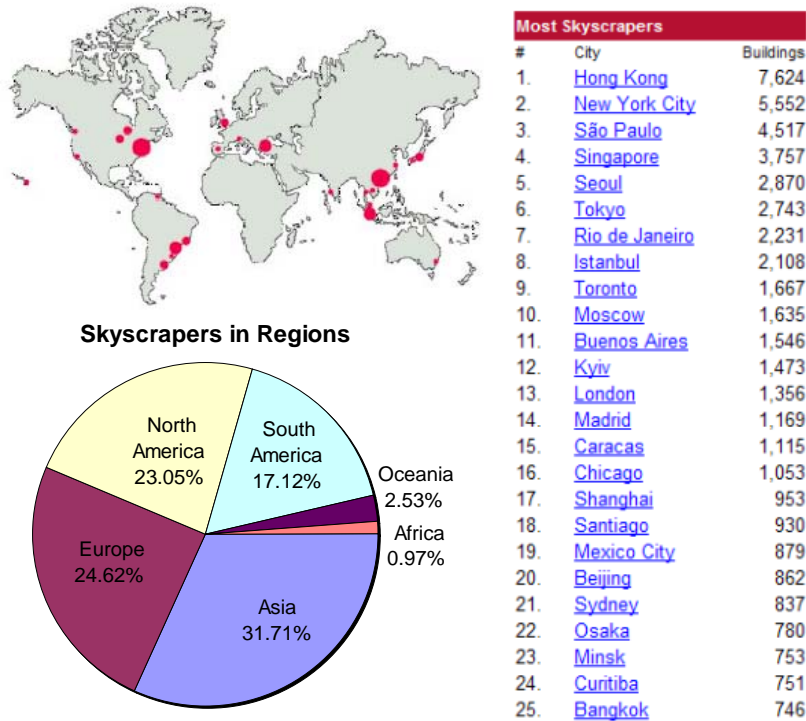


Figure 1.1 Distribution of High-rise Buildings in the World (© <http://www.emporis.com>, 2006)

□ Consequences from Natural Hazard

In urban and metropolitan areas, the increase in the population density and geographical area of many cities places more people and larger communities at risk from natural hazards, especially for developing countries. ‘... *the likelihood of metropolitan disasters, and the enormity of their consequences, are rising. More people in larger areas are facing increasing, and unprecedented risk. Failure to acknowledge and analyze the special conditions of disaster vulnerability that exist in today’s metropolitan areas will costly both in terms of human suffering and in terms of the consequences for economic and social development in poor societies*’ (Anderson (1995)).

- Vulnerability Assessment of Urban Areas

Assessment of the potential severity of the consequences of a particular hazard involves the assessment of vulnerability. Large cities exacerbate the human vulnerabilities because of the difficulties of controlling and mitigating the hazard caused by potential disasters. Residential vulnerability is fundamentally dependent upon the nature of the buildings and infrastructure surrounding them. Among these, high-rise buildings, as residential, commercial, financial or cultural centers, are most significant in the potential consequences from natural hazard events since they usually represent concentrated economic and human assets.

- Fragility Assessment of RC High-rise Buildings

Vulnerability for structures, also referred to as fragility, is directly related to structural damage extent and overall performance during or after the disaster. Damage has direct and indirect consequences. For high-rise buildings, damage can cause significant losses in human life and injuries due to structural collapse and fire. Indirect consequences may include the blockage of transportation, inefficient casualty evacuation, diseases, and other longer-term national and possibly international consequences. Therefore, to predict and mitigate the risk effectively, fragility assessment of high-rise buildings is essential not only for new constructions but also for the existing and largely non-seismically designed stock.

Reinforced concrete (RC) is now the principal structural material used in the construction of high-rise structures. The tendency to use RC systems is expected to continue due to the development of commercial high-strength concretes up to 170 MPa, the advent of admixtures that can provide high fluidity without segregation and advances in construction techniques in both pumping and formwork erection (Ali (2001)). The moldability of concrete is a major factor

in creating exciting building forms with elegant aesthetic expression. Concrete is selected as a primary structural material also because it is a naturally fireproof material and monolithic concrete can absorb thermal movements, shrinkage and creep, and foundation movements. Compared to steel, concrete tall buildings have larger masses and damping ratios that help in minimizing perceptible motion. New structural systems including the composite option that are popular now have allowed concrete buildings to reach new heights.

Due to the significance of wind forces on the lateral load demands in high-rise structures, the effects of lateral loads from seismic action are often not considered in detail under different earthquake scenarios. This can be quite inappropriate, because when assessing the seismic performance of high-rise buildings it is important to consider that: (1) the wide frequency content in real ground motions might excite both lower and higher modes and produce very complex seismic demands; and (2) the imposed displacements in earthquakes may be very substantial since the standard earthquake displacement spectrum peaks in the period of about 3-6 seconds. This period range corresponds to the fundamental modes of many RC high-rise structures, especially when responding in the inelastic range.

There is presently very limited information available to determine the seismic fragility of high-rise buildings. For example, one of the most influential features of RC high-rise building response is the response of RC walls. However, research on different configurations of complex walls is not mature enough to enable the complete understanding of high-rise seismic behavior. In current literature, only a few existing experimental data characterize both global response and localized strain fields of complex walls.

For the reasons above, there is the need for an improved understanding of the inelastic dynamic response of RC high-rise structures subjected to realistic earthquake records representative of near and far earthquakes. Moreover, motivated by the increasing interest in obtaining more accurate assessments of earthquake losses, there is the need for deriving probabilistic fragility relationships for high-rise structures.

1.2 Objectives

This research aims at deriving probabilistic assessment procedures for seismic vulnerability of RC high-rise buildings and demonstrates the procedure through a reference application. The study includes all the essentials included in the framework, such as seismic analysis of typical building, uncertainty modeling of capacity and demand, definition of limit states and final derivation of fragility functions. A comprehensive framework and its demonstration are sought, in order to provide the tools needed for future studies that would cover most different types of high-rise buildings for the purposes of assessing earthquake impact on large cities.

Since most RC high-rise buildings use complex wall systems as the main earthquake resisting system, analytical modeling and corresponding experimental validations for structural walls is a critical part of this research. The goal is to build accurate, reliable and efficient analytical tools for structural walls and the whole building including wall-frame interaction effects.

1.3 Organization of the Report

The report documents completed studies of the essential areas discussed in the previous section,

as well as a literature survey, proposed framework, case study, results, and discussion. Following this introductory chapter, Chapter 2 is a general literature review of RC high-rise buildings and fragility assessments. It includes basic configurations and information related to the structural design of RC high-rise buildings, fragility assessment requirements, and the general framework for deriving fragility relationships.

Chapter 3 describes the analytical structural modeling of a typical RC high-rise building. A literature survey of RC materials, structural components and seismic analysis approaches is briefly summarized. Then detailed modeling descriptions are given both at the material level for concrete and reinforcement steel as well as at the structural component level for frames and walls. Next, the two advanced Finite Element Analysis (FEA) software platforms employed in this study are introduced and verifications are presented. The chapter highlights the importance of developing a lumped-parameter-based model in the fragility assessment for a high-rise building. The lumped-modeling process is illustrated in detail with the selected 54-story high-rise building, and the chapter includes the proposed methodology, the derivation of a two-stage simplified model using the Genetic Algorithm for parametric studies, and final lumped-model evaluations.

Chapter 4 defines new limit states for RC high-rise buildings. Based on the brief literature review, a new qualitative definition is proposed for the limit states. Following this, the chapter discusses the pushover analyses that were conducted to detect both global and local structural behaviors. Then the newly developed multi-resolution distributed FEM analysis (MDFEA) method is summarized, including the concept, model derivation and application for the analysis of real structures. Finally, quantitative definitions of the new limit states are proposed.

Chapter 5 presents a study of uncertainty modeling. After a brief literature survey of probabilistic seismic demand and capacity, major sources of uncertainty, including ground motions and materials, are investigated and discussed. The dominant uncertainty source was determined based on the evaluation of random parameters and the effects on the numerical simulation for fragilities are noted.

Chapter 6 describes the derivation of fragility relationships. This chapter starts with a literature survey of existing fragility curves and then highlights the specific analytical fragility assessment framework used for this study. Numerical simulations were conducted and are presented in the chapter. Specific topics related to the numerical simulations including selecting and scaling intensity measures, adopting effective duration concepts, fragility derivation through dynamic response history analyses, and log-normal regression functions.

Chapter 7 summarizes the report. Conclusions are drawn about the process, proposed framework, fragility results for RC high-rise buildings, and the research findings. Finally, future work is proposed that will extend this research method to types of high-rise buildings besides the reference structure.

2. Seismic Fragility Assessment of RC High-rise Buildings

This chapter provides an overview of the forms of Reinforced Concrete (RC) High-rise buildings, special considerations for the seismic performance and design of these structures, and an introduction to methods for their fragility assessment.

2.1 RC High-rise Building Configuration and Design

As the height of RC concrete buildings increase, so due the complexity of structural forms and the structural engineering design challenge. The design of tall buildings is particularly sensitive to advancements in material science, construction techniques, methods of analysis, and wind engineering. For example, concretes with compressive strength of up 24 ksi (165 MPa) are now commercially available and advancements in mix design and chemical admixtures enable concrete to be more easily and reliably placed. This has enabled reinforced concrete high-rise buildings to become the material of choice in the design of world's tallest buildings, with full-height RC solutions being possible. The design of tall buildings is also very sensitive to the imagination and aspirations of both designers and owners who in their desire to produce ever taller signature structures take advantage of new materials, forms, techniques and innovative approaches. This includes new structural systems such as the introduction of composite construction to tall tubular buildings, first conceived and used by Fazlur Khan in the 1960s, which paved the way for famous composite buildings including the Petronas Towers and Jin Mao building in recent years.

Due to the special features and forms of high-rise buildings, there has arisen the classification of buildings according to both height and structural configuration. These classifications are described in the next two subsections.

2.1.1 High-rise Building Definition

According to *The Council of Tall Buildings and Urban Habitat*, the description of ‘Tall building’, equivalent to ‘High-rise building’ used herein, is: “A building whose height creates different conditions in the design, construction, and use than those that exist in common buildings of a certain region and period.” A traditional height cutoff between high-rise and low-rise buildings is 35 meters or 12 floors as shown in Figure 2.1. This distinction is used as 12-floors is generally considered to be the minimum height needed to achieve the physical presence to earn the recognition as a "high-rise". The twelve-floor limit is also seen as a compromise between ambition and manageability for use in classification of buildings in a worldwide database.

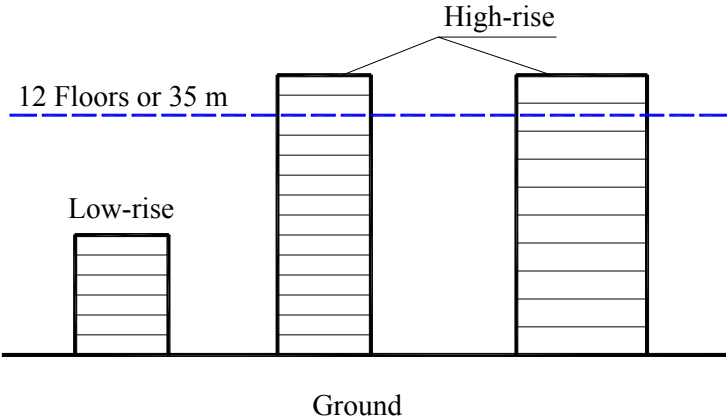


Figure 2.1 Height Limit of High-rise Building

2.1.2 Structural Types

Prior to describing the variety of structural forms used in high-rise construction, it is useful to

first discuss the role taken by “shear” (or “structural”) walls. Khan and Sbarounis (1964) introduced a novel design approach that took advantage of the interaction between rigid frames and shear walls. A combination of the two structural components leads to a highly efficient system, in which the shear wall (or a truss) resists the majority of the lateral loads in the lower portion of the building, and the frame supports the majority of the lateral loads in the upper portion of the building. The innovation of combining the frame with shear trusses or walls allowed Khan to design economically competitive buildings up to 40 stories. This approach is now extensively used in the design of 20- to 40-storey buildings either fully constructed in concrete or composite with steel.

Another significant innovation in high-rises was proposed by Khan and Rankine (1980), who proposed the idea of using a hollow thin-walled tube with punched holes to form the exterior of buildings. By reducing the spacing of exterior columns, the entire system of beams and columns lying on the external perimeter of a building can be made to act as a perforated or framed tube. Figure 2.2 presents the most typical structural forms used in RC high-rise buildings. A brief description of each of these forms is then presented.

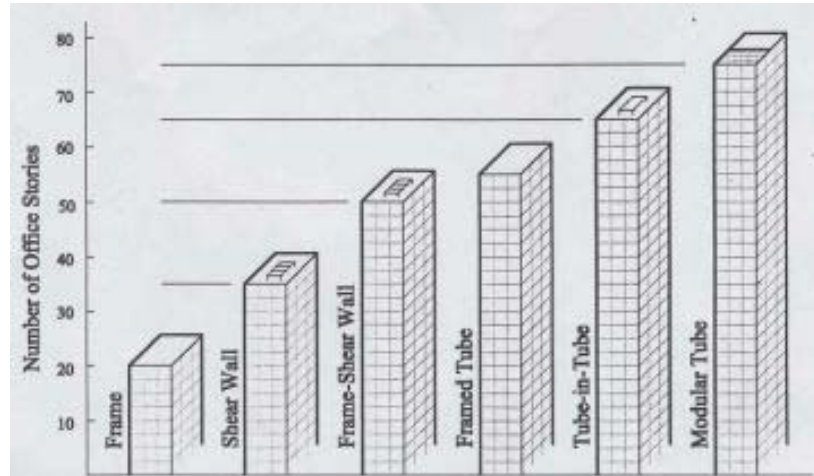


Figure 2.2 Concrete Systems Suitable for Buildings with Different Number of Stories (after Ali (2001))

□ **Moment Resisting Frame Systems (MRF)**

Moment-resisting frames are structures with traditional beam-column frames that carry the gravity loads that are imposed on the floor system. The floors also function as horizontal diaphragm elements that transfer lateral forces to the girders and columns. While a MRF may be designed to resist the lateral load from wind or seismic actions, it is more common to provide another lateral load resisting system.

□ **Braced Frame (BF), Shear Wall Systems (SW)**

To increase the lateral load resisting capacity and reduce relative translations, diagonal braces are frequently added to MRF. These braces enable the downward flow of lateral loads by axial tension and compression in these braces and membrane actions in floors without significant flexural demands being placed on the MRF. Rather than diagonal braces, it is also common to use “shear” (or “structural”) walls. The lateral stiffness of these walls is typically so much greater than that of the MRF in lower high-rise buildings that the lateral load is considered to be entirely

resisted by the walls. Structural walls were first used in 1940s. An additional benefit for the use of RC walls is that their significant mass dampens a building vibration.

□ **Core and Outrigger Systems (COS)**

A combined system called a shear wall-frame interaction system, as first seriously studied by Fazlur Khan, was a milestone in the development of taller concrete buildings. In this system, a central core or dispersed shear walls interact with the remaining beam-column or slab-column framing and in which lateral loads are transmitted by floor diaphragms. The outer part is referred to as the “Outrigger System”. As previously described, the interaction of these two systems enabled a more effective use of both frames and walls.

□ **Tubular Systems (TS)**

A tubular structure acts as a stiffened three-dimensional framework where the entire building works to resist overturning moments. Tubes can be composed of shear walls and frames that act as a single unit. The main feature of a tube is closely spaced exterior columns connected by deep spandrels that form a spatial skeleton and are advantageous for resisting lateral loads in a three-dimensional structural space. The primary types of tubular structures are Framed or Braced Tubes, Trussed Tubes, Tube-in-Tube, and Bundled Tubes.

Tubular core walls are designed to carry the full lateral load or to interact with frames. This gives the building a tube-in-tube appearance although it was designed using the shear wall-frame interaction principle. A tube-in-tube is a system with framed tube that has an external and internal shear wall core which act together to resist the lateral loads. Bundled tubes are used in very large structures as a way of decreasing the surface exposed to wind. Multiple tubes share

internal and adjoining columns depending on their adjacencies.

□ **Hybrid Systems (HS)**

Through advancements in material properties, construction techniques and structural knowledge, more complex but efficient structural form have emerged. They are typically some combination of tube and outrigger system, use either concrete or steel composite systems, and are thereby generally referred to as hybrid systems. One example is the structural frames for the 1,483 ft (452 m) tall Petronas Towers, in Kuala Lumpur, Malaysia, that used columns, core walls, and ring beams made of high-strength concrete but then steel floor beams and decking for faster construction and future adaptation. The core and frame act together to provide the needed lateral stiffness for these very tall towers. Another example of a hybrid system is the 1,380 ft (421 m) high Jin Mao building that was completed in 1999 in Shanghai, China. This structure has a hybrid system with a number of steel outrigger trusses tying the building's concrete core to its exterior composite mega-columns.

2.2 Seismic Design and Performance of RC High-rise Systems

According to Laogan and Elnashai (1999), the characteristics of the previously-described structural forms determine performance during earthquake strikes. Hence a structure's suitability for seismic applications depends on this performance. Table 2.1 presents the general characteristics of each of these forms and their suitability for use in seismic regions.

Table 2.1 Efficiency of RC High-rise Systems for Seismic Applications
(after Laogan and Elnashai (1999))

System Type	Stiffness	Strength	Ductility	Suitability	
				Max number of stories	Seismic application
Moment Resisting Frame	L	H	H	15-20	
Braced Frame	H	H	L-M	20-30	
Structural Wall	H	H	L-M	25-30	
Hybrid Frame	H	H	M-H	30-40	
Core and Outrigger System	H	H	L-M	50-60	
Framed Tube System	H	H	M-H	60-70	
Tube-in-Tube System	H	H	M-H	70-80	
Trussed Tube System	H	H	M-H	80-100	
Bundled Tube System	H	H	M-H	120-150	

Notes: H = High; M = Moderate; L = Low; = Suitable; = Very Suitable.

Due to the economic necessity of incorporating advancements in materials, construction techniques, and analysis methods, the structural design of high-rise buildings is inherently innovative. High-rise buildings typically must be designed to resist significant lateral loads imposed by wind effects from typhoons or hurricanes or due to inertial forces caused by seismic strikes. The overall structural response under wind or seismic loads becomes the controlling factor in most designs. Since the first publication of the Uniform Building Code (UBC) in 1926, provisions for seismic design have been under continuous development and are evolving from their empirical origins (Taranath (2005)). Changes to the provisions are based on improved

understanding of structural behavior as well as advancements in numerical models and computational capabilities.

Due to for the difficulty of precisely evaluating the dynamic response of high-rise structures through laboratory experiments or non-linear analysis, much of our understanding of the seismic behavior of tall structures comes from observations during seismic events. The poor response of many structures during the Northridge (1994) and Kobe (1995) earthquakes inspired a reexamination of structural design methods. For RC high-rise buildings, the limitations of traditional strength-based design were recognized, and performance-based as well as consequence-based evaluation approaches have emerged.

Two building codes have been developed and maintained for seismic design in the United States. The International Building Code (IBC) was developed by the International Code Council (ICC), and the second building code is the National Fire Protection Agency (NFPA) 5000 Code. The seismic design provisions within both codes are consistent with the National Earthquake Hazard Reduction Program (NEHRP) provisions. In addition, both codes incorporate major national standards as references, including the *ACI Building Code Requirements for Structural Concrete* (ACI-318) and the *ASCE Minimum Design Loads for Buildings and Other Structures* (ASCE 7) provisions for seismic loads. To ensure acceptable performance of high-rise RC structures in seismic regions, dynamic analyses and the use of seismic design principles need to be employed at all stages in design.

2.3 Requirements for Fragility Assessment

For hazard mitigation and risk analysis for populations of RC high-rise buildings, it is needed to fully assess and synthesis the potential damage to such structures. A first key step is to define *acceptable* damage and establish performance criteria for different structure forms under different natural hazards. This requires the use of fragility assessment methods, which allow the prediction of the probability of occurrence of different damage states and under different natural hazards. This study focuses on earthquake hazards.

Fragility curves have proven to be essential for making seismic assessments. These fragility functions provide relationships of conditional probability of reaching or exceeding a performance limit state for given level of seismic intensity. The total fragility function can be described mathematically as given below.

$$P(\text{fragility}) = P[LS | S_a = x], \quad P(LS) = P(C < D) \quad (2.1)$$

where, $P(LS) = P(C < D)$, C – capacity and D – demand, and S_a represents the intensity measure of input ground seismic hazard.

Several selection or “choices” need to be made to develop fragility relationships as presented by Rossetto and Elnashai (2003) and given below:

- Choice of sources for the building population damage distributions and associated ground motion values.
- Choice of a ground motion parameter representative of the damage potential of earthquake time histories.
- Determination of a building system and appropriate analytical model for the group of

damage statistics for buildings with similar dynamic response characteristics.

- Selection of damage scales and the definition of limit states for the assessment of building performance.
- Choice of a structural response parameter for estimation of global building damage, and determination of its value at the thresholds of the chosen limit states.
- Determination of a procedure for the interpretation of the building damage statistics in terms of the chosen damage scales.
- Choice of a methodology for the damage data combination and confidence bound estimation.
- Selection of shape functions for fragility curves and of regression procedures.

In this study, an innovative and analytical approach is employed for deriving fragility curves for RC high-rise buildings as shown in Figure 2.3.

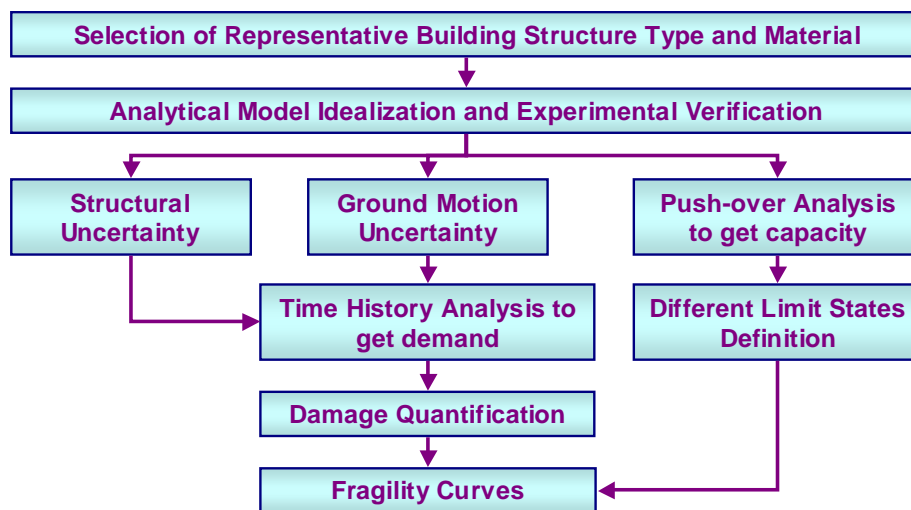


Figure 2.3 General Fragility Assessment Framework

The key features of this process are listed in the Table 2.2:

Table 2.2 Key Features of Fragility Assessment

Item	Components
1	Building system Selection
2	Appropriate analytical modeling
3	Damage scale selection
4	Limit states definition
5	Ground motion intensity scaling
6	Numerical simulations
7	Derivation of fragility relationship
8	Regression and sensitivity analysis

It is not feasible to analytically derive fragility curves for high-rise structures using detailed non-linear finite element models as the time required to conduct the needed parametric studies is prohibitive. Hence, an analysis framework is needed that can provide sufficiently accurate fragility assessments that considers time constraints. A suitable framework was developed in this study that employs parametric Genetic Algorithm optimization and multi-resolution distributed FEM analysis technique. The developed methodologies are used to derive fragility relationships for a selected high-rise RC building as described in Chapter 3 and Chapter 4.

3. Analytical Structural Modeling

3.1 Literature Survey

The analysis methods for RC high-rise buildings have special requirements different from low-to-middle rise buildings, especially for the typical structural system that consists of slender members in frames and more RC stocky structural walls. The complexities of concrete properties, wall-frame interaction and three-dimensional effects need to be accounted for in structural modeling.

The development of an analytical model to predict the response of RC high-rise structures to seismic actions is complicated by the different types of structural elements and the inherently inelastic and non-linear and degrading behavior of reinforced concrete. The behavior of the beams and columns can usually be adequately captured by fiber-based or multi-layer beam elements in which only a strength check is made for shear. For walls, either continuum analysis is required or the effects of shear must be handled separately. While the lateral response of a RC high-rise structure to seismic actions is typically dominated by the response of the wall, it is essential to consider the contribution of the frame and the frame-wall interactions to obtain sufficiently accurate results from the dynamic response-history analyses.

3.1.1 Material Properties

Many researchers have developed constitutive relationships for concrete based on a variety of experimental tests. Shah and Slate (1968) analyzed the micro-mechanism of the idealization of stresses around a single aggregate particle to understand the flow and bond between paste and

aggregates. Darwin and Slate (1970) quantified and compared the effects considering different aggregate types. Ahmad and Shah (1985) and Mendis (2003) obtained the stress-strain curves for concretes for different concrete strengths ranging from 4.0~12.0 ksi. Based on a lot of investigations of test data, many concrete constitutive models have been proposed, for the compressive response of concrete, including the commonly used model by Popovics (1973) and Hognestad Parabolic Model for concrete behavior under uniaxial loading, and nonlinear biaxial stress-strain laws by Kupfer et al. (1969), Kupfer and Gerstle (1973) and Darwin and Pecknold (1977), etc. Other response characteristics have been studied including the modulus of elasticity, Poisson's Ratio, confining effects, cyclic loading responses, and so on. In recent years, high strength concrete (HSC) or high performance concrete (HPC) has become popular for application in high-rise buildings as it increases the height potential for RC construction, reduces weight, and increases available floor areas. ACI Committee 363 has documented the different behaviors of HSC as to their stress-strain relationships, failure modes and time-dependent behavior (ACI (1997)).

Typical stress-strain curves for reinforcing steel bars were obtained from many tests of bars loaded monotonically in tension. For all practical purposes steel exhibits the same stress-strain response in compression as in tension and symmetric cyclic loading responses can be reasonably assumed. Bi-linear or tri-linear (with one flat yield plateau) constitutive relationships have proven to be accurate enough to meet the need of analysis, especially at the structural level (Ngo and Scordelis (1967); Bashur and Darwin (1978)).

3.1.2 Structural Components

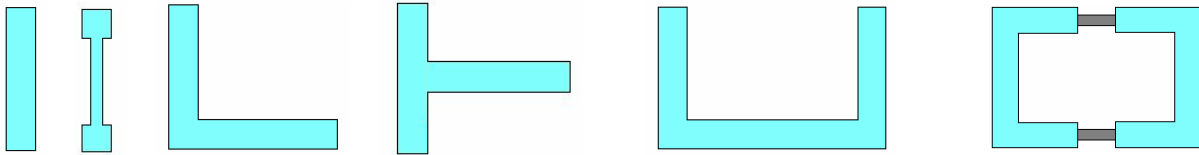
No matter what type and size of RC structure is under investigation the finite element method (FEM) is the most accurate and reliable analytical technique for assessing the demands on structure components in both 2D and 3D domains. The earliest application to the analysis of RC structures was by Ngo and Scordelis (1967). Scordelis et al. (1974) used the same approach to study the behavior of beams in shear. Nilson (1972) introduced nonlinear material properties for concrete and steel and a nonlinear bond-slip relationship into the analysis. Nayak and Zienkiewicz (1972) conducted two-dimensional stress studies that include the tensile cracking and the elasto-plastic behavior of concrete in compression using an initial stress approach. For the analysis of RC beams with material and geometric nonlinearities Rajagopal (1976) developed a layered rectangular plate element with axial and bending stiffness treating concrete as an orthotropic material. RC frame problems have also been treated by many other investigators (Bashur and Darwin (1978); Adeghe and Collins (1986); Bergmann and Pantazopoulou (1988)) using similar methods. At the same time the damage and crack simulation have also been studied and generated some representative models, such as the concept of a smeared crack model introduced by Rashid (1968) and revised or extended by researches like Meyer and Okamura (1985).

According to the buildings categories described in section 2.1.2, typical RC high-rise structures will consist of the following components:

□ Structural Wall

Structural walls serve as the major lateral resisting component, providing much larger stiffness or

capacity in strong directions than other members. The relatively larger width to thickness ratio of walls makes their shear stiffness and strength significantly larger than normal beams and columns. Structural walls usually are designed in practice with cross sections shown in Figure 3.1.



1). Planar 2). L-Shape 3). T-Shape 3). C-Shaped (Flanged) 4). Core Wall System

Figure 3.1 Typical Structural Wall Cross Sections

Independent of the section type of the wall, the lateral stiffness, strength and ductility, are significantly affected by the type and seismic detailing of the joint between superstructure and foundation system. The typical failure modes of the ductile structural walls in high-rise buildings are mainly either flexure or shear failures (Paulay and Priestley (1992)). In actual situation, the failure pattern is always in-between the two failure modes. Most commonly in the literature, analytical modeling of the inelastic response of structural wall systems can be accomplished by using microscopic (detailed finite element) or macroscopic phenomenological models. Microscopic models can provide a refined and detailed definition of the local response, while the other one is better in efficiency and robustness when involved in developing the model and interpreting the results. Both models have to cope with the inherent material inelasticity and complex geometric nonlinearity for high concrete walls and wall-frame interactions. Additional details on this topic are provided in section 3.3.2.

□ **Beam-Column Frame**

Frame members primarily serve to carry the majority of gravity loads in a building, but also serve as part of lateral resisting systems. The beams and columns have varieties of cross section types including rectangular, T-shape and I-Shape. In FEM analysis, it is very straightforward to use beam element connected by rigid joints to form the frame. Bernoulli-Euler beam theory and Timoshenko beam theory (Hjelmstad (2005)) if considering shear effects for deep beam, are widely used and have been implemented into most computer-based frame analysis packages. In order to model inelastic behavior, fiber models are employed as discussed in section 3.3.1.

□ **Floor System**

There are a large variety of floor systems, used in high-rise construction. The selected system must consider the building functionalities, space requirements, construction techniques, reduction of dead loads and cost-effectiveness. Floor system in high-rise buildings functions not only provides gravity load resistance, but also provides constraints between frames, walls, and core and outrigger systems, with great contribution to spatial components interactions. Therefore, in analytical modeling, floor system will be simulated according to the purpose of analysis, which indicates that, if spatial load path and stress strain fields are desired, then detailed modeling for slabs and related beams are necessary in FEA, otherwise simplification into equivalent beam elements or even sets of springs or rigid bars (the part within wall or column regions) are sufficient to obtain overall building response especially in designated directions. Main types of floor systems are listed in Table 3.1 after Taranath (2005).

Table 3.1 Main Types of Floor Systems (after Taranath (2005))

Floor System Type	Main Features
Flat plates	A beamless slab system without any column flares or drop panels
Flat slabs	A beamless slab system with column flares or drop panels
Waffle system (two-way joist system)	Waffle domes are used to reduce weight and solid head applied for strengthening at top of column
One-way concrete ribbed slabs	Has voids between the joists designed as one-way T-beams
Skip joist systems	Extended from the above by increasing joist spacing and removing ribs
Band beam system	Use wide shallow band beams and skip joists
Haunch girder and joist system	A floor framing system with girders of variable depth crossing through joist slab systems
Beam and slab system	Consists of a continuous slab supported by beams large spacing

3.1.3 Seismic Analysis Approaches

As an essential part of the analytical fragility assessment, seismic analysis provides a platform where capacity and demand can be quantified for a given seismic input and structural configuration. Current main categories of approaches are clearly static and dynamic methodologies as listed in Table 3.2. In this study only FEM analyses are under investigation due to the research on RC high-rise buildings. Typically the seismic analysis algorithm with FEM includes the stages shown in Figure 3.2.

Table 3.2 Seismic Analysis Approaches (after Elnashai)

Category	Analysis Type	Seismic Input		Usage for research
		Type	Source	
Static	Equivalent Static	Spectrum	Code	Not applicable
	Conventional Pushover	Spectrum	Code	Get capacity
	Adaptive Pushover	Spectrum	Code provision or by specific record	Get capacity
Dynamic	Multi-Modal spectral	Spectrum	Code	Get demand
	Response History	Time history	Record specific & Site specific	Get demand
	Incremental Dynamic	Time history	Record specific & Site specific	Get demand and capacity

On account of the inherent uniqueness and needs for assessment of seismic fragility, the seismic analysis of RC high-rise buildings should satisfy the following: sufficient accuracy, affordable computational efforts, modeling of critical nonlinearities, and generic compatibility to entire population. Hence, an efficient and reliable macroscopic global modeling for entire building needs to be constructed. This is further discussion in the following sections.

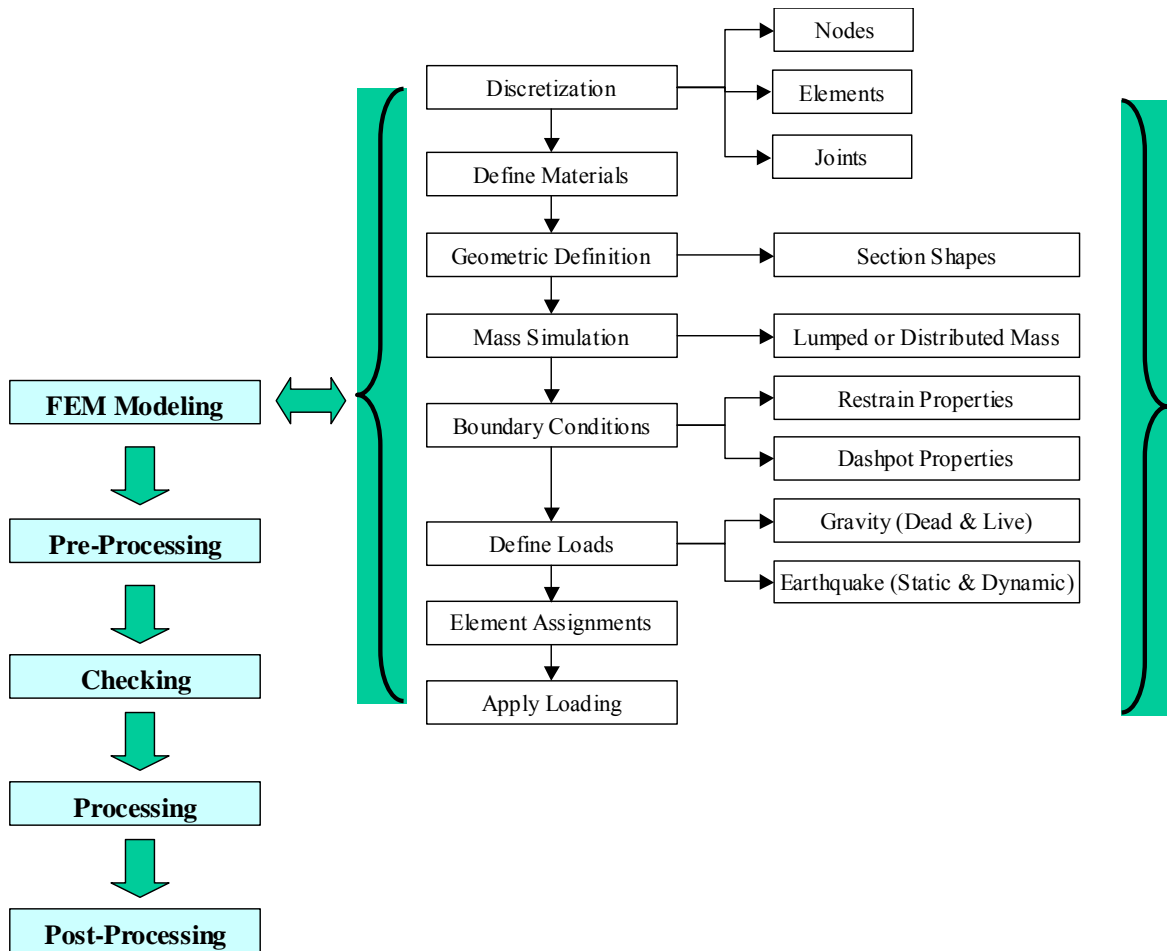


Figure 3.2 Typical Seismic FEM Analysis Algorithm

3.2 Material Constitutive Relationship

3.2.1 Concrete

Concrete is a highly complex heterogeneous material whose response to stress depends on not only individual components like cement and aggregates but also the interaction between these components, showing high inelasticity in both tension and compression. Many mathematical models of the mechanical behavior of concrete are currently in use in the analysis of reinforced concrete structures.

□ Compressive Stress-Strain Behavior

The compressive behavior of plain concrete is normally evaluated using a uniaxial compression test in which a concrete cylinder or prism is loaded along a single axis. A typical compressive stress-strain curve is illuminated in Figure 3.3. Important response characteristics was outlined by Mehta and Monteiro (1993) as follows (see Figure 3.3):

- Linear elastic response: Load reaches 30% f_{co} (f_c)
- Some reduced material stiffness with crack initiation: Stress between 30% and 50% f_{co}
- Further reduction in material stiffness with development of unstable cracks: Stress between 50% and 75% f_{co}
- Further reduction in material stiffness corresponding to spontaneous crack growth and consolidation into crack systems: Stress goes up to f_{co}
- Reduction in compressive strength with increasing compressive strains beyond peak point, corresponding to development of multiple continuous crack systems.

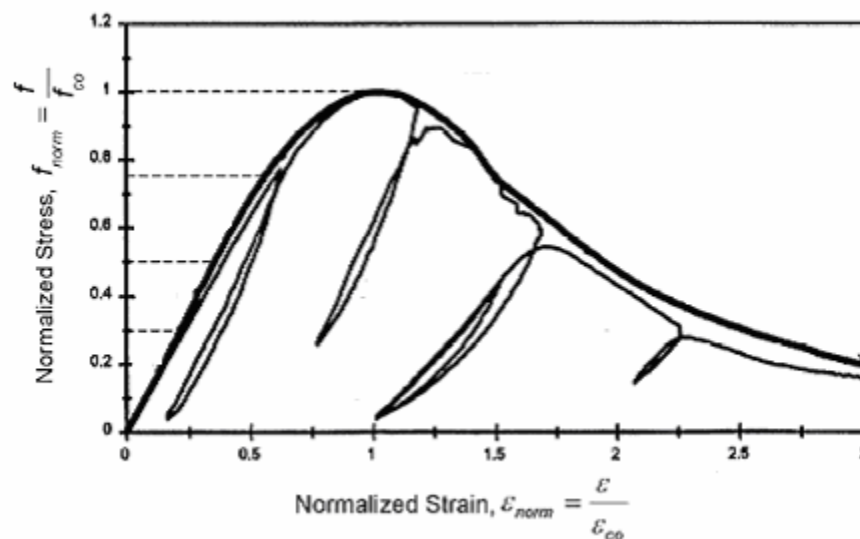


Figure 3.3 Concrete Responses to Compression Load (Mehta and Monteiro (1993))

Some factors influence the concrete stress-strain constitutive relationship, including:

- Compressive strength f'_c . HSC exhibits a longer elastic response and has a more brittle post-peak behavior than NSC as shown in Figure 3.4.

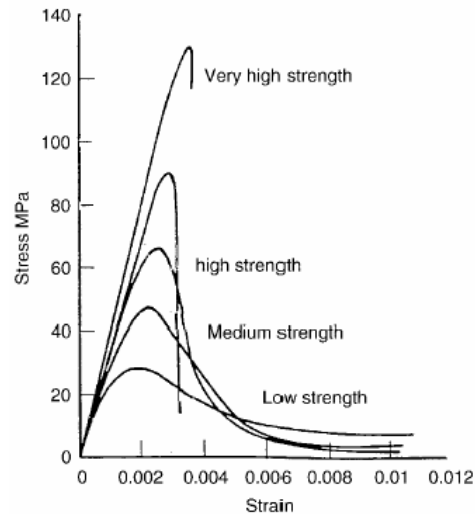


Figure 3.4 Typical Stress Strain Curves of Different f'_c Levels (from Mendis (2003))

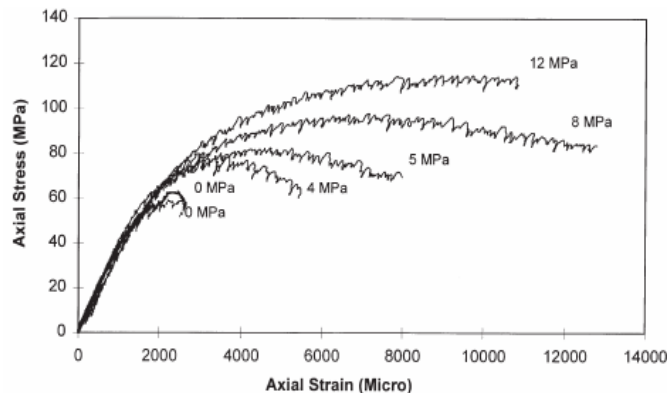


Figure 3.5 Enhancement Effects by Confining Pressures (from Candappa et al. (1999))

- Confinement. Transverse confinements with hoops or spirals increase both the strength and ductility, as shown in Figure 3.5.
- Strain rate. Higher strain rate generally increases the strength value and elastic modulus, and can lead to over-strength effects in seismic behavior as shown in Figure 3.6.

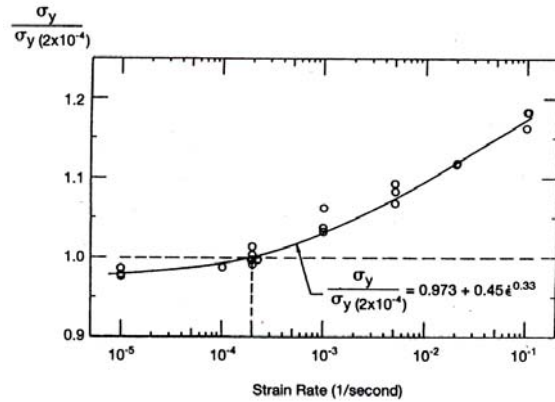
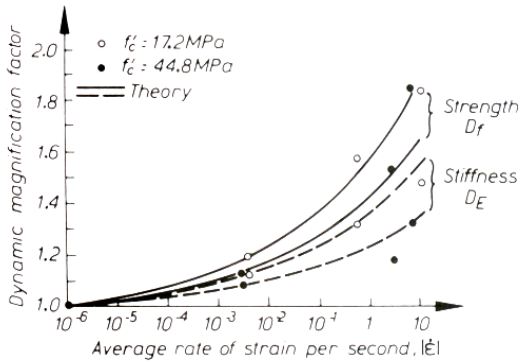
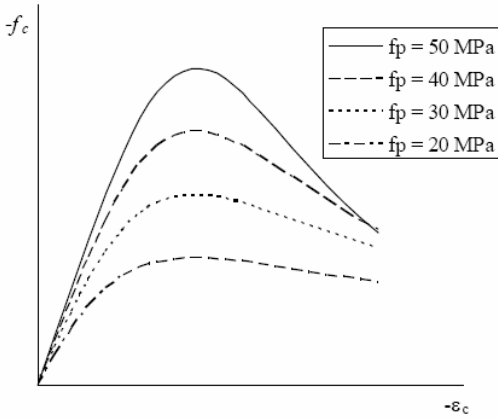


Figure 3.6 Variations of Strength as a Function of Strain-rate: Crushing Strength for Concrete (Left) and Yield Strength for Steel (Right) (from Bruneau et al. (1998))

In analytical models, the previous 5 zones are usually simplified into three stages: Linear elastic to Stiffness reduction and then Strain Softening, or more recently into just two categories: Pre-peak behavior followed by Post-peak behavior.

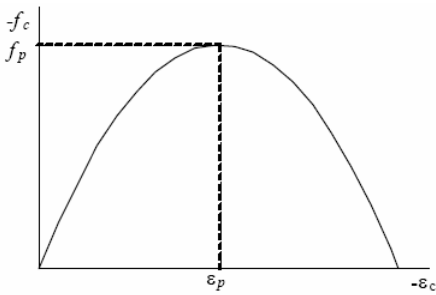
For normal strength concrete (NSC), Popovics (1973) and Hognestad parabola models presented stress-strain curves for a range of normal strength concretes, as shown in Figure 3.7 and Equations 3.1~3.2.

For high strength concrete, Collins and Porasz (1989) modified the stress-strain curve proposed by Popovics (1973) to accommodate the behavior of high strength concrete in compression. The modified Popovics response curve is expressed as Equation 3.3 and shown in Figure 3.8, which primarily differs from the original response curve to create more rapid post-peak stress decay for higher strength concretes that is closer to experimental results.



$$f_c = -\left(\frac{\varepsilon_c}{\varepsilon'_c}\right) f'_c \frac{n}{n-1 + (\varepsilon_c / \varepsilon'_c)^n} \quad (3.1)$$

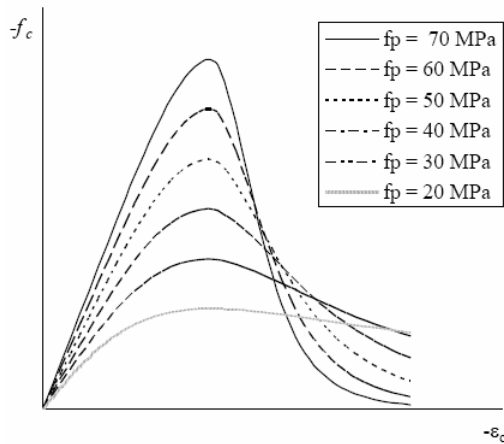
$$\text{where: } n = \frac{E_c}{E_c - E_{\text{sec}}}, \quad E_{\text{sec}} = |f'_c / \varepsilon'_c|$$



$$f_c = f'_c \left[2 \left(\frac{\varepsilon_c}{\varepsilon'_c} \right) - \left(\frac{\varepsilon_c}{\varepsilon'_c} \right)^2 \right] \quad (3.2)$$

$$E_c = |2f'_c / \varepsilon'_c|$$

Figure 3.7 Compressive Constitutive Models Suitable for NSC: Popovics (1973) (Upper) and Hognestad Parabola (Lower)



$$f_c = -\left(\frac{\varepsilon_c}{\varepsilon'_c}\right) f'_c \frac{n}{n-1 + (\varepsilon_c / \varepsilon'_c)^{nk}} \quad (3.3)$$

$$n = 0.80 + \frac{f'_c}{17}, \quad (f'_c \text{ in MPa})$$

$$k = \begin{cases} 1.0, & 0 > \varepsilon_c > \varepsilon'_c \\ 0.67 + \frac{f'_c}{62}, & 0 > \varepsilon'_c > \varepsilon_c \end{cases}$$

Figure 3.8 Modified Popovics Constitutive Model Suitable for HSC (Collins and Porasz (1989))

Considering the normal situation of confinement in RC buildings, the curve can be refined by increasing both the strength and corresponding strain as given in the formulae to take account effects of confinement.

□ **Tensile Stress-Strain Behavior**

In tension, concrete is predominantly brittle and its response can be differentiated into uncracked and cracked response. The practical parameter is cracking strength f_{cr} , which is associated with factors such as specimen size, compressive strength, and the stress states. Some tensile stress strain relationships have been proposed such as those by Vecchio and Collins (1982) Model and its modification as Collins-Mitchell (1987) Model, shown as following Figure 3.9 and Equation 3.4.

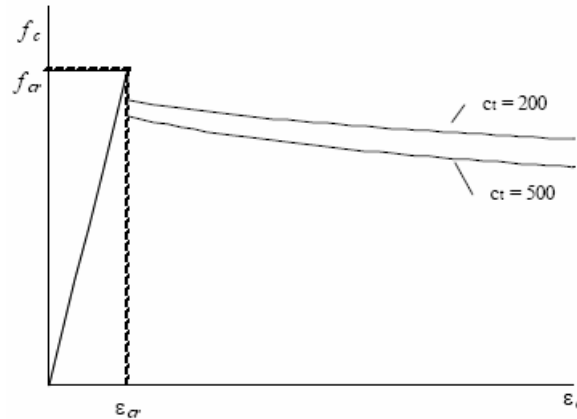


Figure 3.9 Vecchio and Collins-Mitchell Tension Stiffening Response Models

$$f_c = \begin{cases} \frac{\varepsilon_c f_{cr}}{\varepsilon_{cr}}, & \varepsilon_c > \varepsilon_{cr} > 0 \\ \frac{f_{cr}}{1 + \sqrt{200\varepsilon_c}}, & \varepsilon_c > \varepsilon_{cr} > 0, \text{ (Vecchio 1982)} \\ \frac{f_{cr}}{1 + \sqrt{500\varepsilon_c}}, & \varepsilon_c > \varepsilon_{cr} > 0, \text{ (Collins-Mitchell 1987)} \end{cases} \quad (3.4)$$

□ **Elastic Modulus and Poisson's Ratio**

The modulus of elasticity and also the strain corresponding to the peak stress increase with increasing compressive strength, see Equation 3.5 according to ACI 1992. For the Poisson's

Ratio, Mehta and Monteiro (1993) suggest that the Poisson's ratio is generally between 0.15 and 0.20, and that it is lower with high strength concrete. Klink (1985) proposes an average value of Poisson's ratio on the basis of f'_c as Equation 3.6.

$$E_c = 33(w_c)^{1.5} (f'_c)^{0.5} \quad (3.5)$$

$$\nu_c = 4.5 \times 10^{-7} (w_c)^{1.75} (f'_c)^{0.5} \quad (3.6)$$

where, w_c – weight density of concrete, in pcf;

f'_c – uniaxial compressive strength, in psi

□ Multi-Dimensional Loading Behavior

For those components subjected to bi-axial or even tri-axial loadings, monotonic curves are not sufficient to represent the stress and strain states. The two-dimensional failure surface was developed by Kupfer et al. (1969), and further investigated and extended by Yin et al. (1989). The mechanical modeling of concrete in computational analysis such as FEM can be divided into groups: Nonlinear Elasticity Models and Plastic models.

The nonlinear elasticity model is based on the concept of variable moduli defined by elasticity theory (as in Equation 3.7).

$$\sigma_{ij} = D_{ijkl} (\sigma_{ij}) \varepsilon_{kl}$$

where, D_{ijkl} is the secant modulus tensor

$$Or : \sigma_{ij} = D^t_{ijkl} (\sigma_{ij}, \varepsilon_{kl}) \varepsilon_{kl} \quad (3.7)$$

where, D^t_{ijkl} is the tangent modulus tensor

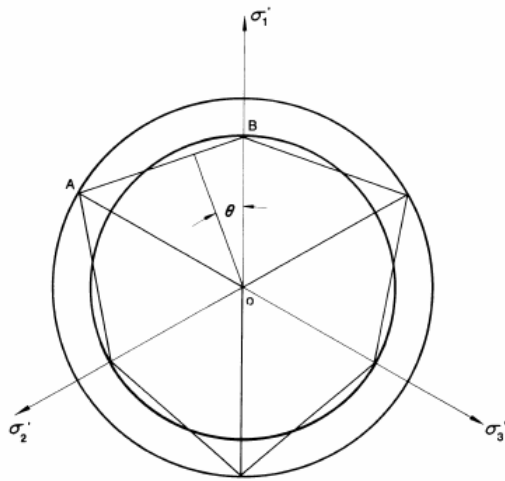
In the pre-failure regime, the inelastic response of concrete is simulated by a piecewise linear elastic model with variable moduli. The model is, therefore, computationally simple and is particularly well suited for finite element calculations.

The plasticity-based model can be considered as a generalization of the previous models introduced with unrecoverable deformation. The conventional way is to decompose the total strain into elastic and plastic parts as illustrated in Equation 3.8.

$$\varepsilon = \varepsilon^e + \varepsilon^p, \quad \dot{\sigma}_{ij} = C_{ijkl} \dot{\varepsilon}_{kl}^e \quad (3.8)$$

where, C_{ijkl} is the material stiffness tensor

The formulation of the constitutive relations in the plastic model is based on three fundamental assumptions: (1) the shape of the initial yield surface; (2) the evolution of the loading surface, e.g. the hardening rule; and (3) the formulation of an appropriate flow rule. For multi-dimensional situation, it is necessary to set the failure criterion during the loading. Many researchers have proposed yield surfaces, such as the well-known Mohr-Coulomb and Drucker-Prager Criterion shown in Figure 3.10 and Equations 3.9~3.10.



Mohr-Coulomb Criterion:

$$f(\sigma_{ij}) = f(I_1, J_2, J_3) = f_c \quad (3.9)$$

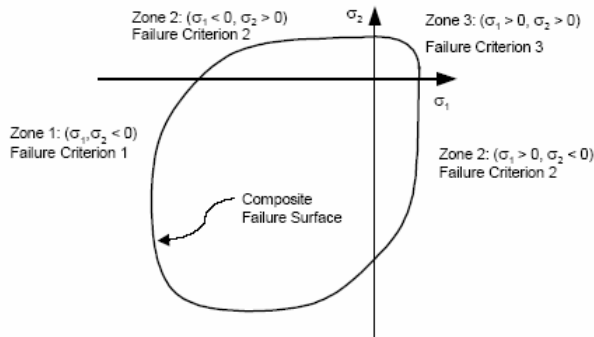
$$\Leftrightarrow |\tau| + \sigma \tan \theta - c = 0$$

Drucker-Prager Criterion:

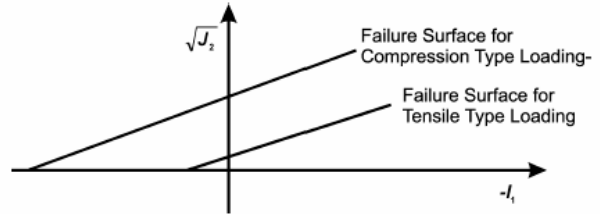
$$f = \alpha I_1 + \sqrt{J_2} = k \quad (3.10)$$

$$\Leftrightarrow \frac{2 \sin \theta}{\sqrt{3}(3 - \sin \theta)} I_1 + \sqrt{J_2} = \frac{6c \cos \theta}{\sqrt{3}(3 - \sin \theta)}$$

Figure 3.10 Mohr-Coulomb and Drucker-Prager Failure Criteria



a. Subjected to Biaxial Loading
(Murray et al. (1979))



b. Subjected to Triaxial Loading
(Lubliner et al. (1989))

Figure 3.11 Multi-surface Plasticity Models for Concrete

According to the criterion above, Kupfer et al. derived the biaxial strength envelope in 1969, which shows that concrete under biaxial compression exhibits an increase in biaxial compressive strength of up to 25% of the uniaxial compressive strength f'_c , when the stress ratio σ_1/σ_2 is 0.5.

To eliminate the potential over-estimation of tensile capacity inherent in Drucker-Prager criterion, researchers have investigated multi-surface failure domains to detect concrete response under various loading conditions. Amongst these is a three surface model (Zone 1 ~ Zone 3) for concrete subjected to biaxial loading proposed by Murray et al. (1979) (see Figure 3.11a) and similar approach in three-dimensional stress state by Lubliner et al. (1989) (see Figure 3.11b).

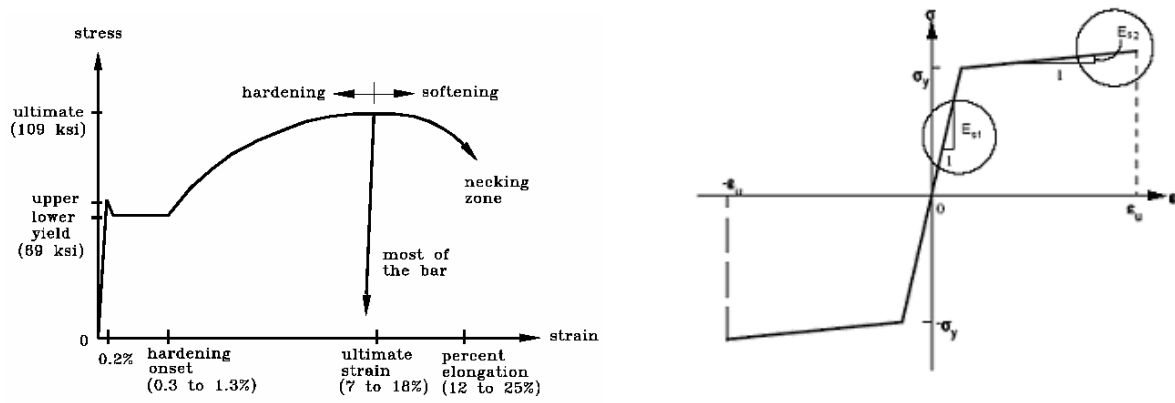
When detecting the evolution of yield surfaces during load history, the hardening rule and flow rule will be employed to track the elastic and plastic regions. Some models have been proposed that used variable shaped yield surfaces, for example, approaches by Han and Chen (1985), Otani et al. (1985), Zaman et al. (1993).

The above discussion and existing approaches are mainly appropriate for normal strength

concrete and already implemented in advanced FEA software platforms, while for more brittle and less ductile HSC, further investigation and experimental validation need to be done to revise the constitutive models.

3.2.2 Reinforcement Steel

The properties of reinforcing steel, unlike concrete, are generally not dependent on environmental conditions or time. Thus, the specification of a single stress-strain relation is sufficient to define the material properties needed in the analysis of reinforced concrete structures. Typical stress-strain curves for reinforcing steel bars used in concrete construction are obtained from coupon tests of bars loaded monotonically in tension. For all practical purposes steel exhibits the same stress-strain curve in compression as in tension.



a. Typical stress-strain curve b. Simplified bi-linear constitutive relationship
(Sample with ASTM A615 Grade 60 steel)

Figure 3.12 Stress-strain Relationship of Reinforcing Steel

The steel stress-strain relation exhibits an initial linear elastic portion, a yield plateau, a strain hardening range in which stress again increases with strain and, finally, a range in which the stress drops off until fracture occurs. The extent of the yield plateau is a function of the tensile

strength of steel. High-strength, high-carbon steels, generally, have a much shorter yield plateau than relatively low-strength, low-carbon steels. In this study the reinforcing steel is modeled as a linear elastic, linear strain hardening material with yield stress σ_y , as shown in Figure 3.12a and 3.12b.

3.3 Beam-Column Members and Wall Panel

Design guidelines for RC high-rise buildings usually assume that the structural wall or core system serve as the main resisting structure for lateral loads, while use beam-column frames to support the gravity loads. This is generally reasonable since columns and beams generally possess lower flexural and shear strengths than structural walls, and higher deformation capacity than the latter. In the mechanism of reinforced concrete, beam and columns are also different from the wall panels, especially in the influencing factors of shear, crack patterns and plastic zone developments.

3.3.1 Beam-Column Members

3.3.1.1 Beam Model with Fiber-Based Sectional Approach

Timoshenko beam theory is the theoretical base for the analysis of RC beams and columns in the present study, as shown in Figure 3.13, with following basics considered:

- The cross section will remain plane as rotating under bending
- Tension stress in concrete will be calculated by available formula using average tensile strain along the member.
- Not only material inelasticity but also geometric nonlinearity (especially for columns)

will be included in the modeling

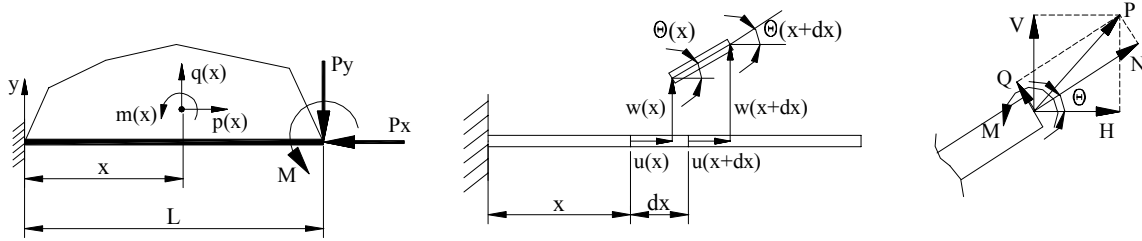


Figure 3.13 Configuration of Beam Using Timoshenko Beam Theory

Fiber-based section frame analysis is one of the most advanced methodologies to model nonlinear behaviors of beam-columns under combined load conditions. Figure 3.14 depicts the concept of a fiber-based element model, where each fiber of a section follows inelastic material hysteresis of concrete and steel. The fiber modeling technique takes account of the strain variation throughout the 2D sections, thus each reinforcing steel bar can be investigated individually and even very complicated section shape can be analyzed directly.

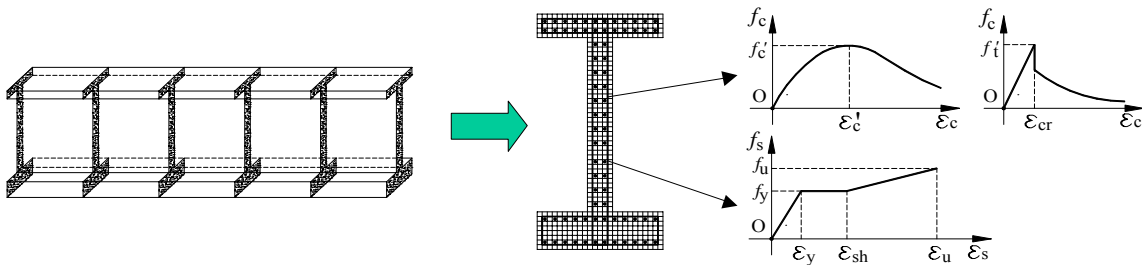


Figure 3.14 Construction of a Fiber Element (after Spacone et al. (1996))

To determine the seismic demand and capacity for frames subjected to earthquake loading, structural analyses using Finite Element Method (FEM) are conducted in this study, including static pushover analysis, modal analysis and dynamic response history analysis. Thus the interpretation of nonlinear structural responses could be assessed at both the member level and section level.

3.3.1.2 ZEUS-NL Application

The Mid-America Earthquake Center analysis environment ZEUS-NL (Elnashai et al. (2002)) is the principal computational tool for the 2D and 3D analysis needs of frames employed in this research. As a promising frame analysis platform, ZEUS-NL has been developed over the past 16 years and used. It is a third generation 3D frame analysis platform, being a development of the programs ADAPTIC (Izzuddin and Elnashai (1989)) and INDYAS (Elnashai et al. (2000)).

In ZEUS-NL, elements capable of modeling material and geometric nonlinearity are available. The sectional force-displacement and moment-rotation responses are obtained through integration of inelastic material responses of individual fibers describing the section. The Eulerian approach towards geometric nonlinearity is employed at the element level. Therefore, full account is taken of the spread of inelasticity along the member length and across the section depth as well as the effect of large member deformations. Since the sectional response is calculated at each loading step from inelastic material models that account for stiffness and strength degradation, there is no need for sweeping assumptions on the moment-curvature relationships as required in other analysis approaches. In ZEUS-NL, conventional pushover, adaptive pushover, Eigen analysis, and dynamic analyses are available that have been tested at the member and structural levels. And axial-shear interaction effects can be taken into account using nonlinear springs (Lee and Elnashai (2002)).

In this study, pushover analysis is executed for load-capacity curves and dynamic response history analysis (DRHA) is in demand for numerical simulations to obtain fragility relationships. ZEUS-NL is chosen as the main analytical platform for selected sample structures.

3.3.2 Structural Wall Panels

Serving as the main lateral resisting structural system, reinforced concrete structural walls have much larger sections, higher stiffness and strength than normal frame members. In high-rise buildings, the wall systems can be quite slender and provide good ductility sufficient ductility and yet exhibit significant shear-critical behavior for which complex cracked damage patterns develop. Thus the Bernoulli-Euler beam model, which is employed in ZEUS-NL, is inadequate for modeling RC structural walls. The typical failure modes of the ductile structural walls are mainly of two types: flexure or shear failures as described in Figure 3.15. The true failure pattern is typically in-between these two failure modes.

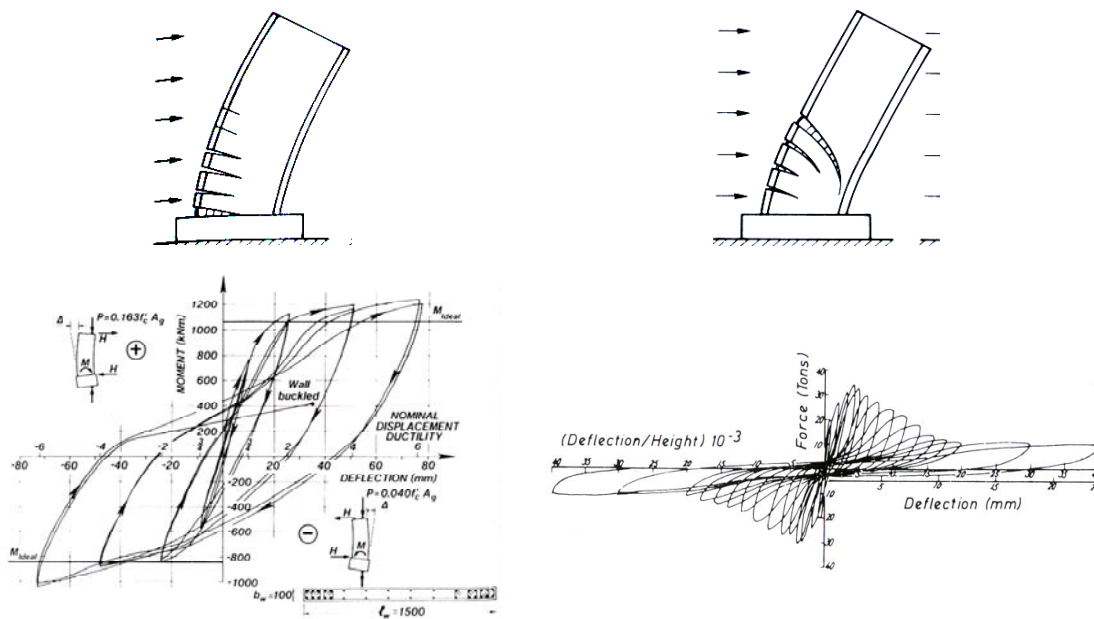


Figure 3.15 Structural Wall Failure Modes (Top) and Cyclic Response (Bottom):
Flexural (Left) and Shear (Right) Modes (Paulay and Priestley (1992))

As previously discussed, analytical modeling includes two categories: macroscopic (lumped parameter based) or microscopic (detailed finite element) models. Both of two ideas are

investigated in this study and conducted for final global model construction.

3.3.2.1 Macroscopic Model

This kind of approach simplifies the wall into lumped beam or truss elements. Several macroscopic models for the analysis of reinforced concrete structural walls are available (Otani et al. (1985); Vulcano and Bertero (1987)). In these models, the wall is taken as equivalent to series of rigid members or trusses connected with nonlinear springs at each floor representing axial and flexural stiffness of both walls, as shown in Figure 3.16a. These models are very simple to implement, however are not capable of accurately representing the shift of the neutral axis along wall cross section.

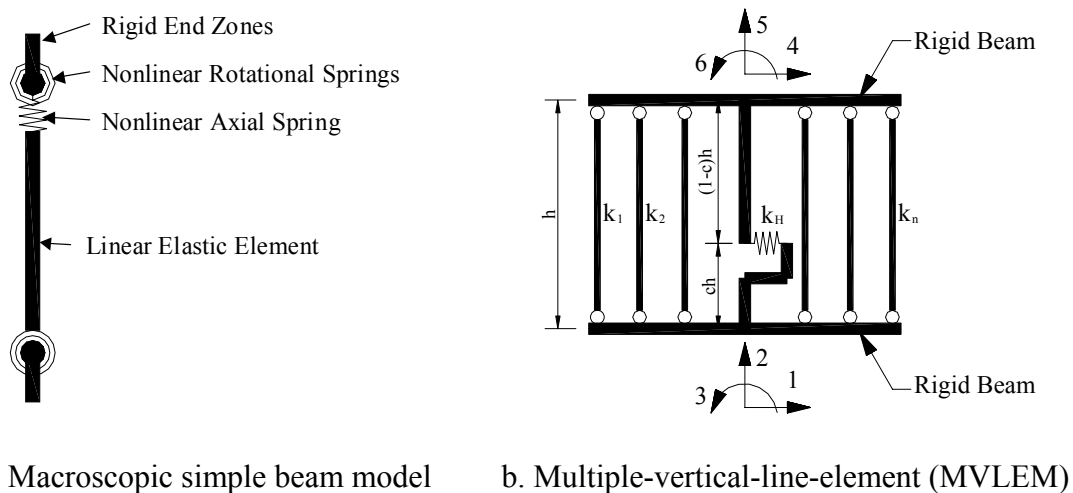


Figure 3.16 Macroscopic Structural Wall Models (after Vulcano (1992))

To improve the model performance, extensive studies have been done taking account of shear effects and interactions with other building parts. Amongst a multiple-vertical-line-element (MVLEM, see Figure 3.16b) was proposed by Vulcano (1992), capturing the shift of neutral axis, effect of fluctuating axial force on strength and stiffness, and nonlinear shear springs.

Ghobarah and Youssef (1999) proposed another similar lumped wall model, treating normally strengthened boundary regions of walls as elastic truss elements at both sides connected with horizontal rigid beams supported by a set of nonlinear springs, and where an elastic beam element is used to connect between the rigid bars at the centre (see Figure 3.17). The inertia of a cross section consisting of the beam element and the two truss elements should be equivalent to that of the wall section. The beam element is cut at one third of its height to allow the positioning of the shear spring. Four steel and four concrete springs $P_{C1} \sim P_{C4}$ and $P_{S1} \sim P_{S4}$ are used to define the plastic hinge region with two exterior springs representing boundary elements and two interior springs representing the middle part of the wall. The four bottom springs are determined through concrete and steel nonlinear hysteretic constitutive relationships and the geometric conditions. Shear spring k_H is defined by using Modified Compression Field Theory (MCFT; Vecchio and Collins (1986)) considering the interaction between axial force, moment and shear.

The equilibrium conditions about axial force and moment should be satisfied:

$$\begin{cases} N = \sum_{i=1}^4 P_{Ci} + \sum_{i=1}^4 P_{Si} \\ M = \sum_{i=1}^4 P_{Ci} x_i + \sum_{i=1}^4 P_{Si} x_i \end{cases} \quad (3.11)$$

P_{Ci}, P_{Si} are axial forces at i th concrete and steel springs, x_i is corresponding position

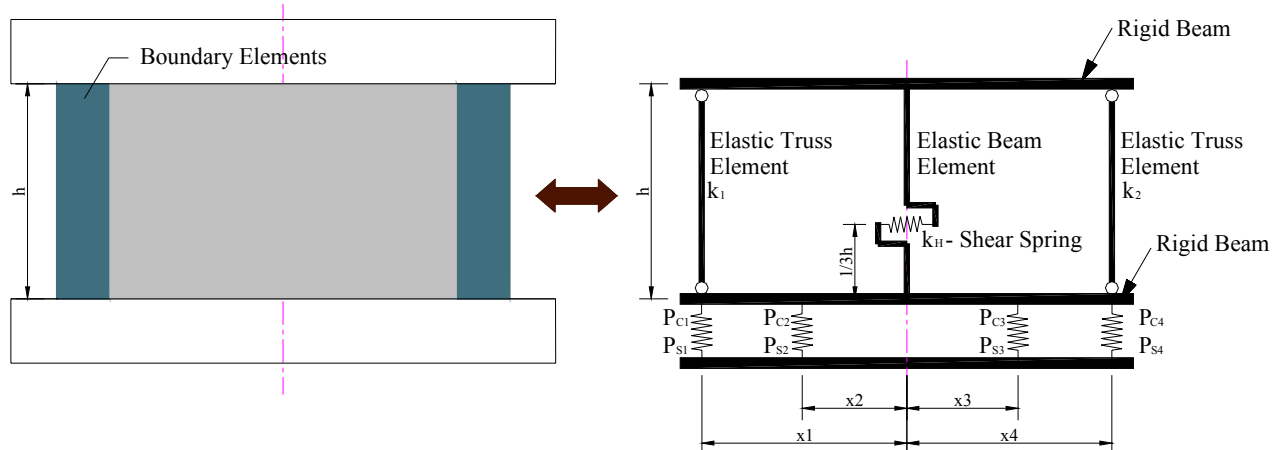


Figure 3.17 Macroscopic Structural Wall Models (after Ghobarah and Youssef (1999))

All of the discussed models can offer a flexible platform to study the influence of various material models, and most importantly for seismic fragility assessment, provides very effective means to model the inelastic seismic behavior of structural walls, which reduces the computational effort greatly.

3.3.2.2 Microscopic Model

Though the macroscopic models are much more computationally efficient, it is still necessary to apply microscopic model with FEM in order to obtain the detailed stress and strain distributions, damage patterns and inelastic behavior throughout the wall. If considered in a wall panel of certain direction or treated as in-plane loading structure, concrete walls can be modeled as an orthotropic nonlinear elastic continuum according to the Modified Compression Field Theory (MCFT, by Vecchio and Collins (1986)), which uses a comprehensive smeared crack model. The MCFT is a rotating angle smeared cracking model that combines compatibility, inelastic constitutive relationship and equilibrium. With the MCFT, quite accurate portrait to predict the response of diagonally cracked membrane elements, of stress and strain distribution under

certain load combination, can be obtained through fast iterations for single element, and then global stiffness matrix will also be assembled easily, which set essential background for FEM analysis. This method assumes that the principal stress and strain coincide and equilibrium is checked at the crack surface. The MCFT for FEA mainly deal with the following:

□ **Smearred Crack and Reinforcement Element Model**

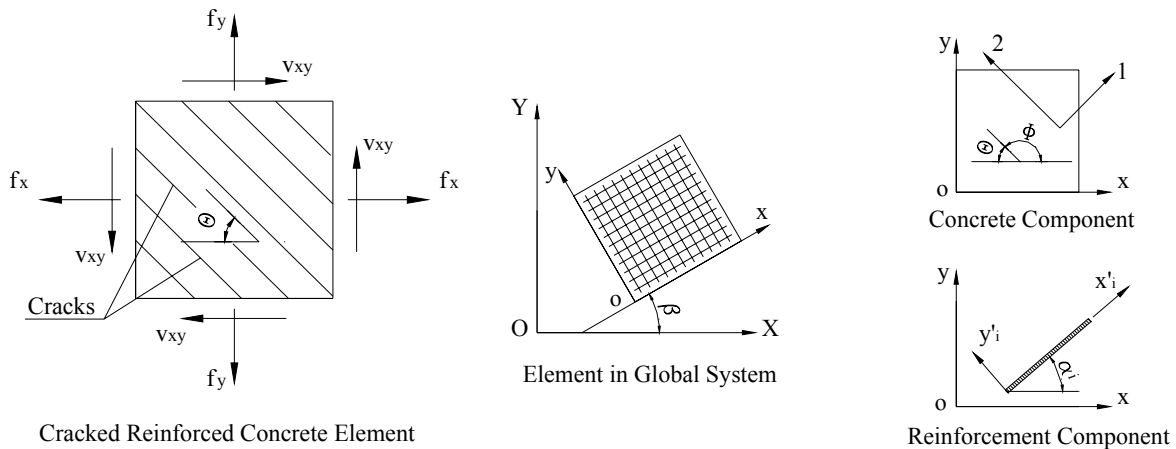


Figure 3.18 Smearred Concrete Element Model

Figure 3.18 describes the stress configuration in the MCFT based on the plane stress model. Vecchio (1990) proposed the algorithm for application of the MCFT to concrete solid problems. The cracked reinforced concrete is treated as an orthotropic material with its principal axes 1, 2 corresponding to the direction of the principal average tensile and compressive strain. Considering plane stress situation, the smeared concrete and steel bars' material stiffness matrices will be

$$D = D_c + \sum_{i=1}^n D_{si} \tag{3.12}$$

□ **Principal Features**

- Strain Compatibility

All relationships among strains within element will be illustrated by Mohr's Circle as below:

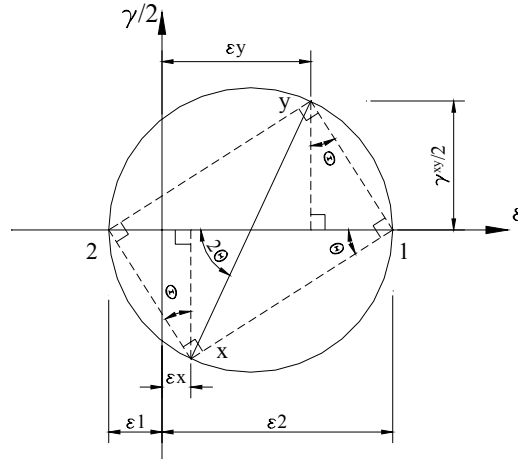


Figure 3.19 Mohr's Circle of Average Strains

- Stress Equilibrium

The concrete and steel stresses: $f_{c1}, f_{c2}, f_x, f_y, f_{sx}, f_{sy}$ need to satisfy the equilibrium conditions in MCFT as follows:

(1). Element Average Value Sense:

$$\begin{cases} f_x = f_{c1} + \rho_{sx} f_{sx} - \frac{v_{xy}}{\tan \theta} \\ f_y = f_{c1} + \rho_{sy} f_{sy} - v_{xy} \tan \theta \\ f_{c2} = v_{xy} \left(\tan \theta + \frac{1}{\tan \theta} \right) - f_{c1} \end{cases} \quad (3.13)$$

(2). Crack Capacity Check

$$\begin{cases} f_x = \frac{v_{ci}}{\tan \theta} + \rho_{sx} f_{sx} - \frac{v_{xy}}{\tan \theta} \\ f_y = \rho_{sy} f_{sy} - v_{ci} \tan \theta - v_{xy} \tan \theta \\ f_{c2} = v_{xy} \left(\tan \theta + \frac{1}{\tan \theta} \right) + v_{ci} \tan \theta \end{cases} \quad (3.14)$$

where, θ indicates the direction of principal stresses referring to Figure 3.19.

3.3.2.3 VecTor2 Application

The inelastic 2D continuum analysis tool VecTor2 (developed at University of Toronto, Vecchio (1990), Wong and Vecchio (2002)) was used to provide the predicted behavior of structural walls in high-rise buildings. VecTor2 employs a rotating-angle smeared crack modeling approach and implements both the MCFT and Disturbed Stress Field Model (DSFM) by Vecchio (2000).

The main difference and improvement from MCFT to DSFM lies in the including of shear slip deformation at the cracks. This leads to the differences between the directions of the principal stress and principal strain fields, hence distinguishing strains due to shear slip from the concrete strains due to stress, which relates the stress and strain by constitutive relationships in a more direct and reliable way. In addition, the shear check required in MCFT is eliminated in the DSFM.

VecTor2 utilizes an iterative secant stiffness algorithm to produce an efficient and robust nonlinear solution technique, with considerations of compression softening and tension stiffening. It can model concrete expansion and confinement, cyclic loading and hysteretic response, construction and loading chronology for repair applications, bond slip, crack shear slip deformations, reinforcement dowel action, reinforcement buckling, and crack allocation processes.

Finite element models constructed for VecTor2 use a fine mesh of low-powered elements. This methodology has advantages of computational efficiency and numerical stability. It is also well suited to reinforced concrete structures, which require a relatively fine mesh to model reinforcement detailing and 3 local crack patterns. The element library includes a three-node

constant strain triangle, a four-node plane stress rectangular element and a four-node quadrilateral element for modeling concrete with smeared reinforcement; a two-node truss-bar for modeling discrete reinforcement; and a two-node link and a four-node contact element for modeling bond-slip mechanisms.

3.3.2.4 Necessity of Lumped-Parameter-Based Modeling

Required by the analytically based seismic fragility assessment, a great many simulations and dynamic analyses must be executed for selected RC high-rise buildings. It is not practical to employ microscopic wall model with continuum FEM for each analysis, e.g. it usually takes more than 2 hours to run one nonlinear DRHA for a RC fiber-based model with more than 1000 beam elements using normal ground motion records. Hundreds of DRHA for analytical fragility assessment would require prohibitively long analysis time. Therefore appropriate lumped-parameter based structural model is one of the major objectives in this study. Referring to the existing lumped models, enhanced simplification techniques are under investigation with the following concerns:

- Simulation of M-N-V interaction
- Constitutive relationships for both normal and high-strength concrete
- Position of shear springs
- Model validation

The computational tool for lumped model will be ZEUS-NL where the final model will consist of beam elements, rigid bars and nonlinear springs. The lumped model will be constructed and refined using mathematical parametric studies on critical joint and spring constants. Both

ZEUS-NL and VecTor2 are used for this process.

3.3.3 Wall-Frame Interaction

Under lateral earthquake loads, the common frame-wall interaction varies along the height of the structure; it also depends upon the type and the stiffness of structural components used to connect the two components of the high-rise buildings, e.g. coupling beams with rigid or semi-rigid connections. Shear racking from the frame and flexural bending from the wall primarily generate the lateral structural deformations. Frame lateral displacements reduce as the height increases; conversely, lateral deflections of braced frames and structural walls increase with the height. This difference in lateral stiffness along the height between the structural components significantly affects the distribution of seismic actions. The shear resisted by the frame increase with the height, while decrease for the interacting wall.

An accurate way to detect the wall-frame interaction is to build detailed FEM models for all structural components, e.g., whole 3D building model with brick elements in ABAQUS. Then the load transfer and redistributions due to different inelastic behavior of different components can be observed and investigated throughout the structure. However the major weakness of this approach is the great computational cost caused by large number of elements and complex nonlinear algorithms required in detailed finite element analyses (FEA). There exist more feasible alternative approaches for the structural modeling by:

- Using beam elements for wall and frame components to form 2D or 3D lumped frame model of the whole structure; for example, 3D frame analysis in ZEUS-NL with fiber-based sectional approach.

- Performing multi-stage FEA, in which a frame model for the whole building is used first and then structural components like wall and frame are analyzed separately in different compatible models with load histories applied on the interfaces obtained from the previous stage results. Through sets of parametric studies, equivalent lumped models for walls and wall-frame interfaces can be derived and integrated into a new simplified structural model for the future analysis especially DRHA, including wall shear effects and wall-frame interactions. This will serve as the main methodology for the derivation of the global structural model for fragility assessment.
- Using a technique called multi-resolution distributed finite element analysis (MDFEA) for the whole building. Different compatible FEM models for different divided sub-structural components are employed in such way that the components subjected to the most complex states of stress are modeled using detailed FE and the remaining parts are in computationally efficient skeletal elements. This might be the most reliable and computationally efficient method to analyze large complex structure. Unfortunately, many existing software do not include all the best material models or finite elements. It is therefore natural to consider the use of more than one analysis platform to make best use of their relative merits. The multiple distinct applications can be combined within a multi-platform simulation framework in a step-by-step fashion with the load history. MDFEA is described in details in section 4.2. However there still exists a major inherent pullback – the huge runtime request of MDFEA makes it impractical to be applied for large amount of simulations for fragility assessment at this time.

3.3.4 Verifications of Frame and Wall FEM Analysis Software

3.3.4.1 ZEUS-NL for Frame Analysis

As the major analysis platform in Mid-America Earthquake (MAE) Center, ZEUS-NL has been used by many researchers from institutes and multiple areas. ZEUS-NL proved itself to be a powerful, accurate and reliable 3D frame FEA software.

During the development, many verifications and enhancements have been executed for ZEUS-NL by the original developers and other researchers. The uniaxial nonlinear constant confinement model was derived by Martinez-Rueda and Elnashai (1997) according to constitutive relationship proposed by Mander et al. (1988) for reasons of numerical stability under large displacements analysis. Pinho et al. (2000) used the application to analyze a full-scale reinforced concrete frame that was tested using the pseudo-dynamic approach at the ELSA laboratory at JRC (Ispra, Italy). The results proved that the experimental response of the model did follow the behavior numerically predicted prior to the test. Most recently, Jeong and Elnashai (2004a) used ZEUS-NL to assess the seismic response of a full-scale 3D RC frame testing structure, showing the blind predictions to be accurate and representative of the subsequent pseudo-dynamic test. Kwon and Elnashai (2005) verified the structural model and analysis environment in ZEUS-NL through comparison of response history analysis with shake table test by Bracci et al. (1992). The verification is undertaken for a multi-storey RC frame building in terms of structural periods and global displacement history since local stress-strain measurements are not available in the published literature.

Therefore ZEUS-NL is functional and reliable enough to meet the requirement of numerical

simulations needed in fragility assessment.

3.3.4.2 VecTor2 for Wall Continuum Analysis

□ Existing Experimental Data

In the analytical modeling process VecTor2 will be used to serve as the primary analysis tool for RC shear walls to include shear contributions and M-V-N interactions. As advanced FEM software, VecTor2 have been widely employed by researchers for different kinds of RC continuum structures, including predictions for large-scale experimental test specimens. Palermo and Vecchio (2004) have verified the performances of VecTor2 for series of shear wall test researches, such as Portland Cement Association (PCA) slender structural walls (Oesterle et al. (1976)), O series wall specimens tested at the University of Ottawa (Wiradinata and Saatcioglu 2002), and DP walls tested by Palermo and Vecchio (2004). Multiple aspects, consist of concrete and steel reverse cyclic constitutive relationships and FEM meshing, are investigated with the evaluation of effects on FEA results and comparisons with experiment results from both global responses and local RC behavior. It was concluded by Palermo and Vecchio (2004) that for both squat and slender walls VecTor2 can handle the microscopic FEA very well and detailed information from global deformation to local stress strain fields and crack propagation can be collected accurately.

Due to the significance of structural wall performance in high-rise buildings, additional verifications are conducted to evaluate VecTor2 from accuracy and stability aspects in this research. Here, the results from two systematic large-scale shear wall experiments conducted by other researchers are compared with the results from FEM analysis. For the purpose of

verifications, wall shapes are considered based on the defined slenderness H/B of the specimens, and all of them are subjected to reversed cyclic loadings during experiments. The selected available test results are listed in Table 3.3.

Table 3.3 Existing Experimental Results Used for Verification

Wall Categories	Slenderness (H/B)	Selected Samples
Squat	< 2.0	MSW and LSW tested in Greece (Salonikios et al. (1999))
Slender	≥ 2.0	SW series tested at Imperial College (Salama (1993))

□ **Analytical Results Comparison and Comments**

The verification procedure starts with the RC continuum model constructions of selected specimens in VecTor2, following the main features defined in Table 3.4. The hysteretic analyses were performed and the results post-processed to obtain the desired data for the comparisons, including:

- Global hysteretic behavior
- Critical points such as cracking, yielding, and ultimate points
- Failure modes and damage patterns
- Other available stress, strain or crack information

Table 3.4 Basics of FEM Analysis in VecTor2

Items	Details
Mesh Size	Medium, from 60 to 200mm (~10 times aggregate size)
Concrete Compression	Popvics model (pre- and post-peak) as base curve
Concrete Hysteretic Model	Nonlinear with plastic offset model by Palermo and Vecchio (2003)
Tension Stiffening	Counted using the model by Bentz (2003)
Confining Effect	Kupfer and Richart model
Convergence Criteria	Within ratio limit 1.001 and max iteration steps 50

Among the basics listed above, the reversed hysteretic modeling is the key influencing factor in the analysis. In this study, the concrete cyclic loading curves proposed by Palermo and Vecchio (2003) is employed in the VecTor2 analysis. According to this model, the backbone shape and strain softening of the unloading and reloading responses are dependent on the plastic offset strain caused by non-recoverable damage resulting from concrete crushing, internal voids cracking and compression. The plastic offset is used as a parameter in defining the unloading path and in determining the degree of damage in the concrete due to the cyclic loadings. The strain components and effective secant constitutive relationship in MCFT are defined in Figure 3.20 and the formulae below.

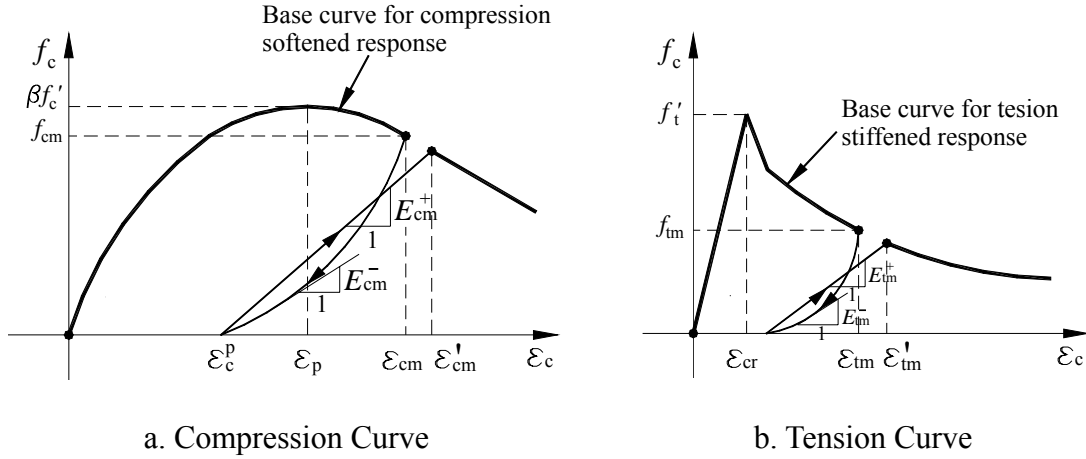


Figure 3.20 Hysteretic Models for Concrete (after Palermo and Vecchio (2003))

In Figure 3.20a, ε_p is the strain at peak stress and f'_c is the corresponding stress, ε_{cm} is the strain at the onset of unloading from the backbone curve and f_{cm} is the corresponding stress. In Figure 3.20b, ε_{cr} is the strain at cracking point and f'_t is the corresponding stress, ε_{tm} is the strain at the onset of unloading from the backbone curve and f_{tm} is the corresponding stress.

$$\varepsilon_c = \varepsilon_c^e + \varepsilon_c^p \quad (3.15)$$

$$\bar{E}_c = \frac{f_c}{\varepsilon_c^e} \quad (3.16)$$

where ε_c is the total strain in the concrete, ε_c^e is the elastic strain component and ε_c^p is the plastic strain component. \bar{E}_c is the effective secant stiffness and f_c is the current stress in the concrete.

Similarly, the constitutive relationship for steel is defined by Equation 3.17:

$$\bar{E}_{si} = \frac{f_{si}}{\varepsilon_{si}^e} \quad (3.17)$$

where ε_{si}^e is the elastic component of total strain in reinforcement bar, \bar{E}_{si} is the effective secant stiffness and f_{si} is the current steel stress. Thus contributions from both concrete and

reinforcement are counted including plasticity.

- Compressive response

The important plastic offset strain ε_c^p can be computed as following:

$$\varepsilon_c^p = \varepsilon_p \left[0.166 \left(\frac{\varepsilon_{cm}}{\varepsilon_p} \right)^2 + 0.132 \left(\frac{\varepsilon_{cm}}{\varepsilon_p} \right) \right] \quad (3.18)$$

The unloading relationship of the model is expressed as:

$$f_c(\Delta\varepsilon) = f_{cm} + E_c(\Delta\varepsilon) + \left[\frac{(E_{cm2}^- - E_{cm1}^-)(\Delta\varepsilon)^N}{N(\varepsilon_c^p - \varepsilon_{cm})^{N-1}} \right], \text{ with } \Delta\varepsilon = \varepsilon_c - \varepsilon_{cm} \quad (3.19)$$

where E_{cm1}^- is the initial unloading stiffness assumed to be equal to the elastic tangent stiffness of concrete E_c , E_{cm2}^- is the end unloading stiffness assumed to be equal to $0.071 E_c$, and N is the Ramberg-Osgood power term computed as below:

$$N = \frac{(E_{cm1}^- - E_{cm2}^-)(\varepsilon_c^p - \varepsilon_{cm})}{f_{cm} + E_{cm1}^-(\varepsilon_c^p - \varepsilon_{cm})} \quad (3.20)$$

For the reloading branch, linear relationship degrading by increasing load cycles is proposed in the employed model. The reloading response can be expressed as:

$$f_c(\Delta\varepsilon) = f_{ro} + E_{cm}^+(\Delta\varepsilon), \text{ with } \Delta\varepsilon = \varepsilon_c - \varepsilon_{ro} \quad (3.21)$$

where f_{ro} is the initial reloading stress and ε_{ro} is the initial reloading strain. Reloading stiffness E_{cm}^+ is computed as:

$$E_{cm}^+ = \frac{(\beta_d f_{\max}) - f_{ro}}{\varepsilon_{cm} - \varepsilon_{ro}} \quad (3.22)$$

Here, β_d is a damage indicator defined to count the degradation of strength by the load cycling.

It was derived through plain concrete test data by researchers before. β_d varies within pre and post peak stages as shown in Equations 3.23 and 3.24.

$$\beta_d = \frac{1}{1 + 0.10(\varepsilon_{rec} / \varepsilon_p)^{0.5}}, \text{ with } \varepsilon_{rec} = \varepsilon_{\max} - \varepsilon_{\min}, \text{ for } |\varepsilon_c| < |\varepsilon_p| \quad (3.23)$$

$$\beta_d = \frac{1}{1 + 0.175(\varepsilon_{rec} / \varepsilon_p)^{0.6}}, \text{ with } \varepsilon_{rec} = \varepsilon_{\max} - \varepsilon_{\min}, \text{ for } |\varepsilon_c| > |\varepsilon_p| \quad (3.24)$$

Where ε_{\max} and ε_{\min} represent the maximum and minimum strains within current hysteresis loop.

- Tensile response

Same concepts and derivation procedure as those for the compression branch are employed for the tension responses. Here the plastic offset strain ε_c^p is expressed in the equation below:

$$\varepsilon_c^p = 146(\varepsilon_{im})^2 + 0.523(\varepsilon_{im}) \quad (3.25)$$

The similar parts of the derivations are not described here, and the details refer to the paper by Palermo and Vecchio (2003).

Table 3.5 shows some of the final FEA results and comparisons with test data for squat and medium walls, regarding the critical point values including ultimate shear capacity and observed failure modes.

The comparisons show very good compatibilities between the FEA prediction and experimental results, and this can be testified through more detailed comparisons on the whole load-displacement response history. For example, Figures 3.21 and 3.22 illustrate the specimen geometry, FEM model, cracked and deformed shape, and hysteretic curves for LSW and MSW series tested by Salonikios et al. (1999).

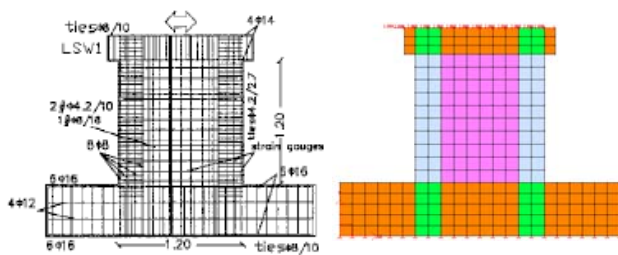
Table 3.5 FEA Results by VecTor2 and Comparisons with Test Data

(Tested walls by Salama and Elnashai, 1993)

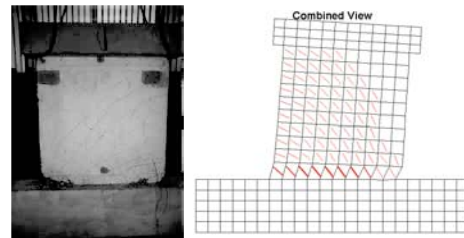
Specimen	B/H	f _{cc} (Mpa)	V _u (Experiment) (kN)	V _u (VecTor2) (kN)	Difference (%)	Failure Mode
SW4	2	49.5	108	110.9	2.69	Flexure
SW9	2	53.7	101	110.3	9.21	Flexure
SW22	2	45.1	98.7	111.0	12.46	Flexure
SW23	2	47.4	123	130.6	6.18	Flexure
SW31	2	46.4	62	64.4	3.87	Flexure

(Tested walls by Salonikios, Kappos, Tegos and Penelis, 1999)

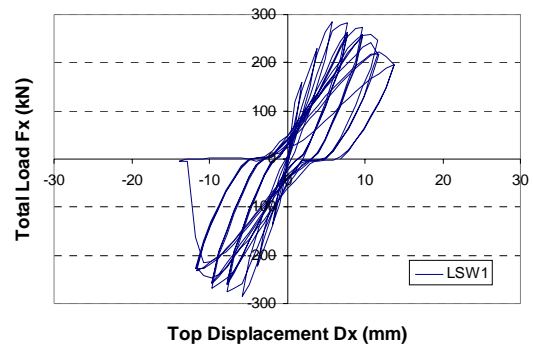
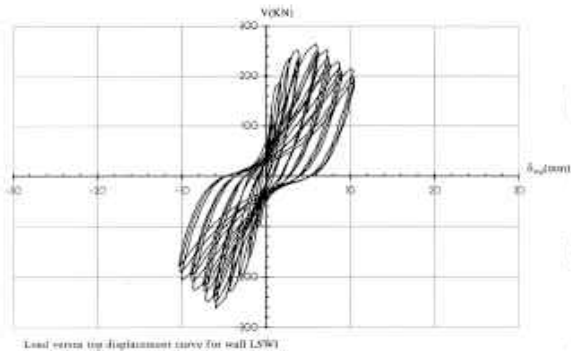
Specimen	B/H	f'c (Mpa)	V _u (Experiment) (kN)	V _u (VecTor2) (kN)	Difference (%)	Failure Mode
LSW1	1	22.2	262	284.3	8.51	Flexure-Shear
LSW3	1	23.9	268	279.6	4.33	Flexure-Shear
MSW1	1.5	26.1	197	198.2	0.61	Flexure
MSW2	1.5	26.2	124	143.4	15.65	Flexure
MSW3	1.5	24.1	176	195.7	11.19	Flexure



a. Specimen Geometry vs. FEM Model

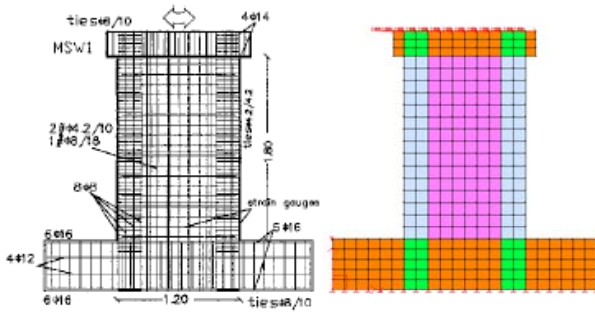


b. Image vs. FEA Plot for Cracked Shape

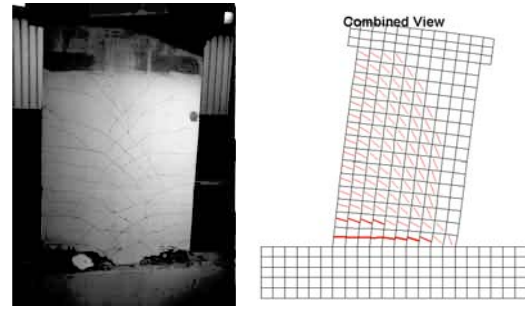


c. Test Data vs. FEA Results for Hysteretic V_{base} - D_{top} Curve

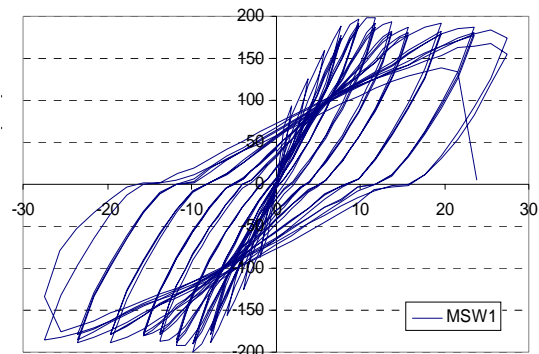
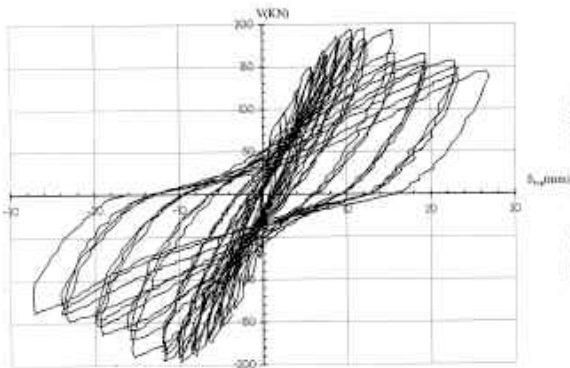
Figure 3.21 LSW1 Test Structure and Data vs. FEM Model and Analysis Results



a. Specimen Geometry vs. FEM Model



b. Image vs. FEA Plot for Cracked Shape



c. Test Data vs. FEA Results for Hysteretic V_{base} - D_{top} Curve

Figure 3.22 MSW1 Test Structure and Data vs. FEM Model and Analysis Results

Hence through many comprehensive studies aiming at the verifications of VecTor2, the applicability and effectiveness of the whole algorithm and FEM formulations are evaluated. VecTor2 has therefore proven to be the appropriate choice for the needs of structural wall microscopic FEM analysis in this research.

3.4 Lumped-Parameter-Based Model Derivation

A two-stage lumped modeling approach is used in order to develop an efficient computational model for conducting DRHA. In Stage I, the outer frame is modeled as equivalent non-linear springs at the wall, while in Stage II the wall is modeled by lumped elements. The ZEUS-NL

environment is adopted for running the analyses as: (i) it can be used to model all elements of the lumped-parameter model including non-linear axial and rotational springs and compressive-tension fibers that have realistic constitutive relationships for the response of structural concrete to cyclic loadings, and (ii) it is capable of conducting conventional pushover, adaptive pushover, Eigen-value analysis, and DRHA. VecTor2 is used to provide the predicted behavior of the walls from which the lumped model Stage II simplification is made.

The proposed two-stage optimization procedure is described here for the selection and calibration of the simplified and lumped ZEUS-NL model that will then be used for running the nonlinear DRHA from which the fragility relationships are derived. The final ZEUS-NL model is designed to consist of only beam elements, rigid bars and nonlinear springs.

□ **Stage I – Outer frame elimination and global system simplification**

The walls and core systems in RC high-rise buildings are dominant in resisting seismic loads while the frames in these buildings principally support gravity loads. Therefore it is acceptable to replace the frames in the dynamic analyses with equivalent nonlinear boundary springs at the connection point of the wall and frame at each floor. This approach provides the reaction forces $[F_x, F_y, M]$ for the outer frame (as within a plane) based on the displacements $[u_x, u_y, \theta_z]$ at the wall joints as described in Figure 3.23.

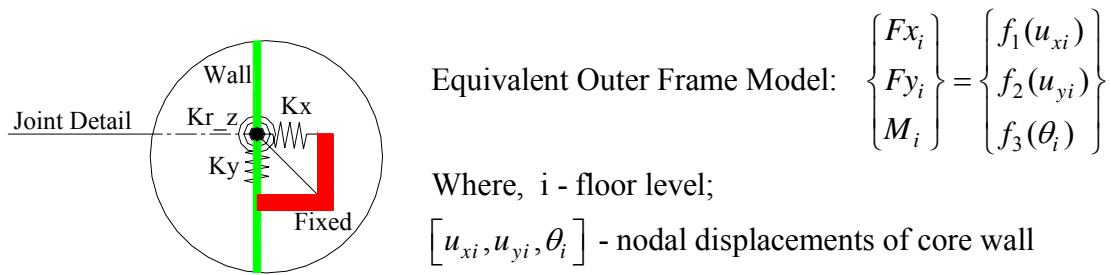


Figure 3.23 Equivalent Nonlinear Springs at Wall Joint

□ **Stage II – Simplify the structural wall into lumped elements**

It is possible to simplify the model for the wall into lumped elements that must be selected to capture the nonlinear longitudinal behavior across the width of the wall as well as its shear behavior. Two different simplified lumped models were used and are compared in this Stage II optimization procedure. The simple-vertical-line-element model (SVLEM) shown in Figure 3.16a and a multiple-vertical-line-element model (MVLEM) is shown in Figure 3.17. Nonlinear shear springs are added for both models introducing the shear deformation contributions to enhance the ZEUS-NL beam modeling.

3.4.1 Methodology

While lumped-modeling approaches are conceptually simple, the selection of a suitable replacement structure that properly considers the influence of the dominant parameters on the nonlinear response is not trivial. The whole procedure is actually dominated by parametric studies. There is no explicit analytical approach to derive this model from inelastic FEA and direct optimization techniques for parametric studies are not appropriate since they all depend on explicit functions. In this proposed framework and computational approach, implicit methodologies that use Genetic Algorithm (GA) are applied.

The Genetic Algorithm, developed by Holland (1975) and his colleagues (Goldberg (1989)), is a goal-seeking technique used for solving optimization problems, based on natural selection, the process that drives biological evolution. Since the appearance as an innovative subject, Genetic Algorithm has become one of the most widely known evolutionary computational methods today. It has been employed in many areas including economics, social science, biology and computer science, and in the past few years extended to the engineering topology and optimizations, mainly in mechanical and industrial engineering fields. The GA applications in structural engineering are still at the beginning of exploration and this is the first time that it is employed for lumped modeling of such large-scale structures.

Table 3.6 Comparisons between Standard Algorithm and Genetic Algorithms (after Goldberg (1989))

Requirement	Standard Algorithm	Genetic Algorithm
General Process	Generates a single point at each iteration	Generates a population of points at each iteration
	Deal with parameters themselves	Deal with coding of parameter sets
	The sequence of points approaches an optimal solution	The population approaches an optimal solution.
Seeking Algorithm	Use functional derivatives	Use objective function (payoff information)
	Selects the next point in the sequence by a deterministic computation	Selects the next population by computations that involve random probabilistic choices

Conceptually different from standard algorithms, GA repeatedly modifies a population of

individual solutions called “generation”, as described in Table 3.6. Based on the fitness values of all individuals in each generation, GA selects those better performing or other specific individuals randomly as parents and reproduce children for the next generation using three methods: *elite*, *cross-over* and *mutation*. Over successive generations, the population "evolves" toward an optimal solution as shown in Figure 3.24.

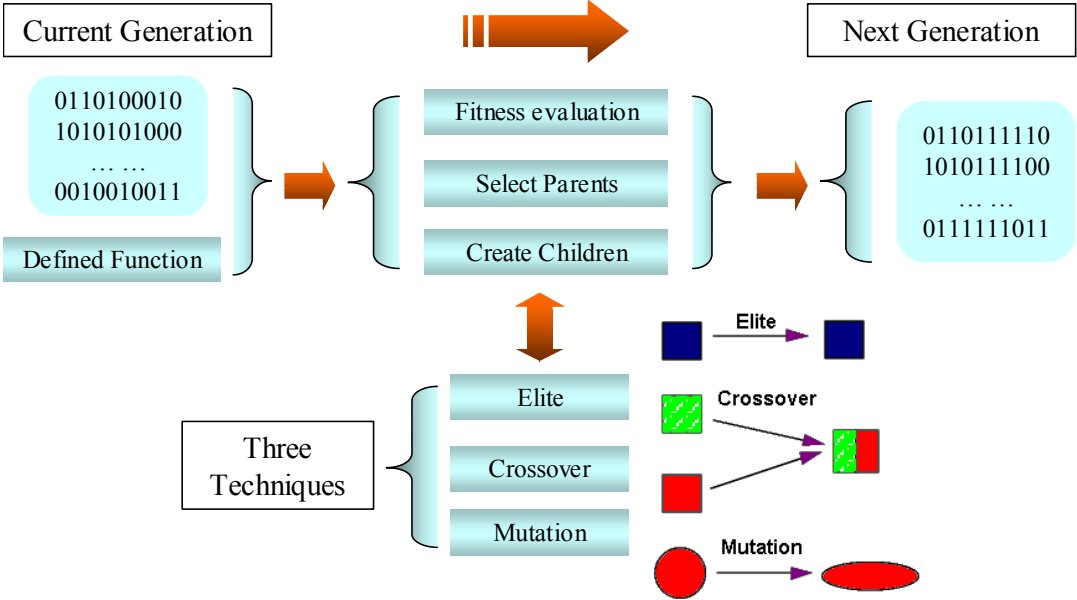


Figure 3.24 Structure of Genetic Algorithm

GA can be applied to solve a variety of optimization problems including those in which the objective function is discontinuous and highly nonlinear. The two-stage structural optimization procedure using GA is illustrated in Figure 3.25.

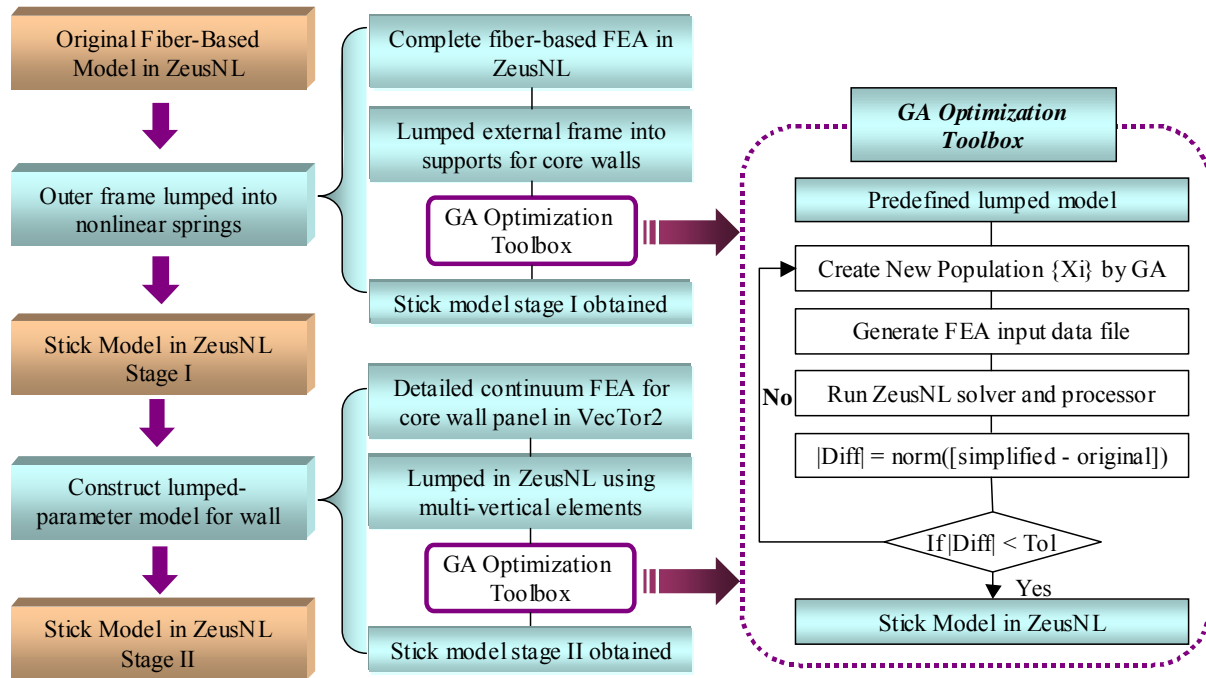


Figure 3.25 Global Stick (Lumped) Model Derivation Using Genetic Algorithm

In Stage I, two ZEUS models are applied including the original complete fiber-based model and the reduced fiber-based model with external springs replacing the outer frames. The nonlinear external spring constants are the results of parametric study using GA. MATLAB codes were written to realize the functionalities presented in Figure 3.25.

In Stage II, the results from detailed FEA conducted using VecTor2 serve as standard values and lumped model in ZEUS-NL is optimized with GA. Both SVLEM (Vulcano (1992)) and MVLEM (Ghobarah and Youssef (1999)) are used to construct the lumped model and nonlinear joint elements created in ZEUS-NL to represent the springs for considerations of axial, flexural and shear behaviors and axial-shear interaction effects. Again the parameters such as stiffness values and corresponding displacements defined for joint elements are the results of a parametric study using GA toolbox written in MATLAB.

3.4.2 Reference Building Selection

To select a representative RC high-rise structure for seismic fragility assessment, it is crucial to take account of general characteristics, such as material properties, structural type, building height, construction year, etc.

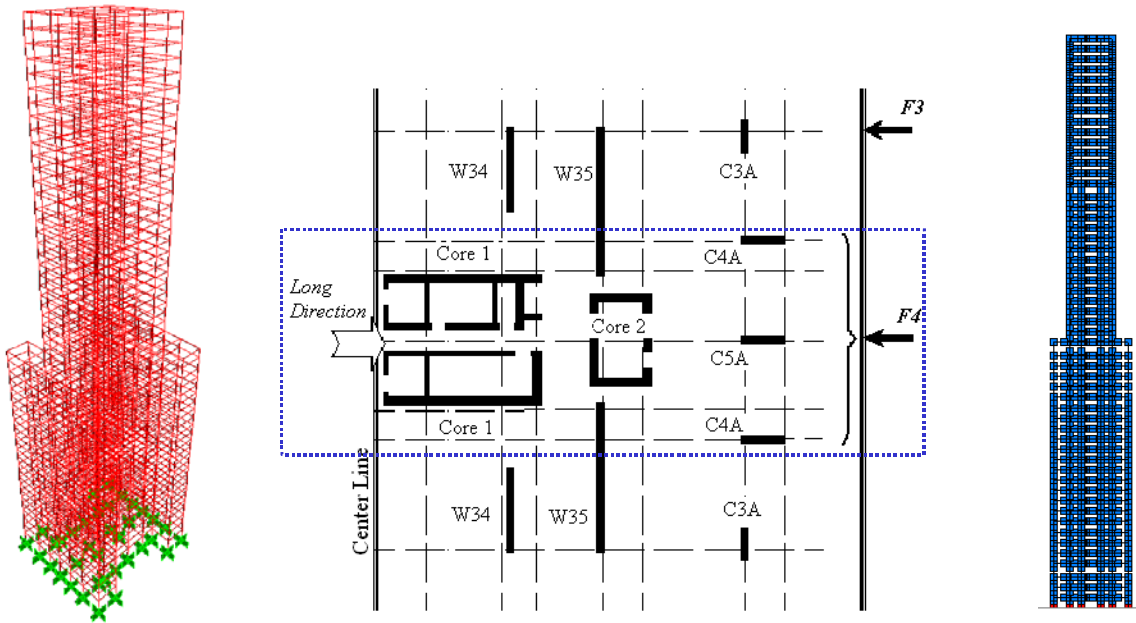


Figure 3.26 Reference Building SAP2000 Model (Left), Half Plane View (Middle) and ZEUS-NL Model (Right)

The framework discussed previously is implemented for the development of a simple lumped-parameter model for a single frame (F4) of an existing and complex RC high-rise structure, the newly constructed high-rise Tower C03 in the Jumerirah Beach development, Dubai, United Arab Emirates as illustrated in Figure 3.26. The primary characteristics of this tower are given in Table 3.7.

Table 3.7 Main Features of Reference Building

Features	Description
Height (m)	184
Total Storeys	54
Regular Storey Height (m)	3.400
Irregular Storey Height (m)	4.488
Core Walls (Exterior and Interior Size)	9.43x3.25 (8.48x2.55) (m)
	9.33x3.15 (8.48x2.55) (m)
	9.18x3.05 (8.48x2.55) (m)
Concrete f'_c (MPa)	60 (wall); 40 (slab)
Reinforcing Bars f_y (MPa)	421 (Grade 60)

3.4.3 Mass Simulation

There are usually two methods to simulate the mass in structural modeling: one is to use continuous mass property throughout the elements; the other is to add lumped masses to selected nodes. Both ways are acceptable in the seismic analysis and the latter one can gain more computational efficiency with a little loss of accuracy. If considering Rayleigh damping in ZEUS-NL, continuous mass distribution will be defined for member elements. In this study, the lumped mass model is the only selection as shown in Figure 3.27.

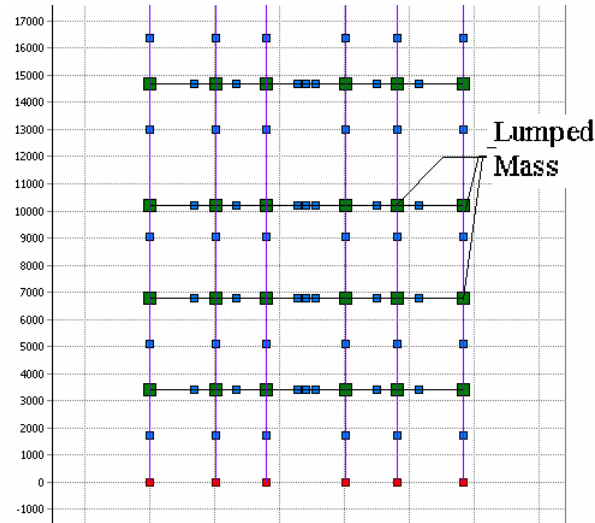
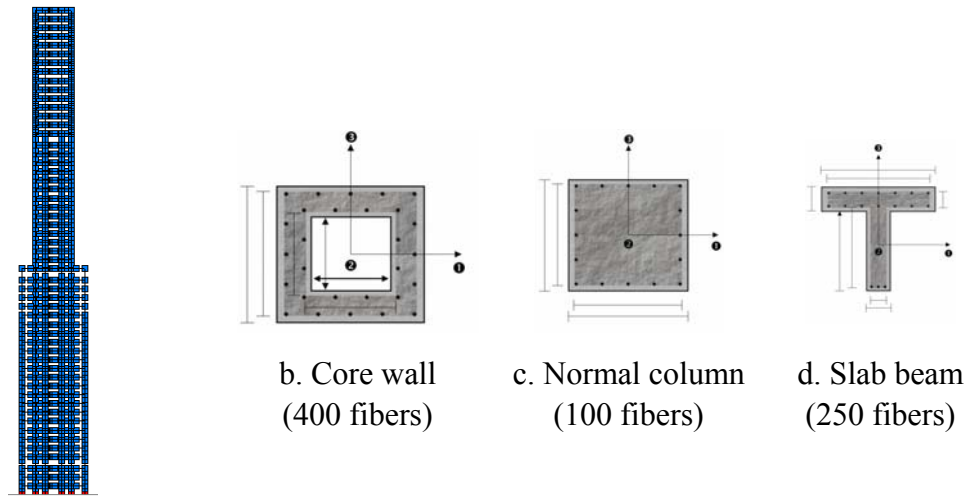


Figure 3.27 Lumped Mass Model in Selected Structure

3.4.4 Simplification Stage I using Genetic Algorithm

3.4.4.1 ZEUS-NL Pushover Analysis of Full Model

The objective of the Stage I simplification is to replace the outer frame with nonlinear springs at the point of the frame-wall connection at each storey level. The more comprehensive model for the outer frame will also be realized using ZEUS-NL in which all structural components are treated as RC fiber-based section models. GA will be used for the selection of model parameters. The assessment of the suitability of the simplified model will be made by a comparison of natural modes as well as the results from pushover and DRHA. The complete frame model is shown in Figure 3.28a and typical cross-sections in Figure 3.28b~d.



a. Whole Model

Figure 3.28 Structural Model in ZEUS-NL (a) and Typical Component Cross Sections (b ~ d)

□ **Execute modal analysis and design pushover loads with original complete model**

From the results of the ZEUS-NL complete model of the outer frame, the modal mass participation factors (MPF) can be determined by Equation 3.26:

$$\text{MPF: } \Gamma_i = \frac{\{\phi_i\}^T [M] \{1\}}{\{\phi_i\}^T [M] \{\phi_i\}} \quad (3.26)$$

For i-th mode, where ϕ_i – normalized i-th mode shape vector

The first 5 fundamental modal shapes of the sample building are collected in Figure 3.29. The corresponding modal periods and related MPFs are listed in Table 3.8 below in which the sum of the modal MPFs of four modes among the first five is 94%.

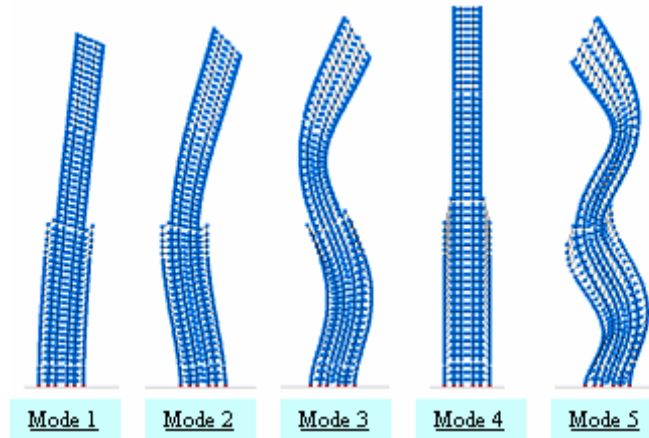


Figure 3.29 First Five Natural Modal Shapes

Table 3.8 Modal Periods and Mass Participation Factors (MPF)

Mode	1	2	3	4 (Vertical)	5
Period (second)	3.05323	0.81950	0.36427	0.32787	0.22872
Mass Participation Factor	0.5610	0.2637	0.0729	Neglected	0.0433
Sum of Mass Participation Factor of listed 5 modes					0.9409

Because of this, it is reasonable to evaluate the lateral distributed loads for a pushover analysis from the 4 horizontal modes as illustrated in Equations 3.27 and 3.28 and which leads to the final lateral load shape shown in Figure 3.30. The vertical mode 4 is not considered as it has little effect on the lateral response that is the focus of this study.

Proportional load vector with single modal shape:
$$F_{ij} = \frac{M_j \phi_{ji}}{\sum_j M_j \phi_{ji}} \quad (3.27)$$

Proportional load vector with mixed modal shape:
$$F_j^* = \sum_{i=1}^4 F_{ij} (MPF)_i \quad (3.28)$$

where, i - i-th mode selected here; j - floor level

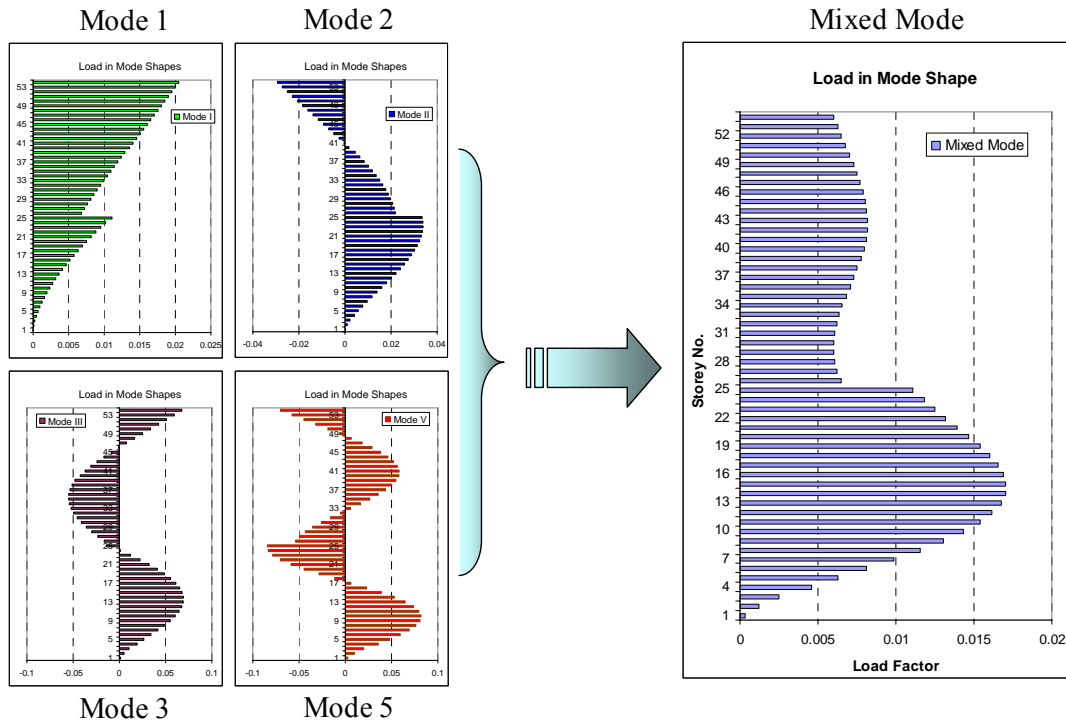


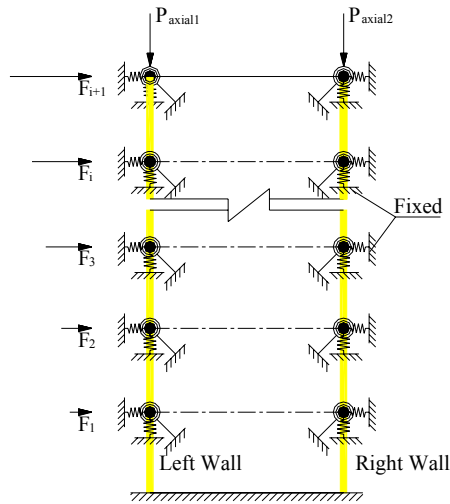
Figure 3.30 Distributed Lateral Loads Following Mixed Modal Shape

□ **Run pushover analysis with load in mixed modal shape in ZEUS-NL**

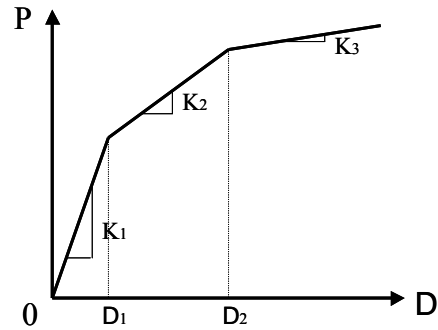
Using this force distribution, a pushover analysis was undertaken in ZEUS-NL from which the overall nodal displacements and wall-frame interface forces were evaluated.

3.4.4.2 Construct Equivalent Wall Boundary Supports

Numerical regression was used to simulate the inelastic behavior of the outer frame resistant forces corresponding to wall deformations at each floor as shown in Figure 3.20. Thereby, the outer frames can be replaced by springs at joints that connect the wall nodes to fixed supports as shown in Figure 3.31a.



a. Simplified Model Protocol



b. Equivalent Tri-linear Joint Spring

Figure 3.31 Main Features in Simplified Model Stage I

3.4.4.3 Parametric Study with Genetic Algorithm

As discussed previously, the first step is to define the population of individuals and fitness functions used in GA. In ZEUS-NL, the main properties of each single tri-linear spring, as shown in Figure 3.31b, are defined below where the initial and two-stage yielding stiffness and corresponding limit state displacements at interested DOFs (x, y, rz) are:

$$\left[K_{1x} \ K_{1y} \ K_{1rz} \ K_{2x} \ K_{2y} \ K_{2rz} \ K_{3x} \ K_{3y} \ K_{3rz} \right]_i \quad \text{and} \quad \left[u_{1x} \ u_{1y} \ \theta_{1z} \ u_{2x} \ u_{2y} \ \theta_{2z} \right]_i$$

where, i – ith floor. The strain hardening and stiffness degradation behaviors can be simulated by the non-negative stiffness values defined using joint elements in ZEUS-NL.

There are two ways to optimize the parameters using GA; one is to directly define the individual population as a group containing all parameters and the other is to simulate the spring constants as functions of other properties.

- For the first method, the protocol parameter vector of the population is

$$\mathbf{C}_i = \left[K_{1x} \ K_{1y} \ K_{1rz} \ K_{2x} \ K_{2y} \ K_{2rz} \ K_{3x} \ K_{3y} \ K_{3rz} \ u_{1x} \ u_{1y} \ \theta_{1z} \ u_{2x} \ u_{2y} \ \theta_{2z} \right]_i \quad (3.29)$$

$i = 1, 2, \dots, 54$

The initial values $\bar{\mathbf{C}}_i$ are obtained through the post-processing of the original ZEUS-NL analysis results in the previous step. In the population, the independent variable vector size is decided by the total number of joint spring parameters which are 810 for the 54-storey tower.

Each individual vector is defined as follows:

$$\mathbf{X} = \left[\text{Rand}(L_B, U_B) \right]_{1 \times 810} \quad (3.30)$$

(L_B, U_B) are lower and upper bounds, set as (0.5, 2.0) here

So for each trial in GA, the individual joint parameter vector \mathbf{K} is computed as:

$$\bar{\mathbf{K}} = [\mathbf{C}_1 \ \mathbf{C}_2 \ \dots \ \mathbf{C}_{54}], \ \mathbf{K}_n = \bar{\mathbf{K}}_n \square \mathbf{X}_n \quad (3.31)$$

$n = 1, 2, \dots, 810$

\mathbf{K} is of dimension 810 by 1, and in each generation the population consists of 20 such individual vectors.

□ For the second method, only selected parameters are subjected for optimization.

This is encouraged by the observation that the stiffness values are decreasing with increasing height. Thereby, the spring parameters \mathbf{C}_i can be assumed to follow certain functional trends, approximately as below:

$$(\mathbf{C}_i)_j = \begin{cases} (\mathbf{C}_1)_j (i^{aj}), \ j=1, 2, \dots, 15 & \text{for } i \leq 25 \\ (\mathbf{C}_1)_j (25^{aj}) \left(\frac{i}{25}\right)^{bj}, \ j=1, 2, \dots, 15 & \text{for } i \geq 25 \end{cases} \quad (3.32)$$

Since the building configuration changes at the 25th floor (refer to Figures 3.27 and 3.28), the stiffness variations are different for the structures below and above 25th floor, thus the functional

expressions for C_i need to change accordingly. Post-processing of the ZEUS-NL analysis is again applied to obtain the initial values. Only \bar{C}_1 is needed here, but additional estimations of \mathbf{a} and \mathbf{b} for each parameter in \bar{C}_1 are also desired for the optimization using genetic algorithms. The final number of independent variable vector size is 45. Each individual is defined as follows:

$$\mathbf{X} = \left[\text{Rand}(L_B, U_B) \right]_{1 \times 45} \quad (3.33)$$

where, (L_B, U_B) are lower and upper bounds, set as (0.5, 2.0) here

So for each trial in GA, the individual joint parameter vector \mathbf{K} is computed as:

$$\bar{\mathbf{K}} = [\mathbf{C}_1 \ \mathbf{a} \ \mathbf{b}], \ \mathbf{K}_n = \bar{\mathbf{K}}_n \square \mathbf{X}_n \quad (3.34)$$

$n = 1, 2, \dots, 45$

\mathbf{K} is of dimension 45 by 1, and in each generation the population consists of 50 such individual vectors.

The basic features of the two parametric studies using genetic algorithm are listed in Table 3.9.

Table 3.9 Basic Features of Parametric Studies with GA at Stage I

Optimization Method	Individual vector length	Lower and upper bounds	Population size per generation	Maximum generations
Full Parameter	810	[0.5, 2.0]	20	100
Simulated Parameter	45	[0.5, 2.0]	50	100

The second approach is finally selected due to its greater computational efficiency. For the evolution, three techniques including *Elite (survival selection)*, *Crossover and Mutation*, are available in the coded MATLAB toolbox. All three methods are employed to enhance performance of the genetic algorithm searching as follows:

Fitness function:

The main comparison between lumped model and original complete model is of the deformed shapes under the same loadings. On account of different influences on whole building behavior from boundary conditions at different heights, weighting factors are introduced in the deformation based fitness function. The fitness function is defined as:

$$F = \left\{ \left| \frac{(D_i^t - D_i^o)}{i \times D_i^o} \right| \right\} \quad (3.35)$$

where, i – Storey number = 1, 2, ..., 54

D_i^t – Wall nodal displacement along X at ith storey, from lumped model

D_i^o – Wall nodal displacement along X at ith storey, from original model

Elite (selected parents with fitness values under 20% level):

$$X_{i+1} = X_i, \quad i - \text{Generation number} \quad (3.36)$$

Crossover (two types of combinations are applied here):

Partial crossover:

$$X_{i+1} = [X_1^{(1)}, X_2^{(1)}, \dots, \alpha_k X_k^{(1)} + (1 - \alpha_k) X_k^{(2)}, \dots, X_{n-1}^{(2)}, X_n^{(2)}] \quad (3.37)$$

where, α_k – Preset or random number, $\in [0 \ 1]$, $1 < k < n$, n is variable vector length

i – Generation number

Complete crossover:

$$X_{i+1} = \alpha X_i^{(1)} + (1 - \alpha) X_i^{(2)} \quad (3.38)$$

where, α – preset value or random number, $\in [0 \ 1]$; i – Generation number

Mutation (scale or shrink according to the fitness performance level):

$$(X_{i+1})_n = (X_i)_n (\beta_i)_n, \quad n = 1, 2, \dots, 45 \quad (3.39)$$

where, β_i – Random vector generated from normal distribution $\mathbf{N}[1, (1 - r_j)]$

r_j – Ranking of parent fitness performance level in percentage

i – Generation number

j – Parent number within [1, Population size]

□ Derived Lumped Model – Stage I

Lumped model stage I is obtained as expected through the GA parametric study. Series of analyses with derived lumped model are performed for both modal and pushover analyses and comparisons with original model results are made for modal analyses (Table 3.10), typical pushover curves (Figure 3.32) and structural deformed shape (Figure 3.33).

Table 3.10 Modal Analyses Comparisons between Original and Simplified Models

Mode	Modal Period (s)		
	Original Model	Lumped Model Stage I	
		Value	Difference (%)
1	3.05323	3.08966	1.2
2	0.81950	0.80381	-1.9
3	0.36427	0.34249	-6.0
4	0.32787	0.28195	-14.0
5	0.22872	0.19274	-15.7

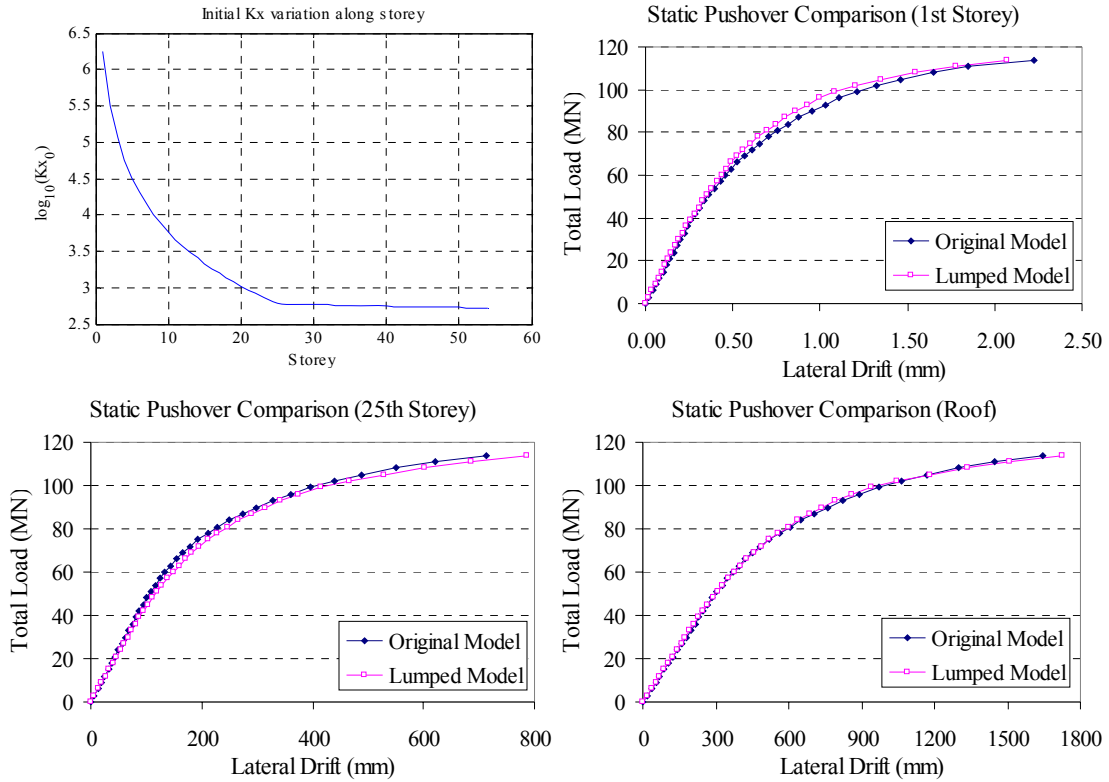


Figure 3.32 Pushover Response Comparisons between Original and Lumped Models

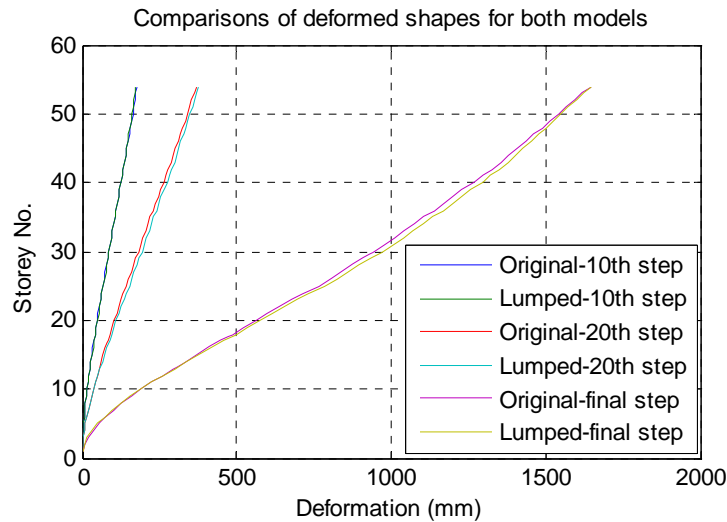


Figure 3.33 Pushover Deformed Shape Comparisons at X Direction

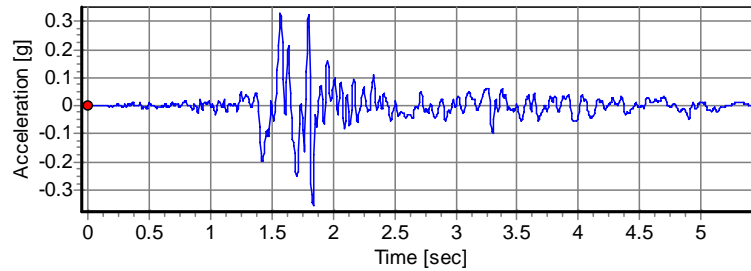
It is concluded from the comparisons that the derived lumped model are sufficient to provide accurate predictions of natural modes and static pushover behaviors. There were some expected

errors including shorter periods for higher modes and larger resistant forces in the highly inelastic range. The explanation for these errors may lie in the computational joint models used in ZEUS-NL that require non-negative tangent stiffness values and thereby make it difficult to detect actual strain softening of the substitute outer frame. Hence, the lumped model is a little stiffer than the complete frame model in some cases, especially for higher modes and large deformation ranges where the RC outer frame members are more likely to get damaged. Such errors may be taken into consideration by slight adjustments in uncertainties.

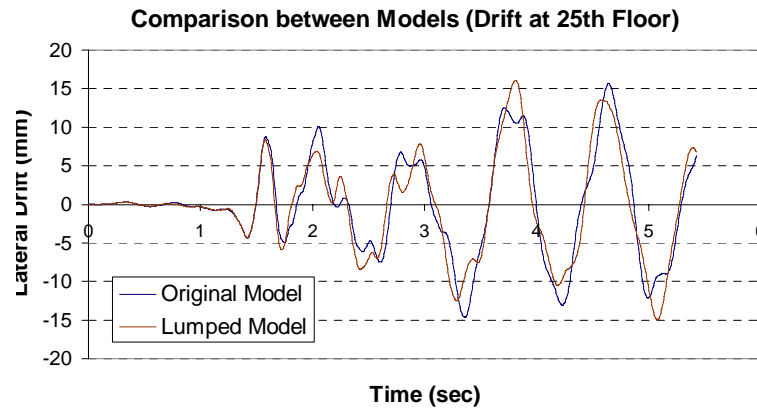
Similar comparisons were also made using DRHA as shown in Figure 3.34b ~ c; the sample ground motion record from Kocaeli Earthquake (1999, Turkey, Duzce station) is given in Figure 3.34a.

At intermediate and top height levels, relative displacement time histories from the lumped model are quite close to those from the original model. That means that the lumped model well replicates the predicted seismic behavior of the selected building.

a. Strong motion



b. 25th Floor



c. Roof

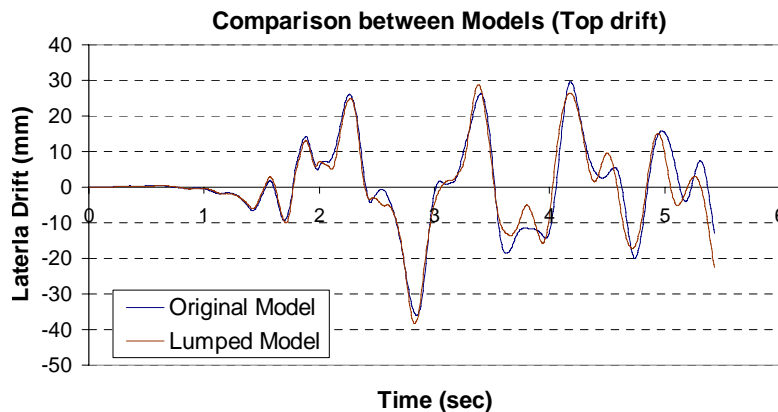


Figure 3.34 Dynamic Response History Comparisons between Original and Lumped Models

3.4.5 Simplification Stage II Using Genetic Algorithm

3.4.5.1 VecTor2 Analysis Using Continuum FEM Model

The objective of this simplification is to produce a simple lumped-parameter model that will provide a similar prediction of the pushover response as that which would be predicted from a 2D continuum analysis for the core wall panels. The program VecTor2 is used to provide the

continuum analysis predictions. Both the SVLEM and MVLEM models, described in Figures 3.16 and 3.17, are considered for developing the lumped model in ZEUS-NL. The GA process is employed for parameter value selection. In addition, the “*hsv*” type joint is applied to consider the axial load-shear interaction effects in ZEUS-NL (Lee and Elnashai (2002)). For all wall panels of the same size, only one parametric study for lumped modeling is required. The core wall panel is modeled as shown in Figure 3.35a~c.

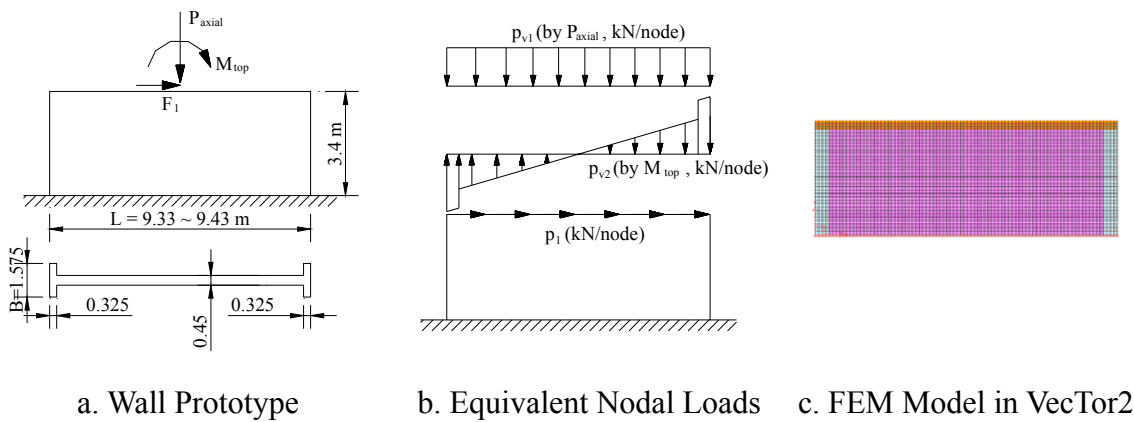


Figure 3.35 Discrete FEM Model of Core Wall Panel

In the VecTor2 pushover analyses, the axial loads at different levels as shown in Table 3.11 are imposed as initial load corresponding for the different analyses as required by the nonlinear *hsv* joints in ZEUS-NL. Horizontal loads are incrementally applied in displacement control. All loads are equivalent to uniformly distributed nodal loads along the floor at the top of wall panel.

Table 3.11 Designed Capacities and Applied Load Information

Design Compression No (kN)	255658					
Compressive Capacity C_{max} (kN)	620000					
Tensile Capacity T_{max} (kN)	80000					
Applied Loads	1	2	3	4	5	6
Axial Load	0	0.5 N_o	1.0 N_o	1.5 N_o	0.075 T_{max}	0.225 T_{max}
Horizontal Displacement (mm)	20					

In the VecTor2 model, the concrete compressive stress-strain curve by Popovics (1973) is used for normal strength concrete and Modified Popovics curve by Collins and Porasz (1989) for high-strength concrete is used for both pre-peak and post-peak concrete behavior. The effect of confinement stresses follows the suggestions by Kupfer et al. (1969).

3.4.5.2 Investigated Wall Lumped Modeling

Two types of lumped models are under investigation: single vertical element (SVLEM) versus multiple vertical elements model (MVLEM), as shown in Figure 3.36.

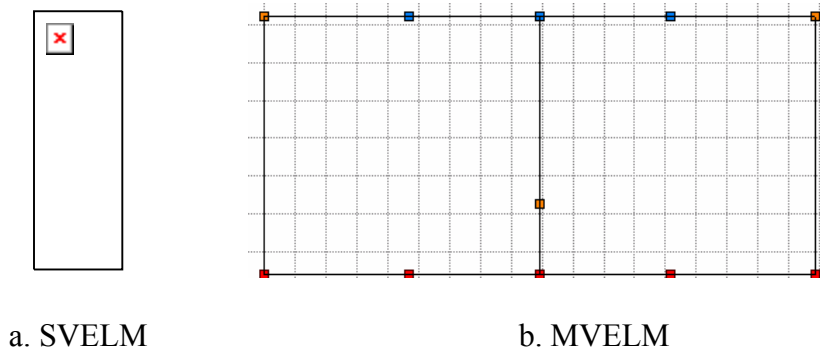


Figure 3.36 Investigated Lumped Wall Models

3.4.5.3 Parametric Study with Genetic Algorithm

The joints in ZEUS-NL have a similar tri-linear nature as previous except that the shear stiffness

represented by ‘*hsv*’ model, which is defined as “Hysteretic Shear model under axial force variation”, requires series of tri-linear shear response curves with stiffness values and related displacements under different axial loads including 4 compressions and 2 tensions (in reference to ZEUS-NL version 1.7 manual by Elnashai et al. (2006)).

For the SVLEM model in ZEUS-NL, only one joint element is needed, with parameters at X, Y and rotation about Z. Thanks to the small population size for only three types of wall sections, direct GA optimization can be used to obtain all relevant values. Initial elastic and the two-stage yielding stiffness values and corresponding limit state displacements are defined as:

$$\begin{cases} \mathbf{K}_X^W = \left[\left[K_{1x}^1 \ K_{2x}^1 \ K_{3x}^1 \right], \left[K_{1x}^2 \ K_{2x}^2 \ K_{3x}^2 \right], \dots, \left[K_{1x}^6 \ K_{2x}^6 \ K_{3x}^6 \right] \right]_{1 \times 18} \\ \mathbf{U}_X^W = \left[\left[u_{1x}^1 \ u_{2x}^1 \ u_{3x}^1 \right], \left[u_{1x}^2 \ u_{2x}^2 \ u_{3x}^2 \right], \dots, \left[u_{1x}^6 \ u_{2x}^6 \ u_{3x}^6 \right] \right]_{1 \times 18} \\ \mathbf{K}_Y^W = \left[\left[K_{1yT} \ K_{2yT} \ K_{3yT} \right], \left[K_{1yC} \ K_{2yC} \ K_{3yC} \right] \right]_{1 \times 6} \\ \mathbf{U}_Y^W = \left[\left[u_{1yT} \ u_{2yT} \right], \left[u_{1yC} \ u_{2yC} \right] \right]_{1 \times 4} \\ \mathbf{K}_{Rz}^W = \left[K_{1rz} \ K_{2rz} \ K_{3rz} \right]_{1 \times 3} \\ \mathbf{U}_{Rz}^W = \left[\theta_{1rz} \ \theta_{2rz} \right]_{1 \times 2} \end{cases}$$

where values with T and C for the Y direction indicate different responses under tension and compression. The 6 rows for the X direction present the data sets for the 6 axial load levels.

The protocol parameter vector of the population is:

$$\mathbf{C}^W = \left[\mathbf{K}_X^W, \mathbf{K}_Y^W, \mathbf{K}_{Rz}^W, \mathbf{U}_X^W, \mathbf{U}_Y^W, \mathbf{U}_{Rz}^W \right] \quad (3.40)$$

The initial values for \mathbf{C}^W are obtained from the VecTor2 analysis results in the previous step.

In this situation, the size of the independent variable vector within each population is 51. As done

for Stage I, each individual vector is defined as follows:

$$\mathbf{X}^W = \left[\text{Rand}(L_B, U_B) \right]_{1 \times 51} \quad (3.41)$$

(L_B, U_B) are lower and upper bounds, set as (0.5, 2.0) here

So for each trial in GA, the individual joint parameter vector \mathbf{K} is computed as:

$$\mathbf{K}_n = \mathbf{C}_n^W \square \mathbf{X}_n^W \quad (3.42)$$

$n = 1, 2, \dots, 51$

A similar procedure is applied for MVLEM model, except now for a total of five joint elements including four vertical springs at the bottom and one horizontal spring at the lower part of the wall panel. The basic features of the two parametric studies using GA are listed in Table 3.12.

Table 3.12 Basic Features of Parametric Studies with GA at Stage II

Model	Individual vector length	Lower and upper bounds	Population size per generation	Maximum generations
SVLEM	51	[0.5, 2.0]	50	100
MVLEM	66	[0.5, 2.0]	50	100

As in Stage I, the three techniques of *Elite (survival selection)*, *Crossover and Mutation*, are employed for generating populations using the genetic algorithm toolbox, as described by Equations 3.36~3.39. In the ZEUS analysis for fragility assessment, nodal displacements at the center of wall panel at each floor level are required. Therefore, the main comparison between the optimized lumped model and the RC continuum model were control point displacements. Because the floor slab is treated as rigid in the ZEUS-NL model, while not in VecTor2, the nodal rotation at control points is excluded from the comparisons. It follows that the fitness function is defined as:

$$F = \frac{|D^t - D^o|}{|D^o|} \quad (3.43)$$

where, D^t – Wall nodal displacement at X and Y direction computed from lumped model

D^o – Wall nodal displacement at X and Y direction obtained from VecTor2 results

The GA optimizations for the parametric study successfully help to finalize the lumped model for Stage II. A comparison of the pushover prediction under designed dead loads for wall section types is presented in Figure 3.37.

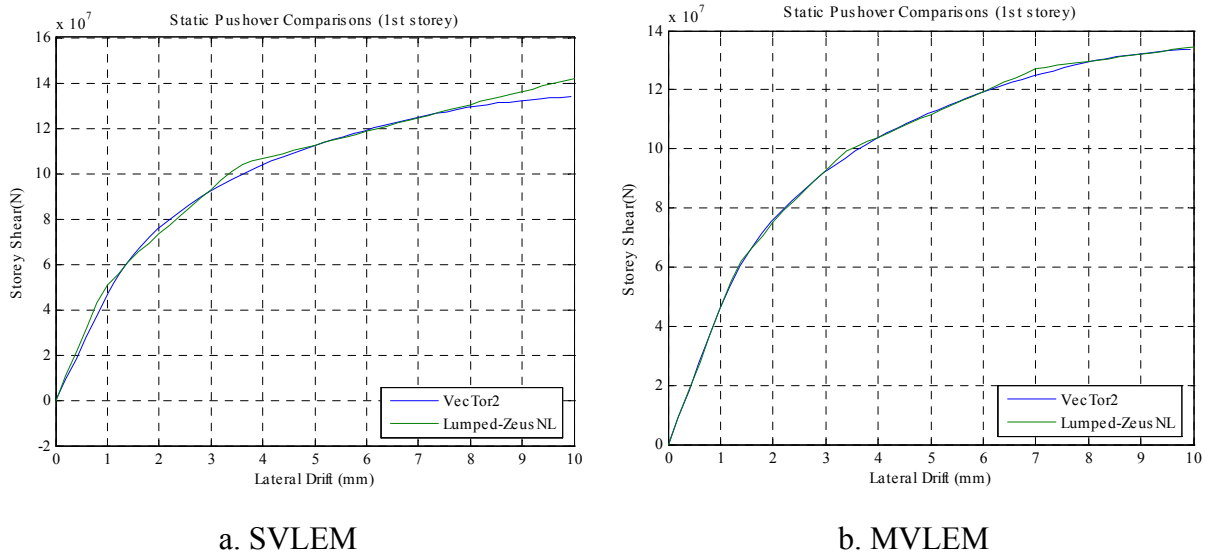


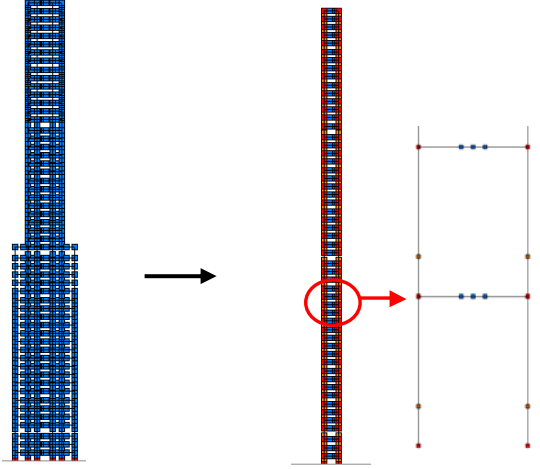
Figure 3.37 Pushover Comparisons for SVLEM and MVLEM with VecTor2 Model

The static pushover response from both the SVLEM and MVLEM are close to the response from the VecTor2 detailed continuum FEM analysis. The SVLEM model does not provide quite as close a fit particularly around the ultimate storey shear but even this error is acceptably small. The comparisons illustrate that using GA optimization in parametric studies, both SVLEM and MVLEM can provide lumped models for wall panels that are reliable and sufficiently accurate for capturing the inelastic behaviors including cracking, steel yielding and concrete crushing.

3.4.6 Lumped Model Evaluation

Through the implementation of the above two-stage model optimization procedure, a comparatively simple lumped-parameter model is created that consists of beam elements, rigid bars, and nonlinear springs. The simplified model is sufficiently accurate for evaluating nodal displacements, global internal forces, and at the same time accounting for shear deformations within the structural walls. The required computational time for completing a DRHA is reduced to a small fraction of what it would have been for an analysis of the original model. Table 3.13 compares the details and computational times between the original whole building frame model and the final lumped model in ZEUS-NL. Though it took around one week to actually complete the lumped modeling process for this specific building, the computational saving of next step DRHA runtime is much more significant compared to this cost. The total estimated runtime of DRHA and post-process for the reference structure is about 3 hours per 1000 time steps which leads to 1800 hours (2.5 months) when considering a total of 600 ground motion records with average 1000 time steps. So the time can be reduced to less than 180 hours (1 week) when using derived lumped model, which creates more research flexibility for making fragility assessments. In addition, the methodology developed in this research can be extended and applied to other complex structures.

Table 3.13 Variation from Original Model to Final Lumped Model

Variation	From original to lumped models
Model Geometry	
Node Number	876 → 472
Element Number	1910 → 632
DRHA Runtime	10~15 → 1

4. Limit States Definition

4.1 Literature Survey

4.1.1 Overview

The definition of limit states plays a significant role in the construction of the fragility curves due to its direct effect on evaluation of building performance levels. The analytical fragility assessment requires the appropriate and easily tracked damage scales for the evaluation of the system demand and capacity. There are two ways to characterize the performance level or limit states: qualitative and quantitative approaches.

□ Qualitative Approach

These kinds of approaches have traditionally been used in building codes. FEMA273 (1997) and its update FEMA 356, has very comprehensive documentation on performance levels that are defined qualitatively and is briefly summarized in Table 4.1. Rossetto and Elnashai (2003) defined seven limit states for derivation of fragility curve based on observational data, and employed a creative damage index so-called the homogenized damage scale for reinforced concrete buildings (HRC-Scale) for the performance level representation from 0 for no damage to 100 for collapse, as shown in Table 4.2, in terms of the typical structural and non-structural damage for the four main types of reinforced concrete structures found in Europe, (i.e. ductile and non-ductile frames, frames with masonry infill and shear-wall structures). Because of the lack of researches for RC high-rise buildings, especially of structural wall systems, current qualitative approaches can only serve as references.

Table 4.1 Performance Levels at Limit States by FEMA273 (1997)

Levels	Description
Immediate Occupancy (IO)	Occupants allowed immediate access into the structure following the earthquake and the pre-earthquake design and strength and stiffness are retained
Life Safety (LS) Or Damage Control (DC)	Building occupants are protected from loss of life with a significant margin against the onset of partial or total structural collapse
Collapse Prevention (CP)	Building continues to support gravity loading, but retains no margin against collapse

Table 4.2 Limit States and Typical Damages Based on HRC-Scale (after Rossetto and Elnashai (2003))

DI_{HRC}	Damage State	Ductile MRF	Non-Ductile MRF	Infilled MRF	Frame-Wall
0	None	No damage	No damage	No damage	No damage
10	Slight	Fine cracks in plaster partitions/infills	Fine cracks in plaster partitions/infills	Fine cracks in plaster partitions/infills	Fine cracks in plaster partitions/infills
20	Light	Start of structural damage	Start of structural damage	Cracking at wall-frame interfaces	Start of structural damage
30		Hairline cracking in beams and columns near joints (<1mm)	Hairline cracking in beams and columns near joints (<1mm)	Cracking initiates from corners of openings	Hairline cracking on shear-wall surfaces & coupling beams
40				Diagonal cracking of walls and crushing at b/c connections	Onset of concrete spalling at a few locations
50	Moderate	Cracking in most beams & columns	Flexural & shear cracking in most beams & columns	Increased brick crushing at b/c connections	Most shear walls exhibit cracks
60		Some yielding in a limited number	Some yielding in a limited number	Start of structural damage	Some walls reach yield capacity
70		Larger flexural cracks & start of concrete spalling	Shear cracking & spalling is limited	Diagonal shear cracking in exterior frame members	Increased diagonal cracking & spalling at wall corners
80	Extensive	Ultimate capacity reached in some elements	Loss of bond at lap-splices, bar pull-out, broken ties	Extensive cracking of infill, falling bricks, out-of-plane bulging	Most shear walls have exceeded yield, some reach ultimate capacity
90		Short column failure	Main re-bar may buckle or elements fail in shear	Partial failure of many infill, heavier damage in frame members, some fail in shear	Re-bar buckling, extensive cracking & through-wall cracks. Shear failure of some frame members
100	Partial Collapse	Collapse of a few columns, a building wing or upper floor	Shear failure of many columns or soft-storey failure	Beams &/or columns fail in shear causing partial collapse.	Coupling beams shattered and some shear walls fail
	Collapse	Complete or near building collapse	Complete or soft-storey failure	Complete or near building collapse	Complete or near building collapse

□ Quantitative Approach

To obtain fragility relationships computationally a more detailed quantitative approach is desired for building performance evaluations. This includes mathematical representations of damage indices based on designated structural responses, such as the three categories of energy, forces, or typical deformation levels.

- Energy-Based Damage Index

A well utilized existing model is the one proposed by Park et al. (1985) which defined the damage index D through a linear function of maximum displacement δ_m and total hysteretic energy dissipation normalized by member ultimate displacement and monotonic loading δ_u , and yield force Q_y .

$$D = \frac{\delta_m}{\delta_u} + \frac{\beta}{Q_y \delta_u} \int dE \quad (4.1)$$

This damage index has been used by Singhal and Kiremidjian (1997) in derivation of fragility curves for California, USA. Corresponding to the damage level, the index value ranges from 0 (no damage) to 1 (complete collapse). However there are problems of using this model for high-rise populations because of its nature of limiting the computed global inelastic energy dissipation for large-scale and complex structures.

- Force-Based Damage Index

The damage index is calculated first at local member range, observing the force vs. deformation behavior to get the parameters representing energy dissipation, for example, Bracci et al. (1989) computed the damage index as the difference between the areas under the monotonic load

response and the cyclic load response envelope curves. The global damage can be found using similar method as Park et al. (1985). The problem for these kinds of indices is that the load response behavior and the damage index calculation are mainly based on some selected predominant modes, which is not adequate for high-rise buildings that have complicated vibration modes and hence it is very difficult to obtain appropriate index value from the energy dissipation investigation.

- Deformation-Based Damage Index

Compared with the previous two, this type is more intuitive, straightforward, comprehensive and easier for calibration with investigation or experimental data, because these measures are sufficient to show the detailed structural behavior under seismic loads, not only including global displacements, but also local damage including cracking and yielding mechanisms. This fits the characteristics of the response of RC high-rise buildings quite well.

Generally, the response parameter mostly used in storey level is the maximum inter-storey drift ratio (ISD) since it is easily to relate to the structural damage and inelastic behavior. But for RC high-rise buildings, it is still necessary to be able to track the global performance. So also global drift ratio is important in this study. Many researchers and institutes have employed the lateral drift ratios for the damage evaluation of structures, such as FEMA273 (1997), Kircher et al. (1997), Mosalem et al. (1997), etc.). Jeong and Elnashai (2004a) have proposed a 3D damage index for irregular RC frame structures counting more complete concerns and influencing factors in spatial building behavior.

Usually the limit states can be detected through sets of pushover analyses for the prototype

structure, and based on selected information about the phenomena such as concrete cracking, plastic hinge initiation, reaching maximum element strength, and maximum concrete strain, etc. Ghobarah (2004) has illustrated the limit states and performance stages relating to ISD as Figure 4.1. The detailed comparisons among definitions of limit states have been performed by Rossetto (2004) and Ghobarah (2004), as shown in Table 4.3 ~4.5.

Table 4.3 General Definitions of Limit States (after Rossetto (2004))

Existing curve	Damage Scale	Limit states	DI value (SW)	Corresponding ISD (%)
Spence et al. (1992)	Medvev Sponheuer Karnik (MSK) scale	D1	0	0.26
		D2	10	0.33
		D3	40	0.72
		D4	80	1.99
		D5	100	3.31
Orsini (1999)	Medvev Sponheuer Karnik (MSK) scale	D1	10	0.33
		D2	80	1.99
		D3	90	2.56
		D4	95	2.91
		D5	100	3.31
Yamazaki & Muraio (2000)	AIJ Classification	Moderate	40	0.72
		Heavy	70	1.54
Rossetto & Elnashai (2003)	Homogenised Reinforced Concrete DI (HRC)	Slight	10	0.26
		Light	20-40	0.34
		Moderate	50-70	0.72
		Extensive	80-90	1.54
		Partial Collapse	100	2.56
		Collapse		>3.31

Table 4.4 Correspondence of Limit States (after Rossetto (2004))

FEMA273 Limit states	Determination of ISD max (%)	
	HRC	FEMA273
Immediate Occupancy	0.00	0.00
Life Safety	0.93	0.50
Collapse Prevention	1.99	2.00

Table 4.5 Definitions of Limit States with ISD for Structural Wall Systems (after Ghobarah (2004))

State of damage	Ductile Walls (%)	Squat Walls (%)
No damage	< 0.2	< 0.1
Repairable damage		
1. Light	0.4	0.2
2. Moderate	< 0.8	< 0.4
Irreparable damage (> Yield point)	> 0.8	> 0.4
Severe damage → Life sate → Partial Collapse	1.5	0.7
Collapse	> 2.5	> 0.8

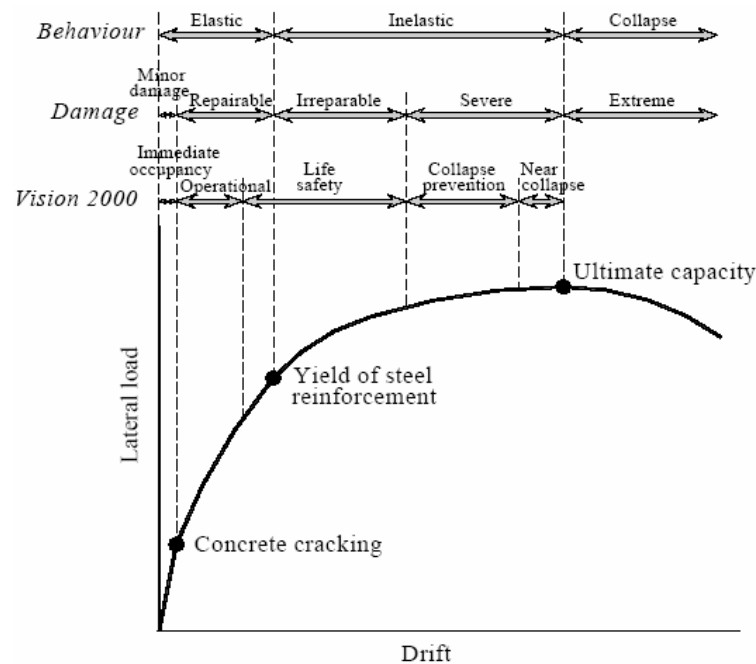


Figure 4.1 Limit Stats Corresponding to Structural Behavior (after Ghobarah (2004))

4.1.2 Consideration of Non-structural Damage

The displacement based damage index in previous sections does not contain all critical information about the impact and damages caused by earthquake strikes. Even though the building structures will not undergo extreme displacements that may lead to structural failures,

the interior or attached non-structural facilities may still be damaged severely and great losses can be expected since most high-rise buildings are either commercial or residential centers. Non-structural components are defined for those attachments or facilities within the building with purposes for either functionalities or decorations, as illuminated in Figure 4.2.

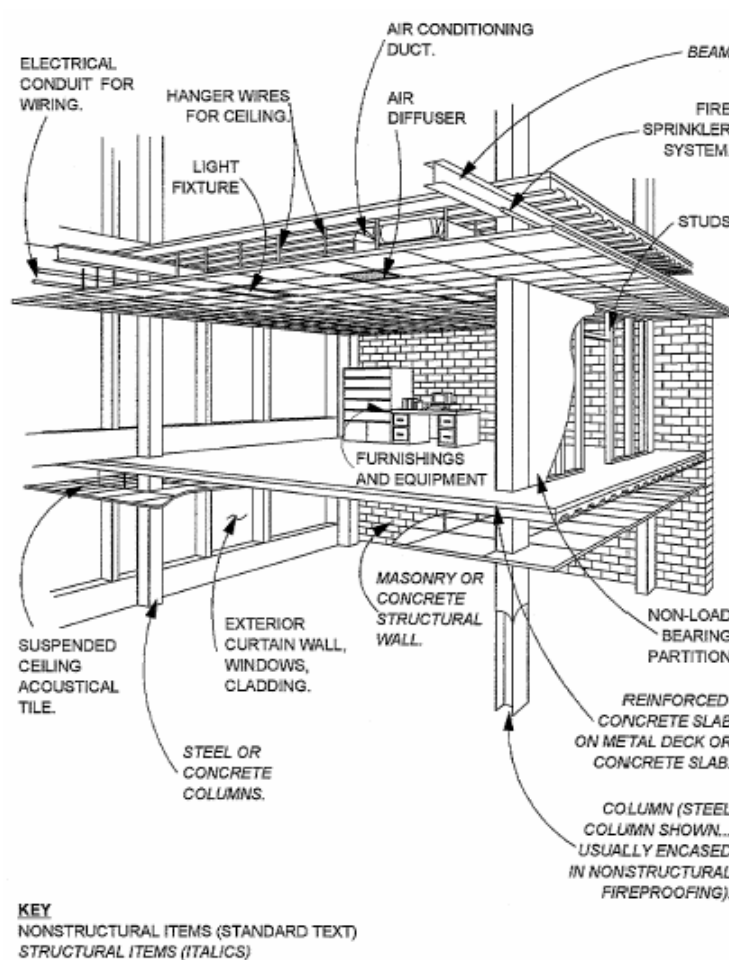


Figure 4.2 Typical Non-structural Components in Building (from WJE (1994))

Ordinary non-structural components include two categories:

- Architectural components. Including ceiling, cladding, exterior and interior non-bearing infill and partitions, furniture and equipments, and other decorations
- Mechanical and electrical components. Containing storage, water and gas piping systems,

electrical utilities, and lighting fixtures, etc

While non-structural damages during earthquakes do not affect the overall structural response, they may have serious consequences including fire, flood, or serious human injuries. Also, the indirect economic loss and social impact are likely to happen due to the disabled functionalities. The significance of non-structural damage effects has attracted increasing concerns by researchers and government organization. Wiss, Janney, Elstner Associates (WJE) and ATC have made many studies on this issue for FEMA in 1994, 1999 and 2002. Phan and Taylor (1996) looked into relative regulations and made an overview and comparisons. Currently Goodno, Craig and Gould are cooperating on a SE-3 research project from Mid-America Earthquake Engineering Center, categorizing non-structural components and determining the seismic vulnerability of the identified non-structural components.

4.2 Proposed Definitions

Limit state definitions are needed for RC high-rise buildings due to a lack of existing standards and definitions for this building type. For most structural systems adopted for RC high-rises, failure modes and damage patterns are strongly influenced by the overall configuration of the building as well as the relative size and aspect ratio of components that include frames, shear walls and other core systems. Their critical response states are the basis for the proposed limit states conceptually defined in Table 4.6.

Table 4.6 Definitions of Limit States

Level	Limit State	Description
Limit State 1 (LS1)	Serviceability	Determined at minor cracks point of main resisting members like core wall here
Limit State 2 (LS2)	Damage Control	First yielding of longitudinal steel reinforcement, or presence of first plastic hinge (may only apply for beam or columns)
Limit State 3 (LS3)	Collapse Prevention	Ultimate point of main resisting members and starting point of decreasing of overall capacity curve

The associated quantitative criteria for these definitions are derived from the results of pushover analyses are presented hereafter. The combination of overall load-displacement relationships and local damage patterns will help to determine the critical structural behavior stages.

4.2.1 Global Pushover Analysis with Whole Frame Model

To obtain the global response of the building, pushover analysis of the entire structure is necessary. Full fiber-based model of whole structure is constructed in ZEUS-NL. The combination of the first 4 natural modal shapes, weighted by modal mass participation factors, is used for the lateral load distribution pattern. By the approach, the overall load-displacement relationships could be assessed, figuring out the critical structural behavior stages by considering two methods:

- The evaluation of yielding and ultimate deformation quantities from pushover curve can be achieved through several ways by finding equivalent bi-linear response curves proposed by

Park (1988): (a) Deformation based on first yield; (b) Deformation based on equivalent elastoplastic system with the same elastic stiffness and ultimate load as the real system; (c) Deformation based on equivalent elastoplastic system with the same energy absorption as the real system; (d) Deformation based on equivalent elastoplastic system with reduced stiffness computed as the secant stiffness at 75% of the ultimate lateral load of the real system.

- Using a non-linear least square method for the whole load history to obtain equivalent multi-linear curves containing critical stages, such as simulations shown in Figure 4.3.

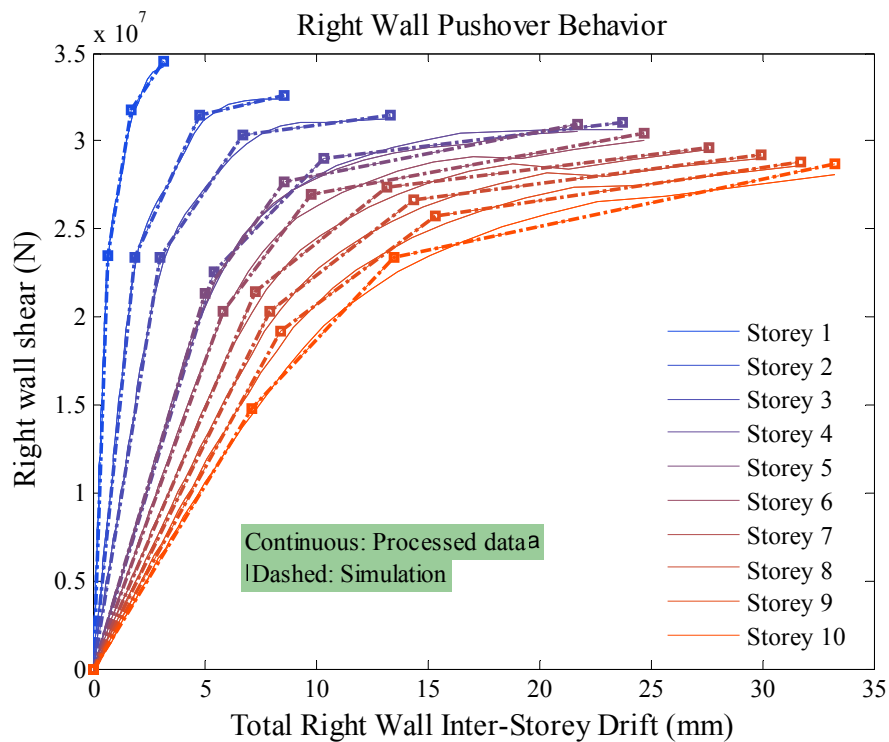


Figure 4.3 Global Pushover Responses and Equivalent Simulations

Both methods can detect yielding and ultimate points. In order to find limit state I, direct detection of cracking must also be used if Park’s methods are employed due to the bi-linear natures.

4.2.2 Structural Wall Pushover Analysis

To capture the real damage behavior of RC high-rise buildings, it is most important to obtain accurate evaluation of the response of structural wall or other core systems responses, which represent the capacity of the main resisting structure under different damage status. With only global structural response, local damage details including concrete cracking, crushing and rebar yielding within walls cannot be well detected for limit state definitions. Microscopic FEM is thus required for structural wall analysis.

VecTor2 is employed here to obtain the desired information including concrete and steel stress and strain distribution, and crack width. One-storey wall panel is used for pushover analyses under different axial load levels to cover a wide range that may be induced by overturning effects from lateral loads. Set axial force N to vary from 0.0 to $1.5N_0$ (designed dead load) covering most situations, then run pushover analyses with horizontal displacement control loads at panel top to get both pre- and post-peak behavior. With post-processing of VecTor2 results, the N-V interaction diagram in pushover analysis is shown in Figure 4.4.

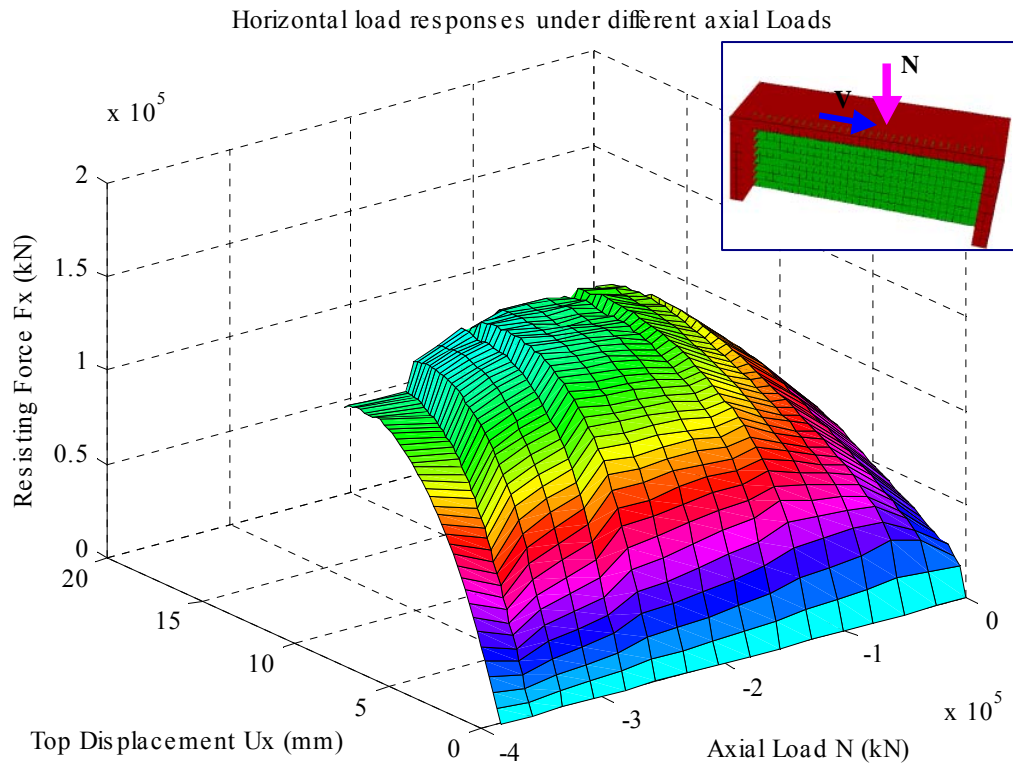


Figure 4.4 One-storey Wall Panel Pushover Analysis with N-V Combinations

Equivalent tri-linear relationships are applied to simulate capacity curves. A method, which combines the Park's criteria (Park (1988)) of same energy absorption for inelastic range and direct detection of considerable cracking point, is employed to seek the critical stages. Figure 4.5 shows the post-processed data from VecTor2, simulated lateral response curves, and relationships of limit state displacements versus different axial load levels. Polynomial expression in Equation 4.2 is employed for the mathematical regression between limit state deformations and axial load levels, and the parameters are listed in Table 4.7.

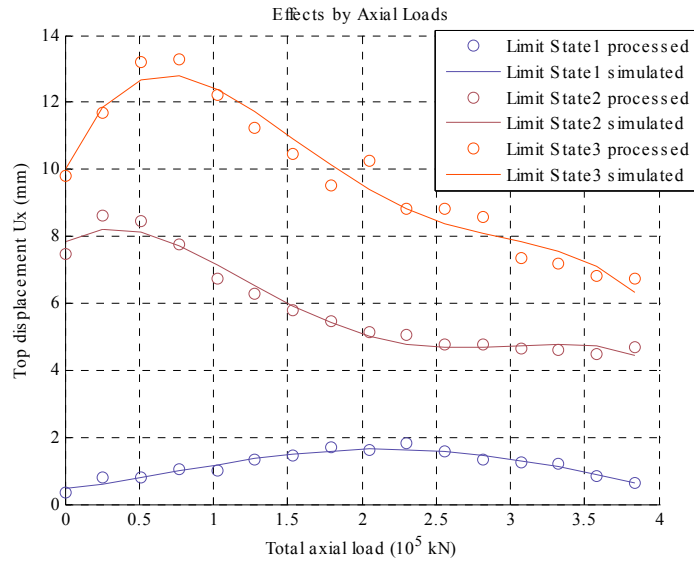
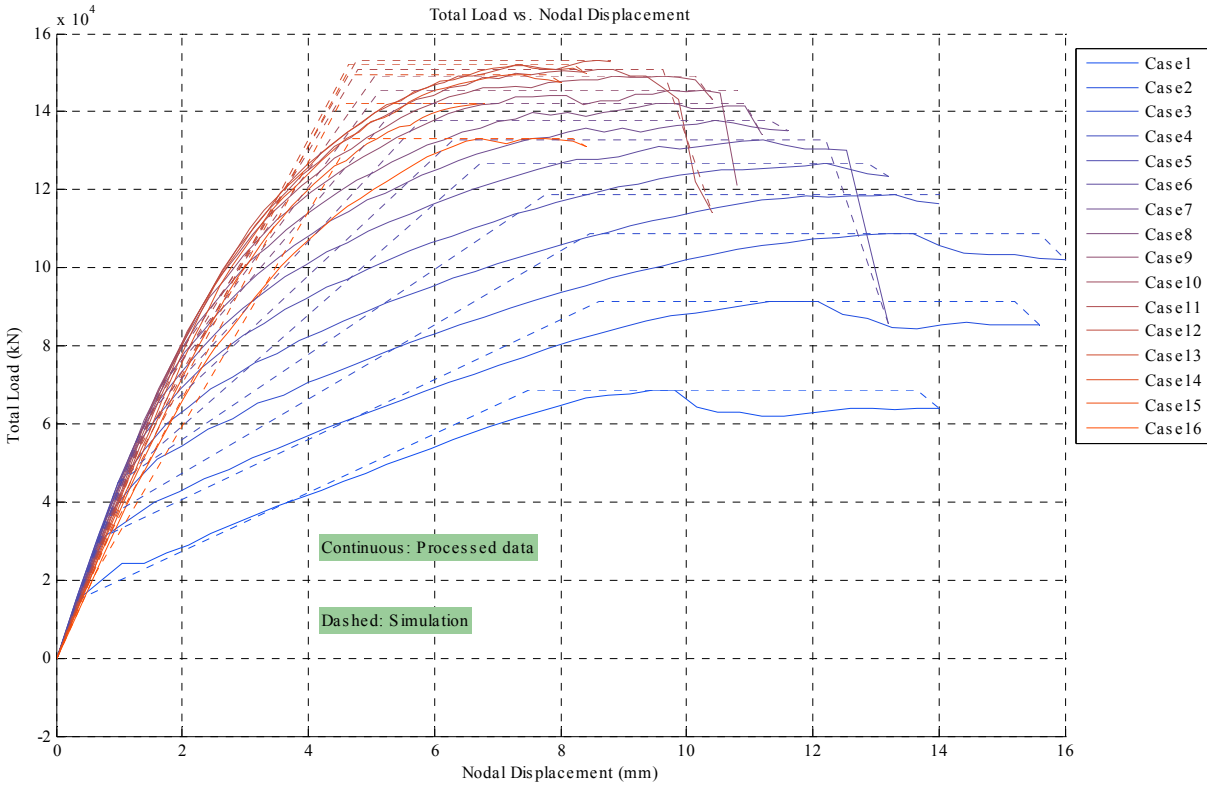


Figure 4.5 Processed and Simulated Pushover Curves (Upper) and Limit State Displacements for Different Axial Load Levels (Lower)

$$U_{xi} = C_1 \bar{N}^4 + C_2 \bar{N}^3 + C_3 \bar{N}^2 + C_4 \bar{N} + C_5 \tag{4.2}$$

where, limit state number $i = 1 \sim 3$, $\bar{N} = N / (10^5)$, all units in kN, mm

Table 4.7 Regression Relationship Constants for Limit State Displacements versus Axial Loads

Level	C1	C1	C1	C1	C1
Limit State 1 (LS1)	0.0264	-0.2434	0.4261	0.4984	0.4553
Limit State 2 (LS2)	-0.2197	1.8586	-4.7798	2.5034	7.8430
Limit State 3 (LS3)	-0.3616	3.2815	-10.001	9.5355	9.9917

4.2.3 Multi-Resolution Distributed FEM Analysis of Whole Building

4.2.3.1 Overview

For the selected reference structure with complex dual wall-frame system, the pushover analyses described in previous sections are not sufficient for the accurate detection of both global and local damages simultaneously. The reason lies in the lack of consistency when dealing with the wall and frame in pushover analyses. Pure ZEUS-NL frame model for the whole building neglects the dominant shear effects within lower level walls, and the VecTor2 wall panel analysis undergoes the artificial load combinations which are inconsistent with the real load transfer and distributions throughout the building from applied lateral and gravity loads. Hence wall-frame interaction effects cannot be taken into account here.

To facilitate this detailed analysis, a new analysis framework referred to as multi-resolution distributed finite element analysis, MDFEA, is presented in this study and then used for the analysis of the reference building. In this distributed analysis framework, the strengths of two computational tools were combined for the integrated analysis of this building. The non-linear beam element in program ZEUS-NL was used to model the RC frames and upper portion of the

RC walls while the non-linear continuum analysis program VecTor2 was used to model the lower portions of the building's RC shear walls. The combined use of these two different programs was made possible by the development of a 'simulation coordinator' program that can seamlessly merge multiple computational components into one structural system. The latter coordinator, UI-SIMCOR developed by Kwon et al. (2005), runs several concurrent components, combining their action-deformation characteristics on a network.

4.2.3.2 Detailed Algorithm

Different state-of-the-art analysis software packages have unique features that other competing packages do not have. Similarly, different research laboratories are equipped with unique experimental facilities that complement each other. The main advantage of multi-platform simulation is the use of the unique features of analytical tools and/or experimental facilities in an integrated fashion, an essence of the distributed Network for Earthquake Engineering Simulations (NEES). The concept of multi-platform simulation is implemented using the pseudo-dynamic (PSD) simulation approach combined with sub-structuring. In the latter simulation, a structure is subdivided into several modules that are either physically tested or computationally simulated. UI-SIMCOR (Kwon et al. (2005)) was developed for this purpose. The Operator Splitting method in conjunction with the α -modified Newmark scheme (α -OS method) is implemented as a time-stepping analysis scheme. The main feature of UI-SIMCOR is that it is capable of coordinating any number of analysis tools. Interfaces are currently exist for ZEUS-NL, OpenSees (McKenna and Fenves (2001)), FedeaLab (Filippou and Constantinides (2004)), VecTor2, and ABAQUS (Hibbit et al. (2001)). Any number of testing sites, or a mixture

of analysis tools and testing sites can be incorporated into a pseudo-dynamic multi-platform simulation. It employs software or hardware supporting NEESgrid Teleoperation Control Protocol (NTCP; by Pearlman et al. (2004)) as well as TCP-IP connections outside of the NEES system. It is also capable of using the same analysis platform while modeling different parts of the system on the same or different processors, thus minimizing computational run time. In this study, UI-SIMCOR is used to combine VecTor2 and ZEUS-NL to model shear-walls and frame elements.

In the use of UI-SIMCOR, an entire structure is divided into components, which are represented by different analysis platforms or experimental models. Mesh refinements and DOF numbering are conducted within sub-structure components. Global stiffness matrix for effective DOFs at control points is assembled in UI-SIMCOR with control points in the sub-structure models. Control points are nodes with lumped masses or at the interface between two structural components. These control points must be defined first in order to form the global mass and stiffness matrices necessary in pseudo-dynamic (PSD) algorithm employed in UI-SIMCOR, and to serve as the common interfaces between sub-structures. Hence one important issue in sub-structuring of RC high-rise buildings is to model the wall-frame interfaces at control points. For frame elements and solid continuum elements connected at control points, degree-of-freedom (DOF) coupling must be considered, such as displacements and load transfer between $[u, v, \theta]$ for 2D beam elements and $[u', v']$ for 2D solid continuum elements. The details for modeling this interface are described in Section 3 of this paper within the description of the complete modeling of 54-story high-rise building example.

In sub-structured simulation, the structure should be divided into sub-components satisfying two basic conditions – displacement compatibility and force equilibrium. The multi-platform simulation framework utilizes unique structural analysis platforms at the user level, which does not allow iteration for path-dependent nonlinear inelastic models. Hence, Kwon et al. (2005) employed a method to avoid iterations. UI-SIMCOR takes advantage of the PSD scheme to combine various analytical platforms and thereby to avoid global nonlinear iterations. Only time integration scheme is coded inside UI-SIMCOR main framework. Other structural models reside within external static analysis modules or experimental facilities if hybrid simulation (combined analysis and experimentation) is engaged. Currently, the α -modified Newmark scheme (α -OS method) is implemented as the PSD scheme in UI-SIMCOR. The α -OS method follows the algorithm presented by Combescure and Pegon (1997).

The architecture of the framework is depicted in Figure 4.6. UI-SIMCOR uses object-oriented programming for easier maintenance and future expansion. There exist two major classes of modules:

- MDL_RF (restoring force module) represents structural components, with functionalities of imposing displacement to the structural components and obtaining restoring forces.
- MDL_AUX (auxiliary module) controls experimental hardware other than actuators, which is not applicable in this study.

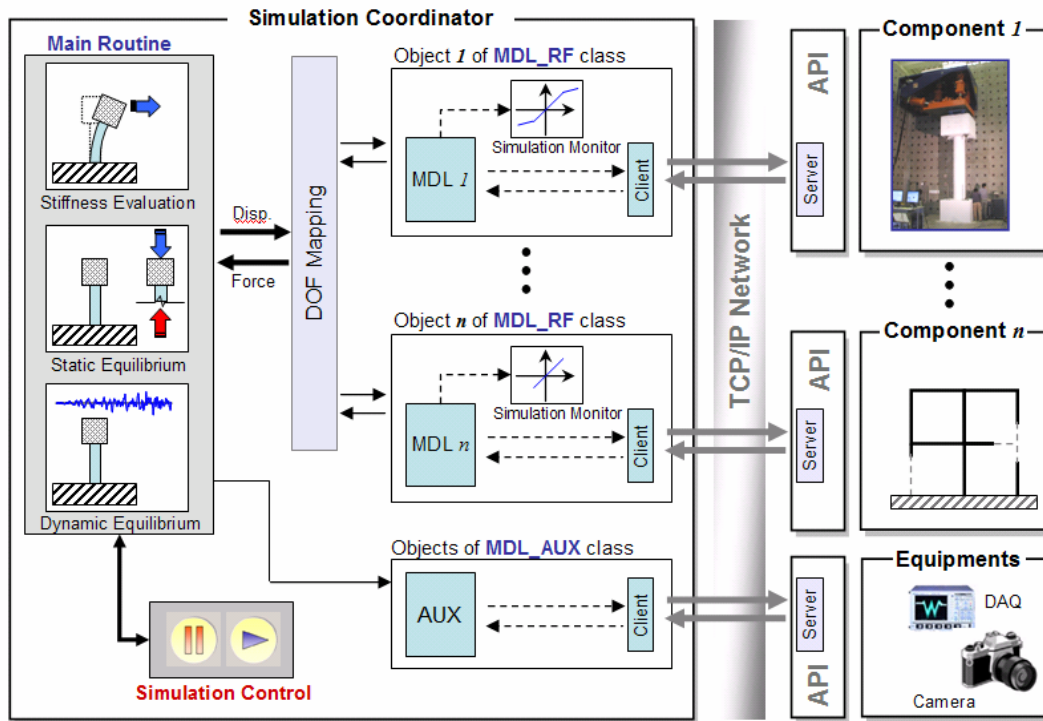


Figure 4.6 Architecture of UI-SIMCOR Framework (Spencer et al. (2006))

A typical simulation procedure and data flow deal with three communication layers are identified as ‘User’, ‘Simulation Framework’, and ‘Remote Sites’. The user is controlling and monitoring the general operations within the simulation framework using monitoring window. Simulation framework is the main function including initialization, stiffness estimation, time history integration, and communication with remote sites. The remote sites are the places where individual modules are under analysis with distinct analytical or experimental platforms, receiving and commanding displacement loads and returning restoring forces and actual movements.

4.2.3.3 Application for Reference Building

The reference building was divided into two main structural components, a box-shaped core wall

and an outer moment resisting frame. The core walls from the 1st through 10th stories, which are likely to fail in shear, were modeled using 2D RC continuum elements in VecTor2. The core walls from the 11th story and above were approximated with fiber section elements in ZEUS-NL. The entire structure was subdivided into three modules as below:

- Module 1: 1st ~ 10th story left wall modeled in VecTor2

This region was modeled in VecTor2. The first 10-stories of the wall was modeled using 2D rectangular elements whose behavior can be captured using the Modified Compression Field Theory (MCFT; Vecchio and Collins (1986)). The mesh size was around 200 mm which is within 10~20 times of aggregate size. Concrete constitutive models were based on Modified Popovics curve by Collins and Porasz (1989), which considers both pre-peak and post-peak concrete behavior. The confinement effects were considered according to Kupfer et al. (1969). The reversed cyclic loading curves of concrete proposed by Palermo and Vecchio (2003) was employed in the analysis.

- Module 2: 1st ~ 10th story right wall in VecTor2

Module 2 is identical to Module 1.

- Module 3: remaining structure in ZEUS-NL

Remaining structural components including all frame members and the core walls from the 11th to the top story.

□ **Interface modeling between beam element and wall continuum element**

UI-SIMCOR (Kwon et al. (2005)) uses control points in the sub-structure models, with lumped masses and DOFs of interest for applying and measuring loads and displacements. These control

points must first be defined in order to form the global mass and stiffness matrices necessary in pseudo-dynamic (PSD) algorithm employed in UI-SIMCOR, and to serve as the common interfaces between sub-structures.

There are two ways to simulate the interface at control points that have a rotational DOF. One method is to use membrane elements for the wall with drilling (out-of-plane rotational) DOFs, but this is not available in VecTor2. The second method and the one used in this study is to simulate the coupling and transfer between control point DOFs and the connected 4-noded plane-stress element nodal DOFs. To illustrate this approach, considered the node between elements 1 and 2 as control points, which is node 1 in Figure 4.7 that is common to both the membrane elements used to model the wall and the beam elements used to model the slab. In order to satisfy compatibility, constraint equations are added between these nodes of the two models to satisfy compatibility of rotation at these common (control) points.

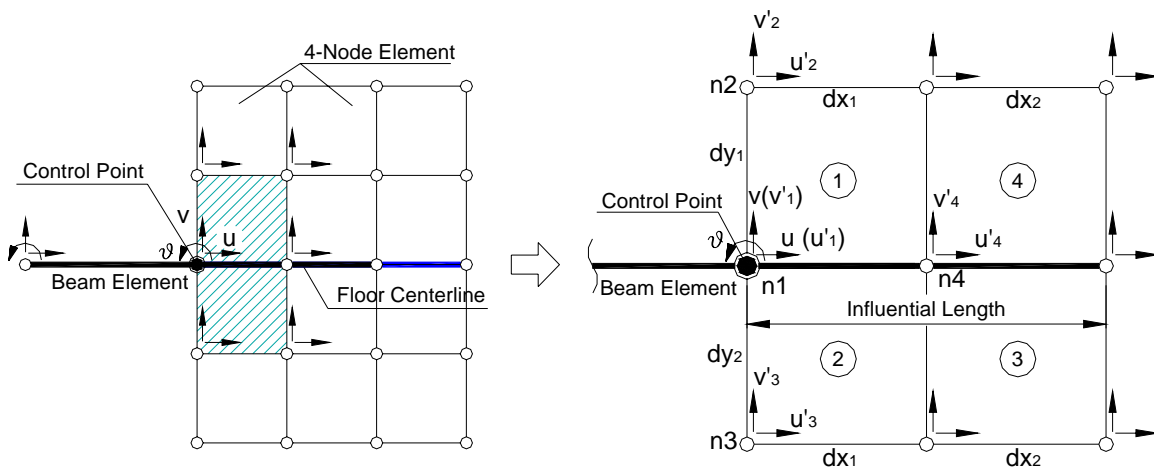


Figure 4.7 Frame Beam Element and Wall Continuum Element Interface (Left) and Model DOFs (Right)

In UI-SIMCOR, displacements are always imposed at control points and reaction forces are

obtained as feedback at the same DOFs. Thus, combining the models requires the calculation of equivalent nodal displacement of continuum elements at the interface connected to control points. The constraint equations for beam-continuum coupling are derived for the interface region shown in Figure 4.7 (right plot), which is formed by elements 1 and 2, and nodes n1 to n4. It is assumed that the left edges of elements 1 and 2 follow the Bernoulli-Euler beam model, with plane section remaining plane during deformation. Hence, the rigid body motion geometric relationships are applied to calculate nodal displacements at left edges following Equation 4.3.

$$\begin{Bmatrix} u_1' \\ v_1' \end{Bmatrix} = \begin{Bmatrix} u \\ v \end{Bmatrix}; \quad \begin{Bmatrix} u_2' \\ v_2' \end{Bmatrix} = \begin{Bmatrix} u - dy_1 \sin \theta \\ v - dy_1 (1 - \cos \theta) \end{Bmatrix}; \quad \begin{Bmatrix} u_3' \\ v_3' \end{Bmatrix} = \begin{Bmatrix} u + dy_2 \sin \theta \\ v + dy_2 (1 - \cos \theta) \end{Bmatrix} \quad (4.3)$$

where, $[u, v, \theta]$ are the displacement loads at control point.

For the nodes along the beam centerline, not all nodes will be considered as being on an interface. Only those within influential length (on account of usual anchorage requirements for rebar) are counted and here the middle node n4 in Figure 4.7 is such a node. The right node to n4 is treated as the fixed end of beam and no displacement is imposed there. Also for the middle node n4, it is assumed that the horizontal and vertical movements are generated by the control point displacement based on beam shape functions following Equation 4.4.

Define: $\xi = \frac{x}{l_e}$, here the element length $l_e = dx_1 + dx_2$

$$\begin{Bmatrix} u_4' \\ v_4' \end{Bmatrix} = \begin{bmatrix} (1-\xi) & 0 & 0 & \xi & 0 & 0 \\ 0 & (1-3\xi^2+2\xi^3) & (\xi-2\xi^2+\xi^3)l_e & 0 & (3\xi^2-2\xi^3) & (\xi^3-\xi^2)l_e \end{bmatrix} \begin{Bmatrix} u \\ v \\ \theta \\ 0 \\ 0 \\ 0 \end{Bmatrix} \quad (4.4)$$

The feedback control point reactions are computed from the nodal forces at these four nodes through equilibrium conditions described by Equation 4.5.

$$F_x = \sum_{i=1}^4 f_{xi}; \quad F_y = \sum_{i=1}^4 f_{yi}; \quad M_z = \sum_{i=1}^4 (f_{xi}y_i + f_{yi}x_i) \quad (4.5)$$

The VecTor2 post-processor can compute and output reaction forces corresponding to the nodes imposed with displacement. MATLAB codes were written as UI-SIMCOR plug-ins to realize the functionalities including receiving the commands through network, calculating interface nodal displacements in VecTor2 model, running VecTor2, and reactions assessment.

□ **Interface modeling between upper wall beam element and lower wall continuum**

Due to the geometric characteristics and common frame-wall interactions in high-rise buildings, structural walls generally exhibit complex behavior under lateral loading. The deformation and failure modes within structural walls usually vary along the building height, transitioning from shear-dominant behavior in lower levels into flexure-dominant behavior in the upper stories. The lower 10 stories of the wall were modeled using 2D continuum elements in VecTor2, while the wall above this level was modeled using beam-column elements in ZEUS-NL. There are two types of interfaces: 1) upper-wall frame elements and lower-wall continuum elements; 2) control point DOFs and wall continuum element DOFs per floor. Two methods have been investigated and compared for modeling of the interfaces between the two substructures:

- An approach was to simulate the interface with one control point in the middle of the floor in which there is one rotational DOF as shown in Figure 4.8(a). The upper wall frame element is then modeled using a fiber approach in ZEUS-NL. The floor system is

treated as rigid so that the equivalent nodal displacements in VecTor2 model can be computed based on the rigid body motion (RBM) of the control point.

- The other approach was to use three control points at the middle and two edge-points at the interface for each floor, as shown in Figure 4.8(b). The upper-wall frame element is divided into three components including two boundary regions and a middle web area, also modeled using fiber elements in ZEUS-NL. The floor slab may strengthen the adjacent region of the wall and at the same time affect wall deformations. Due to the flexibility of the slab-beam and the large attached mass, very significant external loads can be induced in the dynamic analyses. To avoid over-restraining the continuum elements, the floor is considered to have some flexibility as opposed to the full rigidity used in the first method.

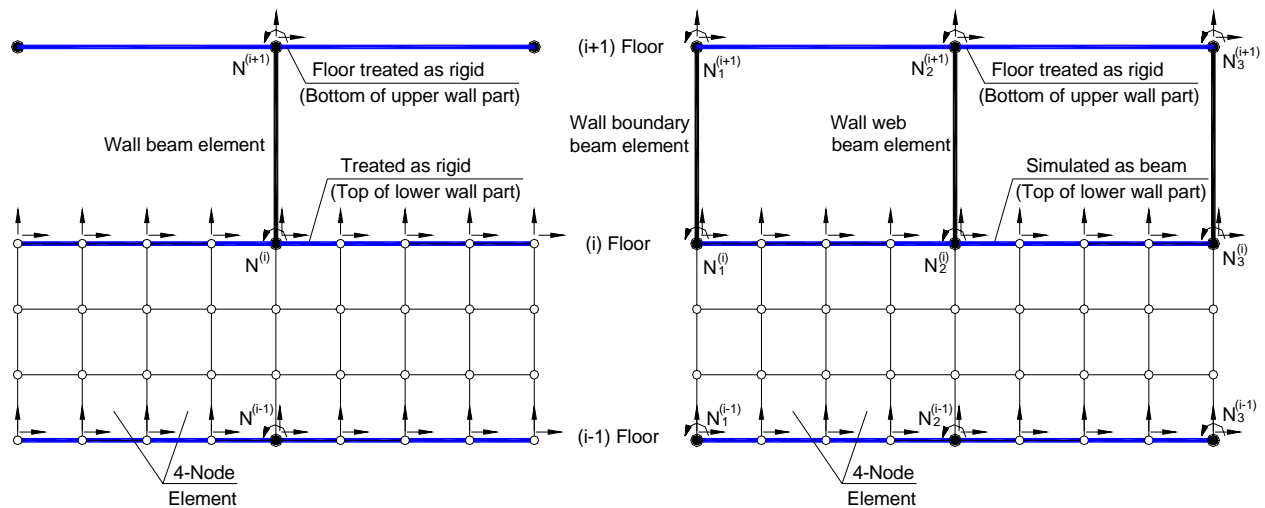


Figure 4.8 Upper Wall Beam and Lower Wall Continuum Element Interface Models:

- (a). Interface Model with One Control Point per Floor (Left); (b). Interface Model with Three Control Points per Floor (Right)

It is also necessary to model the interface using control point DOFs between the lower 10 stories

of the wall that were modeled using continuum elements in VecTor2 and the upper stories that were modeled by beam-column elements in ZEUS-NL. This interface is described in Figure 4.9. As with the previous discussed interface, it is necessary to select a pattern of displacements of the interface nodes along the interface, in this case floor centerline, in the VecTor2 model. Once again, the two previously described methods are considered.

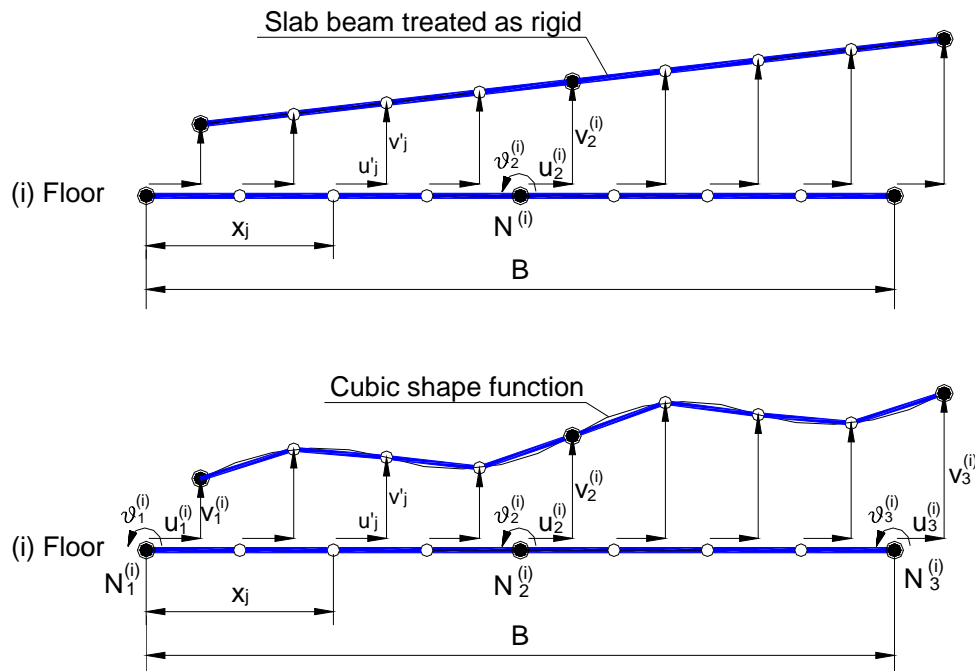


Figure 4.9 Wall Interface Interpolation Approaches and DOFs

(a). One-control-point Approach (Upper). (b). Three-control-point Approach (Lower)

- One-control-point approach

In this approach, the rigid body motion assumption is made for the floor slab system as shown in Figure 4.9(a). The rotational DOF at this control point will generate a linear variation in vertical displacements at all nodes along the i th floor. The constraint equations for both upper wall to lower wall and inter-storey lower wall interfaces are derived using Equation 4.6. The control

point reaction forces are computed from the stress resultants at all of the nodes through equilibrium conditions as evaluated by Equation 4.7.

$$\begin{Bmatrix} u'_j \\ v'_j \end{Bmatrix} = \begin{Bmatrix} u_i + \left(\frac{B}{2} - x_j\right)(1 - \cos \theta_i) \\ v_i - \left(\frac{B}{2} - x_j\right) \sin \theta_i \end{Bmatrix} \quad (4.6)$$

$$\begin{Bmatrix} F_{xi} \\ F_{yi} \\ M_{zi} \end{Bmatrix} = \begin{Bmatrix} \sum_{j=1}^{N_i} f_{xj} \\ \sum_{j=1}^{N_i} f_{yj} \\ \sum_{j=1}^{N_i} f_{yj} \left(\frac{B}{2} - x_j\right) \end{Bmatrix} \quad (4.7)$$

where, i – Control point number, $j = 1, 2, \dots, N_i$, and N_i is the total number of nodes along i^{th} floor in VecTor2 model

- Three-control-point approach

As discussed previously, instead of employing a rigid body motion (RBM) assumption, beam shape functions are used for the calculation of the equivalent nodal displacements in the VecTor2 model. In the above approach, the interface floor system is divided into two beams connected by three control points. In Figure 4.9(b), control points N_1^i, N_2^i, N_3^i form two beam members with lengths equal to half of the wall width. Cubic shape functions are used for the interpolation of continuum model nodal displacement loads $[u'_j, v'_j]$ from $[u, v, \theta]_{1\sim 3}^i$ at these three control points as follows. The shape functions for the two beam members are defined as:

$$\text{Define: } \xi = \begin{cases} \frac{x}{l_e}, & \text{if } x \leq \frac{B}{2} \\ \frac{(x - B/2)}{l_e}, & \text{if } x > \frac{B}{2} \end{cases}, \text{ the element length } l_e = \frac{B}{2}$$

$$[N] = \begin{bmatrix} (1-\xi) & 0 & 0 & \xi & 0 & 0 \\ 0 & (1-3\xi^2 + 2\xi^3) & (\xi - 2\xi^2 + \xi^3)l_e & 0 & (3\xi^2 - 2\xi^3) & (\xi^3 - \xi^2)l_e \end{bmatrix} \quad (4.8)$$

The nodal displacements at all the nodes along ith floor can then be computed as:

$$\begin{cases} \begin{Bmatrix} u'_j \\ v'_j \end{Bmatrix} = \begin{cases} [N] \begin{bmatrix} u_1^i & v_1^i & \theta_1^i & u_2^i & v_2^i & \theta_2^i \end{bmatrix}^T, & \text{for } 0 \leq x_j \leq \frac{B}{2} \\ [N] \begin{bmatrix} u_2^i & v_2^i & \theta_2^i & u_3^i & v_3^i & \theta_3^i \end{bmatrix}^T, & \text{for } \frac{B}{2} \leq x_j \leq B \end{cases} \end{cases} \quad (4.9)$$

where, $j = 1, 2, \dots, N_i$, N_i is the total number of nodes along ith floor in VecTor2 model, and B represents the wall width.

The feedback control point reactions are computed from nodal force results from the VecTor2 output using an equivalent nodal force concept for beam elements as expressed in Equations 4.10 ~ 4.12.

$$\begin{bmatrix} F_{x1} & F_{y1} & M_{z1} & F_{x2}^1 & F_{y2}^1 & M_{z2}^1 \end{bmatrix}^i = \left[\sum_{j=1}^{m1} \left([N]^T \begin{Bmatrix} f_{xj} \\ f_{yj} \end{Bmatrix} \right) \right]^T, \quad \text{for } 0 \leq x_j \leq \frac{B}{2} \quad (4.10)$$

$$\begin{bmatrix} F_{x2}^2 & F_{y2}^2 & M_{z2}^2 & F_{x3} & F_{y3} & M_{z3} \end{bmatrix}^i = \left[\sum_{j=m1}^{m2} \left([N]^T \begin{Bmatrix} f_{xj} \\ f_{yj} \end{Bmatrix} \right) \right]^T, \quad \text{for } \frac{B}{2} \leq x_j \leq B \quad (4.11)$$

$$\begin{bmatrix} F_{x2} & F_{y2} & M_{z2} \end{bmatrix}^i = \begin{bmatrix} F_{x2}^1 & F_{y2}^1 & M_{z2}^1 \end{bmatrix}^i + \begin{bmatrix} F_{x2}^2 & F_{y2}^2 & M_{z2}^2 \end{bmatrix}^i \quad (4.12)$$

where, $m1, m2$ are the number of nodes at middle and right end of the floor, $[f_{xj}, f_{yj}]$ are the forces at j th node in VecTor2.

Both of these approaches have been investigated and compared on the basis of accuracy, runtime and stability. The three-control-point approach proved to be more accurate by introducing

flexibility of the floor as was expected in the real structure. The rigid slab assumptions put severe restraints on the floor nodes and thereby overestimated the stiffness of the lower 10-stories of the walls, which led to smaller flexural deformations of the wall and underestimated the effects on lateral drift. The use of the RBM assumption restricted the development of cracking. The runtime required by one control point approach was somewhat shorter than that with the use of three control points. Based on this evaluation, the accuracy of the results was considered to be more important than runtime and therefore the three-control-point approach was employed for the MDFEA conducted in this study.

□ **Integrated MDFEA Structural Modeling**

The MDFEA framework and sub-structuring methodology used for the 54-story case study building is shown in Figure 4.10.

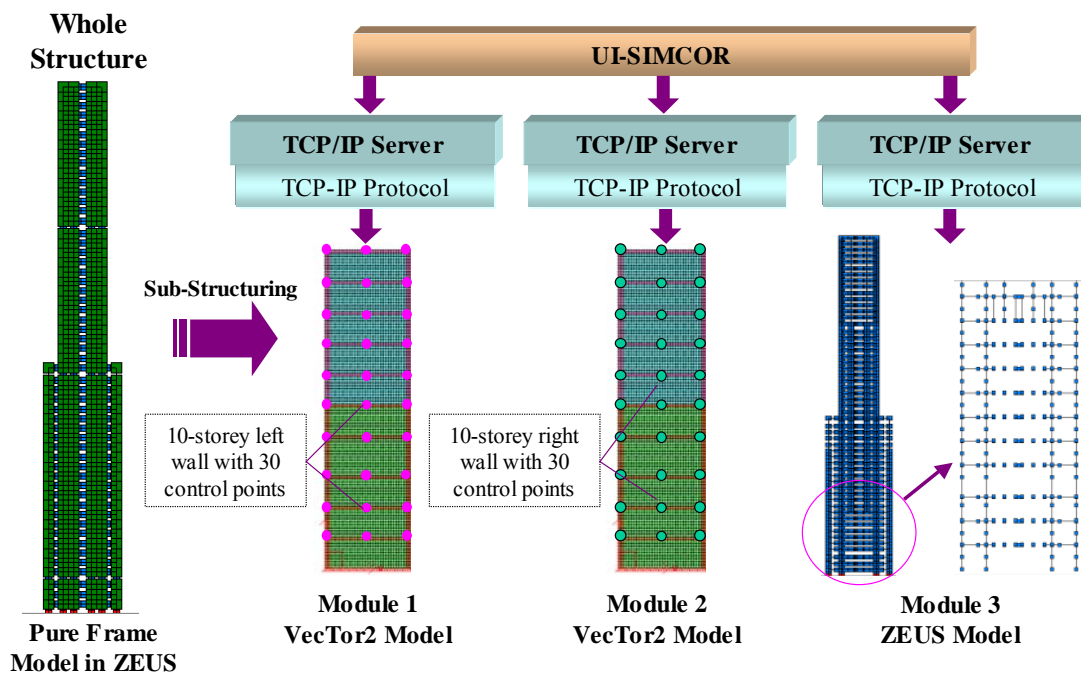


Figure 4.10 Multi-resolution Distributed Simulation for Reference Building Combining ZEUS-NL and VecTor2 within UI-SIMCOR

Dynamic response history as well as static pushover analyses were conducted using the distributed simulation approach. The whole model size including the meshes and control DOFs are listed in Table 4.8.

Table 4.8 MDFEA Model Size and Control DOFs

Module No.	Node Number	Element Number	Control Node	Effective DOF
1 -- Left Wall VecTor2 Model	3640	3502	30	90
2 -- Right Wall VecTor2 Model	3640	3502	30	90
3 -- Whole Frame ZEUS Model	1160	1672	306	426

The MDFEA is performed within UI-SIMCOR combining different modules in ZEUS-NL and VecTor2 through the main control window shown in Figure 4.11.

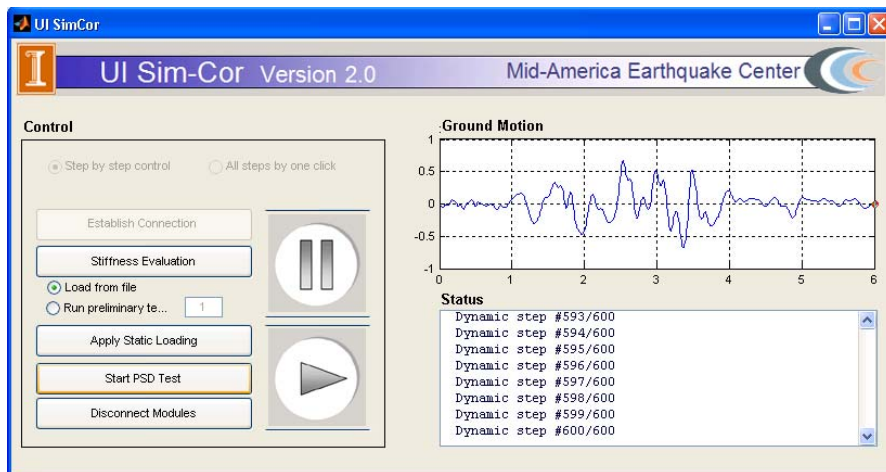


Figure 4.11 UI-SIMCOR Main Control Window

□ Evaluation of MDFEA

Both static pushover analysis and dynamic response history analyses were conducted to evaluate the MDFEA for the selected building. The former was used for the limit states definitions by estimating its ultimate strength and ductility capacity, while the latter served for the investigation

of real building behavior under selected representative ground motion records.

- Static pushover analysis

In UI-SIMCOR, gravity loads were applied to the building prior to conducting this static pushover analysis, as shown in Figure 4.12.

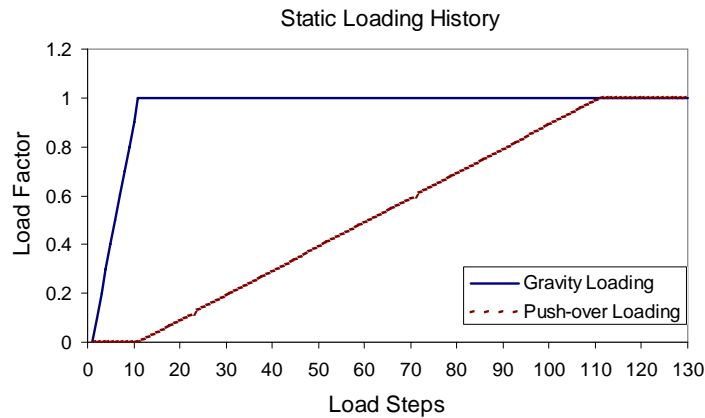
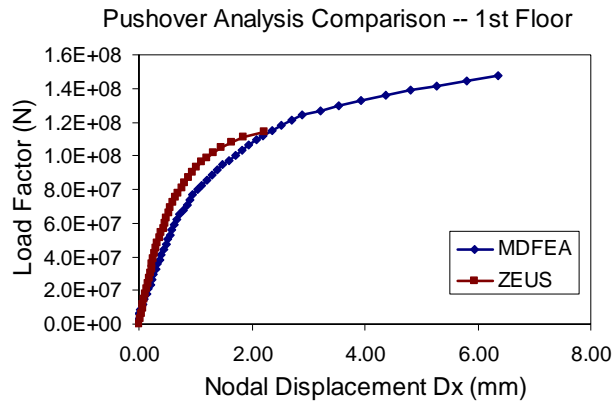


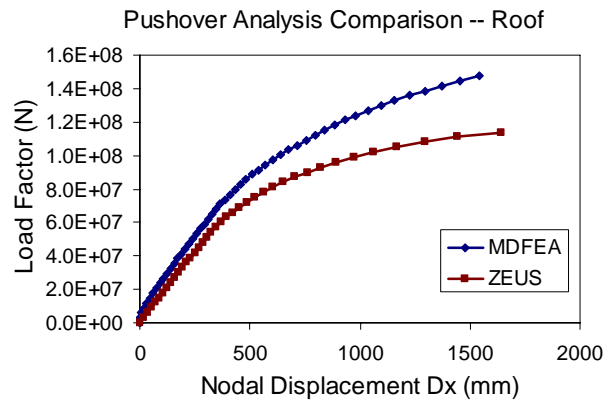
Figure 4.12 Static Loading Histories in MDFEA

Two analyses were conducted in the study, one using the MDFEA framework and the other in which the structure was entirely modeled as a frame using ZEUS-NL. A comparison of the results from these analyses is presented in Figure 4.13.

These comparisons illustrate that the lateral drift in the lower part of the wall has more flexibility and ductility in MDFEA than in the ZEUS-NL analysis. This is mainly due to the much larger shear deformation contributions that were captured in the continuum model of the MDFEA. At higher load levels, the ZEUS-NL model exhibits lower stiffness and ultimately less strength than the MDFEA model. This is mainly because the plane section assumption in the fiber approach leads to concrete crushing at the base of the wall before the concrete compressive capacity is reached in accordance to the continuum model.



a. Response at 1st Storey



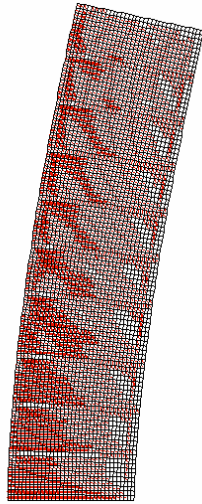
b. Response at Roof

Figure 4.13 Pushover Comparisons between Results from MDFEA and Complete ZEUS-NL Approaches

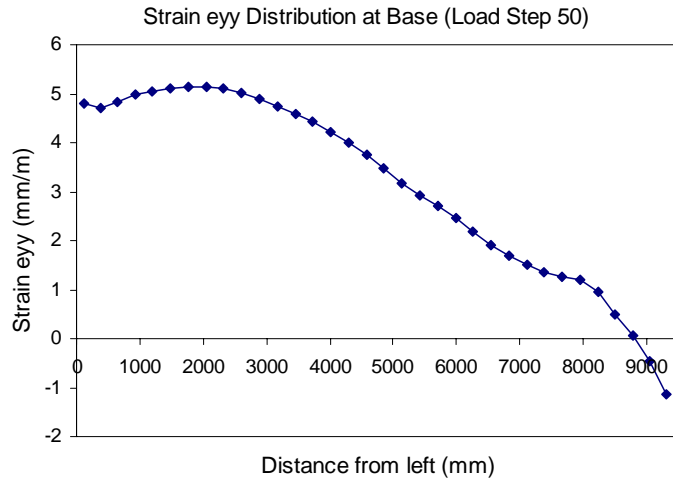
In the MDFEA approach, load redistribution is repeatedly performed at each load step and a confined concrete strength model is applied in the regions of highest compressive stress that follows the Kupfer-Richart Model (Wong and Vecchio (2002)) as expressed in Equation 4.13. This latter feature leads to increased wall capacity and ductility under high load levels even after extensive cracking has been calculated to occur.

$$\beta_l = \left[1 + 0.92 \left(\frac{f_{cn}}{f'_c} \right) - 0.76 \left(\frac{f_{cn}}{f'_c} \right)^2 \right] + 4.1 \left(\frac{f_{cl}}{f'_c} \right) \quad (4.13)$$

where, $f_{cn} = -(f_{c2} - f_{c1}) > 0$, $f_{cl} = -f_{c1} > 0$, $f_{c2} < f_{c1} < 0$



a. Cracked deformation shape
(Step 50, Scale factor: 20)



b. Strain e_{yy} distribution at wall base section
(Step 50)

Figure 4.14 Crack Map and Vertical Strain Distribution of the Wall at Load Step 50

Figure 4.14 shows the extent of cracking, the deformed wall shape and vertical strain distribution along base section at load step 50. It is observed from Figure 4.14 that the wall deforms and is damaged in flexural-shear mode under the incremental pushover loads. It is also illustrated that plane sections are not predicted to remain plane across the width of the wall.

- Dynamic response history analysis (DRHA)

Inelastic dynamic response history analyses were executed using the MDFEA framework for the sample building using selected representative ground motion records. Ground motions were selected to encompass different magnitudes, distance to source, and site soil conditions. The variation of input ground motion shown in Table 4.9 is intended to evaluate the reliability of the MDFEA algorithm for complex structural systems under different types of seismic excitations.

Table 4.9 Selected Ground Motion Records for MDFEA Evaluation

Earthquake	Record	M	Station Data Source	Distance to source (km)	Site Soil Condition	PGA (g)
Chi-Chi, Taiwan 1999/09/20	Chi-Chi_close_stiff	7.6	CHY028-N, (CWB)	7.31	Stiff	0.821
Kocaeli, Turkey 1999/08/17	Kocaeli_close_stiff	7.4	SKR090, Sakarya (ERD)	3.1	Stiff	0.376
Kobe, Japan, 1/16/1995	Kobe_close_stiff	6.9	TAZ090 Takarazuka, (CUE)	1.2	Soft	0.694
	Kobe_close_soft	6.9	SHI000, Shin-Osaka, (CUE)	15.5	Soft	0.243
Loma Prieta, USA 1989/10/18	Loma_dist_soft_1	6.9	SFO090 58223, SF Intern. Airport, (CDMG)	64.4	Soft	0.329

The elastic spectrum acceleration diagrams (damping ratio 5%) of the selected GMs are shown in Figure 4.15.

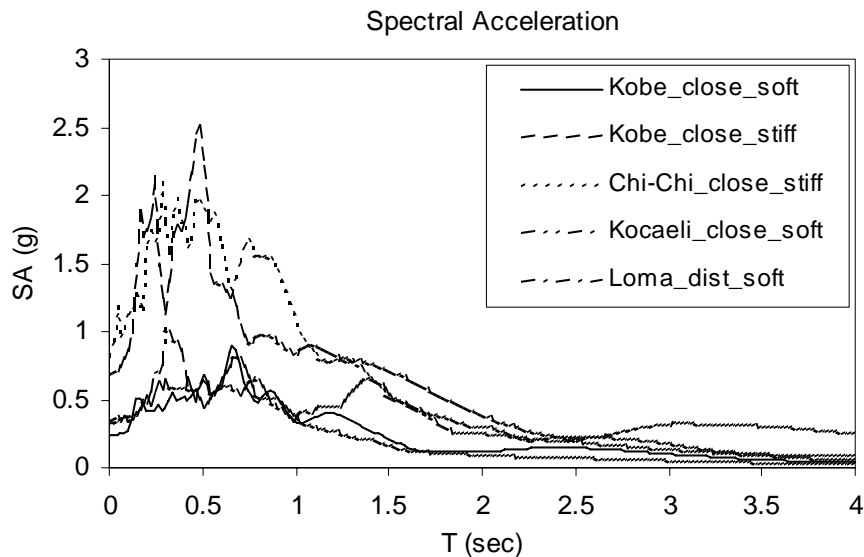


Figure 4.15 Spectral Acceleration Diagrams of Selected GMs for MDFEA

Figure 4.16 presents the deformed sub-structure shapes for the sample building during a dynamic response history analysis (DRHA). The shapes illustrate the synchronized seismic responses of two core walls and the frame as well as the flexibility of floor and shear deformations in the wall.

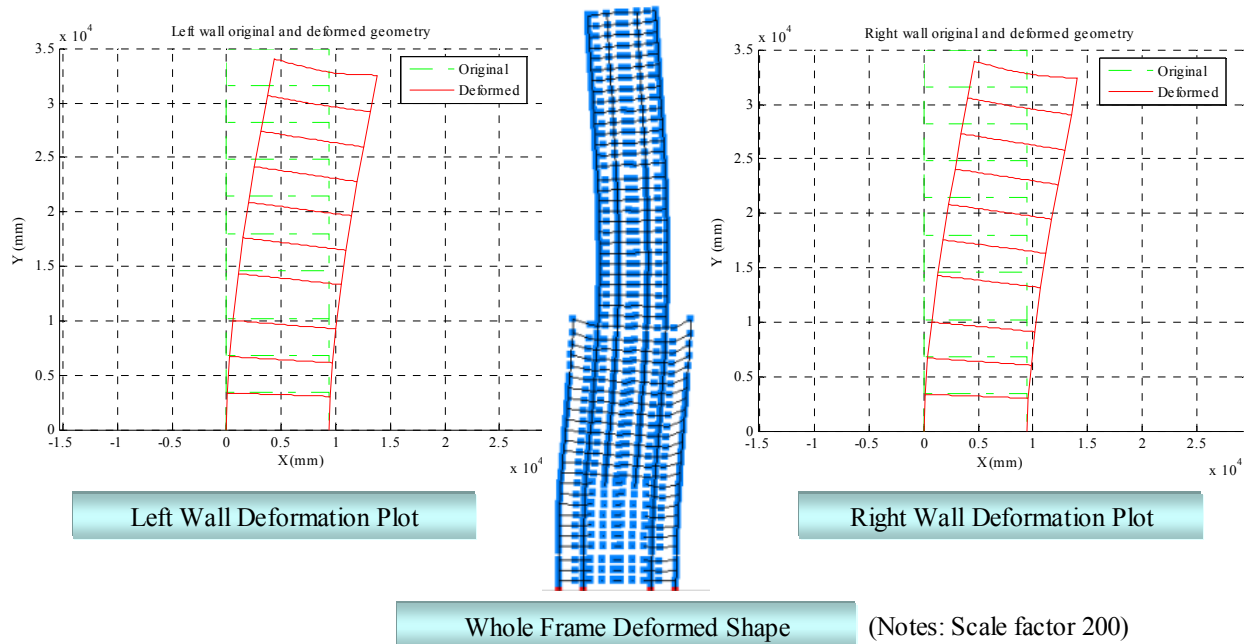


Figure 4.16 Deformed Shapes of Three Modules from DRHA Using the MDFEA Framework

In Figure 4.17, two sets of response history analysis results using both MDFEA framework and the pure frame model using ZEUS-NL are presented. The left wall displacement responses at different height levels are compared between these two models, including total drifts at 1st storey, 10th storey (top of the wall VecTor2 models in modules 1 and 2) and the roof.

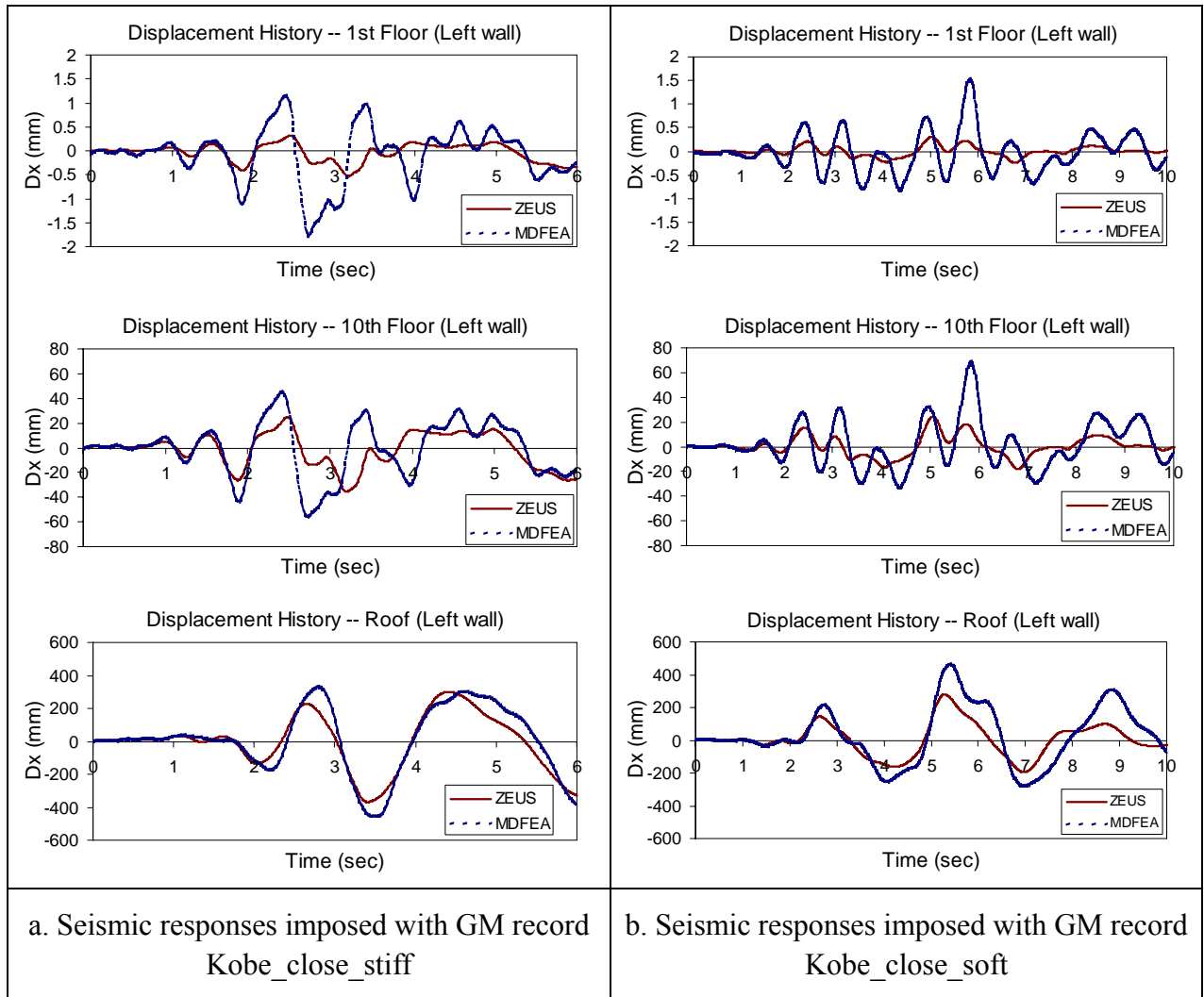


Figure 4.17 Sample Displacement Histories and Comparisons between MDFEA and ZEUS-NL Approaches

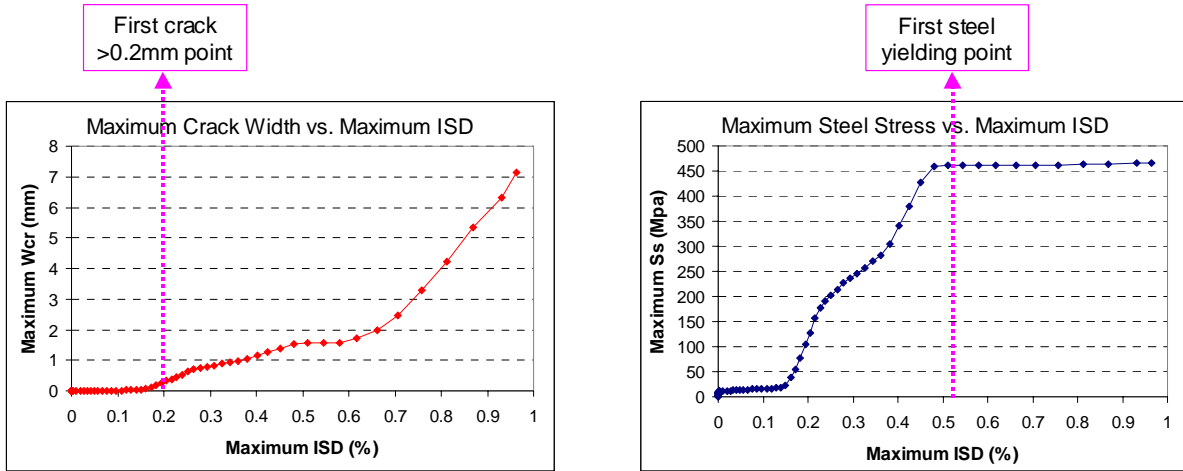
The results presented in Figure 13 illustrate that the drift computed from MDFEA at the lower levels is much larger than that from ZEUS-NL pure frame model, while the roof drifts from the two models are relatively close.

The comparisons presented above illustrate that pure-frame analyses neglect important and critical features of the response of the 54-story high-rise building. The MDFEA procedure can account for response limit states including shear-flexure-axial interaction and can serve as the

platform for derivation of limit states from pushover analysis. However due to the long runtime (around 3 hours per 1000 time steps) demanded by the huge amount of data transfer and coordination in MDFEA using UI-SIMCOR, it is not realistic to apply MDFEA for hundreds of direct simulations for fragility derivations.

4.2.4 New Damage Measure and Limit States

With the use of a MDFEA framework, it becomes feasible to accurately and efficiently predict the static and dynamic response of complex structures. This framework will help researchers tackle important problems, such as developing performance limit states definitions for seismic risk analysis and to make fragility assessments. For RC structures, all the information available from MDFEA, including concrete stress and strain distributions, steel stresses and crack patterns throughout the structural walls, are available for assessing a structures performance. For example, it is now possible to define new limit states for serviceability that consider the state of cracking in the core wall or new limit states for damage control that more accurately consider the yielding of the longitudinal reinforcement. Based on previous pushover analyses, maximum concrete crack width and steel stress can be correlated to global deformation measures including inter-storey drift ratio (ISD) during the loading history, as shown in Figure 4.18.



a. Limit State 1 – Serviceability by Considerable Cracking ($W_{cr} > 0.2\text{mm}$)

b. Limit State 2 – Damage Control by Wall Rebar Yielding ($f_y \geq 460\text{ MPa}$)

Figure 4.18 Quantitative Definitions for Limit States 1 and 2 Using MDFEA Results

For high-rise buildings, it is insufficient to use traditional definitions of ISD for damage measure of the structural performances. The reason is due to the nature of two major sources contributing to the ISD: (1) lateral translations by shear and flexural deformation; and (2) translations from rigid body motion (RBM) due to lower storey rotation. The first one relates structural deformations to member stress and strain resultants, while the latter one does not contribute to structural demand. Figure 4.19 presents the relationship between the right wall shear and inter-storey drift, pure translation component, lower storey rotation, and the ratio of the rotation effect to overall drift. As shown, the total inter-storey drift at level 10 increases to 33 mm while that at the 1st level is only 3.3 mm. The ratio of ISD by lower storey rotation to total ISD rises up from 0.0 at the 1st storey, to 0.68 at the 2nd storey, to 0.97 at the 10th storey. The drift from pure translations at 10th storey is only about 1.5 mm. This illustrates that for high-rise buildings the traditional measure of total ISD cannot be directly related to structural performance.

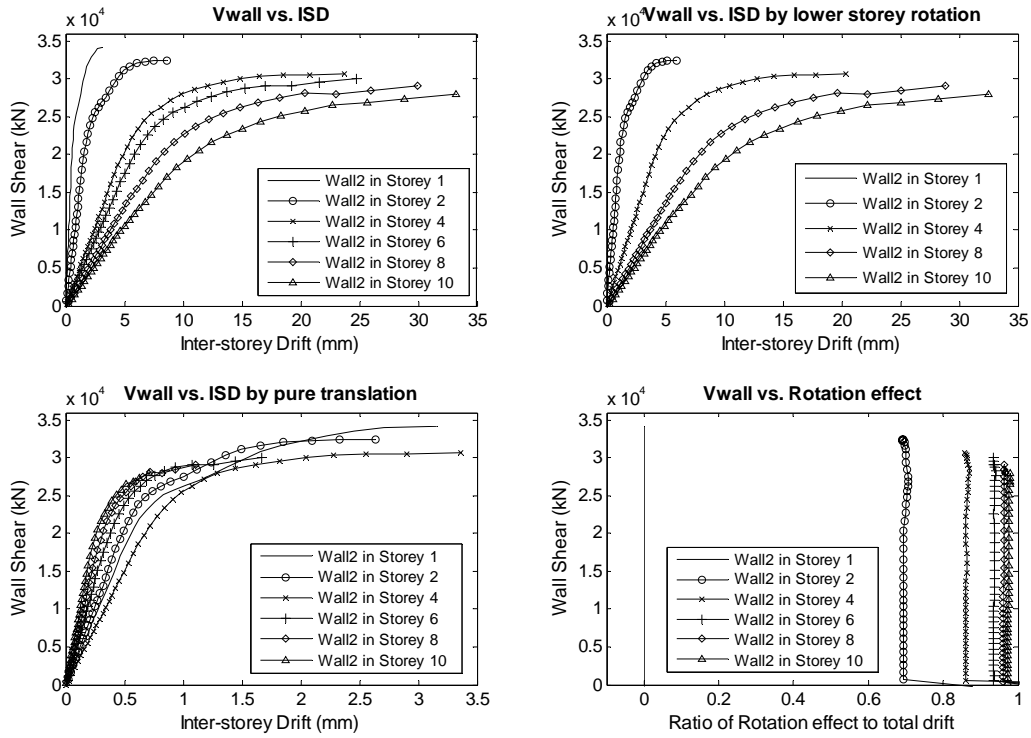


Figure 4.19 Wall Shear versus Inter-storey Drift (ISD) and Drift Components Evaluation

In this study a new measure called inter-storey pure translation ratio (ISPT) is proposed by removing the RBM due to lower storey rotation. ISPT is computed from post-processed member (mainly wall) deformation data as shown in Figure 4.20 and Equation 4.14.

$$ISPT = \frac{1}{H_i} \left[\frac{(dx_i - H_i \sin \theta_1)}{\cos \theta_1} + [dy_i - H_i(1 - \cos \theta_1) - (dx_i - H_i \sin \theta_1) \tan \theta_1] \sin \theta_1 \right] \quad (4.14)$$

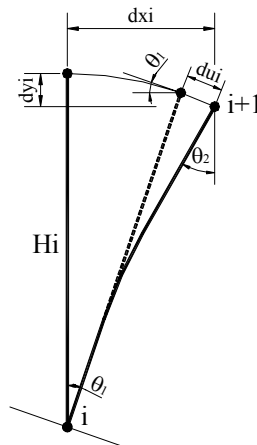


Figure 4.20 Inter-storey Member Deformation Geometry

ISPT counts all deformations due to storey loads and can be corresponded to real local behavior such as concrete cracking, rebar yielding and concrete crushing very easily. On the other hand, total ISD can be related to the influences other than pure structural behavior, e.g., non-structural damages due to overall drift and displacement differences, resident comfortable level under movements, etc. It is also necessary for the literature to have the criteria in maximum ISD due to its common use by other researchers and easy interpretation for comparisons between high-rise and other building structures. Therefore, total ISD needs to remain an important criterion and both ISD_{max} and $ISPT_{max}$ are adopted as the quantitative damage index in this study, and the final limit state criteria are shown in Table 4.10.

Table 4.10 Limit State Criteria for Reference Building Structure

Level	Limit State	ISD_{max} (%)	$ISPT_{max}$ (%)
Limit State 1 (LS1)	Serviceability	0.20	0.035
Limit State 2 (LS2)	Damage Control	0.52	0.147
Limit State 3 (LS3)	Collapse Prevention	1.10	0.265

5. Uncertainty Modeling

5.1 Literature Survey

5.1.1 Overview

A critical and challenging aspect for deriving meaningful fragility relationships is to properly account for uncertainty in seismic actions and the response of the system to these actions. The many sources significantly impact the ensuing technical, economic and social decisions. According to Wen et al. (2003), major uncertainties may be classified into two categories: (1). Inherent randomness at the scale of understanding or customary resolution in engineering or scientific analysis. This randomness is called Aleatory Uncertainty and examples of this are magnitude of earthquake occurred at a known fault; Young's modulus of steel; compression strength of concrete. (2) Errors arising from a lack of knowledge or coarse modeling, and dependent on the model selected; this referred to as Epistemic Uncertainty. Both sources of uncertainty are equally important and must be considered in decision-making.

Probabilistic seismic hazard analysis methodologies have been proposed and developed since 1976 (Algermissen and Perkins (1976)) and are becoming more commonly considered by researchers, building code officials, and design engineers. As an example, the recently completed SAC project addressed uncertainties in ground motion intensity and structural response on the capacity of steel special moment frames. Wen et al. (2003) performed a complete literature review and proposed a systematic framework on uncertainty modeling in earthquake engineering, including the aleatory and epistemic uncertainty models that considered system demand and

capacity.

For a structural system, the demand can be the force (shear, bending moment, axial forces, overturning moment) or the response (displacement, velocity, acceleration, drift, ductility, energy dissipation) in the system caused by ground motion. The capacity of the system is the maximum force or displacement that the system can withstand without member or system failure of a defined level. The definitions of failure and performance limit state are described in Chapter 4.

It is common to use the maximum response or force over a given time period as the demand and this has a strong correlation to the seismic excitation. The capacity is primarily a property of the system. According to Wen et al. (2003), uncertainty in the demand and capacity can be traced back to the sources as shown in Figure 5.1.

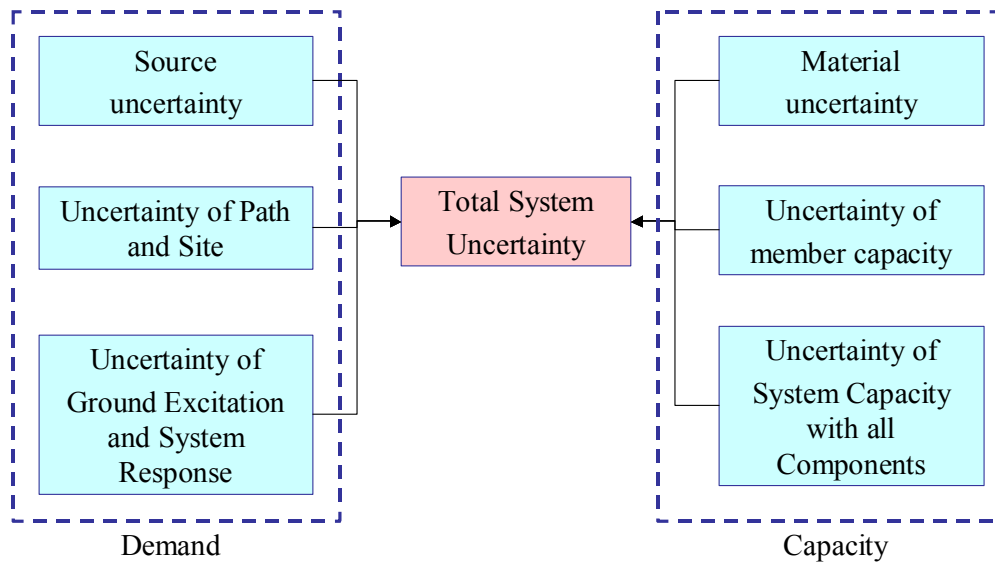


Figure 5.1 Uncertainty Sources for System Demand and Capacity

To fragility of a structure may be defined as the conditional failure probability $P(LS|SA=a)$ for a given certain intensity measure (IM) at building site. Consequently, uncertainties of source, path and site should not be part of the factors included in fragility computation. This approach further

indicates that probabilistic seismic hazard analysis is not needed here. Instead, these uncertainties are accounted for by the selection of ground motions that reflect the uncertainties of site excitation caused by features of the earthquake mechanism and seismic wave propagation. On the capacity side, the basic random effects due to building structural type lie in the material properties and geometry features that need consider imperfect construction and the properties of delivered materials. Therefore, the system uncertainties defined in Figure 5.1 can be combined to be the major sources shown in Figure 5.2.

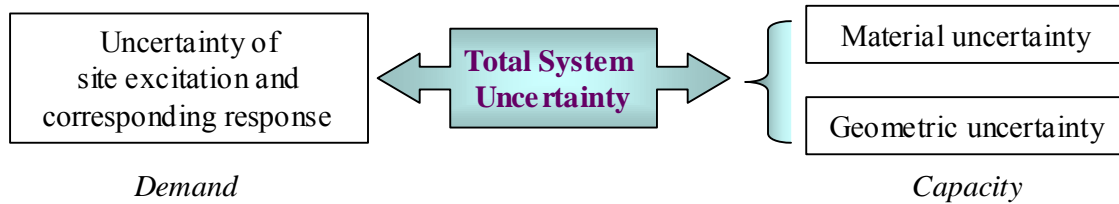


Figure 5.2 Significant Uncertainty Sources for System Demand and Capacity

5.1.2 Probabilistic Seismic Demand

Uncertainty in the structural response to seismic ground excitations presents a challenge when evaluating the probabilistic seismic demand. This is particularly true when evaluating the response of RC high-rise structures for which the material response can be highly inelastic and load path-dependent. It is common to use one of the following two approaches to determine the seismic demand.

□ Random Vibration Approach

In the random vibration approach, the ground motion is treated as a random process, and then the response of the structure to random vibrations is assessed. This method is limited for non-stationary random excitations like earthquake strikes. In addition, due to complex inelastic

RC structural behavior such as brittle cracking, it is difficult to derive analytical solutions using the random vibration approach.

□ **Nonlinear Dynamic Response History Analysis Approach**

A second, and more effective, approach is to conduct nonlinear response history analyses for selected ground motions. In order to cover an appropriately wide range of possible excitations, the selection of ground motions should consider intensity, frequency content, duration, and scaling. Using sets of nonlinear dynamic time history analyses, the probabilistic structural response demand can be obtained using sampling techniques. Alternatively, regression methods may be applied to establish functional relationships between intensity and variables such as global (roof) and local (inter-story) drifts as well as energy dissipation (cumulative damage). For the latter, the power-law expression proposed by Vamvatsikos and Cornell (2002) may be used through Incremental Dynamic Analysis (IDA). Once the functional relationship of interest has been determined, it is possible to estimate the mean and variation for a given IM value. This is typically described using a simulated normal or lognormal distribution.

5.1.3 Probabilistic System Capacity

Structural capacity is the maximum force, displacement, velocity, or acceleration that a member or a system can withstand without reaching a prescribed limit state. The capacity is therefore dependent on the material properties, member dimensions, system configuration, and methods used to describe the capacity. There are no explicit functions that directly relate these basic characteristics to the capacities of complex RC high-rise structures. Numerical simulation with non-linear FEA is the only viable option to evaluate the effects of random system characteristics.

5.2 Ground Motion Uncertainty

Another major source of uncertainty in determining seismic demand is ground excitation, which must consider the combination of source mechanisms, path attenuation, and site effects. These parameters are summarized below.

- Source: Random mechanisms control frequency contents and inherent energy;
- Path: Different wave propagation paths introduce different attenuation effects; and
- Site: Soil conditions may mitigate or amplify the response.

To account for the complex characteristics of RC high-rise structures, it is necessary to include a wide range of frequency and seismic energy levels in the selection of ground motions.

5.2.1 Three Categories of Natural Record Selection

Specific features of the frequency content, such as the ratio of acceleration-to-velocity (a/v ; Zhu et al., 1988) and spectral acceleration (S_a) at key frequency levels, should be considered in relation to the natural periods of the structure when selecting ground motion records. It is often difficult, however, to select the most appropriate records for high-rise buildings because the response frequency range is much wider than for shorter buildings.

In this research, natural strong motion records were selected based on magnitude of events (M), distance to source (D), and site soil condition (S). The ground excitations induced by earthquakes with large magnitudes typically have long effective durations and many significant peaks. These two characteristics usually dominate the dynamic structural behavior, especially during inelastic stages accompanied by stiffness degradation. Distance to source generally influences the site

ground motion through path attenuation and by filtering high-frequency fractions during wave propagations. The specific site soil layers either dissipate or amplify the seismic wave while it travels from bedrock to ground, which affects the dynamic responses of high-rise buildings that are sensitive to wide frequency ranges. For example, ground excitations at soft soil sites will amplify displacement demands for structures with longer structural periods, especially in the first and second vibration modes. These demands are significant for the highly inelastic portion of the response in which the natural vibration periods elongate. Based on the concepts presented above, the selected natural records were categorized into three combinations of representative [M, D, S]: 1) Close to source and large magnitude; 2) Close to source and small magnitude; 3) Far from source and large magnitude.

For each category, 10 natural strong motion records were selected to cover a sufficient range of the natural characteristics mentioned previously. The details for these selections are presented in Table 5.1. Among these, the largest earthquakes (magnitude larger than 6.5) are selected from the U.S. and Asia, and include the Northridge, Chi-Chi, and Kocaeli Earthquakes. Most of the smaller events (magnitude less than 6.5) are taken from the U.S. and Europe. By employing a number of records that represent the various magnitudes, distances, and site conditions, this study account for ground motion uncertainty.

Table 5.1 Selected Natural Ground Motion Records

Category	Earthquake	M	Station (Data Source)	Distance to source (km)	Site Soil	PGA (g)
I. Close and Large	Chi-Chi, Taiwan 1999/09/20	7.6	CHY028-N, (CWB)	7.31	Stiff	0.821
		7.6	TCU110-N, (CWB)	12.56	Soft	0.18
	Kocaeli, Turkey 1999/08/17	7.4	SKR090, Sakarya (ERD)	3.1	Stiff	0.376
		7.4	YPT330, Yarimca	2.6	Soft	0.349
	Loma Prieta, USA 1989/10/18	6.9	CLS000 57007, (CDMG)	5.1	Stiff	0.644
	Kobe, Japan, 1/16/1995	6.9	TAZ090 Takarazuka, (CUE)	1.2	Soft	0.694
		6.9	SHI000, Shin-Osaka, (CUE)	15.5	Soft	0.243
	Northridge, 1/17/1994 12:31	6.7	NEWHALL, 360 (CDMG STATION 24279)	7.1	Soft	0.59
		6.7	TARZANA, (CDMG STATION 24436)	17.5	Stiff	1.779
	Imperial Valley 1979/10/15	6.5	5054 Bonds Corner, H-BCR230	2.5	Soft	0.775
II. Close and Small	Anza (Horse Canyon) 1980/02/25	4.9	5044 Anza, Pinyon Flat (USGS)	12	Stiff	0.131
		4.9	5047 Rancho De Anza (USGS)	20.6	Soft	0.097
	Coalinga 1983/05/09	5.0	1607 Anticline Ridge Free-field (USGS)	12.6	Stiff	0.673
		5.0	46T04 CHP, (temp) (CDMG)	16.7	Soft	0.145
	Ancona, Italy, 6/14/1972	4.7	Ancona-Rocca, N-S, waveform 29	10	Soft	0.5354
	Ionian, Greece, 11/4/1973	5.3	Lefkada-OTE Building, N-S, waveform 42	15	Soft	0.5248
	Aftershock of Friuli earthquake, Italy, 9/11/1976 4:35:03 PM	5.7	Buia, N-S, waveform 122	10	Soft	0.2305
	Alkion, Greece, 2/25/1981	6.1	Korinthos-OTE Building, E-W, waveform 335	25	Soft	0.1199
	Dinar, Turkey, 10/1/1995	6.0	Dinar-Meteoroloji Mudurlugu, W-E, waveform 879	1	Soft	0.3193
	Umbro-Marchigiano, Italy, 9/26/1997 12:33:16 AM	5.6	Colfioito, N-S, waveform 591	3	Stiff	0.3245
III. Distant and Large	Chi-Chi, Taiwan 1999/09/20	7.6	CHY015-N, (CWB)	43.51	Soft	0.157
		7.6	CHY032-W, (CWB)	39.34	Soft	0.088
		7.6	HWA022-W, (CWB)	71.45	Stiff	0.123
	Kocaeli, Turkey 1999/08/17	7.4	CNA000, Cekmece, (KOERI)	76.1	Stiff	0.179
		7.4	ATS000, Ambarli, (KOERI)	78.9	Soft	0.249
	Loma Prieta, USA 1989/10/18	6.9	SFO090 58223, SF Intern. Airport, (CDMG)	64.4	Soft	0.329
		6.9	NAS180, ALAMEDA NAS HANGAR 23, (BYU)	75.2	Soft	0.268
	Kobe, Japan, 1/16/1995	6.9	OKA000, (CUE)	89.3	Stiff	0.081
		6.9	KAK090 Kakogawa, (CUE)	26.4	Soft	0.345
	Northridge, 1/17/1994 12:31	6.7	90086 Buena Park, BPK090 (USC)	64.6	Soft	0.139

5.2.2 Natural Ground Motions Applicability Evaluation

The 30 selected ground motion records were corrected and filtered from natural raw data. Even though the selections account for basic features of earthquake strikes, their frequency contents are investigated to ensure the frequency range is sufficiently wide to affect high-rise building seismic behavior. The evaluations are performed using both response spectra and power spectra for energy distribution over the frequency domain.

□ Source Data Correction and Filtering

Raw ground motion data from stations is not often used. Instead, the strong motion data is processed in order to: (1) correct data by eliminating the effects of a moving recording instrument, and (2) reduce random noise in the recorded signals. Due to technological developments, most recent records are measured by digital instruments. Many old accelerograms, such as some Category II records for earthquakes in the 1970's and 80's, are analog records that must be digitized before processing. The basic processing steps for an acceleration time series obtained by digitizing analog records or from digital instruments are:

- Baseline removal;
- Conditioning and padding the ends of the accelerograms;
- Acausal band pass filtering of the acceleration;
- Integration of corrected acceleration without decimation to velocity and displacement,
and
- Response spectra computation.

Among the 30 ground motion records, 20 from Categories I and III are from U.S. sources, such as the Pacific Earthquake Engineering Research Center (PEER) strong motion database. The remaining records are from the European Strong Motion Database (by Ambraseys et al. (2004)).

PEER's processing concentrates on extending the high and low frequency ranges of the usable signals within the records on an individual component basis. More recent data, especially from digital recorders, generally do not require additional processing and are deposited into the database after review. It is apparent that there is diversity in the data processing and filtering due to the different record instruments, data formats, processing institutes, and techniques. The records from the European database contain strong motion records at permanent, ground level recording stations located in Europe and the Mediterranean region. All uncorrected records have been pre-processed to account for irregularities such as spurious large amplitudes or very high frequency acceleration points, non-zero sloping or translated baselines, poor quality digitization, zero or negative time steps, and duplicate records. The pre-processed records have been subjected to a uniform correction procedure to reduce the low and high frequency noise levels. Eighth-order elliptical bandpass filtering is applied in the procedure using a frequency range between 0.25 Hz and 25Hz. Table 5.2 shows the effective period ranges $[T_L, T_U]$ for the 30 ground motion records. The record names correspond to Table 5.1 and follow the same order.

Table 5.2 Filtering Period Ranges of Selected Ground Motion Records

Category	Named Record	Filter T _L (s)	Filter T _U (s)
I. Close and Large	Chi-Chi_close_stiff	0.020	10.00
	Chi-Chi_close_soft	0.020	25.00
	Kocaeli_close_stiff	0.025	25.00
	Kocaeli_close_soft	0.020	14.29
	Loma_close	0.025	5.00
	Kobe_close_stiff	0.030	7.69
	Kobe_close_soft	0.043	10.00
	Northridge_close_soft	0.043	8.33
	Northridge_close_stiff	0.043	10.00
	Imperial_close_soft	0.025	10.00
II. Close and Small	Anza_1	0.040	5.00
	Anza_2	0.025	3.33
	Coalinga_1	0.025	3.33
	Coalinga_2	0.040	3.33
	Ancona_wave29_X	0.040	4.00
	Ionian_wave42_X	0.040	4.00
	Aftershock_Friuli_wave122_X	0.040	4.00
	Alkion_wave335_Y	0.040	4.00
	Dinar_wave879_Y	0.040	4.00
	Umbro-Marchigiano_wave591_X	0.040	4.00
III. Distant and Large	Chi-Chi_dist_soft_1	0.025	33.33
	Chi-Chi_dist_soft_2	0.020	33.33
	Chi-Chi_dist_stiff	0.033	50.00
	Kocaeli_dist_stiff	0.020	50.00
	Kocaeli_dist_soft	0.020	33.33
	Loma_dist_soft_1	0.033	5.00
	Loma_dist_soft_2	null	10.00
	Kobe_dist_stiff	null	20.00
	Kobe_dist_soft	null	10.00
	Northridge_dist_soft	0.033	4.00

Based on the analysis in Chapter 3, it can be seen that the equivalent tri-linear models show clear stiffness degradation in the inelastic range, and stiffness usually decreases to approximately 1/5 or 1/6 of the first stage stiffness. It follows that a structure's natural periods elongate by a factor

of approximately 2.2 to 2.5 after yielding. After examining the selected ground motion records, the following observations can be made:

- Categories I and III have a good frequency content distribution. Only ground motions one and two do not satisfy the maximum inelastic period limit. Both categories are applicable to the fragility assessment of all limit states for the reference structure.
- Category II exhibits generally low upper bounds for periods. This means the highly inelastic responses of the reference building structure will be underestimated in some cases. For this reason, the modeling of collapse prevention may not be as accurate as for categories I and III.

□ **Random Effects on Spectral Acceleration**

The 30 selected ground motion records consist of wide ranges of three basic features: magnitude (M), distance to source (D), and site condition (S). For further understanding of the effects of uncertainty on the demand, it is necessary to evaluate the influences of these basic features of ground motion records.

The basic dynamic natures of the ground motions are analyzed to provide the basis for further comparisons of seismic demands. Figure 5.3 shows the elastic spectral acceleration diagrams corresponding to the reference structure's first four fundamental modes.

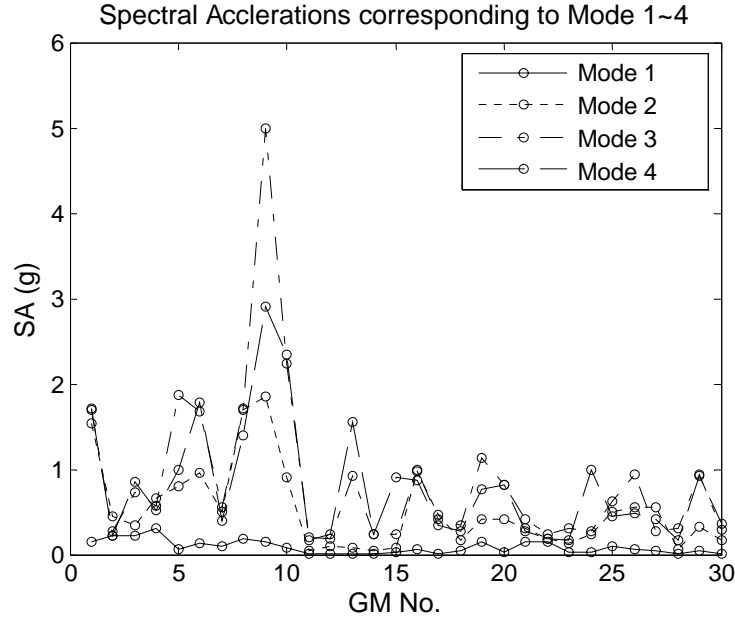


Figure 5.3 Selected GM Spectral Accelerations at First Four Modes of Reference Structure

In Figure 5.4, the Modal Significance Factor (MSF) is shown for all the ground motions. The MSF is defined in Equation 5.1 and is used to evaluate the influence of the frequency contents from different GMs.

$$\text{Modal Significance Factor: } MSF_{ij} = \frac{(MPF)_i (SA)_{ij}}{\sum_{i=1}^4 [(MPF)_i (SA)_{ij}]} \quad (5.1)$$

where, i indicates the i^{th} mode, j is the j^{th} ground motion record, MPF is the Mass Participation Factor, and SA is the elastic spectral acceleration when the damping ratio is 5 percent. It can be observed that generally the sum of MSF for modes one and two ($T = 3.05, 0.82$ seconds) is larger than that of modes three and four ($T = 0.36, 0.23$ seconds) for the selected ground motions.

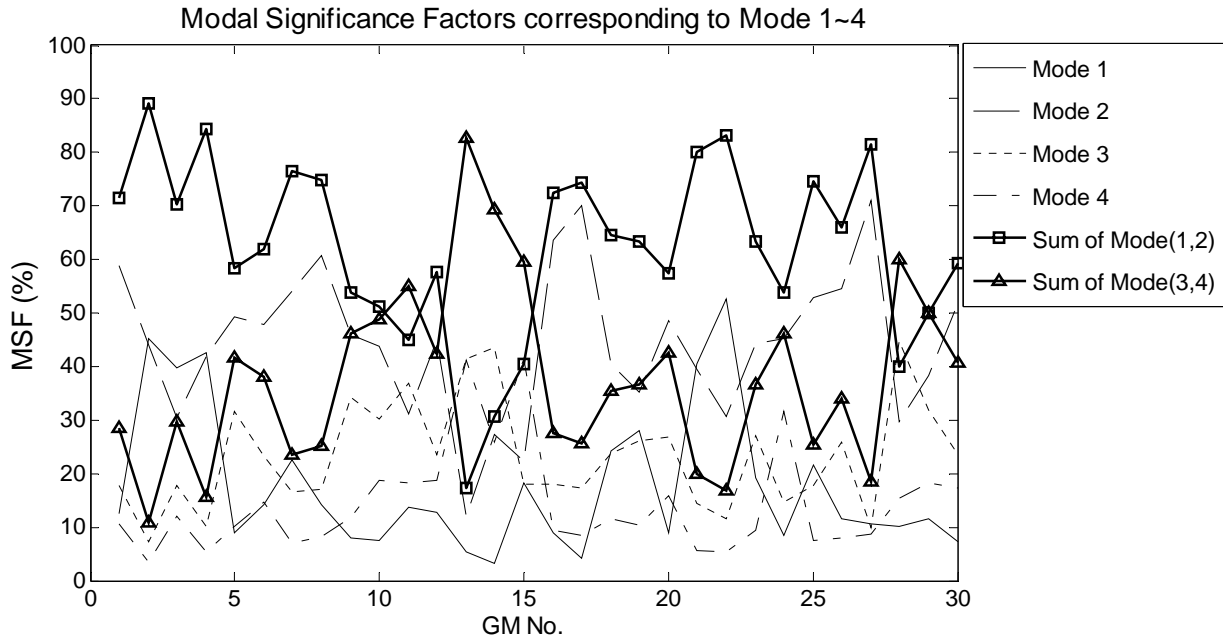


Figure 5.4 Modal Significance Factor (MSF) of Ground Motions

□ **Random Effects on Seismic Demand**

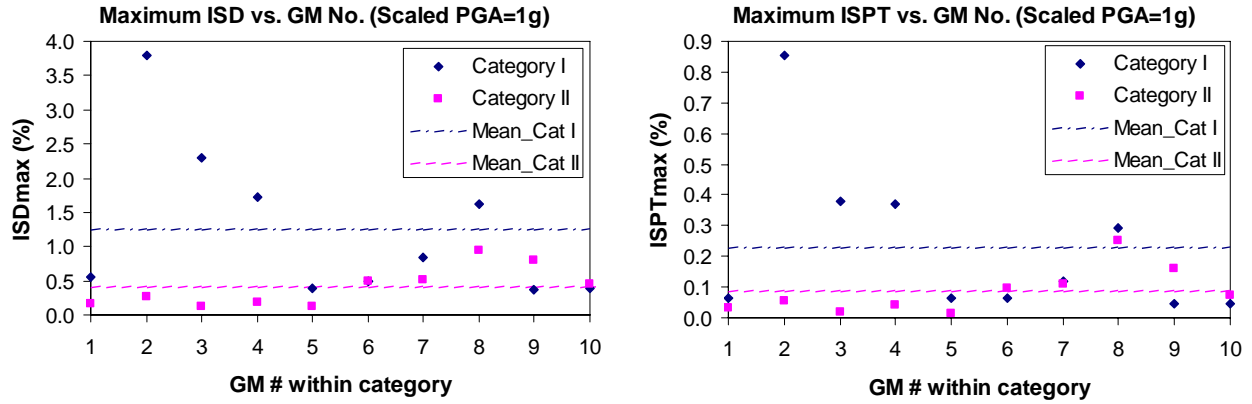
The comparisons between seismic demands for the selected GMs are performed considering all three features (M, D, S):

- Comparison I: Use GM categories I and II, which are close to the source, but the magnitudes are at different levels separated by $M = 6$;
- Comparison II: Use GM categories I and III, which are large earthquakes with $M > 6.5$, but the distances from the source are different; and
- Comparison III: The GM categories are divided into two groups, but a distinction is made between records with soft and stiff site soil conditions for the same earthquakes as listed in Table 5.3. Then the derived fragility relationships are compared.

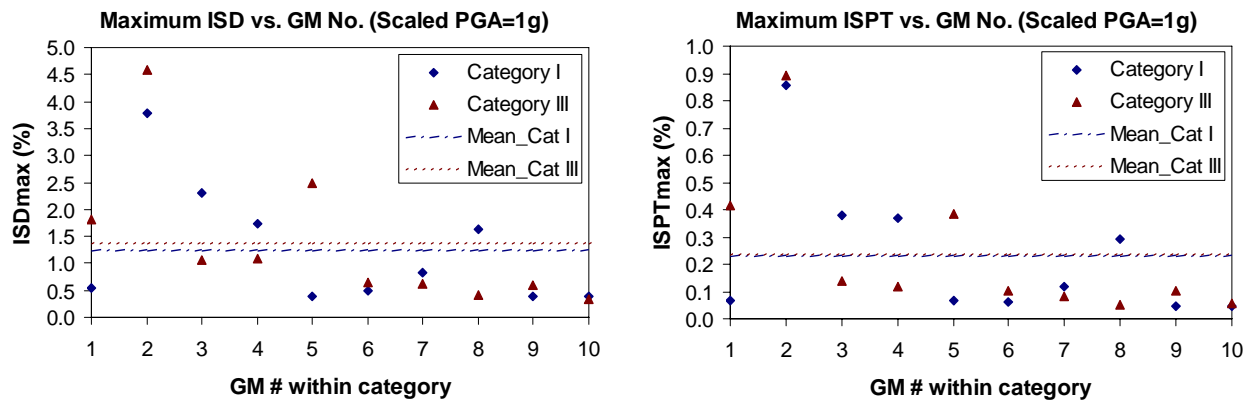
Table 5.3 Earthquakes and Corresponding Ground Motion Records for Comparison III

Case No.	Earthquake	M	D (km)	Station (Data Source)	Site Soil
1	Chi-Chi, Taiwan 1999/09/20	7.6	7.31	CHY028-N, (CWB)	Stiff
		7.6	12.56	TCU110-N, (CWB)	Soft
2	Kocaeli, Turkey 1999/08/17	7.4	3.1	SKR090, Sakarya (ERD)	Stiff
		7.4	2.6	YPT330, Yarimca	Soft
3	Northridge, 1/17/1994 12:31	6.7	7.1	NEWHALL, 360 (CDMG STATION 24279)	Soft
		6.7	17.5	TARZANA-CEDAR HILL, (CDMG STATION 24436)	Stiff
4	Anza (Horse Cany) 1980/02/25	4.9	12	5044 Anza, Pinyon Flat (USGS)	Stiff
		4.9	20.6	5047 Rancho De Anza (USGS)	Soft
5	Coalinga 1983/05/09	5.0	12.6	1607 Anticline Ridge Free-field (USGS)	Stiff
		5.0	16.7	46T04 CHP, (temp) (CDMG)	Soft
6	Chi-Chi, Taiwan 1999/09/20	7.6	43.51	CHY015-N, (CWB)	Soft
		7.6	71.45	HWA022-W, (CWB)	Stiff
7	Kocaeli, Turkey 1999/08/17	7.4	76.1	CNA000, Cekmece, (KOERI)	Stiff
		7.4	78.9	ATS000, Ambarli, (KOERI)	Soft
8	Kobe, Japan, 1/16/1995	6.9	89.3	OKA000, (CUE)	Stiff
		6.9	26.4	KAK090 Kakogawa, (CUE)	Soft

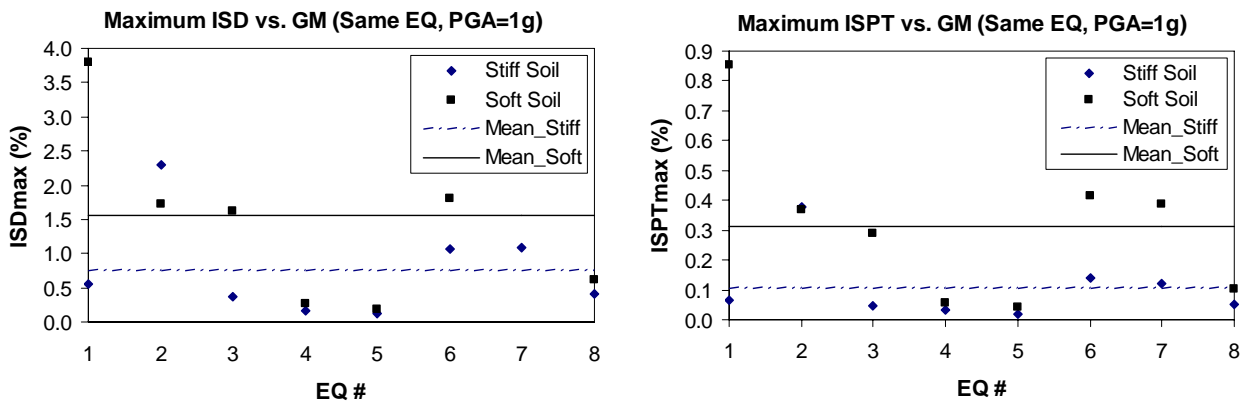
Figure 5.5 shows the variations in the extreme seismic demand (all GMs scaled to PGA=1.0g), including maximum inter-story drift ratio (ISD) and inter-story pure translation ratio (ISPT), caused by different ground motion features.



(a). ISD_{max} and $ISPT_{max}$ within Comparison I



(b). ISD_{max} and $ISPT_{max}$ within Comparison II



(c). ISD_{max} and $ISPT_{max}$ within Comparison III

Figure 5.5 Effects of Ground Motion Features on Maximum Seismic Demand

As expected, Comparison I demonstrates that large earthquakes cause large seismic demands.

ISD_{max} values for large magnitude earthquakes are greater than for small magnitude earthquakes

even at the same PGA level. This is because the ground excitations induced by large-magnitude earthquakes usually have much longer effective durations and more significant peaks. These two characteristics usually dominate the dynamic behavior of the structure, especially when accompanied by stiffness degradation during the inelastic stages.

Comparison II exhibits only a small variation in seismic demand due to the different distances from the source. The selected large magnitude earthquakes in the two categories are similar in source mechanisms and energy levels even when the traveling distance varies, leading to similar final structural responses under scaled ground excitations. The filtered high frequency fractions over long distances do not excite significant structural displacements for high-rise buildings with fundamental modes that have low frequency contents and when the corresponding mass participation factors are much larger than those from higher modes.

Comparison III illustrates the influence of specific site conditions on high-rise buildings. Site soil layers have filtering, dissipation, or amplification effects on the seismic waves traveling from bedrock to ground. Frequency content and peak distribution will thus be changed at specific sites, and the ground excitations will affect the dynamic responses of high-rise buildings accordingly. Generally ground excitations at soft soil sites will induce larger responses from a long period range, such as modes one and two, and become even more significant once inelasticity develops and the degraded stiffness elongates the natural vibration periods. This phenomenon is clearly demonstrated by Comparison III.

Figures 5.6 and 5.7 show the random effects on the maximum ISD and ISPT values from the selected ground motion records. Since both soft and stiff soil sites are taken into account when

selecting GMs, variations among maximum demand values are large even within the same GM category. In addition, the different frequency contents and peak numbers contribute to the seismic demands for high-rise buildings.

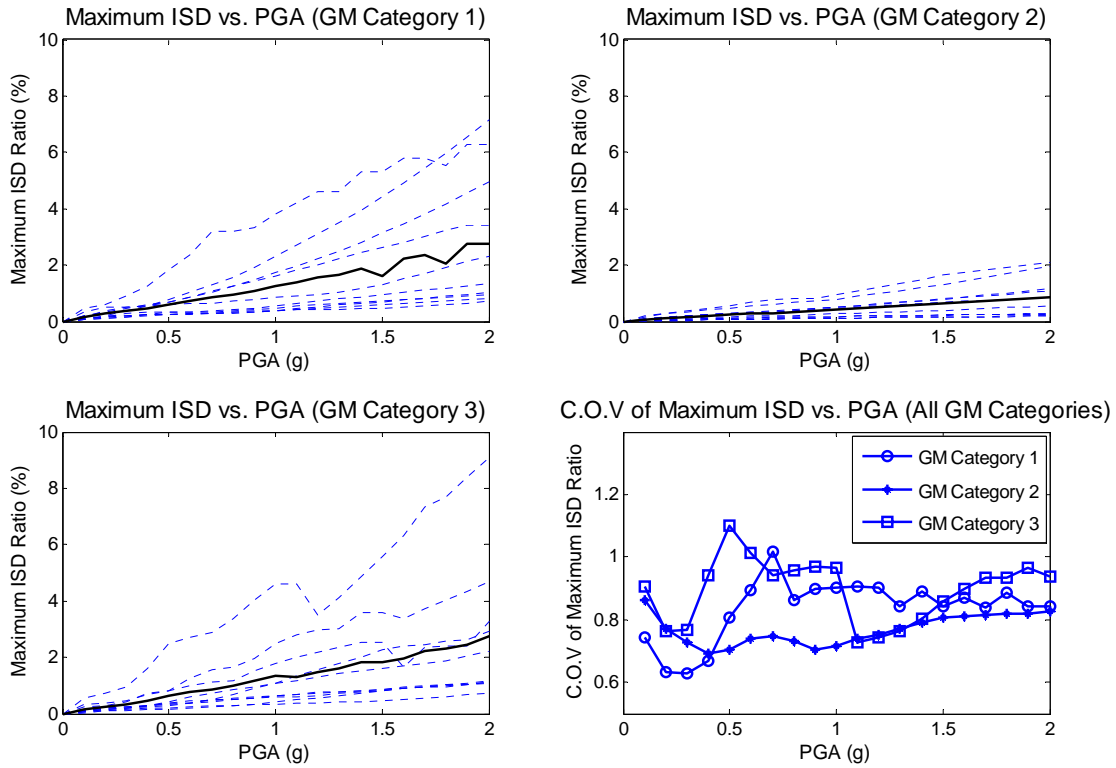


Figure 5.6 ISD_{max} Result, Mean, and C.O.V. Values for Selected GM Categories (Continuous Lines in ISD_{max} vs. PGA Plots Are Mean Values, Dashed Lines Are Individual GMs)

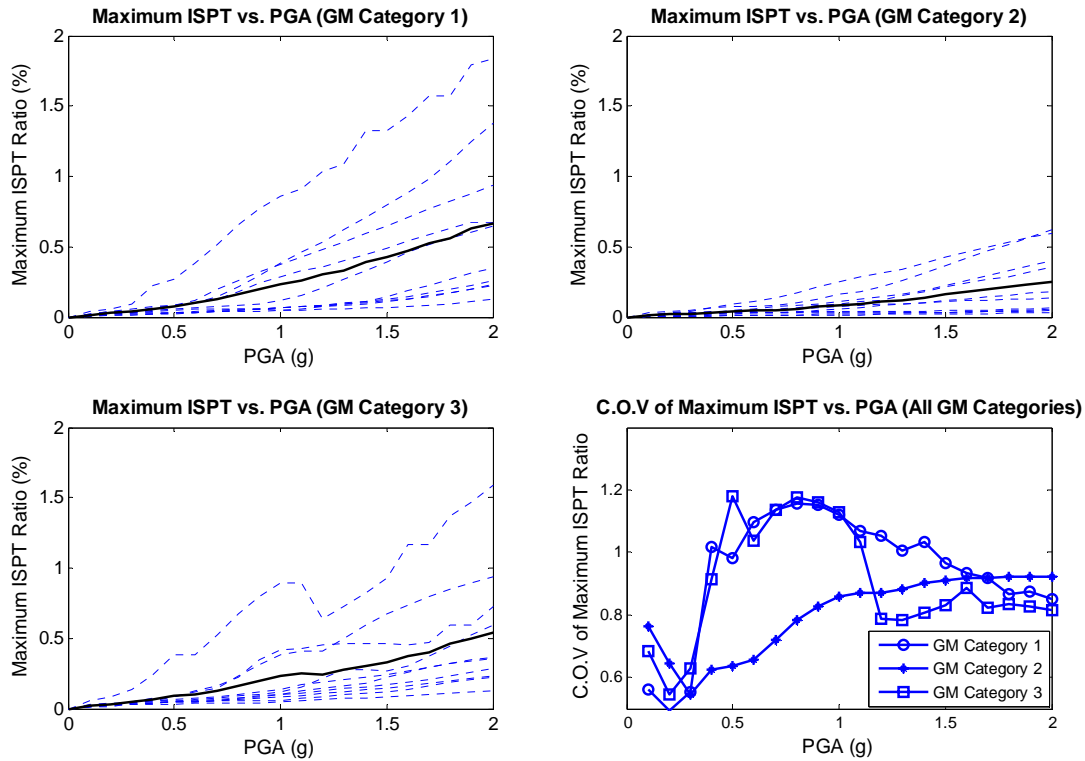


Figure 5.7 $ISPT_{max}$ Result, Mean, and C.O.V. Values for Selected GM Categories (Continuous Lines in $ISPT_{max}$ vs. PGA Plots Are Mean Values, Dashed Lines Are Individual GMs)

An important observation is that the ground motion sets significantly influence the seismic demand of high-rise buildings, and hence greatly affect the fragility relationship assessment.

□ Random Effects on Fourier and Power Spectra

To gain further insight into the frequency contents and energy distributions, Fourier amplitudes and power spectra densities were computed for all selected natural ground motion records over the frequency domain. They are normalized and plotted separately for each GM category in Figures 5.8 through 5.10. The most influential period range is related to the reference structure's elastic and inelastic natural modal periods, and in this case the range between 0.1 and 10 seconds is of interest.

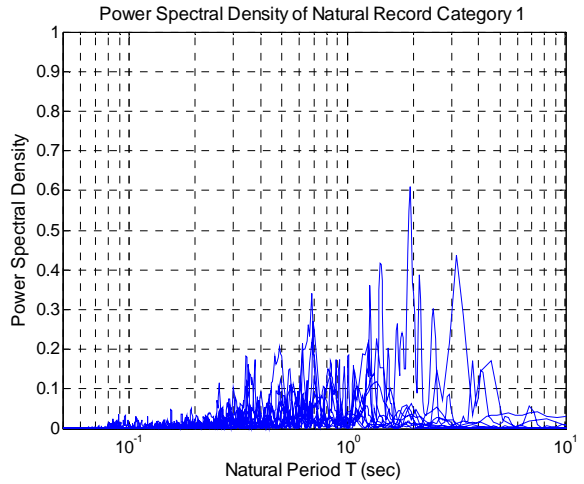
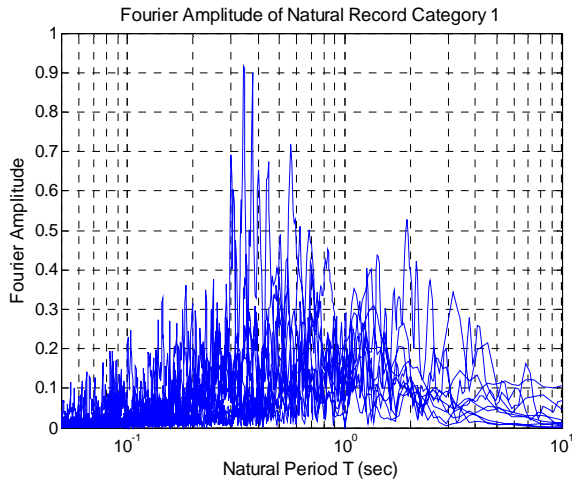


Figure 5.8 Fourier and Power Spectra of Category I

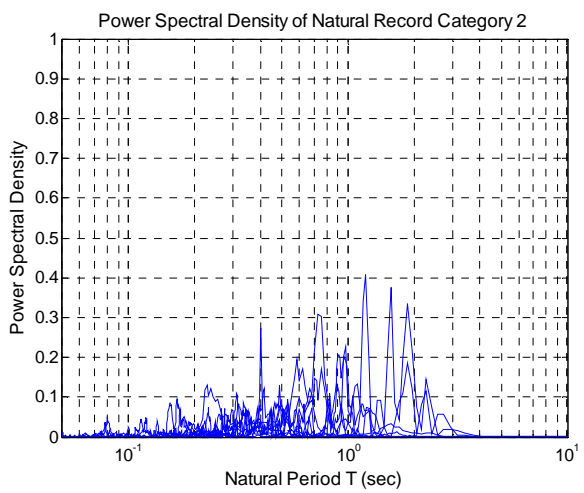
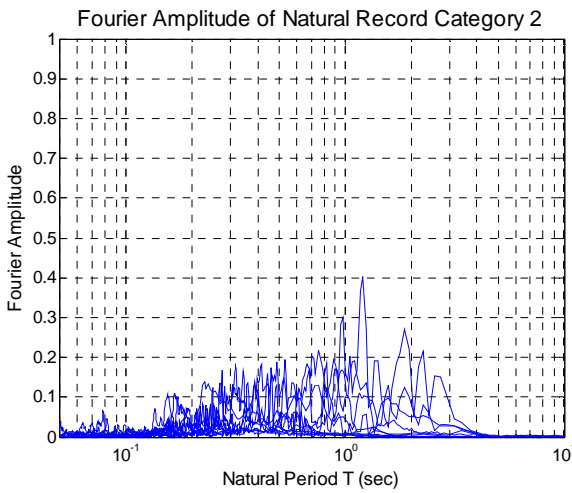


Figure 5.9 Fourier and Power Spectra of Category II

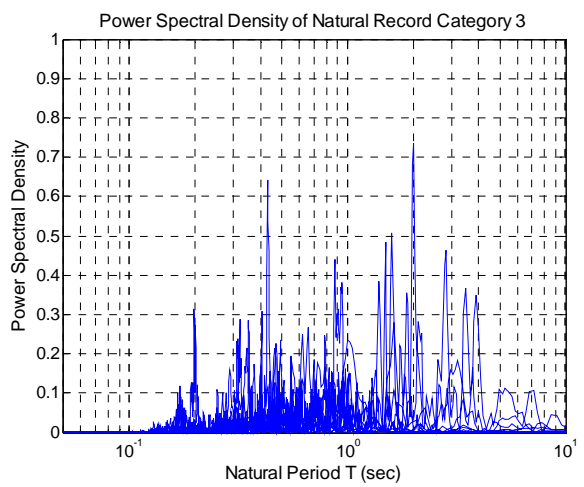
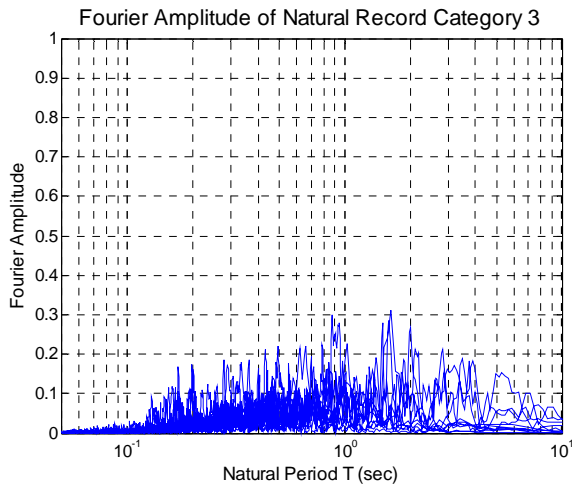


Figure 5.10 Fourier and Power Spectra of Category III

As expected, the Category I and III GMs exhibit significant energy distributions over a wide period range (0.2 to 5 seconds), while Category II primarily affects a shorter period range (up to 3 seconds). Hence for the reference structure with a fundamental period of 3 seconds and a second modal period of 0.8 seconds, the seismic demands within the elastic and inelastic ranges from Categories I and III should be larger than those from Category II.

5.2.3 Artificial Strong Motion Record Application

Natural data records are important as references for structures located in many regions, but the adoption of artificial strong motions is also necessary for this type of research. Reasons for this include:

- Not all natural records were originally recorded in digital format. The digitization of analog data can create artificial noise, and procedures to correct digital or digitized records must follow predefined standards and be restricted to preset filters, which to some extent shed inaccuracies and biases onto the final acceleration time histories;
- In this research, seismic risk analyses of high-rises are intended to apply to geographical regions worldwide rather than specific regions. The selected natural ground motion records have limitations because they are regional seismic hazards and may not accurately represent other areas. This can be the result of incomplete geological and geophysical coverage, different recurrence periods, individual source mechanisms, and specific path and site conditions, among other factors.

□ Artificial Strong Motion Records Generation

In order to broaden the range of fragility relationships of RC high-rises within the literature, sets of artificial accelerograms are used in this study in accordance with the seismic hazard research done by Sigbjornsson and Elnashai (2005) for Dubai, UAE. In their study, they focus on the structural responses of a large building population due to seismic hazards. The study includes modern high-rise buildings in the Dubai area. Simulations for artificial records were executed based on available geophysical and seismological information using a rigorous mechanical model to represent the source, path, and site effects. A simplified Fourier approach by Ólafsson et al. (2001) was conducted using a point source and Fourier spectrum to represent the source, path, and site. This model is known to give fair approximations for engineering purposes, especially if the source distance is large. The advantage of this approach is it keeps the same average statistical properties while generating many records, which is useful for inelastic structural analysis. The artificial records generated using this simulation technique are consistent with the uniform hazard spectrum designed for the major building population in the Dubai area. Such an approach results in acceleration records that are rich in a wide range of frequencies, which is important in this study.

The artificial records derived by Sigbjornsson and Elnashai (2005) were directly utilized as ground excitations, in addition to the 30 natural GMs, to develop fragilities. There are two sets of simulated records that primarily focus on magnitude and focal distances:

- BEQ Series – Large and distant scenario

Ten records were created through the simplified Fourier approach. These correlate with the

response spectra of large, distant earthquakes and exhibit a relatively low response for stiff structures, an increased response for long period structures, and the apparent intermediate period gap. All the synthetic records were simulated independently, and each one should be regarded as a sample of many possibilities. Figure 5.11 shows three sample records from this category.

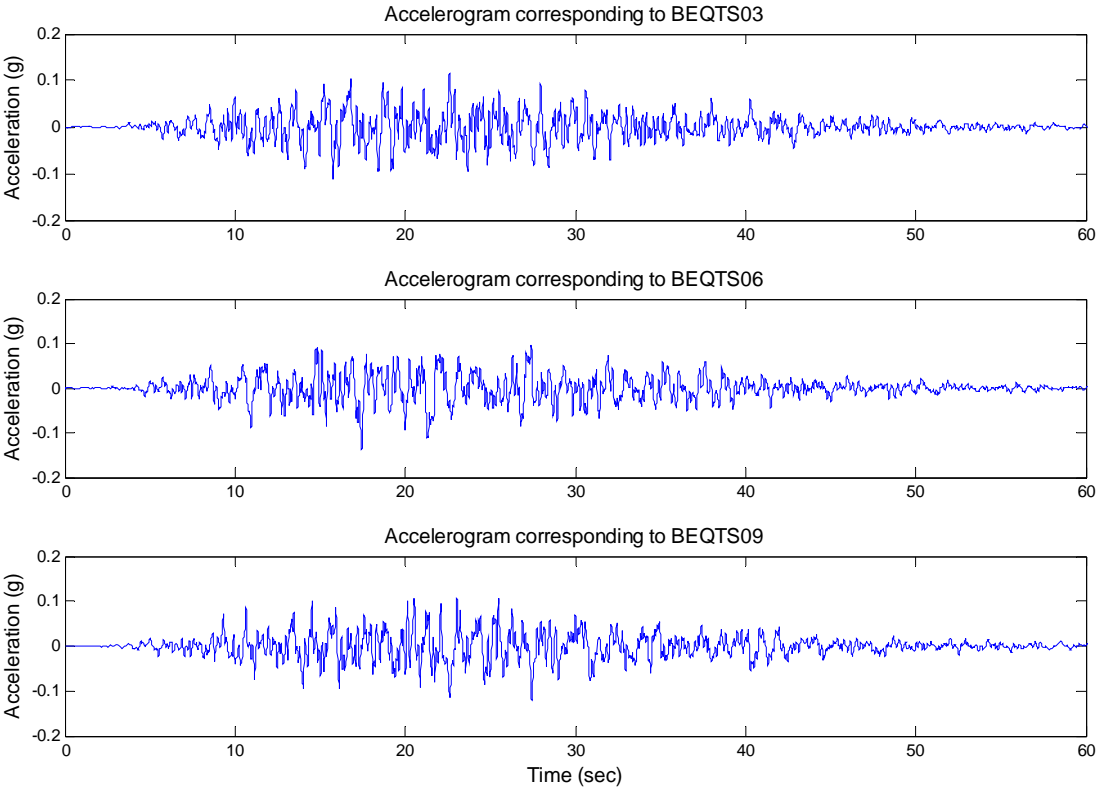


Figure 5.11 Three Artificial Accelerograms Samples from BEQ Series

- SEQ Series – Moderate and close scenario

Ten records were created through the simplified Fourier approach. These correlate with the response spectra of small, close earthquakes, which tend to excite the higher modes of high-rise building structures. As with the BEQ series, all the synthetic records are simulated independently.

Figure 5.12 shows three sample records from this category.

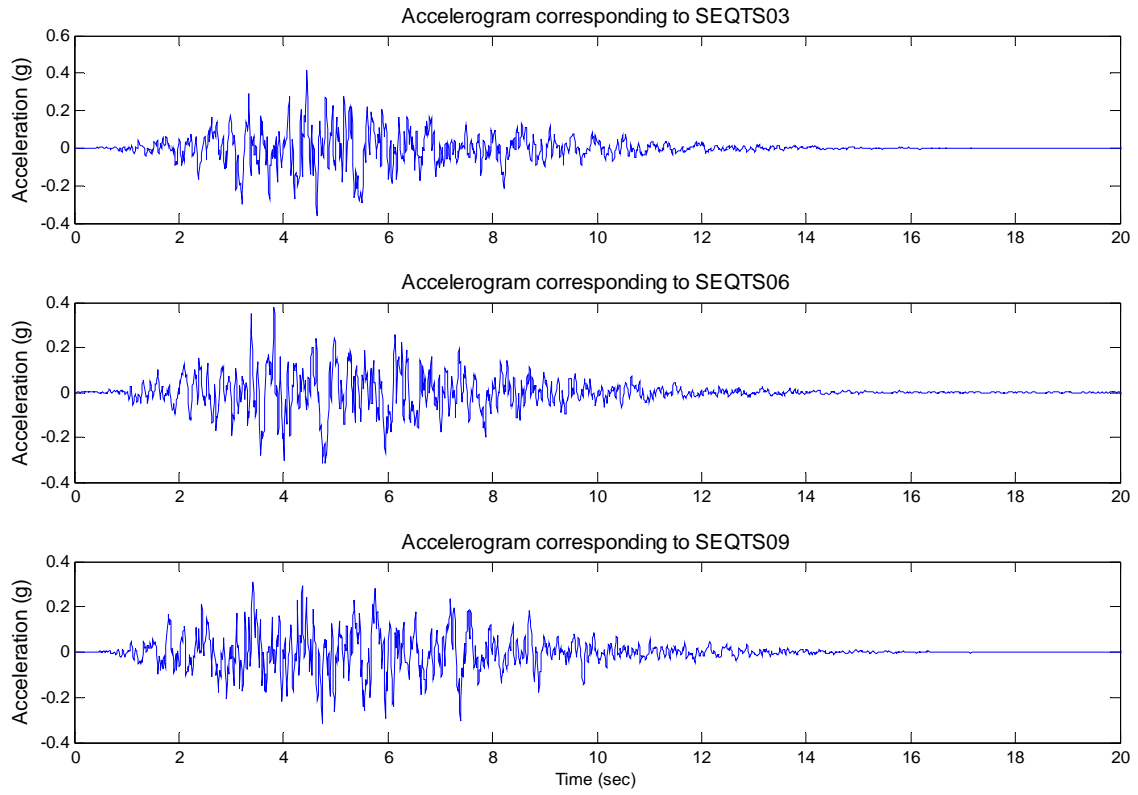


Figure 5.12 Three Artificial Accelerograms Samples from SEQ Series

The detail information of these two artificial record series is listed in Table 5.4.

Table 5.4 Artificial Strong Motion Record Details

Earthquake Scenario	M	D (km)	Record Name	PGA (g)
Distant and Large	7.4	100	BEQTS01	0.1246
			BEQTS02	0.1108
			BEQTS03	0.1150
			BEQTS04	0.1331
			BEQTS05	0.1475
			BEQTS06	0.1371
			BEQTS07	0.1392
			BEQTS08	0.1610
			BEQTS09	0.1207
			BEQTS010	0.1227
Close and Small	6.0	10	SEQTS01	0.3413
			SEQTS02	0.3398
			SEQTS03	0.4144
			SEQTS04	0.3609
			SEQTS05	0.3839
			SEQTS06	0.3784
			SEQTS07	0.4432
			SEQTS08	0.2707
			SEQTS09	0.3144
			SEQTS010	0.3398

□ **Random Effects on Fourier and Power Spectra**

Using the same concepts and methodologies, energy distribution is analyzed for the artificial ground motion records over frequency domain. They are also normalized and plotted separately for BEQ and SEQ series as following Figures 5.13 and 5.14, and the interested period range is again set here within [0.1, 10] seconds.

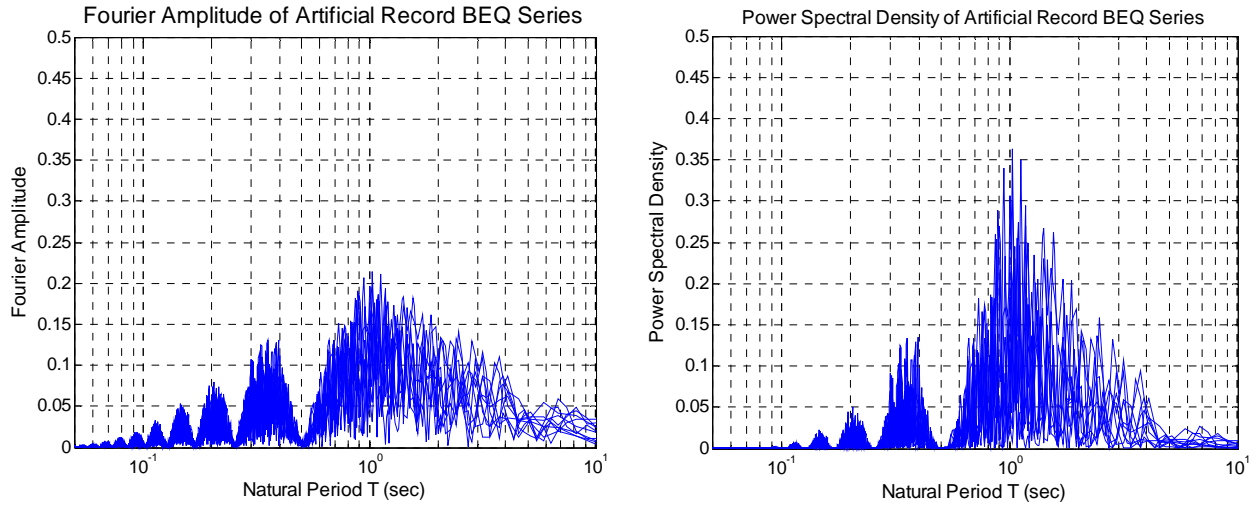


Figure 5.13 Fourier and Power Spectra of BEQ Series

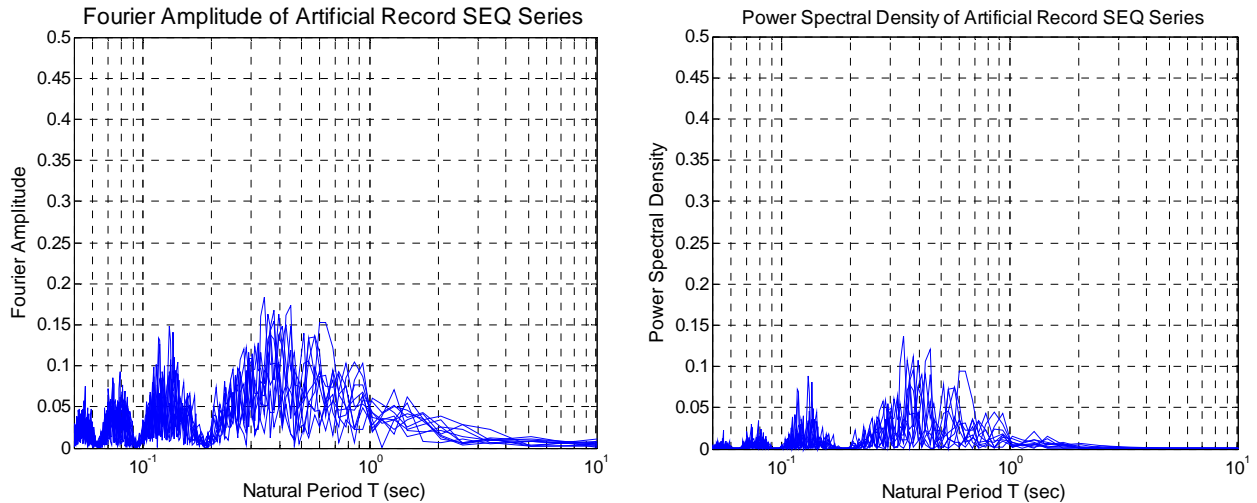


Figure 5.14 Fourier and Power Spectra of SEQ Series

It is clearly seen from Figure 5.13 and 5.14 that the frequency contents distributions of BEQ series records are wide in energy dominant region from 0.2 sec up to 5 sec which corresponds to elastic and inelastic fundamental periods, while SEQ series reasonably has major effects on shorter period upper bound at 2 sec but smaller lower bound at about 0.05 sec in correspondence to very high structural modes. Again it can be predicted that for high-rise buildings similar to the reference structure, the seismic demands induced by BEQ ground motion series should be larger

than those by SEQ series.

5.3 Material Uncertainty

One of the main sources of uncertainty for predicting the response a reinforced concrete structure is the inherent variability of material strengths. In this study, the compressive and tensile strengths of concrete, as well as steel yield strengths have been chosen as principal random variables.

5.3.1 Concrete Strength

The inherent randomness of concrete strength can be observed from test data. For convenience, normal or lognormal distributions are typically assumed. For RC high-rise buildings, concrete strength varies within a single structure due to large volume (especially for structural walls) and non-uniform construction conditions or techniques. The variation of strength throughout the structure for a given mean in-place strength depends on the number of members, number of batches, and type of construction.

The variability in concrete strength test data up to 1980 was made available by Ellingwood et al. (1982). Hueste et al. (2004) provided an update that includes properties for higher strength concretes and considered the compressive and tensile properties using normal distribution functions as shown in Tables 5.5 and 5.6.

Table 5.5 Coefficient of Variation for Concrete Compressive Strength (after Hueste et al. (2004))

Source	Specified compressive strength level, MPa (ksi)	Coefficient of variation, %
Hueste et al. (2004)	40.7 ~ 63.4 (5.9 ~ 9.2)	9.1 (6.9*)
Ellingwood et al. (1982)	20.7 (3.0)	15.5 (18 [†])
	27.6 (4.0)	15.5 (18 [†])
	34.5 (5.0)	11.9 (15 [†])
Tabsh and Aswad (1997)	< 41.4 (< 6.0)	12.5
	41.4 ~ 48.3 (6.0 ~ 7.0)	7.6
	> 48.3 (> 7.0)	6.5

* Value based on mean values of all precasters

[†] Values for in-place conditions (originally reported)

Table 5.6 Coefficient of Variation for Concrete Tensile Strength (after Hueste et al. (2004))

Source	Specified compressive strength level, MPa (ksi)	Coefficient of variation, %
Hueste et al. (2004)	40.7 ~ 63.4 (5.9 ~ 9.2)	12.2 (9.4*)
Ellingwood et al. (1982)	20.7 (3.0)	18 [†]
	27.6 (4.0)	18 [†]
	34.5 (5.0)	18 [†]

* Value based on mean values of all precasters

[†] Values assumed as under in-place conditions

Compared with strength values, there is less uncertainty associated with the modulus of elasticity. The aggregates, water-cement ratio, air-drying effects, time, and compressive strength f'_c all contribute to the determination of E_c . Lydon and Iacovou (1995) presented the results of work that examined the influence of key factors on the modulus of elasticity.

5.3.2 Steel Strength

Mirza and MacGregor (1979) reported results of approximately 4000 tests on Grade 40 and 60 steel reinforcing bars. The results from these tests were examined to obtain statistical relationships for various mechanical properties. The sample included No. 3 through No. 18 sizes of Grades 40 and 60 reinforcements. The means and coefficients of variation of the mill test yield strengths were found to be 48.8 ksi (337 MPa) and 10.7% for Grade 40 and 71 ksi (490 MPa) and 9.3% for Grade 60 bars. Beta distributions were used to represent both of these sets of data. The static yield strength was found to be 3.5 ksi (24 MPa) lower on average than the mill test yield strength in both cases, with a coefficient of variation of 13.4%.

Bournonville et al. (2004) assessed the variability of the mechanical properties and weight of steel reinforcing bars produced by more than 34 mills in the United States and Canada under ASTM A615, A616, and A706 in 1997. Using a similar approach to that of Mirza and MacGregor (1979), beta functions were obtained from parametric studies to represent the yield and tensile (ultimate) strength distributions for different bar sizes, grades, and steel types. After comparing the test data with previous findings, Bournonville et al. (2004) concluded that:

- The beta distributions for yield strengths covering all A615 Grade 40 and all A615 Grade 60 bars provide good representations for the distributions for individual bar sizes within each of these grades, with the exception of A615 No. 14 and No. 18 bars, which exhibit significantly different distribution functions. This is illustrated in Figure 5.15.

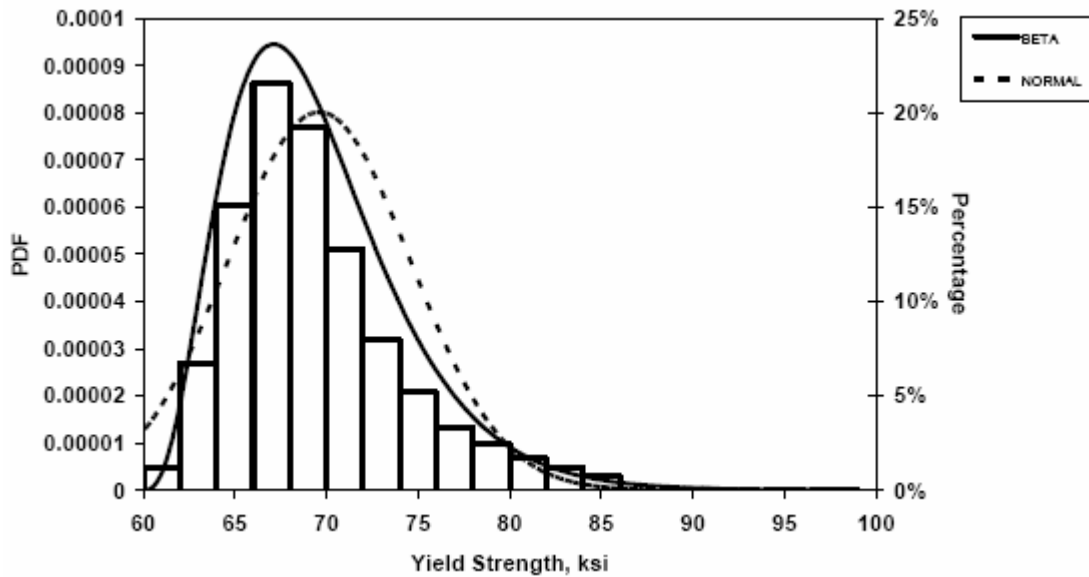


Figure 5.15 Histogram with Probability Density Function for the Yield Strength of All A615 Grade 60 Bars (by Bournonville et al. (2004))

- Both normal and beta distribution functions can be used to represent the distributions of yield strength for A615 Grade 75, A616, and A706 bars.
- The beta distribution for tensile strength covering all A615 Grade 40 bars provides a good representation for individual bar sizes within this grade.
- The beta functions representing tensile strength for the individual bar sizes for A615 Grade 60 bars provide a good match with the actual distributions, with the exceptions of No. 3 through No. 5 and No. 7 bars.
- Both normal and beta distribution functions can be used to represent the distributions of tensile strength for A615 Grade 75, A616, and A706 bars.

In conclusion, beta distribution functions were observed to be better descriptors the strength values of steel bars than normal distribution function for a wide range of bar grades and sizes.

Consequently, in this study beta distribution function were employed for the uncertainty

modeling of reinforcing bar properties as presented in Equation 5.2:

$$PDF = C \left(\frac{f - LB}{UB - LB} \right)^\alpha \left(\frac{UB - f}{UB - LB} \right)^\beta \quad (5.2)$$

where C is the beta function parameter, LB and UB represent the lower and upper bounds of the probability distribution, f is the strength variable, and α and β are exponents. The statistics for the A615 Grade 60 bars employed in this study is shown in Table 5.7.

Table 5.7 Statistics and Beta Distribution for A615 Grade 60 Rebar

Items	Yield Strength	Tensile (Ultimate) Strength
Mean Value (psi)	69610	105572
Standard Deviation (psi)	4976	6645
Coefficient Of Variation	0.0715	0.0629
5% Fractile (psi)	63500	97000
C	37337	37338
α	3	11.09
β	813.21	20.17
LB	60000	74000
UB	2000000	160000

5.3.3 Material Uncertainty Random Effects

Because they are sources of uncertainties, material properties were investigated with assumed probability distribution functions as discussed in previous sections. Other parameters were not assumed to be random variables in this study. For a particular ground excitation and structure, the demand can be written in terms of material strengths as shown in Equation 5.3:

$$D = F(f'_c, E_c, f_y, E_y) \quad (5.3)$$

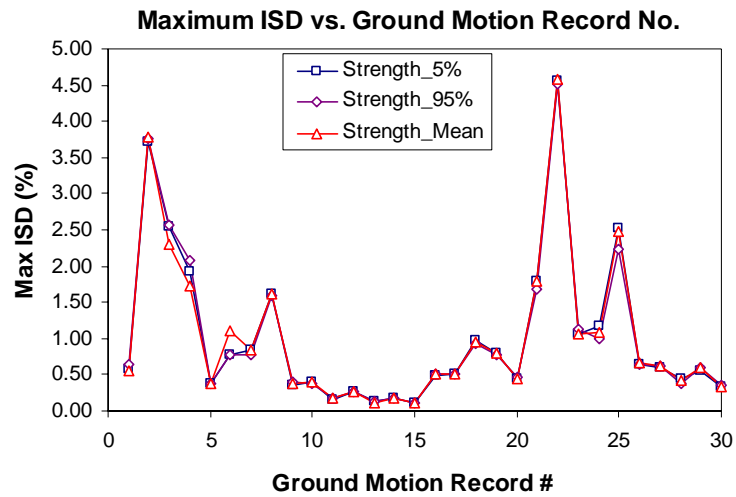
where D is a demand value such as ISD_{max} and $ISPT_{max}$, f'_c is the concrete compressive strength, E_c is the concrete elastic modulus, f_y represents steel reinforcing yield strength, and E_y is the steel elastic modulus.

Since there are no explicit functional forms to directly relate material properties to levels of ISD , $ISPT$, or other measures of demand and response, analytical approaches such as First- or Second-Order Reliability Methods (FORM or SORM; Der Kiureghian et al., 2002, and others) are not applicable. In order to determine the sensitivity of the results to the variations in material property values, numerical simulations are required. To reduce the computational effort for this study, 5 and 95 percentile values were taken as lower and upper bounds for material strengths. The probabilistic distribution functions for concrete and rebar are described by the parameters in Tables 5.5, 5.6, and 5.7. The modulus of elasticity of concrete, E_c , was computed from f'_c , and E_y of rebar was taken as a constant 200,000 MPa. Both static pushover and DRHA were conducted to examine the influence of the random variables on the seismic capacity and demand. The influences on the ISD and $ISPT$ were examined in this study.

□ Effects on Seismic Demand

For the DRHA, a medium intensity level was chosen at $PGA = 1.0g$, and all 30 natural ground motion records were scaled to this value to generate inelastic seismic responses within the reference structure. The ISD_{max} and $ISPT_{max}$ values obtained in the study are shown in Figure 5.16.

(a). ISD_{max} variation



(b). $ISPT_{max}$ variation

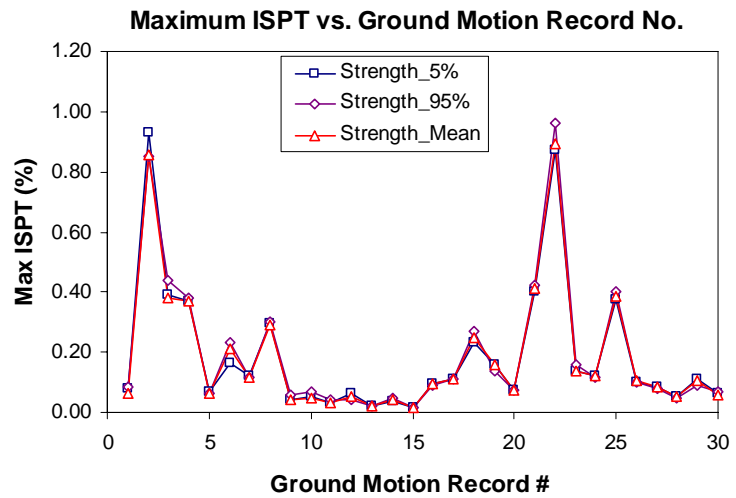


Figure 5.16 ISD_{max} and $ISPT_{max}$ Variation for Each Natural Ground Motion Record with Three Levels of Material Strengths f'_c and f_y : 5%, 95%, Mean

An important observation is that the seismic demand values do not all follow the same trend as the material strength bounds, which indicates that higher material strength does not necessarily reduce the structural deformation response. Another observation is that compared to the differences between ISD_{max} and $ISPT_{max}$ caused by variable material strengths, those due to different ground motions are much larger---especially for larger earthquakes. These observations indicate:

- Dynamic response uncertainties are dominated by the random nature of the ground excitation for high-rise building structures; and
- The seismic deformation demand is primarily influenced by structural stiffness rather than strength because the former affects the vibration period.

A statistical analysis of these results was performed to evaluate the probabilistic features of ISD_{max} and $ISPT_{max}$ for each ground motion record. A normal distribution of results was assumed to evaluate the coefficient of variation. The relative deviations were calculated using regression analyses as demonstrated in Figure 5.17 and Equation 5.4. The C.O.V. values were found to be less than 10% on average and less than 20% for extreme cases, as Figure 5.18 shows.

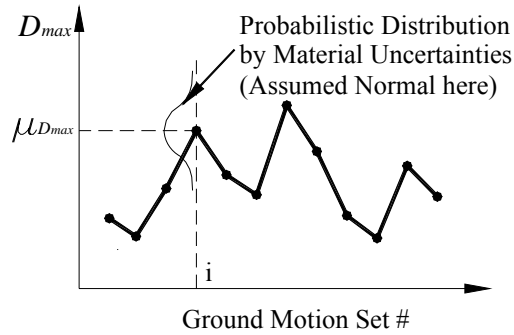


Figure 5.17 Variation of Maximum Demand Values due to Material Uncertainties

$$p_i = \frac{1}{\sigma_i \sqrt{2\pi}} e^{-\left(\frac{x_i - \mu_i}{\sqrt{2}\sigma_i}\right)^2}, \quad \delta_i = \frac{\sigma_i}{\mu_i}, \quad i = 1 \sim 30 \quad (5.4)$$

where, p_i – Probability density function of seismic demand at i th ground motion record

μ_i – Normal distribution mean value at i th ground motion record

σ_i – Normal distribution standard deviation at i th ground motion record

δ_i – Normal distribution C.O.V at i th ground motion record

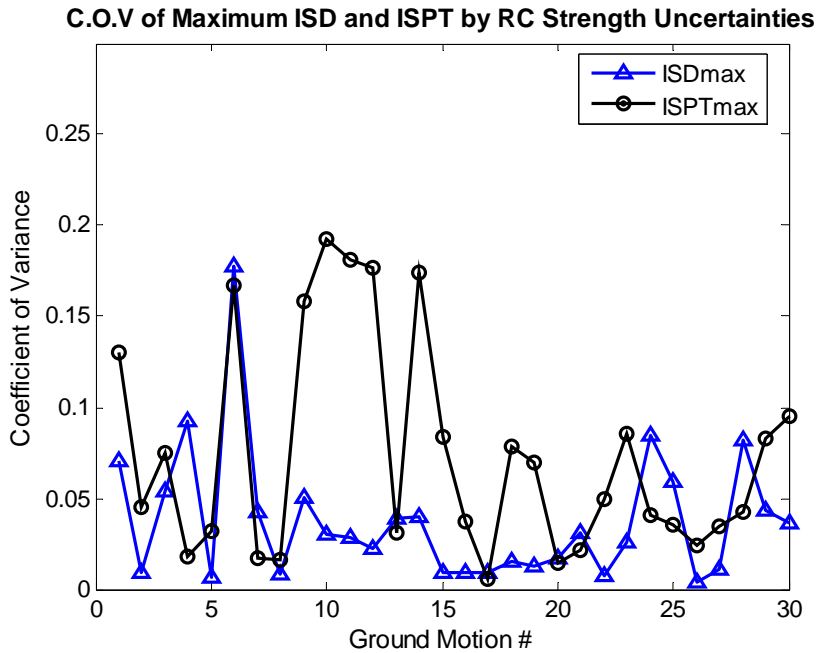


Figure 5.18 C.O.V. of ISD_{max} and $ISPT_{max}$ for Each Natural Ground Motion Record due to Material Strength Uncertainties

The final overall deviations due to material strength uncertainties were computed assuming normal distribution functions. The average C.O.V. with bounds and a 95% confidence level are listed in Table 5.8.

Table 5.8 Average C.O.V. and Bounds of Demands due to Material Uncertainties

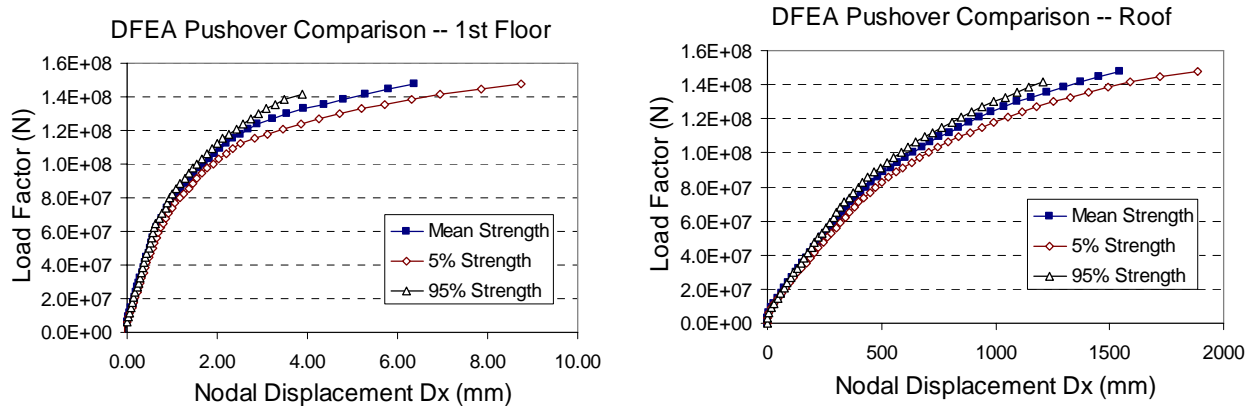
Demand Value	Average C.O.V. throughout all GMs (With bounds)
ISD_{max}	0.038 ± 0.036
$ISPT_{max}$	0.074 ± 0.058

□ **Effects on Structural Capacity**

Because the strength values also affect the structural load resistance and ductility, they bring uncertainties into the fragility analyses. MDFEA, introduced in Chapter 4, was employed in the

pushover analysis to detect variations in the capacity and limit states caused by material strength uncertainties.

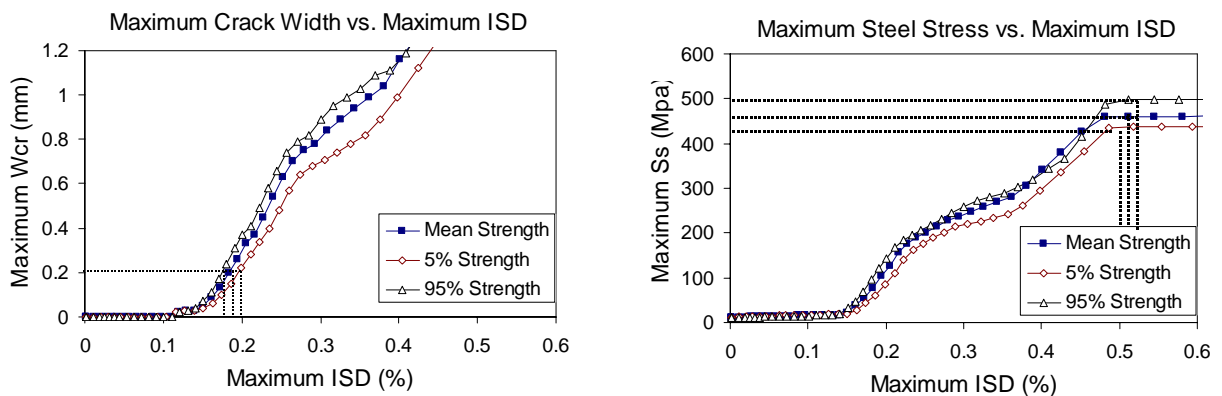
Figure 5.19 shows the comparisons between the pushover results with three material strength levels: mean, 5, and 95 percentiles. The observed differences in deformation due to stiffness are as expected---greater stiffness results in lower nodal drifts if the load levels are equal.



a. Total Load versus Drift at 1st Storey

b. Total Load versus Drift at Top Roof

Figure 5.19 MDFEA Pushover Comparisons for Different Material Strengths



a. Determination of Limit State 1
($W_{cr} > 0.2\text{mm}$)

b. Determination of Limit State 2
($f_y > 434, 460$ and 486 Mpa for 5%, Mean and 95% Strengths)

Figure 5.20 Quantitative Definitions for Limit States 1 and 2 Using MDFEA Results with Material Uncertainty-induced Variation

Limit states 1 and 2 were derived from relationships between local reinforced concrete behavior and global deformation demands and are shown in Figure 5.20.

High-strength concrete exhibits a stiff but more brittle response. In the VecTor2 analyses, this reduced the LS1 level. High-strength steel increased the LS2 criterion. As shown in Figure 5.20, the relative deviations are not large, and the C.O.V., based on the normal distribution assumption, is less than 10% for both limit states. The deviation is much larger for LS3, however, because it includes more inelastic behavior than in the first two. The normal C.O.V. for ISD_{max} and $ISPT_{max}$ for each load step were computed and is plotted in Figure 5.21. Note that the ultimate C.O.V. values at the final converged load step are 30% for ISD_{max} and 32% for $ISPT_{max}$.

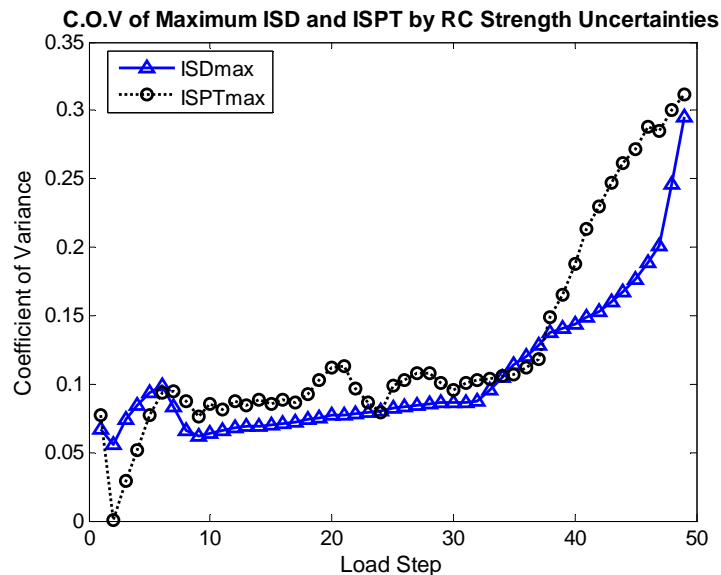


Figure 5.21 ISD_{max} and $ISPT_{max}$ Capacity Variations due to Material Uncertainties along Pushover Loading History

The overall relative deviations were obtained to define the capacities at three limit states, as listed in Table 5.9.

Table 5.9 C.O.V. of Capacities at Limit States due to Material Uncertainties

Limit States	C.O.V. for damage measure: ISD_{max} and $ISPT_{max}$
LS1	0.073
LS2	0.085
LS3	0.32

5.4 Geometric Uncertainty

Another source of uncertainty is the constructed building geometry. This is the difference between the designed structure and the as-built structure and includes member dimensions as well as the location of reinforcement within the structure. These influences are typically minor compared to other parameters unless a gross error in construction is made. In this study, geometric uncertainties were ignored.

5.5 Uncertainty Consideration in Simulation

In order to account for the uncertainties described above, a conventional approach is to conduct Monte Carlo simulations that include all random variables. This would require tens of thousands of nonlinear DRHA solutions in order to derive fragility relationships. This is prohibitively expensive, and it is more practical to focus on the dominant factors that control the probabilistic response.

The analysis results presented in section 5.3 illustrate that the random nature of ground excitation is the most significant feature to consider when performing DRHA. The basic GM characteristics contribute to the seismic demand due to large sensitivities to the different inherent energy

distributions and frequency contents. Material uncertainties can be taken into account as additional epistemic uncertainty in fragility relationships using statistical confidence levels, such as 5 and 95 percentile bounds.

6. Fragility Curve Assessment

6.1 Literature Survey

6.1.1 Existing Fragility Curves

Fragility curves are defined as the relationship between the conditional probability of reaching or exceeding a certain damage states given the intensity measure of ground motion. Fragility is influenced by the nature of ground excitation, structure characteristics and the simulation environment. The latter component comprises selection of structural model, limit states definition and analysis platform. There are several proposed fragility relationships for different reinforced concrete structural systems, using a variety of methodologies and parameters for representation of seismic demand and damages. Rossetto and Elnashai (2003) classified the existing fragility curves into four generic groups:

- Empirical Fragility Curves. These are derived through statistical analysis of real buildings in past earthquakes. Examples of such fragilities are those proposed by Miyakoshi et al. (1997), Orsini (1999) and Yamazaki and Murao (2000).
- Analytical Fragility Curves. This approach uses numerical techniques to simulate the behavior of systems including variation of structural capacity and seismic demands. Studies done in this category include: Singhal and Kiremidjian (1997) that has some considerations for high-rise buildings, and Mosalem et al. (1997).
- Judgmental Fragility Curves. These are fragility curves that are based partially or wholly on expert opinion. An example of these fragility curves are those implemented in

HAZUS (reference to FEMA). The main advantage of this approach is that a wide range of structure types are dealt with in the same manner hence the level of uncertainty, though unknown, is uniform.

- Hybrid Fragility Curves. The hybrid categories are constructed through combination of more than one of the approaches discussed above.

6.1.2 Limitations of Existing Fragility Curves

These four fragility derivation approaches have some limitations and deficiencies. For example,

- Empirical vulnerability curves are highly regional. Their applicability is limited to environments similar to that associated with the data used in their derivations. Also, the quality of field-collected data is highly variable and is subject to human judgment and errors.
- Analytical vulnerability curves are derived through a set of numerical models and simulations. The choice of analysis method, model idealization, seismic hazard, potential uncertainties and damage models affect fundamentally the fidelity of the functions. There are no universally accepted models of response of complex structures and therefore there is no basis for verification but against very limited experimental results.
- Judgmental vulnerability curves are dependent on the individual experience of assigned experts. Potential lack of knowledge of concerned structural types always puts weak base to the judgments by experts.
- Even though there have been many proposed fragility curves, currently the approaches available for RC high-rise buildings are still very few; only the one proposed by Singhal

and Kiremidjian (1997) using the damage index from Park et al. (1985) as damage scale.

Also no systematic investigation and survey of post-earthquake damage statistics has been done for high-rise building population till now.

It is concluded that the few studies that attempted to investigate the fragility of high-rise buildings are deficient and do not provide a framework for repeatable and verifiable fragility analysis. A robust framework and application example are provided below. The framework is transparent, uses the best available analytical tools and is indeed repeatable and verifiable.

6.2 Proposed Analytical Fragility Assessment Framework

6.2.1 Existing Analytical Fragility Assessment

In existing analytical fragility relationships, the assessment procedures range in complexity from elastic analysis of equivalent SDOF system (Mosalem et al. (1997)), to inelastic time history analyses of 3D RC structures (Singhal and Kiremidjian (1997)). Generally the analytical approaches can be divided into the types: FORM Based Methods, Response Surface Methods and Simulation Based Methods (Pinto et al. (2004)).

□ FORM Based Methods

This class of methods, including First Order Reliability Method (FORM) and Second Order Reliability Method (SORM), is based on the widely used approach dealing with the limit function correlated to space domain of random variables. By iterating for the closest direction and distance to the failure surface, the reliability index can be found and hence the failure probability – fragility relationships are also obtained. The calculation steps are:

Define: Limit state function $g(x_1, x_2, x_3, \dots, x_n)$

Use first order linearization to iterate minimum reliability index β to reach $g(\tilde{x}) \leq 0$

$$\text{Then the fragility : } P_f = P_r(g(\tilde{x}) \leq 0) \approx P_r(\bar{g}(\tilde{x}) \leq 0) = \Phi(-\beta) \quad (6.1)$$

Due to the inherent errors associated with linearization around the failure point, a second order approximation is proposed to enhance the solution, leading to the SORM calculation steps below:

Approximation of limit state function is given by:

$$g(\tilde{x}) \approx \tilde{g}(\tilde{x}) = \nabla g(\tilde{x}^*)[(\tilde{x} - \tilde{x}^*)] + \frac{1}{2}(\tilde{x} - \tilde{x}^*)^T H^*(\tilde{x}^*)(\tilde{x} - \tilde{x}^*) = 0 \quad (6.2)$$

$$\text{where, } H^* \text{ is the Hessian matrix : } H^*(\tilde{x}^*) = \left\{ \frac{\partial^2 g}{\partial x_i \partial x_j} \right\}$$

Through the iterations, an approximate closed form solution for the fragility is given by:

$$P_f \approx \Phi(-\beta) \prod_{i=1}^{n-1} \frac{1}{\sqrt{1 + \beta \kappa_i}} \quad (6.3)$$

where, κ_i is the principal curvature of limit state surface in \tilde{x}^*

In practice only single failure mode is not sufficient for real structure especially RC high-rise building with complex structural system. Usually system failure modes will be evaluated using different limit state functions, and global fragility will be evaluated from well-known bounds for series system reliability.

The FORM based methods have been widely applied to find failure probabilities and shown good efficiency. An important advantage over other methods is that it easily provides the sensitivities of P_f on the components of x , information that is quite useful for practical purposes.

□ Response Surface Methods

For many real situations, it is very difficult to get explicit limit state functions and FORM or SORM are not appropriate accordingly. Response Surface Method (RSM) functions as a promising and straightforward tool for the approximation of limit state function, investigation of the relationship between desired value and influencing factors, and interactions among sub random variables. The most often used model is a form of a polynomial function with no higher than the second order, as in Equation 6.4.

$$Y = \beta_0 + \sum_{i=1}^k \beta_i x_i + \sum_{i=1}^k \sum_{j \geq i}^k \beta_{ij} x_i x_j + \varepsilon \quad (6.4)$$

where, Y is any interested variable of response,

$\beta_0, \beta_i, \beta_{ij}$ are unknown coefficients, ε is the error term

Thus the effects of uncertainties of basic random variables can be observed and integrated into final fragility assessment.

□ Simulation-Based Methods

The most straightforward and accurate approach is simulation based Method, through the direct simulation input over all potential domains of random variables. The main types are:

- Monte Carlo Method

$$P_f = \int_F f_X(x) dx \Rightarrow P_f \approx \hat{P}_f(N) = \frac{1}{N} \sum_{i=1}^N I_f(x_i) = \frac{N_f}{N} \quad (6.5)$$

where, N – Sampling size, $I_f(x_i) = \begin{cases} 1, & \text{if fail} \\ 0, & \text{if not fail} \end{cases}$

- Importance Sampling

The purpose for this is to generate the samples x according to a more favorable distribution.

$$P_f \approx \hat{P}_f(N) = \frac{1}{N} \sum_{i=1}^N I_f(x_i) \frac{f_x(x_i)}{h(x_i)} \quad (6.6)$$

where, $h(x_i)$ – an optimal sampling density.

- Directional Simulation

It is a more enhanced simulation technique, for which preliminary transformation to standard normal is required (Pinto et al. (2004)). Random variables y can be expressed in spherical coordinates, as following:

Define: $\tilde{y} = \tilde{\theta}r$, $r = |y|$, θ is unit vector of direction cosines of \tilde{y}

$$P_f = \int_F \phi(\tilde{y}) d\tilde{y} = \int_{\Omega} \left[\int_{\Omega} f_r(r|\theta) dr \right] \int_{\Omega} f_{\theta}(\theta) d\theta \quad (6.7)$$

$$P_f \approx \hat{P}_f = \frac{1}{N} \sum_{i=1}^N \left[1 - x_n^2(r_0^2(\theta_i)) \right] \quad (6.8)$$

6.2.2 Proposed Framework

The fragility curves for the reference structure – Tower03 in Dubai will be developed using the analytical procedures presented in Figure 6.1. Some basic features, including structural lumped modeling, uncertainty modeling and limit state definition, have already been introduced and accomplished earlier in previous sections. Therefore the dynamic response history analysis (DRHA) for the evaluation of seismic demand is the main focus of the discussion below..

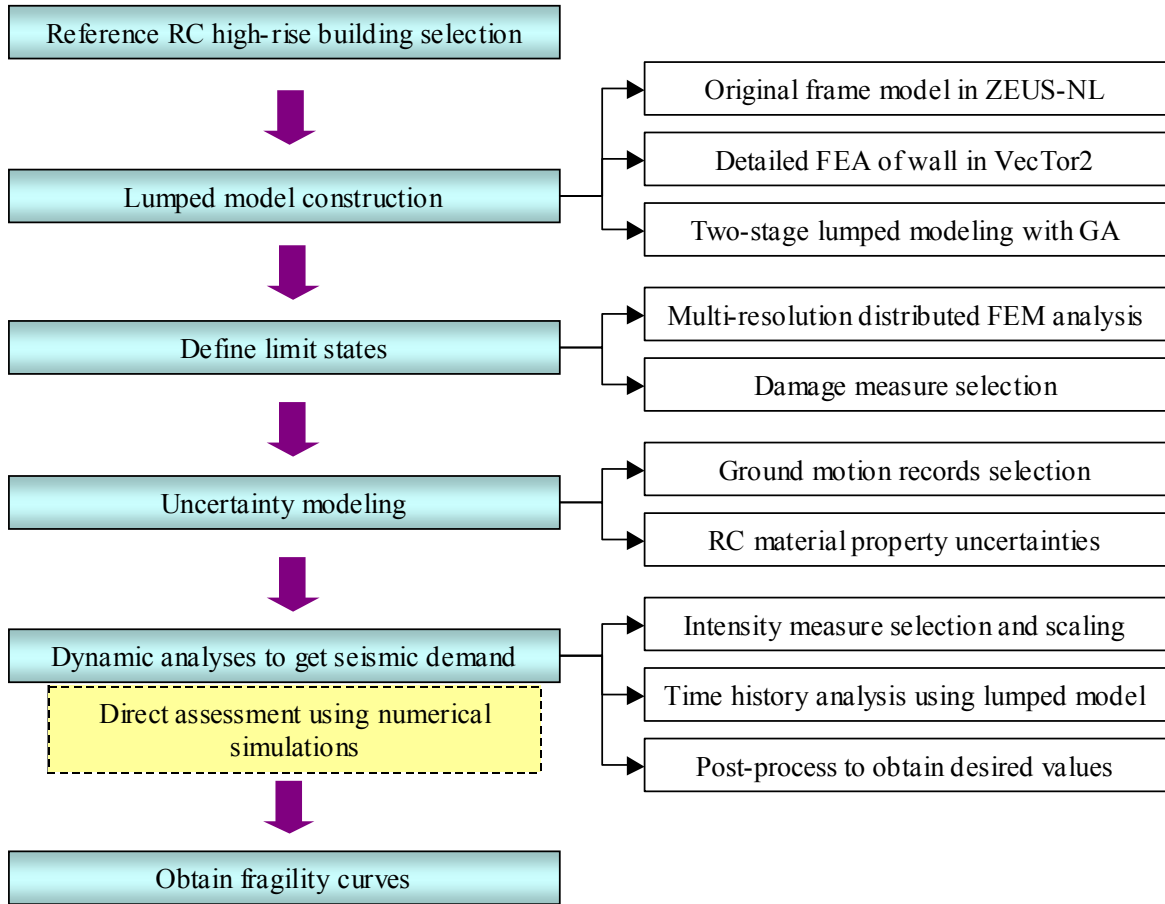


Figure 6.1 Proposed Analytical Fragility Assessment Framework

6.3 Numerical Simulation to Assess Fragility Relationships

6.3.1 Selection and Scaling of Intensity Measures

There are several intensity measures used by researchers to derive fragilities. The most common ones are: peak ground acceleration (PGA) (Mosalem et al. (1997)), spectral acceleration (SA) at some periods (Singhal and Kiremidjian (1997)), and spectral displacement (SD) at selected periods (Rossetto and Elnashai (2003)). The choice of ground motion parameter determines the distribution of the statistics along the horizontal axis of the fragility plot. It is expected that an increase in the damage potential of an earthquake will coincide with an increase in the

probability of building damage. A better fragility curve fit can therefore be achieved through the choice of a ground motion parameter that correctly represents the seismic demand in terms of the earthquake damage potential.

□ **Selection of Intensity Measures**

Elnashai et al. (2005) conducted systematic research on the selection, evaluation, and scaling of intensity measures for ground motions. Their work assessed available techniques for scaling strong motions and insuring a consistent level of seismic demand for a selected set of records. A number of approaches for scaling are recommended for application to the selected records.

The PGA scaling in dynamic analyses relates the seismic forces directly to the excitation acceleration values. It has advantages in that it is simple to apply and agrees with the methods by which design codes normally define seismic loads. PGA has the greatest influence on structural seismic response at high frequencies (periods less than 0.5 seconds); low-frequency structures (periods greater than 0.5 seconds) are more sensitive to peak ground velocity (PGV) and peak ground displacement (PGD), especially structures with very long fundamental periods (i.e. greater than 3.0 seconds).

Another method is to use scale-based spectral parameters such as spectral acceleration, velocity, and displacement. It may be more straightforward to select intensity according to specific periods for certain structures. These parameters can be related to some important features within inelasticity, such as the ductility demand imposed on structural systems when the effects of varying yield strengths must be considered.

Due to the fact that PGA and PGV or SA and SV only represent certain frequency points, the effective range of the reference structure's frequency contents are insufficient to provide the complete response. Researchers have proposed other types of spectral intensity measures to improve analysis over a wide range of natural frequencies. In research by Elnashai et al, several typical spectral intensity scales are compared and evaluated to achieve an understanding of the correlations between ground motion intensity and seismic demand. The intensity measures investigated by Elnashai et al. are:

- Housner Spectrum Intensity

Housner (1952) proposed that the velocity spectrum could provide a measure of the severity of building response due to strong ground motion. The intensity of shaking at a given site was represented by the spectrum intensity SI_H , defined as the area under the elastic velocity spectrum between the periods 0.1 and 2.5 seconds:

$$SI_H = \int_{0.1}^{2.5} SV(T, \xi) dT \quad (6.9)$$

where SV is the velocity spectrum curve and ξ is the damping coefficient.

- Intensity Scales of Nau and Hall

Nau and Hall (1984) conducted a study on scaling methods for earthquake response spectra. A three-parameter system of spectrum intensities, computed within low, medium, and high frequency regions was proposed. This system accounts for the sensitivity of the response to acceleration, velocity, or displacement and is given by:

$$SI_a = \int_{0.028}^{0.185} SV(T, \xi) dT \quad \text{for } T \text{ of } 0.118 \text{ to } 0.5 \text{ seconds} \quad (6.10)$$

$$SI_v = \int_{0.285}^{2.000} SV(T, \xi) dT \quad \text{for } T \text{ of } 0.5 \text{ to } 5.0 \text{ seconds} \quad (6.11)$$

$$SI_d = \int_{4.167}^{12.500} SV(T, \xi) dT \quad \text{for } T \text{ of } 5.0 \text{ to } 14.085 \text{ seconds} \quad (6.12)$$

where: SI_a is the spectrum intensity in the acceleration region, SI_v is the spectrum intensity in the velocity region, and SI_d is the spectrum intensity in the displacement region.

- Matsumura Spectrum Intensities

Matsumura (1992) conducted a parametric study of the strong motion intensity measures and their correlation with structural damage. SI_M is referred to as the Matsumura spectrum intensity and is defined as the mean spectral velocity between T_y and $2T_y$, where T_y is the period corresponding to yield of a single-degree-of-freedom structure (SDOF) with a critical damping ratio ξ of 0.05. The adopted period interval $[T_y, 2T_y]$ is based on the assumption that the response of the structure is associated with the resonance linked to excitation frequencies around the natural frequency of the structure.

A recent study (Martinez-Rueda (1997)) conducted an analytical examination of inelastic performance for a large number of earthquake records in order to identify the scaling procedure that optimizes the correlation between spectrum intensity and seismic demand represented by displacement ductility demand. Through a parametric study of the nonlinear behavior of a SDOF system under earthquake excitation, its correlation with various spectrum intensity scales including SI_H and SI_M , as well as a third intensity scale SI_{yh} suggested by Martinez-Rueda (1997), significant insight was achieved. The highlights of this study are summarized below.

- Average Spectrum Intensities

To remove the different integral range influences, the spectrum intensity scales were represented

as average spectrum velocities for $\xi=0.05$ such that:

Housner average spectrum intensity:

$$\overline{SI_H} = \frac{1}{2.4} \int_{0.1}^{2.5} SV(T, 0.05) dT \quad (6.13)$$

Matsumura average spectrum intensity:

$$\overline{SI_M} = \frac{1}{T_y} \int_{T_y}^{2T_y} SV(T, 0.05) dT \quad (6.14)$$

Martinez-Rueda (1997) suggested changing the second integration limit of Matsumura to T_h , which represents the new vibration period of the structure in the hardening range after yielding.

This was based on the assumption that the ground motion frequencies contributing to the failure of the structure are contained within the period interval of T_y to T_h . Using these integration limits, a new average spectrum intensity is defined as:

$$\overline{SI_{yh}} = \frac{1}{T_h - T_y} \int_{T_y}^{T_h} SV(T, 0.05) dT \quad (6.15)$$

Following a statistical evaluation of the correlation between ductility demand and considered spectrum intensity scale using 100 accelerograms, final suggestions were made by Martinez-Rueda (1997) for the choice of spectrum intensity scales:

- (1) Long-period structures ($T_y > 1.6$): $\overline{SI_M}$
- (2) Medium-period structures ($0.6 < T_y < 1.6$): $\overline{SI_H}$
- (3) Short-period structures ($T_y < 0.6$): $\overline{SI_M}$ or PGA

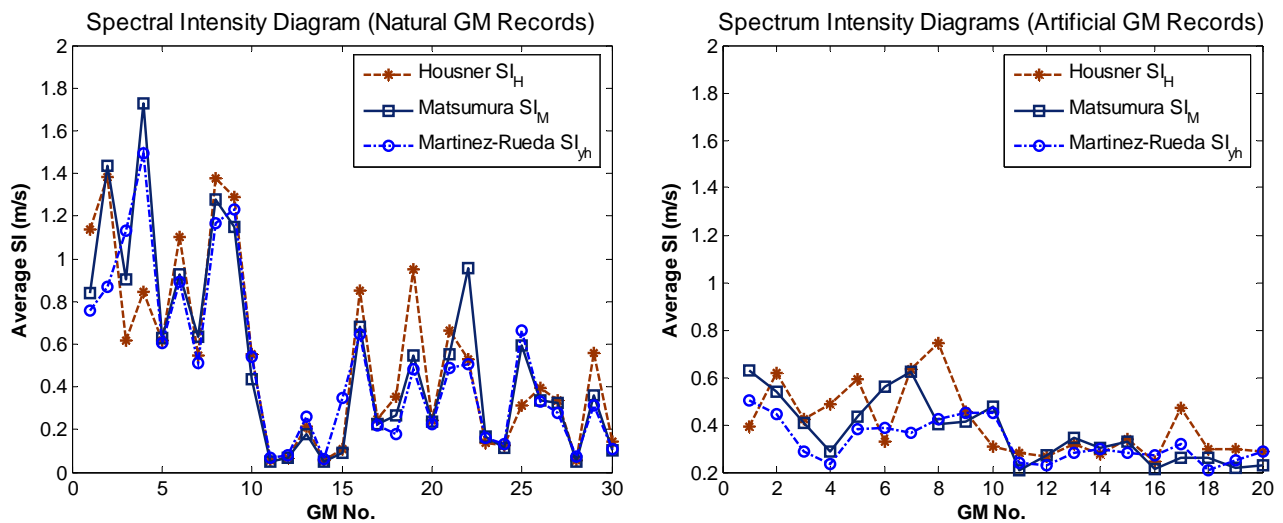
Using the recommended scales resulted in correlation coefficients well above 85% in most cases.

If a problem calls for the use of single spectrum intensity for simplicity, using $\overline{SI_M}$ is recommended for this purpose, provided that the period of the structure can be estimated in

advance.

In this research, the simple rules outlined above could not be utilized because of the complex structural characteristics of the reference high-rise. Because creating fragility assessments is not yet a common practice in design, clear seismic demand standards do not exist and wide frequency ranges must be examined. In research it may not be appropriate to scale all ground motions by just one spectral intensity measure. For example, Figure 6.2 shows three different spectral intensity distributions for 30 natural ground motion records and 20 artificial records. The yield period, T_y , is computed from the *MPF* weighted average of the first four modal periods.

This procedure is discussed in Chapter 3.



(a) $\overline{SI_H}$, $\overline{SI_M}$, $\overline{SI_{yh}}$ for 30 Natural Records

(b) $\overline{SI_H}$, $\overline{SI_M}$, $\overline{SI_{yh}}$ for 20 Artificial Records

Figure 6.2 Average Spectral Intensities for All Ground Motion Records

Figure 6.2 shows that large variations exist among different ground motion categories, and thus the seismic displacement demand also varies. This warrants the question of whether the scaling criteria should be selected for all GMs or for each category separately. A careful choice should be

made to avoid misleading results.

On the other hand, with proper incorporation of the important basic features during the selection of earthquake ground motions (Chapter 5), it is safe to not scale ground motion records based on spectral intensities and keep the original selection of GMs. Thus a simple method was employed in this study---both PGA and SA are adopted as intensity measures for the fragility assessment. Considering the complexity of high-rise building behavior, SA at two periods---0.2 seconds and 1.0 second---are taken into account to cover both low and high-range modes as presented in

Figure 6.3.

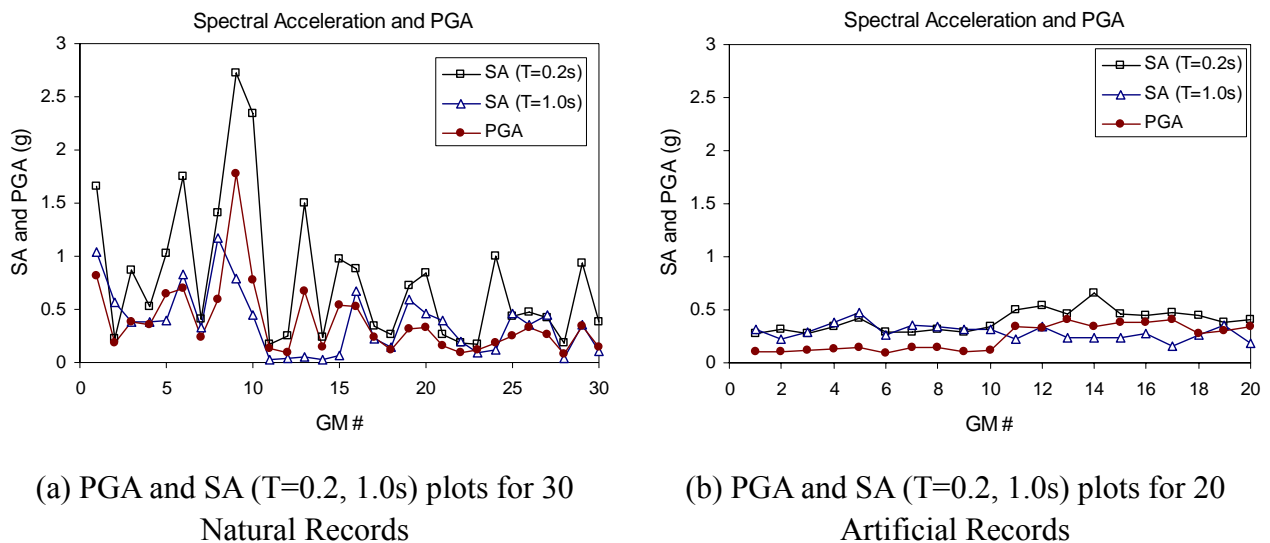


Figure 6.3 PGA and SA (T=0.2s, 1.0s) for All Ground Motion Records

For the natural ground motion records, the three categories offer significant exposure to uncertainties. In addition, the frequency contents of the ground motion records are more significant to the response than PGA or SA. The intensity measure scales were simply set within a fixed range [0.1g, 2.0g] at increments of 0.1g. There were 600 DRHA numerical simulations for each fragility derivation using one intensity measure. The additional artificial record group,

which is the BEQ and SEQ series containing 20 strong motions, included varying source distances and magnitudes. The intensity measures and scales are the same as those for the natural records and follow a fixed IM range, [0.1g, 2.0g] with 0.1g increments. Thus another 400 numerical simulations of DRHA were required for each fragility derivation using one intensity measure.

6.3.2 Effective Duration

Conducting the DRHA with the full ground motion records would be an unnecessarily computationally-intensive way to perform the fragility assessments due to the long time histories. For example, the 30 natural records have durations ranging from 9.835 seconds to 120 seconds with up to 18,000 time steps. The artificial records all have 10,000 steps and a 0.01 seconds step size. The DRHA solution demands hours of runtime using the final lumped-model derived in Chapter 3. The effective duration concept, as developed by Bommer and Martinez-Pereira (1999), is therefore employed to truncate the insignificant parts of the selected GM records. Arias Intensity (AI), expressed in Equation 6.16, was used to measure the seismic energy contained in a ground motion strike.

$$AI = \frac{\pi}{2g} \int_0^{t_r} a^2(t) dt \quad (6.16)$$

where $a(t)$ is the ground acceleration time history, t_r is the total duration of the record, and g is the gravity acceleration.

Effective duration is determined based on the time for which the AI value applies and the AI of whole duration, as described in Equation 6.17.

$$DE = t_f - t_o \quad (6.17)$$

where, DE -- the effective duration

t_f, t_o -- the ending and starting time of DE

Based on the significant duration concept, Bommer and Martinez-Pereira (1999) suggested that the start and end of the strong motion be identified by the absolute criteria:

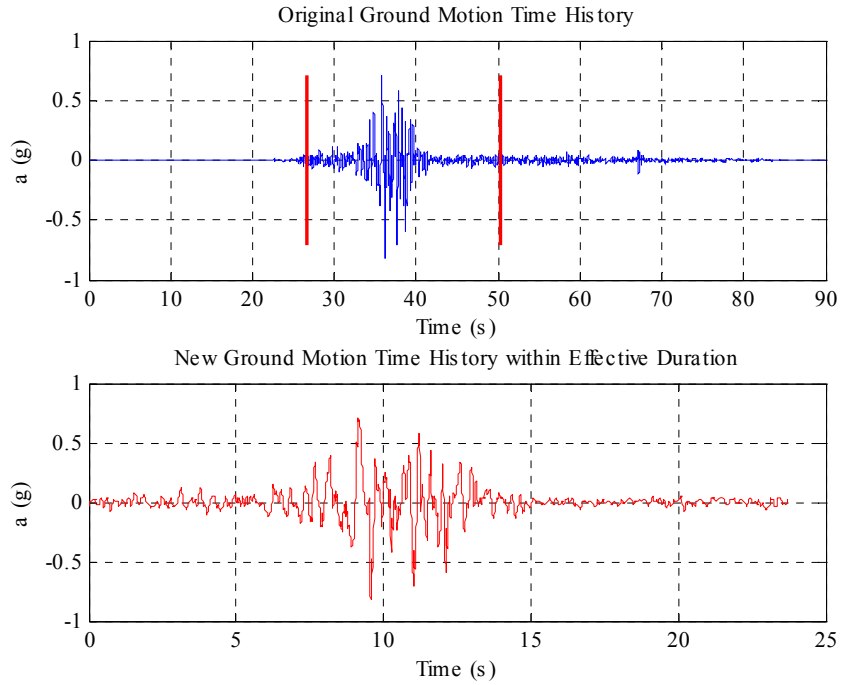
$$AI_o = 0.01 \text{ m/s}; \quad \Delta AI_f = AI_{total} - AI_f = 0.125 \text{ m/s} \quad (6.18)$$

where, AI_o, AI_f represent AI values up to t_o and the remaining of the period after t_f .

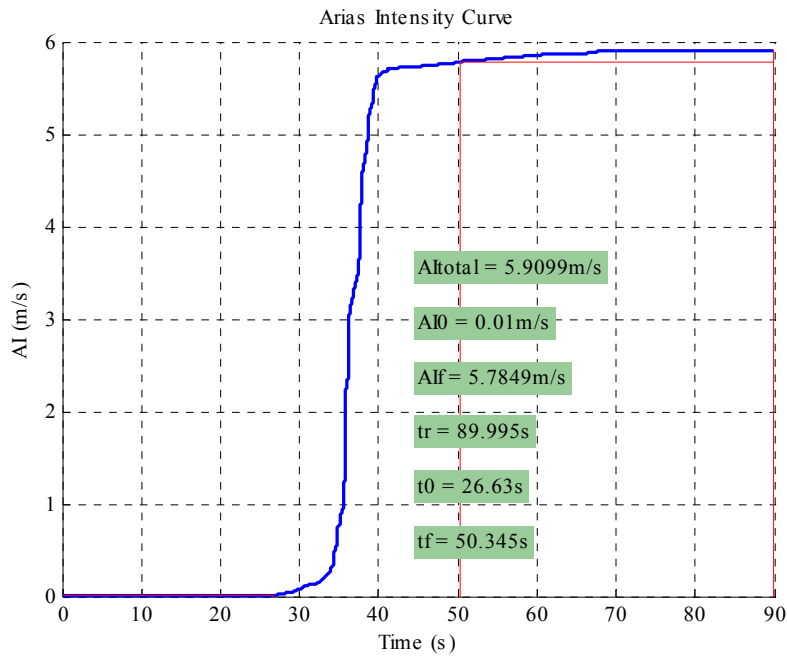
In cases where some records have very low AI_{total} values, using only absolute criteria will be insufficient and misleading, and relative ratio limits are employed to provide additional restraints and avoid the underestimation of structural seismic responses. The effective duration also needs to satisfy:

$$AI_o \leq 0.5\% AI_{total}; \quad AI_f \geq 95.5\% AI_{total} \quad (6.19)$$

Through the application of the criteria above, effective durations were derived for all selected accelerograms, and one example is shown in Figure 6.4.



(a). Whole Time History and Derived Effective Duration and of the Chi-Chi Earthquake Record (1999) at Station CHY028 (North)



(b). Arias Intensity Plot and Determination of Effective Duration

Figure 6.4 Sample Derivation of Effective Duration for Selected Ground Motions

□ **Effective Duration of 30 Natural Ground Motion Records**

Through the application of the effective duration approach, the most significant segments of the accelerograms were selected for use in the DRHA, and the computation time was significantly reduced. Elastic spectral accelerations with a 5 percent damping ratio were calculated for the effective durations of ground motions and compared with those from the original time histories, which are shown in Figure 6.5 and Table 6.1. The results show very good conformity and thus exemplify the high consistency of the seismic energy and dynamic characteristics.

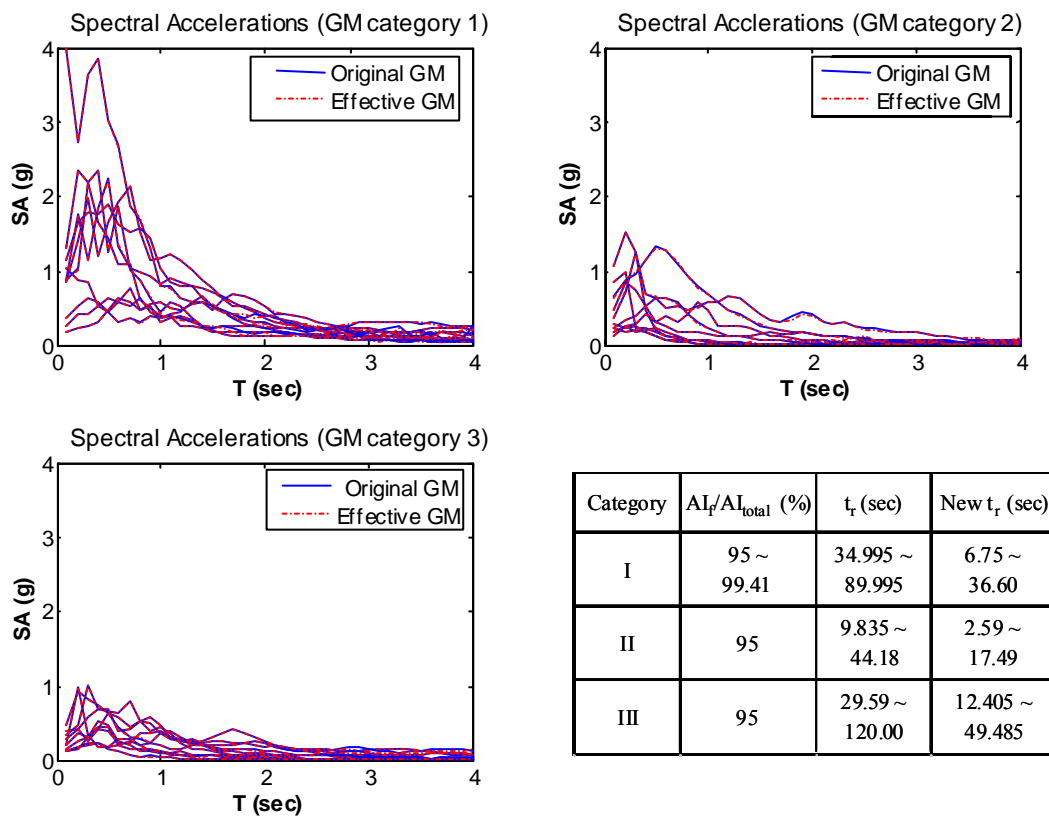


Figure 6.5 Spectral Acceleration Plots for Original and Effective Natural Accelerograms

Table 6.1 Evaluation of Natural Accelerograms Reduced by Effective Duration Concept

No.	Earthquake GM	Alf/AI_total (%)	Tr	Tr_new	Tr_new/Tr (%)
1	Chi-Chi_close_stiff	97.71	89.995	23.715	26.4
2	Chi-Chi_close_soft	95.05	89.995	36.6	40.7
3	Kocaeli_close_stiff	95	59.99	11.59	19.3
4	Kocaeli_close_soft	95	34.995	17.11	48.9
5	Loma_close	95.83	39.94	9.035	22.6
6	Kobe_close_stiff	96.57	40.95	6.75	16.5
7	Kobe_close_soft	95	40.95	12.51	30.5
8	Northridge_close_soft	97.61	39.98	10.62	26.6
9	Northridge_close_stiff	99.41	39.98	21.66	54.2
10	Imperial_close_soft	97.74	37.6	13.215	35.1
11	Anza_1	95	10.305	2.995	29.1
12	Anza_2	95	10.375	5.85	56.4
13	Coalinga_1	95	9.835	2.59	26.3
14	Coalinga_2	95	39.99	7.385	18.5
15	Ancona_wave29_X	95	18.77	3.02	16.1
16	Ionian_wave42_X	95	26.51	6.96	26.3
17	Aftershock_Friuli_wave122_X	95	20.29	3.77	18.6
18	Alkion_wave335_Y	95	28.61	17.49	61.1
19	Dinar_wave879_Y	95	27.95	17.16	61.4
20	Umbro-Marchigiano_wave591_X	95	44.18	6.17	14.0
21	Chi-Chi_dist_soft_1	95	110	45.336	41.2
22	Chi-Chi_dist_soft_2	95	89.995	49.485	55.0
23	Chi-Chi_dist_stiff	95	76.995	26.885	34.9
24	Kocaeli_dist_stiff	95	100	39.625	39.6
25	Kocaeli_dist_soft	95	120	45.445	37.9
26	Loma_dist_soft_1	95	39.945	13.335	33.4
27	Loma_dist_soft_2	95	29.59	12.405	41.9
28	Kobe_dist_stiff	95	77.98	22.44	28.8
29	Kobe_dist_soft	95	40.95	14.33	35.0
30	Northridge_dist_soft	95	34.98	20.75	59.3

□ **Effective Duration of 20 Artificial Ground Motion Records**

Similarly the effective durations are much shorter than original ones, amongst BEQ series are reduced by more than 50%, while SEQ series are shortened tremendously by around 90%.

Elastic spectral accelerations with damping ratio at 5% are calculated for ground motion data of effective durations and compared with those from original time histories as Figure 6.6 and Table 6.2. The results also show very good conformity as natural records and keep the consistency very well of the seismic energy and dynamic characteristics.

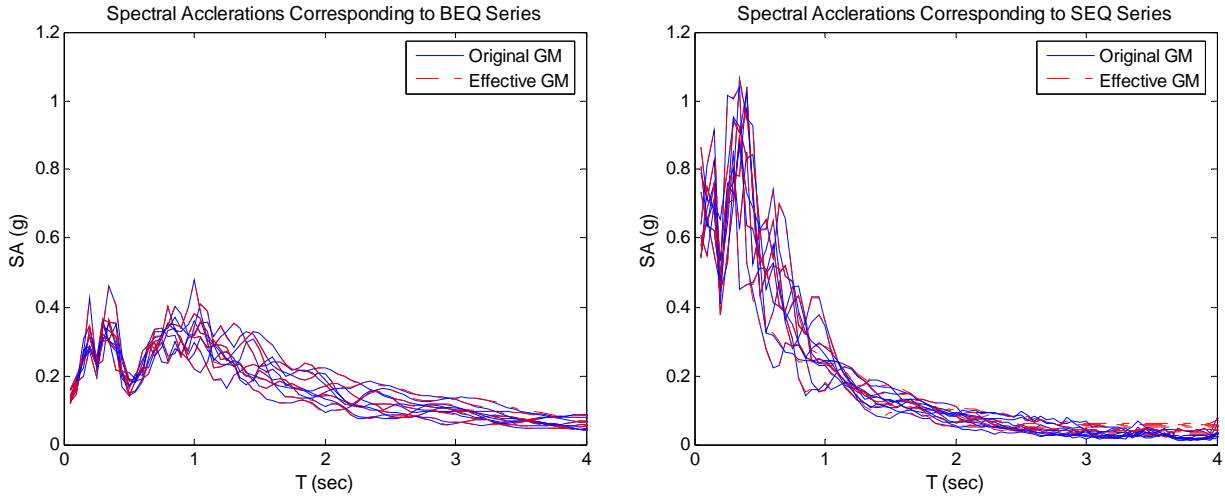


Figure 6.6 Spectral Acceleration Plots for Original and Effective Artificial Accelerograms

Table 6.2 Evaluation of Artificial Accelerograms Reduced by Effective Duration Concept

No.	Earthquake GM	AI _f /AI _{total} (%)	Tr (sec)	Tr _{new} (sec)	Tr _{new} /Tr (%)
1	BEQTS01	95	99.99	33.46	33.46
2	BEQTS02	95	99.99	34.69	34.69
3	BEQTS03	95	99.99	33.69	33.69
4	BEQTS04	95	99.99	33.93	33.93
5	BEQTS05	95	99.99	33	33.00
6	BEQTS06	95	99.99	33.4	33.40
7	BEQTS07	95	99.99	32.74	32.74
8	BEQTS08	95	99.99	34.26	34.26
9	BEQTS09	95	99.99	32.98	32.98
10	BEQTS010	95	99.99	36.49	36.49
11	SEQTS01	95	99.99	7.23	7.23
12	SEQTS02	95	99.99	7.24	7.24
13	SEQTS03	95	99.99	7.01	7.01
14	SEQTS04	95	99.99	6.85	6.85
15	SEQTS05	95	99.99	7.3	7.30
16	SEQTS06	95	99.99	6.76	6.76
17	SEQTS07	95	99.99	7.1	7.10
18	SEQTS08	95	99.99	7.48	7.48
19	SEQTS09	95	99.99	6.93	6.93
20	SEQTS010	95	99.99	7.16	7.16

6.3.3 Dynamic Response History Analyses

MATLAB codes were written to control the execution of the analyses and include: modification of ZEUS-NL input data based on ground motion record loop and scaling, running the ZEUS-NL DRHA solver, and post-processing the results to obtain ISD_{max} and $ISPT_{max}$ values. For the 30 natural records and 20 artificial records, 20 scales were set for each intensity level for both groups. For natural records, the execution of the 600 DRHA performed for each set of fragility derivations required approximately 200 hours of runtime on a computer with a P4 2.8 GHz CPU and 1GB of memory. The total runtime using artificial records was slightly shorter. The computed values for ISD_{max} and $ISPT_{max}$ along the building height are plotted in Figure 6.7, and the overall ISD_{max} and $ISPT_{max}$ can be obtained easily.

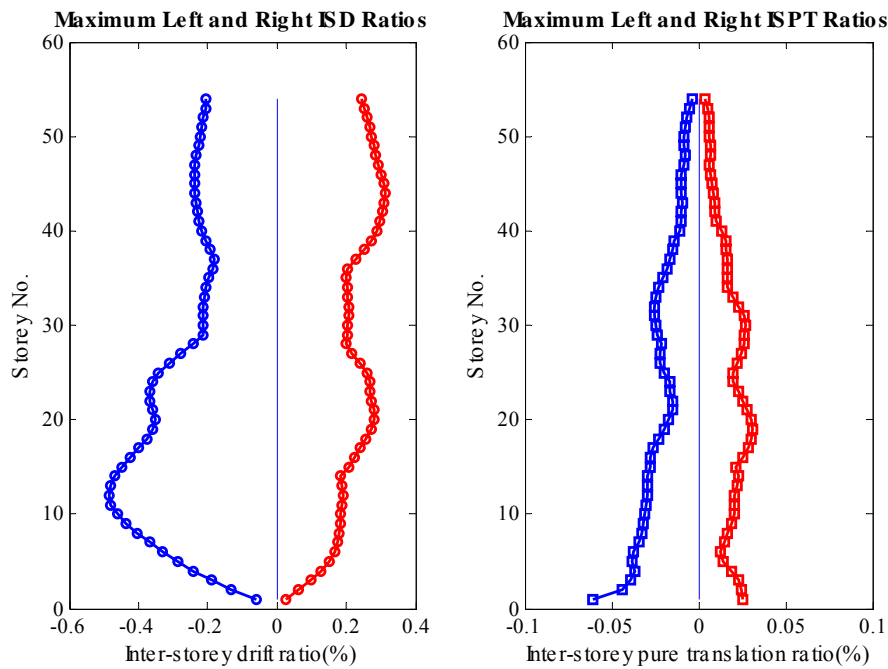


Figure 6.7 ISD_{max} and $ISPT_{max}$ along Height within Time History

6.3.4 Fragility Derivation and Log-Normal Regression Function

Upon obtaining the ISD_{max} and $ISPT_{max}$ values, limit states definitions were applied to assess the

performance levels of the building subjected to a particular ground excitation. If the computed values were larger than a limit state level for either ISD_{max} or $ISPT_{max}$, the event that exceeded the LS was counted within the sample containing all GM scales. The direct sampling probability for each type of intensity measure over the 30 selected natural and 20 artificial GMs on all 20 scales were thereby assessed.

It was not possible to complete the full DRHA for all GM records at all scales due to non-convergence in some analyses. ZEUS-NL automatically reduces the step size down to 1/100 of the original time step if the convergence is not achieved. If the solution does not converge at the reduced time step, then subsequent results are not trustworthy, and the DRHA is terminated for that run. This failure to converge can be a result of material inelasticity or geometric nonlinearity at some local elements, and it does not necessarily indicate the structure is near collapse. When an analysis run failed due to lack of convergence, it was necessary to determine whether the analysis was predicting collapse, or the lack of convergence was caused by another issue for which the analysis results should be dismissed. For a structure to be judged near collapse, one of the following conditions had to be satisfied:

- ISD_{max} or $ISPT_{max}$ at current GM scale exceeded limit state 3 (LS3) before divergence;
- ISD_{max} or $ISPT_{max}$ at previous GM scale exceeded LS3;
- ISD_{max} or $ISPT_{max}$ at previous GM scale were close to the LS3 (within 90%), and the current values were larger than values from the previous time step.

For situations not listed above, it was necessary to assess the performance level based on a comparison between the calculated maximum values and defined limit state values. The

sampling probabilities of exceedance were then obtained from the results of the DRHA as described by Equation 6.20.

To provide usable and comparable results for the literature and practice, probability functions are needed to simulate the sample probability curves and generalize the fragility relationships. A lognormal distribution was employed for regression of comprehensive functional fragility relationships as described by Equation 6.21.

$$P(LS | IM)_{sample} = \frac{N(exceeding)}{Sample\ Size}, \text{ Sample Size is 30 here} \quad (6.20)$$

$$P(LS | IM)_{function} = \Phi\left(\frac{\ln IM - \lambda_c}{\beta_c}\right) \quad (6.21)$$

where $P(LS | IM)$ indicates the probability of exceeding a limit state for a given IM value, Φ is the standard normal cumulative distribution function, IM is the intensity measure value within the range [0.1g, 2.0g], and λ_c , β_c are function parameters.

The fragility curve control parameter λ_c represents the median point for a 50% probability of exceeding the limit state, and β_c indicates the slope of the curve to match the discrete points. Nonlinear curve fitting techniques were employed for the optimization of these two parameters for each fragility relationship.

□ **Derived Fragility Relationships from Natural Ground Motion Records**

Figure 6.8 presents the fragility curves for the reference building developed from the 30 selected natural ground motion records, based on the intensity measure of PGA and SA at $T = 0.2$ seconds and $T = 1.0$ second, including both the direct sample probability and simulated lognormal functions. The simulated lognormal distribution function parameters are listed in Table 6.3.

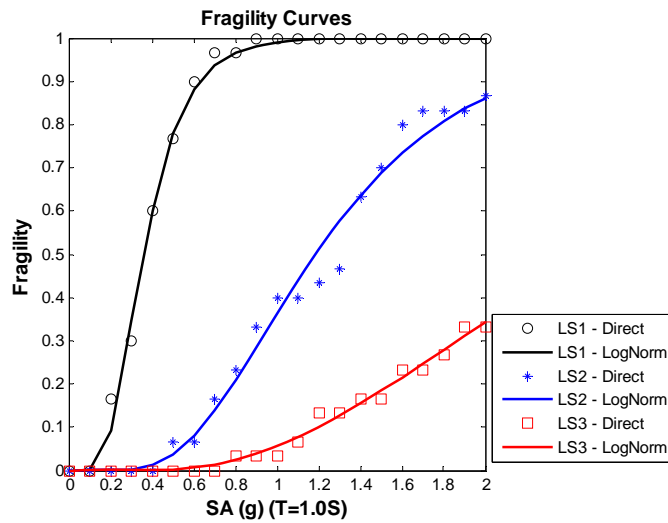
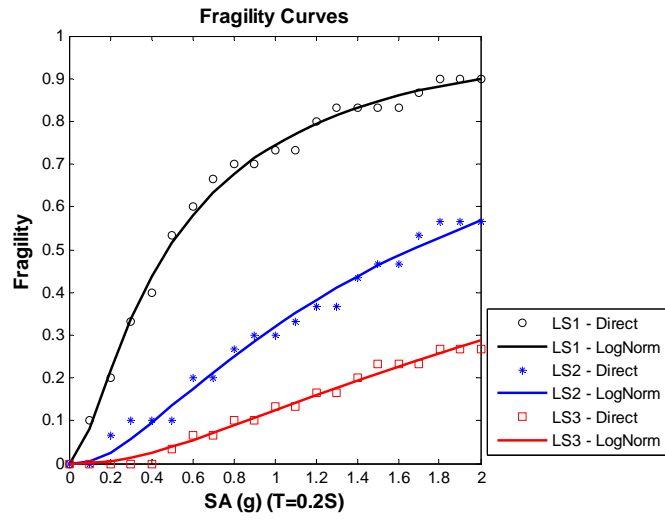
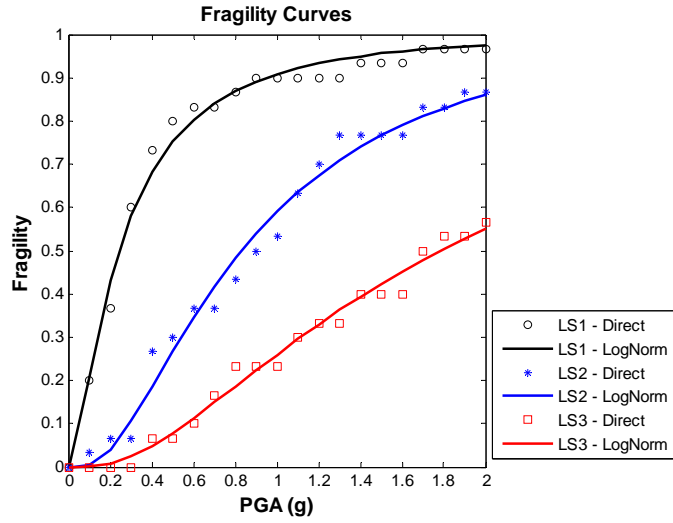


Figure 6.8 Derived Fragility Relationships for All Intensity Measures (from Natural GMs)

Table 6.3 Simulated Log-Normal Distribution Function Parameters for Fragilities (Natural GMs)

Limit States	Intensity Measure Type					
	PGA (g)		SA (T=0.2s) (g)		SA (T=1s) (g)	
	λ_c	β_c	λ_c	β_c	λ_c	β_c
LS1 (Serviceability)	-1.4247	1.0717	-0.7358	1.1155	-1.1145	0.3874
LS2 (Damage Control)	-0.1875	0.8134	0.5085	1.0886	-0.0175	0.4919
LS3 (Collapse Prevention)	0.5785	0.8996	1.3462	1.1648	0.7820	0.4829

□ **Derived Fragility Relationships from Artificial Ground Motion Records**

Figure 6.9 presents the developed fragility curves for the reference building from the 20 artificial strong motion records, based on the intensity measure of PGA, including both direct sample probability and simulated lognormal functions.

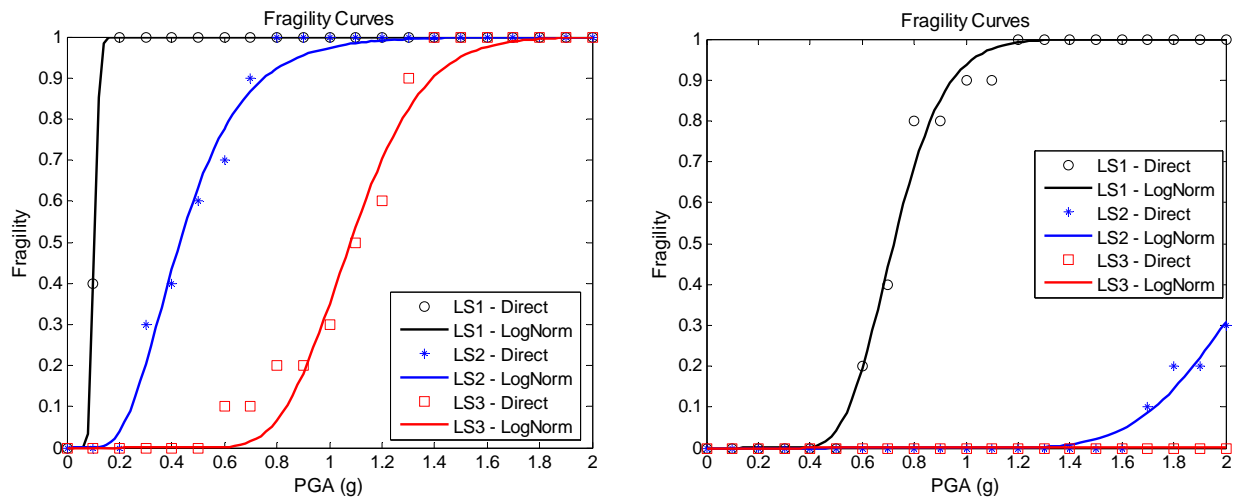


Figure 6.9 Derived Fragility Relationships for Intensity Measure Using PGA from Artificial GMs: BEQ Series (Left Plot); SEQ Series (Right Plot)

In this figure, fragilities from BEQ and SEQ series are separated due to the large differences

between the basic features of these two groups and the conformity within each group. The simulated lognormal distribution function parameters are listed in Table 6.4.

Table 6.4 Simulated Log-Normal Distribution Function Parameters for Fragilities (Artificial GMs)

Limit States	BEQ series with IM in PGA		SEQ series with IM in PGA	
	λ_c	β_c	λ_c	β_c
LS1 (Serviceability)	-2.2670	0.1403	-0.3268	0.2130
LS2 (Damage Control)	-0.8430	0.4359	0.7870	0.1880
LS3 (Collapse Prevention)	0.0766	0.1995	2.8621	0.4685

6.3.5 Fragility Comparisons and Discussions

The derived fragilities were compared to each other in order to distinguish the different features from the ground excitations. The effects of record sources, magnitude, distance to source, and site conditions were investigated.

□ Fragility Comparisons with Respect to Natural and Artificial Ground Motion Records

Figures 6.10 and 6.11 present the comparisons between fragilities derived using natural and artificial ground motion records. Comparisons were made between: 1) natural GM Category II and the artificial SEQ series representing close and small earthquakes, and 2) natural GM Category III and the artificial BEQ series for distant and large earthquakes. All fragility curves are based on PGA scales.

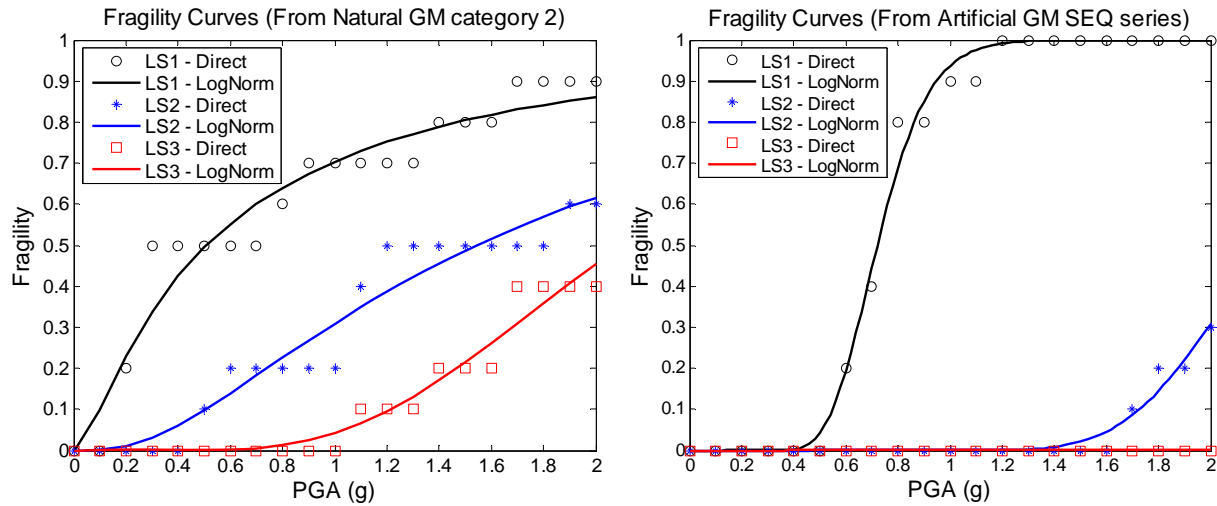


Figure 6.10 Fragility Comparisons for Close and Small Earthquake Categories (Derived from Natural (Left) and Artificial (Right) Records)

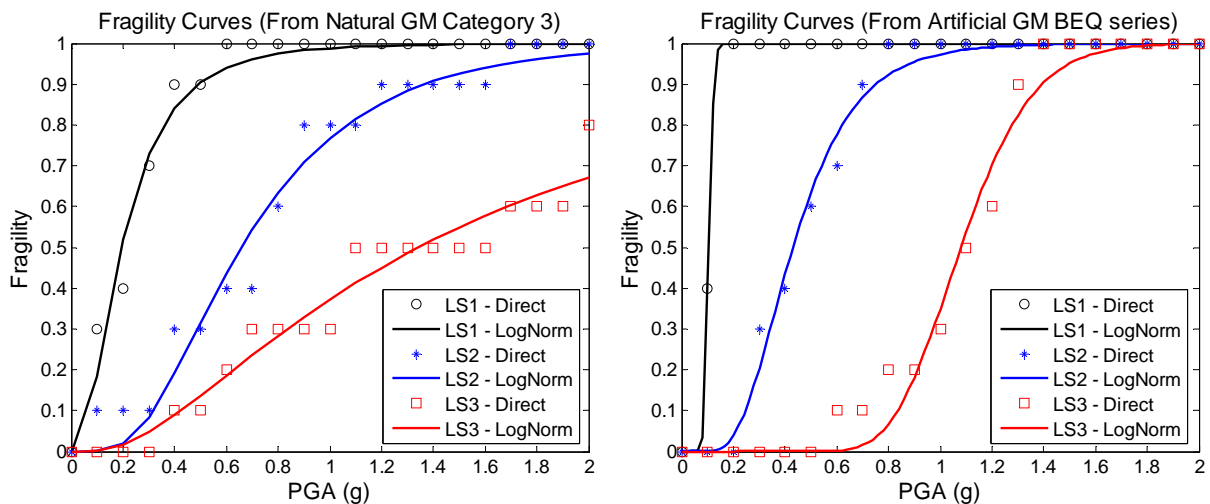


Figure 6.11 Fragility Comparisons for Distant and Large Earthquake Categories (Derived from Natural (Left) and Artificial (Right) Records)

For close and small earthquakes, the fragility for limit state 1 derived from Category II is generally smaller than that derived from the SEQ series at the same intensity level, but those for limit states 2 and 3 show opposite results. For distant and large earthquakes, fragilities from Category III are generally smaller than those from the BEQ series at the same PGA levels. Both the median values and slopes are different between the two types of ground motions. The

disparities are due to differences between natural and artificial ground records. Natural GMs cover very wide ranges of basic earthquake features such as magnitude (M), distance to source (D) and site soil condition (S). They also introduce large variations into seismic demands. On the other hand, the artificial GMs were generated from specific earthquake scenarios, which set M=7.4 and D=100 km for the BEQ series and M=6.0 and D=10 km for the SEQ series. This leads to a smaller variation in seismic demand, which was observed in the analyses.

The comparisons demonstrate that the selected natural ground motion records are preferable to artificial ones for the seismic hazard analysis of high-rise buildings. For regions where neither recorded strong motion data nor known rupture mechanisms exist, artificial strong motion data is necessary and provides fairly good risk prediction.

□ **Fragility Comparisons with Respect to Earthquake Magnitude (M)**

Figure 6.12 shows the comparisons between derived fragilities with respect to natural record Categories I and II, which are both close to the source but at different magnitude levels. All fragility curves are based on PGA scales.

It can easily be observed in Figure 6.12 that fragilities from Category I are much larger than those from Category II for the same limit states and PGA levels. Large differences exist between the basic parameters λ_c and β_c in the simulated fragility functions. The results of these comparisons are reasonable because the Category I ground excitations (with larger magnitudes) usually contain much longer effective durations and more significant peaks than those in Category II. These two characteristics usually dominate the seismic demands for high-rise buildings, especially when accompanied by stiffness degradation in the inelastic stages.

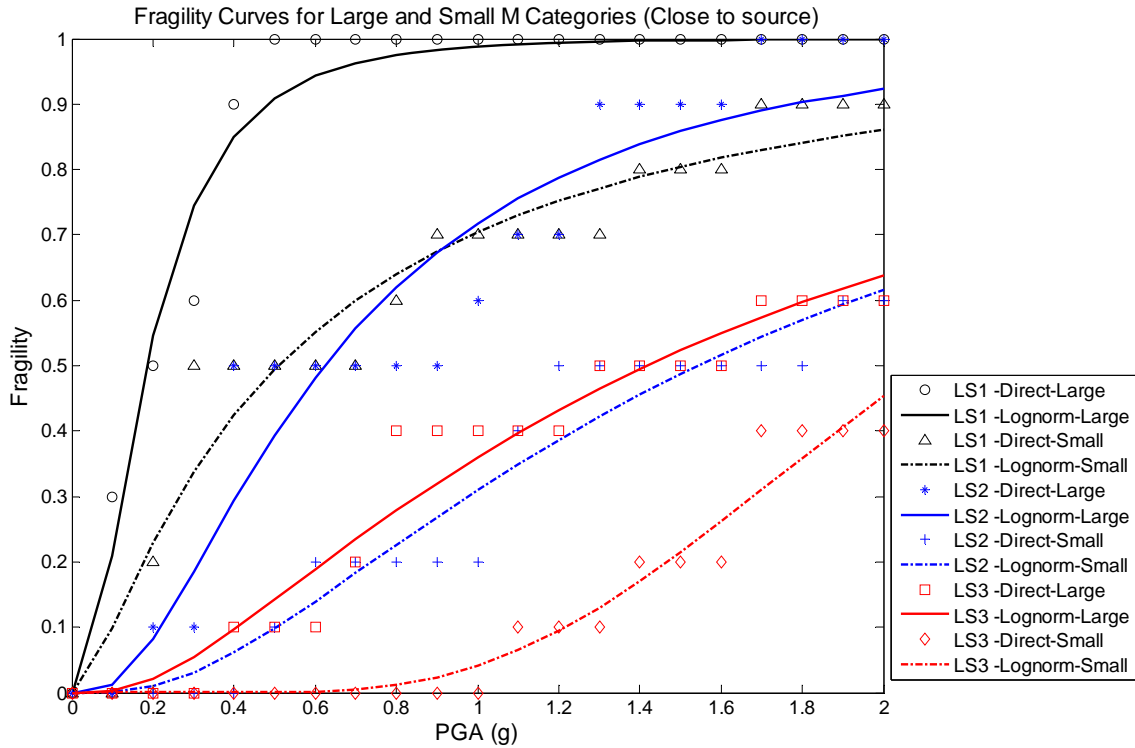


Figure 6.12 Fragility Comparisons for Close to Source Earthquake Categories with Different Magnitude Levels

Hence the magnitude has a significant influence on the seismic risk evaluation of high-rise building populations. The fragility results and comparisons can also relate the earthquake magnitudes to structural performance levels. They can be combined with probabilistic seismic hazard analysis to guide building design for given target earthquake magnitudes and recurrence rates.

□ **Fragility Comparisons with Respect to Distance to Source (D)**

Figure 6.13 shows the comparisons between derived fragilities with respect to natural record Categories I and III, which consist of large magnitudes but at different rupture distance ranges. All fragility curves are based on PGA scales.

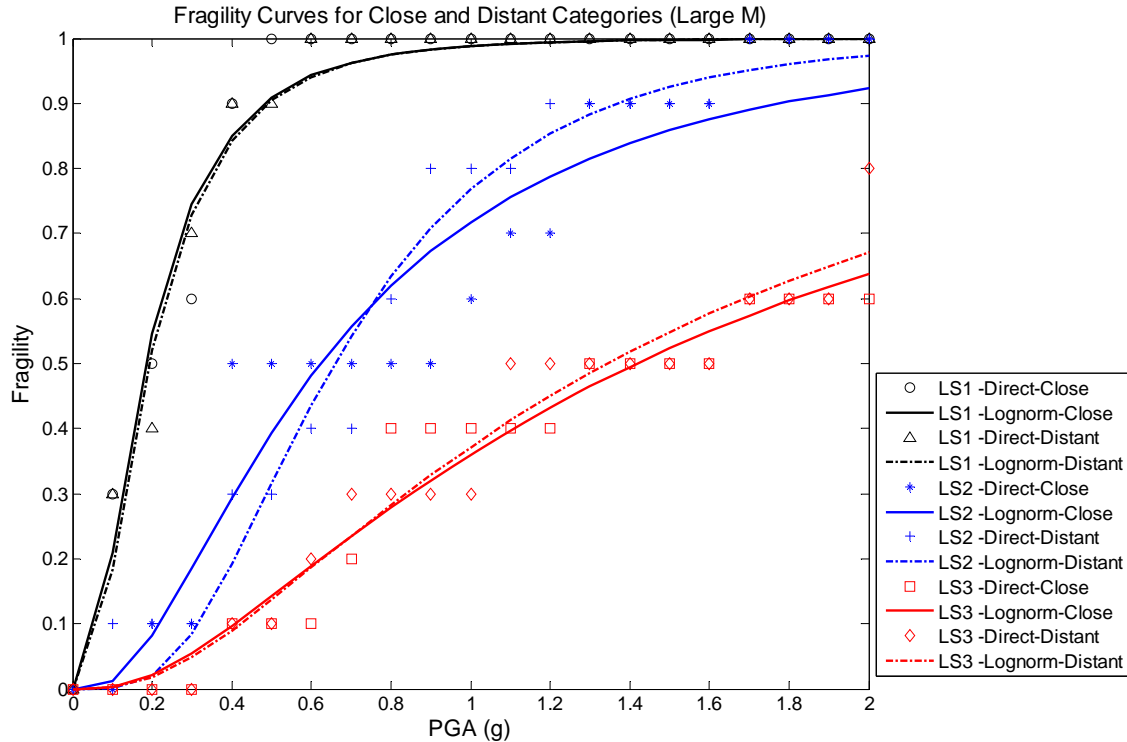


Figure 6.13 Fragility Comparisons for Large Magnitude Earthquake Categories with Different Distances to Source

The two sets of fragilities from Categories I and III are similar as shown in Figure 6.13. One important reason for this is that the selected large magnitude earthquakes in the two categories are very similar in source mechanisms and energy levels, and this leads to similar seismic demands at the same intensity levels. The high frequency contents included in Category I are relatively trivial to the high-rise building dynamic response because the corresponding mass participation factors are much smaller than those from lower modes. After the path attenuation effects filter out the high frequency contents over longer distances, the remaining low frequency fractions of seismic waves still excite considerable structural displacements in high-rise buildings. High fragility is also noticeable in the curves derived from artificial strong motion records, as shown in Figure 6.11.

The discussion above illustrates the truth that a large distance to the source does not necessarily indicate low seismic risk for high-rise buildings. Proper structural analysis and design should consider potential seismic hazards for high-rise buildings even if the site is far from known faults and typically categorized as a low-level seismic zone.

□ **Fragility Comparisons with Respect to Site Soil Condition (S)**

In Figure 6.14, comparisons are presented for fragilities with respect to the GM data from identical earthquakes recorded at different sites, which are listed in Table 5.3. All fragility curves are based on PGA scales.

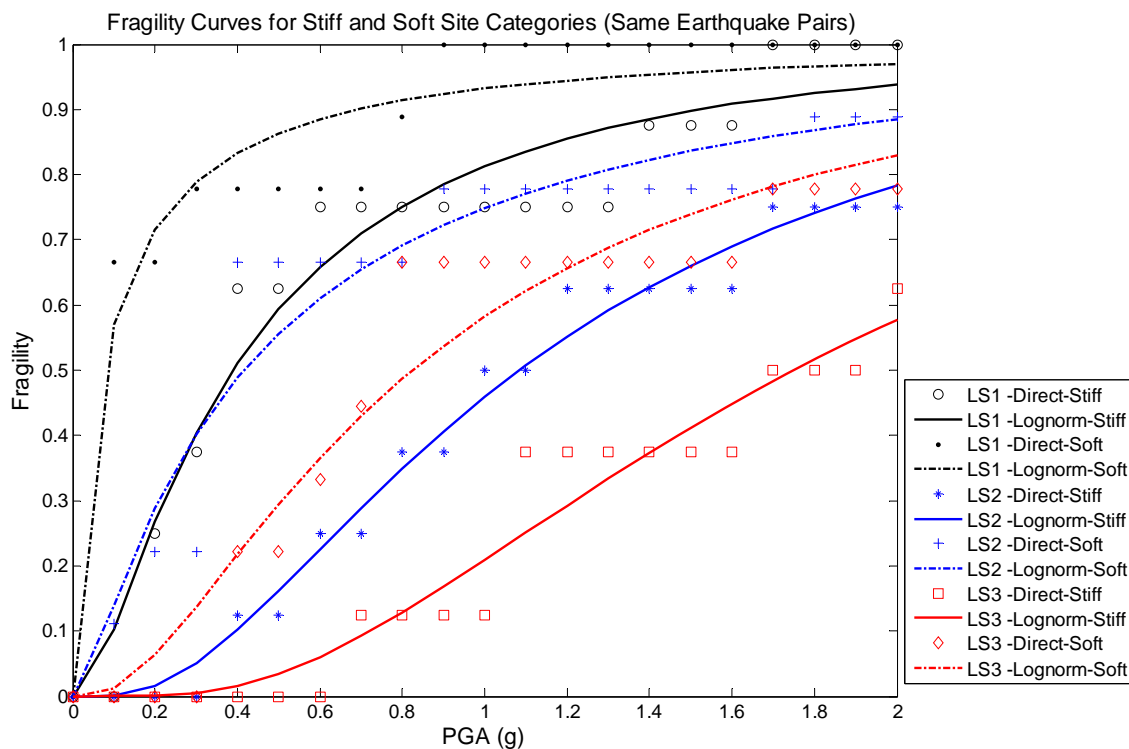


Figure 6.14 Fragility Comparisons for Selected Ground Motion Sets from Same Earthquakes but with Different Site Soil Conditions

The comparison in Figure 6.14 illustrates that the site soil conditions influence the seismic demands of high-rise buildings. Seismic risk at a soft soil site is generally larger than that at a

stiff soil site when the rupture distance range is similar. Soft soil layers dissipate the high frequency energy fractions and amplify low frequency energy fractions while the seismic waves travel from bedrock to ground. Stiff soil exhibits the opposite behavior. Hence ground excitations at soft soil sites will induce larger responses from longer period modes, and these responses become even more significant after inelasticity develops and stiffness degradation elongates the periods.

It can be concluded that the soft soil sites are more likely to impose large seismic demands on the high-rise buildings than stiff soil sites. There are other types of site responses that are not included in this research but may be critical to large-size structures, such as liquefaction at sandy sites and differential settlements.

7. Conclusions and Future Work

7.1 Conclusions

High-rise buildings are on the increase around the world, therefore their detailed assessment under accidental loads is of great importance. The literature is devoid of practical and reliable means of deriving fragility relationships for RC high-rise buildings.

In this study, an innovative seismic fragility assessment framework for RC high-rise buildings is proposed and realized. The framework includes advanced structural analysis of typical buildings, uncertainty modeling of capacity and demand, definition of limit states and the derivation of fragility functions in an efficient and reliable manner. In the course of creation of this framework and development of fragility relationships, the following was accomplished:

- Literature survey on: (i) high-rise RC buildings types, including utilization of RC walls, (ii) current researches on structural fragility curves, (iii) analytical modeling of RC structures with complex systems, and (iv) uncertainty modeling, ground motion characterisation and limit state definitions.
- Tuning of advanced analytical tools of FE building models using Genetic Algorithm optimization for parametric studies. Development of lumped-parameter-based models for the representations for: (i) interactions between core wall and external frame members equivalent by sets of nonlinear interface springs at x, y and rz directions (ii) the behavior of the wall panel itself, such as M- θ , V- Δ relationships and M-N-V interaction patterns, under complex actions and boundary conditions. A final reduced FEM model in ZEUS-NL is created

through the calibration with original complete fiber-based model in ZEUS-NL and continuum FEA in VecTor2.

- Establishments of exceptionally efficient computational procedure for analysis leading to the realization of probabilistic fragility analysis of complex high-rise RC buildings.
- Selected experimental results of shear wall structures are utilized to validate the RC continuum FEM modeling and MCFT solution algorithm in VecTor2. The FEA results on wall specimens with different aspect ratios show very good prediction capacity and consistency with the test data, not only with regard to global action-deformation response, but also on damage patterns and failure modes.
- Fragility derivation that considers: (i) determination of the modeling of inherent uncertainties, mainly from ground excitation, structural material, and geometric properties, (ii) selection and scaling of strong-motion records representative of the scenarios of short and long source-to-site distance earthquakes, different magnitudes and site classifications, and (iii) defining limit states that signify three different levels of impaired use and damage to high-rise buildings based on capacity analyses.
- Limit states are defined based on not only global deformation measures, but also local damage quantities including crack width and steel reinforcement stress. An innovative approach – multi-resolution distributed FEM analysis (MDFEA) is proposed to detect reliably the structural response of RC high-rise buildings, applying the fiber-based inelastic approach in ZEUS-NL to model the beam and column members and the RC continuum FEA in VecTor2 within the UI-SIMCOR simulation coordination framework. To complement the

application of traditional ISD for damage assessment, inter-storey pure translation ratio (ISPT) is introduced as a new measure that removes the rigid body motion effects. Not considering rigid body motion may lead to misinterpretation of high-rise building deformations.

- Through the random fields evaluations, it is concluded that:
 - 1) The concrete strength variation affects the structural response even within the elastic range since the elastic modulus is correlated to f'_c and hence influences the deformation, especially at initial limit states.
 - 2) Accompanied with the increase of concrete strength, stiffer and more brittle behavior is observed and the capacity for limit state LS1 reduces slightly. While an increase of steel yield strength may improve the RC structural performance in the post-cracking stages and thus increase the limit state LS2 criterion.
 - 3) Through the detailed comparisons between response under different acceleration records, the response uncertainties caused by ground excitations are proven to be much more significant in structural dynamic responses than the randomness of material strengths. Hence it is necessary to select appropriate ground motion records and to scale them carefully. In this study, not only natural but also representative artificial strong motion records are chosen, both covering wide ranges in their fundamental features such as magnitude, distance to source and site soil conditions.
- The effective duration concept is utilized to reduce the acceleration record lengths of selected ground motions. Large amount of computational time is saved thereby without compromising

the monitoring of critical features of the dynamic response.

- Development of a complete workable program for the derivation of fragility curves using ZEUS-NL was achieved and verified. Fragilities obtained for all three limit states, through direct simulations with dynamic response history analyses using the selected 30 natural strong motion records based on 20 scales of three intensity measure types: PGA, SA at $T=0.2s$ and SA at $T=1.0s$. An additional 20 artificial strong motion records were employed to derive two distinct sets of fragility curves corresponding to two earthquake scenarios: distant-large earthquake; close-small earthquake.
- Comparisons were made for fragility curves with respect to different strong motion data resources: natural and artificial records. Natural ground motion data are believed to be more appropriate for the seismic risk evaluations of RC high-rise building population than artificial ones. But the latter can be considered as supplemental references especially for the regions where very limited knowledge or records exist for seismic hazard.
- Other fragilities comparisons were also made with respect to different basic features of ground excitations, i.e., magnitude (M), distance to source (D) and site soil condition (S). Amongst, the M and S were proven to have significant effects on the seismic demand of RC high-rise buildings. The other important finding here is the very necessary awareness of the great seismic risk brought to high-rise buildings from distant large earthquakes. All fragilities were categorized into different groups that the literature and community can directly apply for different situations.

7.2 Future Work

The complete and verified functionality of the proposed framework make it practical to extend its application to high-rise building types other than the reference structure. In order to accomplish this, the following work is required:

- The lumped modeling process for RC high-rise buildings must be revised using experimental data---especially for structural walls. Large-scale experimental research that studies the behavior of complex RC walls is currently underway at the University of Illinois at Urbana-Champaign. It includes specimens with different wall shapes, reinforcement ratios, and boundary conditions (Lowe et al. (2004)). Test results could offer more complete and convincing data for structural wall model validation.
- The definitions of limit states must be enhanced to take advantage of the multi-resolution distributed simulation methodology for complex structural systems. This will allow wall-frame interaction effects to be evaluated more accurately. The combination of ZEUS-NL and VecTor2 within UI-SIMCOR can be applied to other structural types, and incremental dynamic analysis can be employed using MDFEA to derive the limit states in addition to the results from static pushover analyses.
- System uncertainties need additional investigation, especially the material properties of high strength concrete and high yield strength steel because they are becoming increasingly popular for modern high-rise construction. More literature surveys and data collections are necessary to obtain this information.
- The simulated lognormal distribution functions should be enhanced by evaluating epistemic

errors caused by the derived material uncertainty effects. Contributions from geometric uncertainties and the construction process need to be taken into account as well. Lower and upper bounds can be provided for the analytical fragility curves at confidence levels, following the methodology proposed by Wen et al. (2003).

- The responses of other building structures should be evaluated using the framework and concepts of this research program. Fragility relationships parameterized by the generic characteristics of high-rise RC buildings will lead researchers and designers to account for uncertainty in a uniform manner when assessing the impact of earthquakes on urban communities.

References

- ACI, (1997), "State-of-the-Art Report on High-Strength Concrete", ACI 363R-92 (reapproved in 1997), ACI Committee 363
- Adeghe, L. N. and Collins, M. P., (1986), "A Finite Element Model for Studying Reinforced Concrete Detailing Problems", Publication No. 86-12, Department of Civil Engineering, University of Toronto
- Ahmad, S. H. and Shah, S. P., (1985), "Behavior of hoop confined concrete under high strain rates", ACI Structural Journal, Vol. 82, No. 5, pp. 634-647
- Algermissen, S. T. and Perkins, D. M., (1976), "Probabilistic estimate of maximum acceleration in rock in the contiguous United States", U.S. Geol. Survey Open-File Report, 76-416, Reston, VA; pp. 45
- Ali, M. M., (2001), "Evolution of Concrete Skyscrapers: from Ingalls to Jinmao", Electronic Journal of Structural Engineering
- Ambraseys, N. N., Smit, P., Douglas, J., Margaris, B., Sigbjörnsson, R. and Olafsson, S., (2004), "Internet site for European strong-motion data", Bollettino di Geofisica Teorica ed Applicata, In press
- Anderson, M. B., (1995), "Metropolitan Areas and Disaster Vulnerability", World Bank Discussion Paper No. 168, edited by Kreimer and Munasinghe
- Bashur, F. K. and Darwin, D., (1978), "Nonlinear Model for Reinforced Concrete Slabs", Journal of Structural Division, ASCE, Vol. 104, No. ST1, pp. 157-170
- Bergmann, R. and Pantazopoulou, V. A., (1988), "Finite Element for R/C Shear Walls Under Cyclic Loads", Report UCB/SEMM-88/09, Department of Civil Engineering, University of California, Berkeley
- Bommer, J. J. and Martinez-Pereira, A., (1999), "The effective duration of earthquake strong motion", Journal of Earthquake Engineering, Vol. 3, No. 2, pp. 127-172
- Bournonville, M., J., D. and Darwin, D., (2004), "Statistical Analysis of the Mechanical Properties and Weight of Reinforcing Bars", A Report on Research Sponsored by The University of Kansas Structural Engineering and Materials Laboratory, Structural Engineering and Engineering Materials SL Report 04-1 December 2004
- Bracci, J. M., Reinhorn, A. M., B., M. J. and Kunnath, S. K., (1989), "Deterministic model for seismic damage evaluation of RC structures", Report NCEER-89-0033, National Center for Earthquake Engineering Research, State University of New York at Buffalo
- Bracci, J. M., Reinhorn, A. M. and Mander, J. B., (1992), "Seismic Resistance of Reinforced Concrete Frame Structures Designed only for Gravity Loads: Part I-Design and Properties

- of a One-Third Scale Model Structure", Technical Report NCEER-92-0027
- Bruneau, M., Uang, C. M. and Whittaker, A., (1998), "Ductile design of steel structures", McGraw-Hill, New York, USA.
- Candappa, D. P., Setunge, S. and Sanjayan, J. G., (1999), "Stress versus strain relationship of high strength concrete under high lateral confinement", Cement and Concrete Research, Vol. 29, No. 12, pp. 1977-1982(6)
- Collins, M. P. and Porasz, A., (1989), "Shear Design for High Strength Concrete", Proceeding of Workshop on Design Aspects of High Strength Concrete, Comité Euro-International du Béton Bulletin d'Information, CEB, Paris; pp. 77-83
- Combescure, D. and Pegon, P., (1997), " α -operator splitting time integration technique for pseudodynamic testing, Error propagation analysis", Soil Dynamics and Earthquake Engineering, Vol. 16, pp. 427-443
- Darwin, D. and Pecknold, D. A., (1977), "Nonlinear Biaxial Stress-Strain Law for Concrete", ASCE Journal of Engineering Mechanics Division, Vol. 103, pp. 229-241
- Darwin, D. and Slate, F. O., (1970), "Effects of Paste-Aggregates Bond Strength on Behavior of Concrete", Journal of Materials, Vol. 5, No. 1, pp. 86-98
- Ellingwood, B. R., T.V., G., G., M. J. and A., C. C., (1982), "Probability-Based Load Criteria: Load Factors and Load Combinations", Journal of Structural Division, ASCE, Vol. 108, No. 5, pp. 978-997
- Elnashai, A. S., Papanikolaou, V. and Lee, D. H., (2002), "Zeus-NL - A System for Inelastic Analysis of Structures"
- Elnashai, A. S., Papanikolaou, V. and Lee, D. H., (2006), "ZEUS-NL User Manual Version 1.7", Mid-America Earthquake Center, University of Illinois at Urbana-Champaign;
- Elnashai, A. S., Pinho, R. and Antoniou, S., (2000), "INDYAS - A Program for INelastic DYnamic Analysis of Structures", Engineering Seismology and Earthquake Engineering Report No. ESEE 00-2, Imperial College, London
- FEMA273, (1997), "NEHRP guidelines for seismic rehabilitation of buildings", Federal Emergency Management Agency, Washington D.C.
- Filippou, F. C. and Constantinides, M., (2004), "FEDEASLab - Getting Started Guide and Simulation Examples," NEESgrid Report 2004-22 and SEMM Report 2004-05, pp. 42
- Ghobarah, A., (2004), "On Drift Limits Associated with Different Damage Levels", BI'04 Conference, June 28-July 1, 2004, Bled, Slovenia
- Ghobarah, A. and Youssef, M., (1999), "Modeling of reinforced concrete structural walls", Engineering Structures, Vol. 21(10), pp. 912-923

- Goldberg, D. E., (1989), "Genetic Algorithms in Search, Optimization and Machine Learning", Addison-Wesley Longman Publishing Co., Inc.
- Han, D. J. and Chen, W. F., (1985), "A Non-Uniform Hardening Plasticity Model for Concrete Materials", Journal of Mechanics of Materials, Vol. 4, No. 4, pp. 283-302
- Hibbit, Karlsson and Sorensen, (2001), "ABAQUS theory manual. Version 6.2"
- Hjelmstad, K. D., (2005), "Fundamentals of structural mechanics", 2nd edition, ISBN 038723330X, Springer
- Holland, J. H., (1975), "Adaptation in Natural and Artificial Systems: An Introductory Analysis with Applications to Biology, Control, and Artificial Intelligence", Ann Arbor, MI: University of Michigan Press
- Housner, G. W., (1952), "Spectrum intensities of strong motion earthquakes", Proc. of Symposium on earthquake and Blast Effects on Structures, EERI.
- Hueste, M. B. D., Chomprea, P., Trejo, D., Cline, D. B. H. and Keating, P. B., (2004), "Mechanical Properties of High-Strength Concrete for Prestressed Members", ACI Structural Journal, Vol. 101, No. 4
- Izzuddin, B. A. and Elnashai, A. S., (1989), "ADAPTIC-a program for static and dynamic analysis of structures by adaptive mesh refinement, user manual", ESEE Report 89/7. Imperial College, London
- Jeong, S. H. and Elnashai, A. S., (2004a), "Analytical assessment of an irregular RC frame for full-scale 3D pseudo-dynamic testing, Part I: Analytical model verification", Journal of Earthquake Engineering, Vol. 9, No. 1, pp. 95-128
- Khan, F. R. and Rankine, J., (1980), "Structural Systems", Tall Building Systems and Concepts Council on Tall Buildings and Urban Habitat/American Society of Civil Engineers, , Vol. SC, pp. 42
- Khan, F. R. and Sbarounis, J. A., (1964), "Interaction of Shear Walls and Frames in Concrete Structures under Lateral Loads", Journal of the American Society of Civil Engineers, 90 (ST3)
- Kircher, C. A., Nassar, A. A., Kustu, O. and Holmes, W. T., (1997), "Development of Building Damage Functions for Earthquake Loss Estimation", Earthquake Spectra, Vol. 13, No. 4, pp. 663-681
- Klink, S. A., (1985), "Actual Poisson Ratio of Concrete", ACI Journal (Nov.-Dec. 1985), pp. 813-817
- Kupfer, H. B. and Gerstle, K. H., (1973), "Behavior of Concrete under Biaxial Stresses", ASCE Journal of Engineering Mechanics, Vol. 99, EM4, pp. 853-866

- Kupfer, H. B., Hilsdorf, H. K. and Rusch, H., (1969), "Behavior of Concrete under Biaxial Stress", *ACI Journal*, Vol. 87, No. 2, pp. 656-666
- Kwon, O. S., Nakata, N., Elnashai, A. S. and Spencer, B., (2005), "A Framework for Multi-Site Distributed Simulation and Application to Complex Structural Systems", *Journal of Earthquake Engineering*, Vol. 9, No. 5, pp. 741-753
- Laogan, B. T. and Elnashai, A. S., (1999), "Structural performance and economics of tall high strength RC buildings in seismic regions", *The Structural Design of Tall Buildings*, Vol. 8, pp. 171-204
- Lee, D. H. and Elnashai, A. S., (2002), "Inelastic seismic analysis of RC bridge piers including flexure-shear-axial interaction", *Structural Engineering and Mechanics*, Vol. 13, No. 3, pp. 241-260
- Lowes, L., Lehman, D., Kuchma, D. A. and Zhang, J., (2004), "Seismic Behavior, Analysis and Design of Complex Wall Systems: Project Summary", *Research Program NSF 03-589 (2004)*
- Lubliner, J., Oliver, J., Oller, S. and Oñate, E., (1989), "A Plastic-Damage Model for Concrete", *International Journal of Solids and Structures*, Vol. 25, No. 3, pp. 299-326
- Lydon, F. D. and Iacovou, M. C., (1995), "Some Factors Affecting the Dynamic Modulus of Elasticity of High Strength Concrete", *Cement and Concrete Research*, Vol. 25, No. 6, pp. 1246-1256
- Mander, J. B., Priestley, M. J. N. and Park, R., (1988), "Theoretical stress-strain model for confined concrete", *Journal of Structural Engineering*, Vol. 114, No. 8, pp. 1804-1826
- Martinez-Rueda, J. E., (1997), "Energy Dissipation Devices for Seismic Upgrading of RC Structures", PhD thesis, University of London.
- Martinez-Rueda, J. E. and Elnashai, A. S., (1997), "Confined concrete model under cyclic load", *Materials and Structures*, Vol. 30(197), pp. 139-147
- Matsumura, K., (1992), "On the intensity measure of string motions related to structural failures", *Proceedings 10WCEE*, Vol.1, pp. 375-380
- McKenna, F. and Fenves, G. L., (2001), "The OpenSees Command Language Manual, Version 1.2", Pacific Earthquake Engineering Research Center, University of California at Berkeley. (<http://opensees.berkeley.edu>)
- Mehta, P. K. and Monteiro, P. J. M., (1993), "Concrete: structure, properties, and methods", Englewood Cliffs: Prentice-Hall, Inc.
- Mendis, P., (2003), "Design of high-strength concrete members: state-of-the-art", *Progress in Structural Engineering and Materials*, Vol. 5, No. 1, pp. 1 -15

- Meyer, C. and Okamura, H., (1985), "Finite Element Analysis of Reinforced Concrete Structures", Proceedings of the US-Japan Joint Seminar on Finite Element Analysis of Reinforced Concrete, Tokyo, Japan
- Mirza, S. A. and MacGregor, J. G., (1979), "Variability of Mechanical Properties of Reinforcing Bars", ASCE Journal of structural division, Vol. 105, No. ST5
- Miyakoshi, J., Hayashi, Y., Tamura, K. and Fukuwa, N., (1997), "Damage Ratio Functions of Buildings using Damage Data of the 1995 Hyogoken-Nanbu Earthquake", ICOSSAR 1997
- Mosalem, K. M., Ayala, G., White, R. N. and Roth, C., (1997), "Seismic Fragility of LRC Frames with and without Masonry Infill Walls", Journal of Earthquake Engineering, Vol. 1, No. 4, pp. 693-719
- Murray, D. W., Chitnuyanondh, L., Rijub-Agha, K. Y. and Wong, C., (1979), "Concrete Plasticity Theory for Biaxial Stress Analysis", ASCE Journal of the Engineering Mechanics Division, Vol. 105, No. EM6, pp. 989-1006
- Nau, J. M. and Hall, W. J., (1984), "Scaling methods for earthquake response spectra", Journal of Structural Engineering, ASCE, Vol. 110, No. 7, pp. 1533-1548
- Nayak, G. C. and Zienkiewicz, O. C., (1972), "Elasto-Plastic Stress Analysis", International Journal of Numerical Methods in Engineering, Vol. 5, pp. 113-135
- Ngo, D. and Scordelis, A. C., (1967), "Finite Element Analysis of Reinforced Concrete Beams", ACI Journal, Vol. 64, No. 2, pp. 152-163
- Nilson, A. H., (1972), "Internal Measurement of Bond Slip", Journal of ACI, Vol. 69, No. 7, pp. 439-441
- Oesterle, R. G., Fiorato, A. E., Johal, L. S., Carpenter, J. E., Russel, H. G. and Corley, W. G., (1976), "Earthquake-Resistant Structural Walls -Tests of Isolated Walls", Report to National Science Foundation, Construction Technology Laboratories, Portland Cement Association, Skokie, ILL. pp. 315
- Ólafsson, S., Remseth, S. and Sigbjörnsson, R., (2001), "Stochastic models for simulation of strong ground motion", Earthquake Engineering and Structural Dynamics, Vol. 30
- Orsini, G., (1999), "A model for buildings' vulnerability assessment using the parameterless scale of seismic intensity (PSI)", Earthquake Spectra, , Vol. 15, No. 3, pp. 463-483
- Otani, S., Kabeyasawa, T., Shiohara, H. and Aoyama, H., (1985), "Analysis of the Full Scale Seven Story Reinforced Concrete Test Structure", ACI SP-84, American Concrete Institute, pp. 203-239
- Palermo, D. and Vecchio, F. J., (2003), "Compression Field Modeling of Reinforced Concrete Subject to Reversed Loading: Formulation", ACI Structural Journal, Vol. 100, No. 5

- Palermo, D. and Vecchio, F. J., (2004), "Compression Field Modeling of Reinforced Concrete Subject to Reversed Loading: Verification", *ACI Structural Journal*, Vol. 101, No. 2
- Park, R., (1988), "Ductility evaluation from laboratory and analytical testing", *Proceedings of the 9th World Conference on Earthquake Engineering*, Tokyo-Kyoto, Japan, Vol. VIII, pp. 605-616
- Park, Y. J., Ang, A. H. S. and Wen, Y. K., (1985), "Seismic Damage Analysis of Reinforced Concrete Buildings", *Journal of Structural Engineering*, ASCE, Vol. 111, No. 4, pp. 740-757
- Paulay, T. and Priestley, M. J. N., (1992), "Seismic design of reinforced concrete and masonry buildings", John Wiley & Sons, Inc., New York, N.Y.
- Pearlman, L., D'Arcy, M., Johnson, E., Kesselman, C. and Plaszczak, P., (2004), "NEESgrid Teleoperation Control Protocol (NTCP)", NEESgrid TR-2004-23, <http://www.neesgrid.org>
- Phan, L. T. and Taylor, A. W., (1996), "State of the Art on Seismic Design Requirements for Nonstructural Building Components", NISTIR 5857, National Institute of Standards and Technology, Building and Fire Research Laboratory, Gaithersburg, MD, U.S. Department of Commerce, Diane Publishing, ISBN 0788142429
- Pinto, P. E., Giannini, R. and Franchin, P., (2004), "Seismic Reliability Analysis of Structures", IUSS Press, Italy
- Popovics, S., (1973), "A Numerical Approach to the Complete Stress-Strain Curve of Concrete", *Cement and Concrete Research*, Vol. 3, No. 5, pp. 583-599
- Rajagopal, K. R., (1976), "Nonlinear Analysis of Reinforced Concrete Beams, Beam-Columns and Slabs by Finite Elements", Ph.D. Dissertation, Iowa State University
- Rossetto, T., (2004), "Vulnerability Curves for the Seismic Assessment of Reinforced Concrete Building Populations", Ph.D. Thesis, Department of Civil and Environmental Engineering, Imperial College, University of London
- Rossetto, T. and Elnashai, A., (2003), "Derivation of vulnerability functions for European-type RC structures based on observational data", *Engineering Structures*, Vol. 25(10), pp. 1241-1263
- Salama, A. I., (1993), "Repair of Earthquake-Damaged Reinforced Concrete Structures", Ph.D. Thesis, Civil Engineering Department, Imperial College of Science Technology and Medicine, University of London
- Salonikios, T. N., Kappos, A. J., Tegos, I. A. and Penelis, G. G., (1999), "Cyclic Load Behavior of Low-Slenderness Reinforced Concrete Walls: Design Basis and Test Results", *ACI Structural Journal*, Vol. 96, No. 4, pp. 649-660
- Scordelis, A. C., Ngo, D. and Franklin, H. A., (1974), "Finite Element Study of Reinforced

- Concrete Beams with Diagonal Tension Cracks", Proceedings of Symposium on Shear in Reinforced Concrete, ACI Publication SP-42.
- Shah, S. P. and Slate, F. O., (1968), "The Structure of Concrete", edited by A. E. Brooks and K. Newman, Cement and Concrete Association, London; pp. 82-92
- Sigbjornsson, R. and Elnashai, A. S., (2005), "Hazard assessment of Dubai, UAE, for close and distant earthquakes", Journal of Earthquake Engineering (in press)
- Singhal, A. and Kiremidjian, A. S., (1997), "A Method for Earthquake Motion-Damage Relationships with Application to Reinforced Concrete Frames", NCEER-97-0008, National Center for Earthquake Engineering Research, State Univ. of New York at Buffalo; pp. 200
- Spacone, E., Filippou, F. C. and Taucer, F., (1996), "Fiber Beam-Column Model for Nonlinear Analysis of R/C Frames: I. Formulation", International Journal of Earthquake Engineering and Structural Dynamics, Vol. 25, No. 7, pp. 711-725
- Spencer, J., B.F., Elnashai, A. S., Park, K. and Kwon, O., (2006), "Hybrid Test Using UI-SimCor, Three-Site Experiment", Final report to NEESit for Phase I project of hybrid simulation framework development, University of Illinois at Urbana-Champaign;
- Tabsh, S. W. and Aswad, A., (1997), "Statistics of High-Strength Concrete Cylinders", ACI Material Journal, Vol. 94, No. 5, pp. 361-364
- Taranath, B. S., (2005), "Wind and Earthquake Resistant Buildings: Structural Analysis and Design", Marcel Dekker, NY
- Vamvatsikos, D. and Cornell, C. A., (2002), "Incremental Dynamic Analysis", Earthquake Engineering and Structural Dynamics, Vol. 31, No. 3, pp. 491-514
- Vecchio, F. J., (1990), "Reinforced Concrete Membrane Element Formulations", Journal of Structural Engineering, Vol. 116, No. 3
- Vecchio, F. J., (2000), "Disturbed Stress Field Model for Reinforced Concrete: Formulation", ASCE Journal of Structural Engineering, Vol. 126, No. 8, pp. 1070-1077
- Vecchio, F. J. and Collins, M. P., (1982), "Response of Reinforced Concrete to In-Plane Shear and Normal Stresses", Publication No. 82-03, Department of Civil Engineering, University of Toronto; pp. 332
- Vecchio, F. J. and Collins, M. P., (1986), "The modified compression field theory for reinforced concrete elements subjected to shear", ACI Structural Journal, Vol. 83(2), pp. 219-231
- Vulcano, A., (1992), "Macroscopic Modeling for Nonlinear Analysis of RC Structural Walls", Nonlinear Seismic Analysis of RC Buildings, Elsevier Science Publishers Ltd., London and New York; pp. 181-190

- Vulcano, A. and Bertero, V. V., (1987), "Analytical Models for Predicting the Lateral Response of RC Shear Walls: Evaluation of Their Reliability", EERC Report No. UCB/EERC-87/19, Earthquake Engineering Research Center, University of California, Berkeley, California; pp. 99
- Wen, Y. K., Ellingwood, B. R., Veneziano, D. and Bracci, J., (2003), "Uncertainty Modeling in Earthquake Engineering", Mid-America Earthquake Center Project FD-2 Report
- WJE, (1994), "Reducing the Risks of Nonstructural Earthquake Damage - A Practical Guide", FEAI 74/September 1994 Supersedes 1985 Edition, 3rd Edition
- Wong, P. S. and Vecchio, F. J., (2002), "VECTOR2 & FORMWORKS USER'S MANUAL", University of Toronto
- Yamazaki, F. and Murao, O., (2000), "Vulnerability Functions for Japanese Buildings based on Damage Data from the 1995 Kobe Earthquake", Implication of Recent Earthquakes on Seismic Risk, Series on Innovation and Construction, Imperial College Press; Vol. 2, pp. 91-102
- Yin, W. S., Su, E. C. M., Mansur, M. A. and Hsu, T. T. C., (1989), "Biaxial Tests of Plain and Fiber Concrete", ACI Materials Journal, Vol. 86, No. 3, pp. 236-243
- Zaman, M., Najjar, Y. M. and Faruque, M. O., (1993), "Modelling of Stress-Strain Behavior of Plain Concrete Using a Plasticity Framework", Materials and Structures, Vol. 26, pp. 129-135